



# ENHANCING THE PERFORMANCE OF SPREAD SPECTRUM TECHNIQUES IN DIFFERENT APPLICATIONS

**Dissertation**

zur Erlangung des akademischen Grades

**Doktoringenieur**

**(Dr.Ing.)**

von **M.Sc. Omar Abdel-Gaber Mohamed Aly**

geb. am 24.9.1970 in Assiut-Egypt

genehmigt durch der Fakultät Elektrotechnik und Informationstechnik  
der Otto-von-Guericke-Universität Magdeburg

Gutachter: Prof. Dr.-Ing A. S. Omar

Prof. Dr.-Ing habil. Bernd Michaelis

Promotionskolloquium am 07.11.2006

*To my parents, my wife (Amira) and my children (Adham  
and Yahya).*

# Table of Contents

<b>Table of Contents</b>	<b>iii</b>
<b>Acknowledgements</b>	<b>x</b>
<b>Zusammenfassung</b>	<b>xi</b>
<b>Abstract</b>	<b>xiv</b>
<b>1 Introduction</b>	<b>1</b>
1.1 Objectives . . . . .	1
1.2 What Does Spread Spectrum (SS) Mean? . . . . .	6
1.3 State of the Art . . . . .	8
<b>2 Fundamentals of Spread Spectrum</b>	<b>18</b>
2.1 Introduction . . . . .	18
2.2 History of the Development of SS techniques . . . . .	19
2.2.1 Radar Techniques . . . . .	19
2.2.2 Communication Theory . . . . .	20
2.2.3 Other Developments . . . . .	20
2.2.4 Early SS Systems . . . . .	20
2.3 General Concepts Related to SS . . . . .	21
2.4 Direct Sequence Spread Spectrum (DSSS) . . . . .	23
2.5 Ranging Using (DSSS) . . . . .	25
2.6 Generation and Characteristics of PN Sequences . . . . .	27
2.6.1 Maximal Length Sequences . . . . .	27
2.6.2 Autocorrelation of a PN Sequence . . . . .	29
2.6.3 Power Spectral Density of a PN Sequence . . . . .	29
2.6.4 Chip Rate and Code Length . . . . .	30
2.6.5 Choosing a Linear Code . . . . .	31
2.7 Software-Implemented Codes . . . . .	31
2.8 Hardware-Implemented Codes . . . . .	31
2.8.1 Linear Feedback Shift Register (LFSR) . . . . .	32
2.8.2 Peripheral Interface Controller (PIC) . . . . .	32

2.8.3	Field Programmable Gate Arrays (FPGA)	34
2.8.4	Arbitrary Waveform Generator (AWG)	34
<b>3</b>	<b>Wavelet Transform and Higher Order Statistics</b>	<b>36</b>
3.1	Introduction	36
3.2	Fourier, Wavelet and Wavelet Packet Transforms	36
3.3	Fourier Transform	38
3.3.1	The Continues Fourier Transform (CFT)	39
3.3.2	The Discreet Fourier Transform (DFT)	39
3.3.3	Short Time Fourier Transform (STFT)	39
3.4	Wavelet Transform (WT)	41
3.5	Wavelet Packet Transform (WPT)	44
3.6	Higher Order Statistics (HOS)	45
3.6.1	Moments and Cumulants of Stationary Random Processes	46
3.6.2	Variance, Skewness and Kurtosis Measures	48
3.6.3	Moments and Cumulants for Gaussian Distributed Random Processes	48
3.7	Denoising	49
3.7.1	Wavelet and Wavelet-Packet Denoising	49
3.7.2	Threshold Selection Based on HOS	51
3.7.3	Algorithms for Signal Denoising Using WPT and HOS	52
3.7.4	Simulation and Results	53
3.7.5	Pulse Localization	54
3.8	Wavelet Denoising of PN Codes	55
3.8.1	Denoising PN Codes Using Harr Wavelet	57
3.8.2	Denoising PN Codes Using Daubechies Wavelet	57
3.8.3	Comparison of Different Mother Wavelets	58
3.9	Applying the Wavelet Denoising to the SS Modulation	59
3.10	Discussions and Conclusion	61
<b>4</b>	<b>Spread Spectrum Automotive Radar</b>	<b>69</b>
4.1	Introduction	69
4.2	Different Types of Automotive Radars	70
4.3	Structure of the Automotive Radar	70
4.3.1	Antenna	71
4.3.2	Radio Frequency (RF) Part of the Automotive Radar	76
4.3.3	Intermediate Frequency (IF) Part of the Automotive Radar	76
4.3.4	Radar Signal Processing (RSP)	77
4.4	Spread Spectrum Automotive Radar Signal Processing	77

4.4.1	Processing of Distance Measurement . . . . .	77
4.4.2	Processing of Velocity Measurement . . . . .	82
4.4.3	Processing of Angle Measurement . . . . .	85
<b>5</b>	<b>Spread Spectrum Indoor Ultrasonic Positioning System</b>	<b>87</b>
5.1	Introduction . . . . .	87
5.2	Application Areas . . . . .	88
5.3	System Hardware Structure . . . . .	89
5.3.1	Ultrasonic Transducer . . . . .	89
5.3.2	Transmitter Unit . . . . .	90
5.3.3	Receiver Unit . . . . .	92
5.3.4	Signal Generation . . . . .	92
5.3.5	Digital Signal Processing . . . . .	93
5.4	Multilateration Algorithm . . . . .	94
5.4.1	Processing of Distance Measurements . . . . .	94
5.4.2	Position Finding . . . . .	96
5.5	Test Configurations . . . . .	98
5.5.1	System Problems . . . . .	99
5.5.2	Multipath Reflections . . . . .	100
5.6	Experimental Results . . . . .	102
<b>6</b>	<b>Spread Spectrum Nondestructive Testing (NDT) &amp; Non-destructive Evaluation (NDE)</b>	<b>106</b>
6.1	Introduction . . . . .	106
6.2	Some NDT/NDE Technologies . . . . .	107
6.2.1	Visual and Optical Testing (VT) . . . . .	107
6.2.2	Radiography (RT) . . . . .	107
6.2.3	Magnetic Particle Testing (MT) . . . . .	107
6.2.4	Ultrasonic Testing (UT) . . . . .	107
6.2.5	Penetrant Testing (PT) . . . . .	108
6.2.6	Electromagnetic Testing (ET) . . . . .	108
6.2.7	Leak Testing (LT) . . . . .	108
6.2.8	Acoustic Emission Testing (AE) . . . . .	108
6.3	History of Ultrasonic Imaging . . . . .	108
6.3.1	History of Nondestructive Evaluation . . . . .	109
6.4	The Concept of Imaging . . . . .	110
6.4.1	Format of the Transmitted Signal . . . . .	110
6.4.2	Pulse Compression Techniques . . . . .	112
6.4.3	Principle of Pulse Compression . . . . .	112
6.5	Spread Spectrum Ultrasonic Imaging . . . . .	114
6.5.1	Signal Coding and Modulation . . . . .	114
6.5.2	Measurement of Reflection and Transmission Coefficients . . . . .	116

6.5.3	Time Domain Impulse Response . . . . .	118
6.5.4	The Root Multiple Signal Classification (RMU-SIC) Algorithm . . . . .	120
6.5.5	Simulation Results . . . . .	122
6.6	Microwave Imaging . . . . .	124
6.6.1	Problem Formulation . . . . .	124
6.6.2	Impact of Limited Bandwidth . . . . .	125
6.6.3	Super Resolution Techniques . . . . .	126
6.6.4	Reconstructing Permittivity Profiles . . . . .	129
6.6.5	Experimental Results . . . . .	130
<b>7</b>	<b>Conclusion and Future Work</b>	<b>136</b>
7.1	Spread Spectrum Automotive Radar . . . . .	136
7.2	Spread Spectrum Ultrasonic Location System . . . . .	137
7.3	Ultrasonic and Microwave Imaging . . . . .	138
	<b>Bibliography</b>	<b>139</b>

## List of Abbreviations

Abbreviation	Meaning
SS	Spread Spectrum
NDT	Non-Destructive Testing
LPI	Low Probability of Intercept
WLAN	Wireless Local Area Network
CDMA	Code Deviation Multiple Access
CW	Continues Wave
DSSS	Direct Sequence Spread Spectrum
PW	Pulsed Wave
SNR	Signal to Noise Ratio
GPS	Global Positioning System
PN	Pseudo Noise
AWGN	Additive White Gaussian Noise
HOS	Higher Order Statistics
IVHS	Intelligent Vehicle Highway Systems
ICC	Intelligent Cruise Control
ITS	Intelligent Transport Systems
CWR	Collision Warning Radar
MMW	MilliMeter Wave
MMIC	MilliMeter wave Integrated Circuit
FMCW	Frequency Modulation Continuous Wave
PD	Probability of Detection
HOS	Higher Order Statistics
TOA	Time Of Arrival
RMUSIC	Root MUltiple SIgnal Classification
BPSK	Binary Phase Shift Keying
LFSR	Linear Feedback Shift Register
PIC	Peripheral Interface Controller
FPGA	Field Programable Gate arrays
AWG	Arbitrary Waveform Generator

FT	Fourier Transform
STFT	Short-Time Fourier Transform
CFT	Continues Fourier Transform
DFT	Discreet Fourier Transform
WT	Wavelet Transform
WPT	Wavelet Packet Transform
DWT	Discrete Wavelet Transform
PRQMF	Perfect Reconstruction Quadrature Mirror Filters
ITS	Intelligent Transport Systems
FLR	Forward-Looking Radar
DSP	Digital Signal Processing
SIMMWIC	Silicon Monolithic Millimeter Wave Integrated Circuit



## List of Symbols

Symbol	Meaning
$p(t)$	PN random binary sequence
$\theta$	Random phase caused by time delay
$L$	PN sequence length
$T_{ch}$	Chipping rate of the PN code
$f_{ch}$	Chipping frequency of the PN code
$\Phi(t)$	Scaling function
$\Psi(t)$	Mother wavelet
$f_s$	Sampling frequency
$f_d$	Doppler frequency
$v$	Speed
$\delta(t)$	Impulse signal
$\Gamma_i$	Local reflection coefficient
$Z_i$	Characteristic impedance
$c_o$	Speed of light in free space
$\varepsilon$	Relative permittivity
$V_i$	Eigenvectors
$\lambda_i$	Eigenvalues

# Acknowledgements

Seldom is anything accomplished without the assistance or encouragement of others. This thesis would also not have been in its present form without the support of many people who, in one way or other, provided help to me. It is my humble duty to thank all those people at this stage.

First and foremost, I would like to thank my supervisor Prof. Dr.-Ing. A. S. Omar for his suggestions and constant support during this research work. I had the opportunity to learn many things from his profound knowledge and experiences and hope to continue collaboration with him in the future. I am also grateful to Prof. Dr.-Ing. habil. Bernd Michaelis, University of Magdeburg for kindly agreeing to be referee for this thesis in spite of his hectic schedules.

Really, I was lucky during my Ph.D research to be able to work with several enthusiastic people. Thanks are due to all colleague of my institute, who were always quite helpful during my stay.

Finally, I express my appreciation to my family specially my parents, whose kind blessings and support have always been with me. I am grateful to my parents for their patience and *love*. Without them this work would never have come into existence (literally). I would also like to thank my wife for her patience with me especially during the final stage of preparing this thesis.

Magdeburg, Germany  
October 2, 2006

Omar Aly

# Zusammenfassung

Das Hauptziel dieser Arbeit ist die Verbesserung der Performance von Spread-Spectrum Techniken für verschiedene Anwendungen. Zu den Anwendungen, die im Rahmen dieser Arbeit betrachtet werden, zählen:

1. Automobilradarsysteme.
2. Ortungssysteme.
3. Ultraschallbildgebung.

Zu den Problemen, die mit den oben genannten Systemen verbunden sind, gehören:

1. Rauscheffekte.
2. Genauigkeit der Systeme.
3. Auflösung der Systeme.

Für Automobilradarsysteme wird eine effiziente, präzise und einfach zu installierende Methode für die Signalverarbeitung eines seitwärtsblickenden Radars vorgestellt. Das System wurde dafür entworfen, Spread-Spectrum Signalen zu verarbeiten. Dabei wird eine neue Methode für die Umsetzung der PN-Code Verschiebung vorgestellt, durch welche die Korrelationsfunktion ermittelt werden kann, mit deren Hilfe der Abstand zum Ziel bestimmt wird. Die vorgestellte Methode erhöht die Genauigkeit ohne die Chiprate des PN-Codes zu erhöhen, was mit einer Erhöhung der Bandbreite verbunden wäre. Es wird eine variable Genauigkeit ermöglicht ohne dadurch die Komplexität des Systems zu erhöhen. Die Ergebnisse der Messung von Abstand und Geschwindigkeit eines bewegten Fahrzeuges werden präsentiert. Für Automobilradaranwendungen ist es notwendig, die Sendeleistung zu reduzieren, um Interferenzen mit anderen Radargeräten zu minimieren und die Batterie des Fahrzeuges zu schonen. Die Reduzierung der Sendeleistung führt zum Problem der Detektion schwacher Signale. Detektion und Lokalisierung von schwachen Signalen sind schwerwiegende Probleme bei der Radarentwicklung. Die Performance des Radars kann durch die Verbesserung des Signal-Rausch-Abstandes (SNR) des Empfängers erhöht werden. Dies ist durch Rauschreduzierungsverfahren möglich, ohne dass dafür die Sendeleistung

erhöht werden muss. Es wird ein Algorithmus beschrieben, der es ermöglicht, einen RF Radarpuls in einem verrauschten Hintergrund zu lokalisieren und zu extrahieren. Dieser Algorithmus vereint zwei wirkungsvolle Methoden: die sogenannte Wavelet Paket Analyse und die Statistik höherer Ordnung. Die Anwendung dieser Techniken ermöglicht die Detektion und Lokalisierung von Radarpulsen in einer Umgebung mit nur sehr geringem Signal-Rausch-Abstand, wodurch die benötigte Sendeleistung reduziert bzw. der Detektionsbereich des Radarsystems erhöht werden kann.

Die zweite Anwendung ist das Problem der Ortung. Einer der großen Vorteile von Spread-Spectrum Techniken ist deren Multi-User Kapazität, welche die Entwickler von Ortungssystemen ermutigt, diese Techniken zu verwenden. Viele mobile Anwendungen können stark erweitert werden, wenn die Position der Geräte bzw. Nutzer ermittelt werden kann. Ein Ultraschall-ortungssystem stellt hochaufgelöste Positionsinformationen für diese Anwendungen zur Verfügung. In dieser Arbeit wird ein Ultraschallsystem betrachtet, das für die Überwachung der Position bewegter Zielobjekte entwickelt wurde. Die Verwendung von Spread-Spectrum Techniken für das Ultraschall-Ortungssystem ermöglicht die Anwendung in einer verrauschten Umgebung. Gleichzeitig wird das Problem der Signalkollision gelöst, das immer dann entsteht, wenn mehr als ein Sendesystem zur selben Zeit aktiv ist. Testergebnisse demonstrieren, dass das vorgestellte Ultraschall-Ortungssystem in der Lage ist die Position bewegter Zielobjekte mit hoher Genauigkeit zu bestimmen. Die meisten der existierenden Ultraschallerzeuger, die in Positionierungssystemen verwendet werden, haben eine begrenzte Bandbreite. Verursacht durch Mehrwegeausbreitungen in der Umgebung kommt es deswegen zu einer Ziellokalisierung mit nur schlechter Auflösung. Unterschiedliche Super-Resolution Techniken wie Estimation of Signal Parameter via Rotational Invariance Techniques (ESPRIT) und Multiple Signal Classification (MUSIC) sind für die Bestimmung des Spektrums verwendet worden. Das in dieser Arbeit beschriebene System löst das Problem der begrenzten Bandbreite der Ultraschallübertrager durch die Anwendung der Super Resolution Technik Root Multiple Signal Classification (RMUSIC) bei der Bestimmung der Signallaufzeit der Ultraschallsignale.

Als eine dritte Anwendung wird die Bildgebung betrachtet. Auflösung und Rauscheffekte sind primäre Kriterien für die Bildqualität. Ursprünglich wurde die große Bandbreite für die Auflösung durch kurze Pulse erzeugt, was ein Abwägen zwischen Auflösung und Rauscheffekten notwendig macht. Die Schallspitzenleistung begrenzt den Signal-Rausch-Abstand von Ultraschallsystemen zur Bildgebung. Ein codiertes System überträgt einen Breitbandpuls mit einem endlichen Zeit-Bandbreite-Produkt. Das empfangene Bild muss decodiert werden, um aufgrund der höheren durchschnittlichen Anregungsleistung einen bildgebenden Puls mit verbessertem SNR zu gewinnen. Decodierung kann jedoch beträchtliche Nebenkeulen erzeugen und die Bildqualität bzw. die Auflösung reduzieren. Alle praktischen Codiersystementwürfe stellen deshalb einen Kompromiss zwischen Verbesserung des Signal-Rausch-Abstandes

und Nebenkeulenbildung dar. Der sogenannte RMUSIC Algorithmus ist ein bekanntes Verfahren für die Detektion von Signalen in Kommunikationssystemen mit Mehrpfadausbreitung. In dieser Arbeit wird die Verwendung des RMUSIC Algorithmus zur Behebung des Nebenkeulenproblems vorgestellt. Die Ergebnisse zeigen, dass durch Verwendung von RMUSIC der decodierte Puls ohne zusätzliche Nebenkeuleneffekt fast perfekt wiederhergestellt werden kann. Dies führt zu einer starken Verbesserung des SNR von codierten Anregungstechniken, ohne dass dabei die Bildqualität bzw. die Bildauflösung reduziert wird.

Neben der Bildgebung durch Ultraschall wird das Problem der Bandbreitenbegrenzung auch für Mikrowellensysteme betrachtet. Diese Arbeit beschreibt eine Technik für die Rekonstruktion eindimensionaler geschichteter Permittivitätsprofile. Die vorgestellte Technik basiert auf der Inversion der im Frequenzbereich gemessenen Reflexionskoeffizienten in einen virtuellen Zeitbereich. Die Inversion der Reflexionskoeffizienten basiert ebenfalls auf der Super Resolution Technik RMUSIC. Der Vorteil der Anwendung dieser Methode ist dessen Fähigkeit, Nebenkeuleneffekte vollständig zu entfernen, welche durch die begrenzte Bandbreite verursacht werden. Messungen mit verschiedenen Materialprofilen belegen die Qualität der vorgestellten Technik.

# Abstract

The main objective of this work is to improve the performance of spread spectrum techniques in different applications. The applications that will be considered in this thesis are.

1. Automotive Radar.
2. Indoor Positioning Systems.
3. Ultrasonic and Microwave Imaging.

The problems associated with the above mentioned systems are:

1. Noise Effect.
2. Accuracy of the System.
3. Resolution of the System.

For the automotive radar an efficient, accurate and easy to implement system for a sideways-looking radar signal processing is presented. The system is designed to work with a spread spectrum signal. A new method for implementing the shifting of the PN code is proposed. It is applied for calculating the correlation function which is used to measure the target range. The proposed method results in a higher accuracy without increasing the chip rate of the PN code (which necessitates increasing the bandwidth). Also the proposed method has the facility of variable accuracy without increasing the complexity of the system. Results on measurement of the distance to and the velocity of a moving vehicle are presented. In the automotive radar it is very important to reduce the required transmitted power in order to reduce the interference due to the existence of multi radar systems on the high ways and also to save the battery of the car. Reducing the transmitted power will lead to the problem of weak signal detection. Weak signal detection and localization are therefore basic and important problems in radar systems. Radar performance can be improved by increasing the receiver output signal-to-noise ratio (SNR) without the need for increasing the transmitted power. This can be achieved by cleaning up the received signal from the noise (denoising). An algorithm is described for extracting and localizing an RF

radar pulse from a noisy background. The algorithm combines two powerful tools: The wavelet packet analysis and the higher-order-statistics (HOS). The use of the proposed technique makes detection and localization of RF radar pulses possible in very low SNR conditions, which leads to a reduction of the required microwave power or alternatively extending the detection range of radar systems.

The second application to be considered is the positioning. One of the great advantages of spread spectrum techniques is the multi user access, which encourage the people working in the filed of local positioning systems to use it. Many mobile applications can be greatly enhanced when provided with the locations of people and devices. Indoor ultrasonic positioning systems provide fine-grained position data for such applications. An ultrasonic tagging system developed for monitoring the location of a moving target is considered in this work. Use of spread spectrum in ultrasonic location systems allows the system to work at a noisy environment. At the same time it solves the problem of signal collisions when more than one transmitter transmit at the same time. Test results demonstrate that the system is able to locate the position of a moving target with high accuracy. Most of the existing ultrasonic transducers used in local positioning systems have a limited bandwidth, which leads to a poor resolution in locating the position of a target duo to multi-path reflections from the surroundings. Different super resolution techniques such as Estimation of Signal Parameters via Rotational Invariance Techniques (ESPRIT) and Multiple Signal Classification (MUSIC) have been used for spectral estimation applications. The proposed system in this thesis solves the problem of limitation in ultrasonic transducers bandwidth by applying the RMUSIC super resolution technique to estimate the time of arrival of ultrasonic signal.

As a third application imaging is considered. Resolution and noise effects are primary criteria. Conventionally, high bandwidth for resolution was achieved with a short pulse, which results in a trade-off between resolution and noise effect. Peak acoustic power limits the SNR of real-time ultrasound imaging. The SNR can be significantly increased using coded excitation. A coded system transmits a broadband pulse with a finite time-bandwidth product. The received signal must be decoded to produce an imaging pulse with improved SNR resulting from higher average power in the excitation. However, decoding can produce significant range side lobes greatly reducing image quality or image resolution. All practical coding designs, therefore, represent a trade-off between SNR gain and range side lobes. The root multiple signal classification (RMUSIC) algorithm is a known technique in multi-path detection in communication. In this thesis we propose using the RMUSIC algorithm to overcome the problem of range side lobes. Results indicate that the RMUSIC algorithm is able to perfectly reconstruct the decoded pulse without any range side lobes effect. This will leads to a greet improvement in SNR coded excitation techniques without reduction in the image quality or image resolution.

Beside the ultrasonic imaging the problem of bandwidth limitation in microwave imaging is considered as well. The thesis proposes a technique for reconstructing one-dimensional stratified permittivity profiles. The proposed technique is based on the inversion of the measured frequency-domain reflection coefficient of the profile into a virtual time domain. The inversion of the reflection coefficient is based on the super resolution technique RMUSIC. The advantage of using this technique is its ability to remove the side lobe effect caused by the limited measurement bandwidth. Measurements using different materials have been carried out to validate the quality of the proposed technique.



# Chapter 1

## Introduction

### 1.1 Objectives

Development of the first spread spectrum (SS) systems began at least six decades ago [1–9]. During the world war II SS devices were already in action. They were used mostly in radar. The early systems were designed to provide low detectability or protection from jamming or interface. Most of the applications of SS techniques previously were in the fields of military applications such as radar and communication systems. Recently SS technique becomes very popular in many civilian applications. In the field of communications the SS technique is used in mobile networks communication and wireless local area network (WLAN). In these two fields the SS technique is known with the name code deviation multiple access (CDMA) [1], [10]. The uses in communication alone include anti-jamming, anti-interference, low probability of intercept (LPI), message privacy, multiple-users access, and selective addressing.

As a modern civilian application of the SS technique in radar is the automotive radar [11–40] (more details about automotive radar will take place in chapter 4). In the automotive radar application the SS technique is used in two modes. The first mode is the continues wave (CW) mode, in which the radar continuously transmit an encoded signal. This encoded signal is constructed from a carrier which is amplitude modulated with a certain pseudo noise (PN) binary sequences code. This kind of modulation is called direct sequence spread spectrum (DSSS) modulation. The second mode is the pulsed wave (PW) mode, in which the radar transmits a modulated encoded pulse. This technique of transmitting an encoded pulse in radar is conventionally known as pulse compression technique. In automotive radar the SS modulation has a number of features that make it easy to achieve the following characteristics:

- Accurate distance measurements.
- Separation and detection of multiple vehicles located in the range direction.
- Improving signal to noise ratio (SNR), and interference eliminating capability.

For the reasons mentioned above, the SS modulation was considered more suitable for modern automotive radar, and it was used in the development of the millimeter wave radars. Fig. 1.1 shows two different applications of the automotive radar, the upper panel is a stop and go and the lower panel is pedestrian detection automotive radar.

Another potential application of the SS technique is in the field of navigation. In this field the SS is very popular in the well-known global positioning system (GPS) [41]. Fig. 1.2 shows the real-time differential GPS. Now a days with the existence of WLAN and Ubiquitous computing [42] applications, which require context information in order to blend seamlessly into the environment and to unobtrusively aid people in their everyday lives, a particularly important component of context is the location of people and the objects they interact with, numerous ubiquitous applications utilizing location information have been developed. For this the necessity for indoor location systems (more details about indoor location system will take place in chapter 5) is increased [43–54]. Some of these indoor location systems are based on the SS technique [55–57]. Fig. 1.3 shows different applications, which are based on indoor and outdoor location systems.

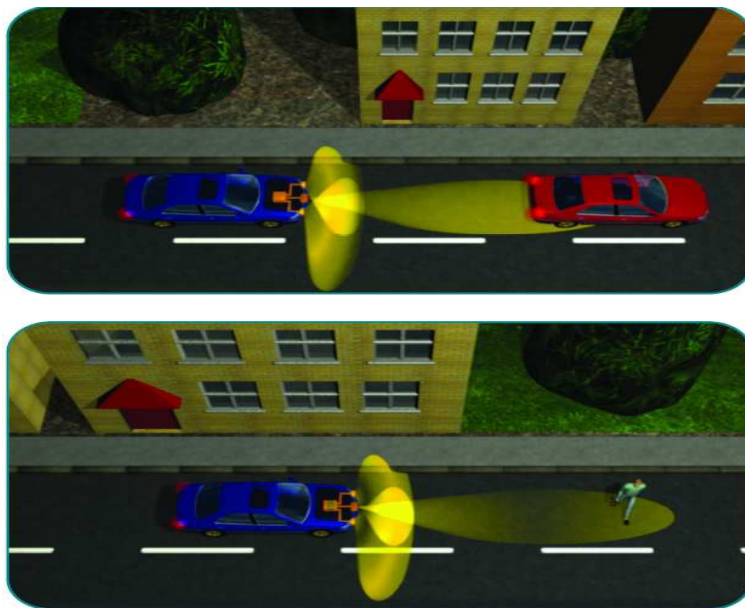


Figure 1.1: Two important applications for automotive radar.

As was mentioned previously the pulse compression technique or coded excitation technique is well established in radar, producing dramatically improved SNR at modest peak power levels compared to the conventional pulsed technique [58], [59]. As the problems are comparable, there have been many attempts to implement the pulse compression technique within ultrasonic nondestructive testing (NDT) applications (more details about ultrasonic NDT will take place in chapter 6) [60–76]. It was not until the very mid-seventies and early eighties that the application of coded excitation

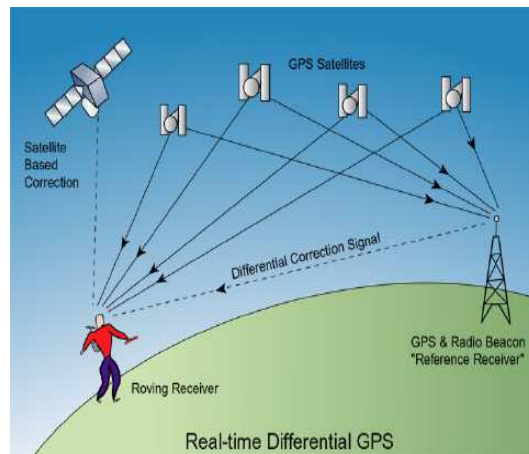


Figure 1.2: Real-time differential GPS.

was discussed in the context of ultrasound medical imaging. Among the earliest discussions of coded waveforms in the field of NDT are those by Newhouse and Furgason in the mid 1970's using a random noise generator as a signal source and performing correlation on the received echo signals and a reference copy of the transmitted noise signal. A few years later, in 1980, Lee and Furgason described the use of PN binary sequences, including Goaly codes, in the context of phased array-based flow detection. About the same time, Takeuchi described the use of SS techniques for medical ultrasonic imaging. It is interesting to reflect in the fact that these early works were presented practically simultaneously with the introduction of phased array medical ultrasonic imaging. However, it was not until the late 1990's that General Electric successfully introduced coded waveforms to diagnostic ultrasound scanner. Fig. 1.4 shows two applications of ultrasonic in NDT in the field of material testing Fig. 1.4(a) and medical diagnostics Fig. 1.4(b).

The objective of this thesis is to investigate the difficulties of applying the SS technique in the following three applications:

- Millimeter wave automotive radar.
- Ultrasonic indoor location system.
- Ultrasonic and microwave imaging.

The common thing, between the above three mentioned applications, is the ranging. The objective of the automotive radar is to sense the surrounding environment (some kind of imaging) of the vehicle, which is occupied by the radar. Sensing the surrounding environment means detecting the existence of other vehicle or objects and measuring the relative distances and velocities of these objects to give the driver of this vehicle a complete view of the road in order to avoid accidents. In the case of indoor location systems, the main requirements for determining the location of a

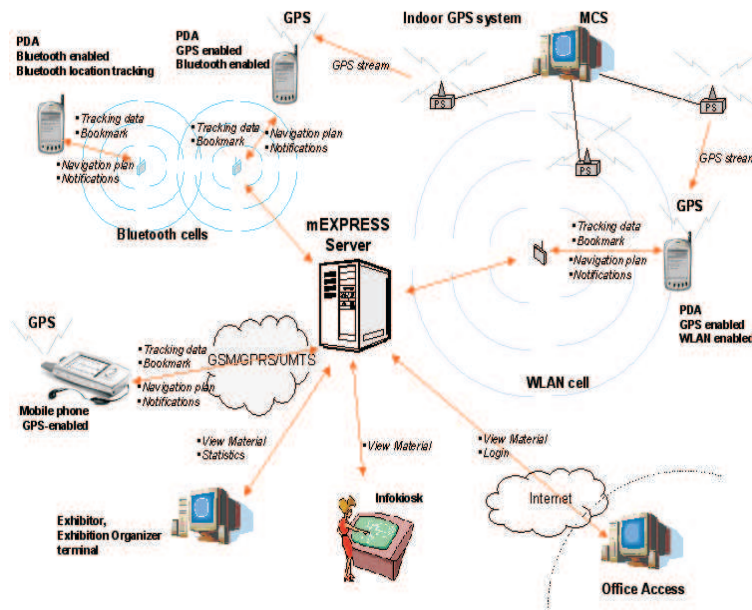


Figure 1.3: Different applications, which are based on user location information.

user is to measure the distances between the user transmitter and fixed receivers. In the case of ultrasonic or microwave imaging the objective is the reconstruction of inhomogeneous density (ultrasonic imaging) or permittivity (microwave imaging) profiles of layered media, which include measuring the thickness and the mechanical or electrical properties of each layer.

The overall process of imaging can be well understood with the help of Fig. 1.5, where  $h(t)$  represents the impulse response of the object under test, which can be the surrounding environments (automotive radar) or a material under test (NDT). It is possible to get some useful information (like mechanical or electrical properties) about this object if we are able to measure its impulse response  $h(t)$ . In order to measure the impulse response of the object one needs to illuminate it with a signal  $x(t)$ , which can be electromagnetic waves or ultrasonic waves, and measure the scattered signal  $y(t)$  interacting with the object to obtain the image of the distribution of the properties of the object from these measurements. The relation between the transmitted signal  $x(t)$ , the received signal  $y(t)$  and  $h(t)$  is given as:

$$y(t) = x(t) * h(t) + n(t) \quad (1.1)$$

where the  $*$  denotes convolution and  $n(t)$  is an additive white Gaussian noise (AWGN) associated with the measurements. The process of obtaining the impulse response of the object is called the direct problem, which is associated with an inverse problem to get some information about the properties of the object using the result of the direct problem. In the direct problem there are three main factors that affect the quality of the measurements. These three factors are;



(a)



(b)

Figure 1.4: (a) Air coupled ultrasonic transmission through a thick (2 inches, about 250 plies) carbon composite laminate (b) Diagnostic medical ultrasonic scanner.

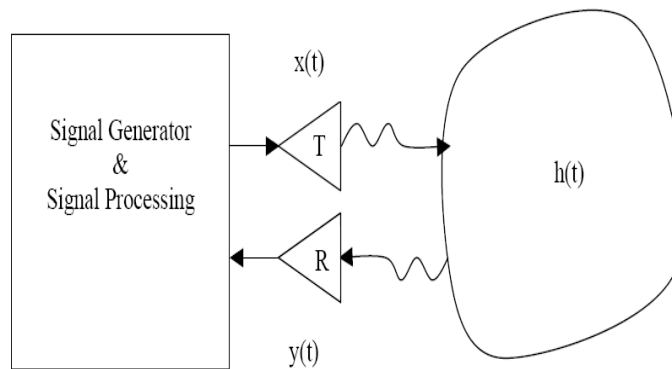


Figure 1.5: A typical example of imaging.

- Noise during the measurements.
- Accuracy of the measurements.
- Resolution of the measurements.

Any measurements are accompanied with measurement noise, which can limit the reconstruction of weak reflections this can lead to errors in measuring the impulse response of the system. In the same time any measurement system has limited measurement accuracy, which is defined as how accurate the system is able to locate a target, and measurement resolution, which is defined as how accurate the system is able to differentiate between two targets, these limitations in the accuracy and resolution will also lead to limitations in the reconstruction of the impulse response of the system. In this thesis an investigation for the performance of the SS technique

for the above-mentioned applications will take place. In the same time we will try to improve the performance of the SS technique against the above-mentioned three difficulties of the measurements.

This thesis is organized as follows. In the next section of this chapter, the concept behind SS technique is briefly discussed, which indicates the powerful behind the use of SS technique in different applications. The last section of this chapter provides a state of the art indicating the different techniques for solving for the limitations of applying the SS technique in the above-mentioned applications. The second chapter gives more details about the SS technique in general, the requirements for the implementation of SS technique and explains the difficulties associated with it. In the third chapter, a general explanation for the different signal processing algorithms, which will be used in this thesis in enhancing the performance of the SS technique, will take place. These signal processing tools will include the use of wavelet and wavelet packet transform and higher order statistics (HOS) to improve the noise performance of SS system. Also the discussion will include the super resolution techniques, which will be used to improve the resolution of SS system. Different examples will be given in this chapter to indicate the use of the above-mentioned signal processing algorithms in improving the performance of the SS technique. The fourth chapter describes in detail the use of SS technique in automotive radar application, which will include the requirements for the automotive radar, the limitations of applying the SS technique in automotive radar and different approaches to overcome for these limitations. Also it will include different results indicate the improvement in the performance of SS technique in this application. The same approach will be followed in chapter 5, for SS ultrasonic indoor positioning system, and chapter 6 for SS nondestructive testing, which will include ultrasonic and microwave imaging, we have reconstructed a number of permittivity profiles using experimental reflection coefficient data to validate our technique. Finally, a summary of the overall work is given in the seventh chapter.

## 1.2 What Does Spread Spectrum (SS) Mean?

After exploring the potential applications of the SS technique in different fields and the objectives of this thesis, let us first understand the idea behind the SS technique, which make it very popular in many applications. Literally, a SS system is one in which the transmitted signal is spread over a wide frequency band, much wider, in fact, than the minimum bandwidth required to transmit the information being sent. A SS system employs two identical PN sequence generators, one that interfaces with the modulator at the transmitting end and the second that interfaces with the demodulator at the receiving end. These two generators produce a PN sequence, which is used to spread the transmitted signal at the modulator and to despread the received signal at the demodulator. Fig. 1.6 shows a comparison in the time and frequency domain between the transmitted signal with and without SS modulation

for pulse compression technique. As it is clear from Fig. 1.6(a, b) the total duration of the transmitted signals in the time domain are the same. In the other hand Fig. 1.6(c, d) the required bandwidth with SS is larger than that without SS technique. In both cases one should notice that the average power is the same. The difference in the case of SS is the distribution of the same average power through a larger bandwidth as its clear from Fig. 1.6(c, d).

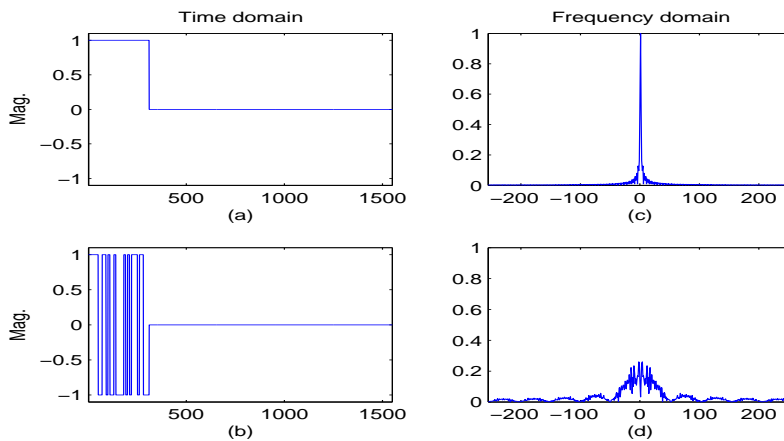


Figure 1.6: (a, c) Transmitted pulse without SS modulation (in time and frequency domain), (b, d) Transmitted pulse with SS modulation (in time and frequency domain).

In the receiving side it is required to decode the received signal in order to reconstruct the original pulse with high resolution and in the same time improving the noise performance. For decoding the received signal it should be passed to a linear transform, which is able to localize the signal and reduce the noise. In general any linear transform could be represented as a correlation between the received signal and the kernel of the transform. To satisfy high correlation, which is a measure for the similarity between the received signal and the kernel of the transform, a copy from the transmitted code should be used as the kernel of the transform. For the above-explained reason the coded signal is decoded using a correlation-based procedures, which can be implemented using matched filtering or mismatched filtering techniques. Fig. 1.7 shows pulse compression filter used for decoding the received signal. The left hand side shows the received signal and the right hand side shows the compressed pulse. The pulse compression filter is used to convert a wide duration signal with low amplitude to a narrow duration signal with high amplitude, which leads to a gain in the SNR of the received signal.

From the previous discussion one can conclude that pulse compression technique is a convenient method of increasing the signal duration without a proportionate decrease in the bandwidth. Increasing the signal duration will leads to increasing the average power of the signal without increasing the peak power. In the other hand



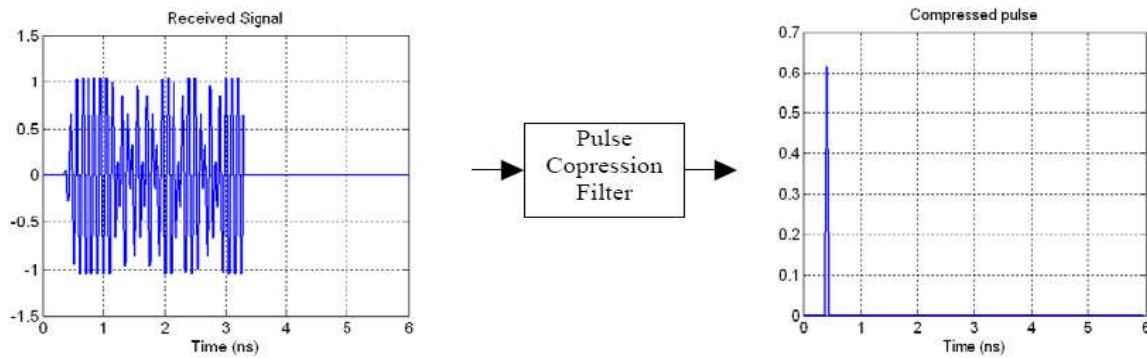


Figure 1.7: Decoding the received signal using pulse compression filter.

this will not lead to a reduction in the bandwidth, which mean that we still have high resolution in the measurements. With pulse compression technique, it is possible to design signals of extreme complexity and yet leave the associated equipment relatively manageable.

### 1.3 State of the Art

Spread spectrum technique, applied in recent years, has produced results in communications, navigation, and test systems that are not possible with standard signal formats. In many applications the advantage of high-speed electronics was the key to practical sized-and-powered equipment based on SS modulation. Over the past few years, automotive sensors/radar have become an important and interesting area for microwave and millimeter wave (MMW) applications. They are not only have the huge market potential of the automotive industry but also will play an important safety role in the future intelligent vehicle highway systems (IVHS). Many automobile manufactures now believe that intelligent cruise control (ICC) systems go some way to alleviating these problems and that high definition radars operating in the MMW bands are the ideal distance sensors for these systems. There are many research efforts related to radar sensors using MMW technology, which is fundamental to enable all-weather conditions operation of intelligent transport systems (ITS). It is hoped that the wider use of automotive MMW radar will reduce serious traffic accidents that so frequently occur on limited-access highways in foggy or snowy conditions. Automotive radar systems for highway vehicles are designed to be a countermeasure to one or more classes of recognized crash types. Crash avoidance systems product development is currently focused on automotive systems, that is, systems that are totally self-contained within the host vehicle and require no external support from other vehicles or roadside infrastructure. Sensors for autonomous systems will be precursor to the sensor required for cooperative and fully automatic highway systems of the next decade. Autonomous crash avoidance systems generally fall into two main



categories based on the applications and the requirements of the radar. These two categories are the ICC and the collision warning radar (CWR).

There are several sensor types that have or could be used in automotive applications. Including among them are acoustic, optical (visual, laser, and infrared), and MMW radar. The environment in which the sensor must operate plays an important role in the decision to pick one technique over another. The sensor should be able to adequately perform in any commonly encountered weather condition, including rain, snow and fog. The physical effects of inclement weather, such as water, ice, or mud buildup on the sensor face must not catastrophically affect its performance. While infrared and laser systems can penetrate fog and rain to some degree, they severely degrade in sensitivity with any buildup of foreign material on the sensor face. The laser-based system has the disadvantage of limited field of view and poor close-range resolution as well as possible eye safety concerns. The potential health hazard posed by a large number of crash avoidance systems operating in dense traffic must also be considered, an issue more challenging for laser radars. The effects of weather on visual light sensor are even more severe. Acoustic sensors are not sensitive enough to effectively perform at the required ranges. MMW radar performs well in all weather conditions likely to be encountered and tolerates the physical effects of weather without catastrophic consequences.

There are two dominant factors, in addition to the performance requirement for all-weather conditions, which drive the technology for automotive MMW radars: cost and hardware size. Low cost is the key factor for consumers to accept the radar as a safety and affordable component of their vehicle. The size constraint is essential for easy integration of the radar on the vehicle without major impact on the vehicle design and performance. Within the radio wave spectrum, the use of MMW (30-300 GHz), was found to offer a number of advantages over the microwaves, (3-30 GHz), which is a congested frequency band and require large antenna size, include.

- Higher directionality, reducing spurious operation and interference.
- More compact and lightweight equipment, particularly antennas.
- Greater Doppler shift, improving the accuracy of velocity measurements.
- Wider band for higher range resolution.
- Comparatively high attenuation in air, reducing interference when two systems are installed close together, and thereby allowing a number of systems to coexist.
- Good angular resolution to be obtained from antennas, which are small enough to be used in a car.

A frequency band of 76-77 GHz has been made available for DRIVE and PROMETHEUS automotive radar in Europe. For the introduction of novel low-cost radar system with

improved performance further advancement in MMW technologies, like high yield semiconductor processes with high throughput, highly integrated MMW circuit with high efficiency and sensitivity, and innovative antennas are required. Advances in GaAs or Silicon millimeter wave integrated circuit (MMIC) technology enable operation at millimeter wavelengths, providing reduction in size, weight, and production costs. Higher resolution radar and fusion with other on board sensors will improve the performance and functionality of future car electronic systems which finally will lead to novel intelligent features such as automatic tracking or autonomous driving.

There are three common signal modulation techniques exist in radar applications, pulsed radar [13], frequency modulation continuous wave (FMCW) radar [11–17], and SS radar [18–29], [77–80]. The choice of the modulation technique depends mainly on the application. It must be suitable for multi-target situations and resistant to interferences between a great number of cars, which can be equipped also with such radars. In FMCW the radar measure the range using the swept frequency technique. To achieve good distance resolution, the FMCW approach requires a linearization circuit also it shows some problems with the separation of distance and speed information. In FMCW in order to achieve 0.5 m range resolution, the VCO requires a tuning range of more than 350 MHz. The target range resolution decreased at longer distance, indicating that the VCO linearity needs to be further improved for better results. Pulsed radar is very simple in construction and uses few MMW components but it is very inefficient since energy transmitted in the inter-pulse period is wasted, so this system requires more output power. The SS modulation has a number of features that make it easy to achieve the following characteristics:

- Accurate distance measurement.
- Separation and detection of multiple vehicles located in the range direction.
- Accurate measurement of the reception power.
- Interference eliminating capability.

For the reasons mentioned above, the SS modulation was considered more suitable for automotive radar, and it was used in the development of the MMW radar. On the other hand there are some difficulties facing the use of SS technique in automotive radar. In SS automotive radar the target range is evaluated by the correlation between the received PN code and the reference one. In order to implement the correlation function it is required to shift the reference PN code with a very precise known step. The accuracy of the measured distance as well as the required processing time will be affected by the selection of the shifting step of the reference PN code. There are two commonly methods that have been used to implement the shifting of the PN code. The one chip shifting [16, 18–24, 79, 80] and the sliding correlation [23, 78]. In the one chip shifting method, to improve the accuracy of measuring the distance and

reduce the processing time it is required to increase the chip rate of the PN code. The disadvantages in using this method are:

- The accuracy is limited by the bandwidth that can be handled by the modulator/demodulator in the IF stage, while still preserving phase and amplitude balance.
- Increasing the noise corrupting the radar signal due to increasing the bandwidth.
- Fixed accuracy (except if we have variable chip rate as in [80], which will lead to complex implementation).

In the sliding correlation technique [4], the clock frequency of the reference PN code on the receiving side was set slightly lower than that of the modulation PN code on the transmitting side. Using the sliding correlation will give better accuracy without increasing the required bandwidth for the system, because the accuracy obtained by this method is not depending directly on the chip rate of the PN code. It depends on the difference in frequency of the two PN codes. The difficulty in the sliding correlation is that in order to have better accuracy it is required to implement two slightly different, synchronized and stable, clock frequencies, which is not an easy job in practical situations. In the same time it faces the same problem of the previous method that the accuracy of the system is fixed. It is required to search for another technique to implement the correlation function and avoiding the above mentioned limitations.

In this thesis a new method was developed for implementing the shifting of the PN code that overcomes the limitations of the previous methods. The proposed technique can achieve high accuracy without increasing the required bandwidth. On the other hand the complexity is less than that of the sliding correlation. This proposed method also has the facility of variable accuracy, which is required to switch the radar system from detection phase to tracking phase.

The automotive radar system creates for radar designers another problem, as there will be occasions where a number of radars operate in close proximity and transmit the same frequency. This is the case in heavy traffic when these systems needed most and make the operation prone to false reading and unsafe decisions. One of the solutions for reducing the interference is to reduce the transmitted power, which will lead to a trade off between the transmitted power and the noise limitations. It is known that in order to increase the detection range and the probability of detection (PD) of the radar one should increase the transmitted power [8]. In the automotive radar application the transmitted power should be kept as low as possible to reduce the interference with the existence of other radar in the way and also to save the power. It is known that the advantages of using the SS technique are improving the SNR and interference elimination. The raised question now is it possible to improve

the SNR farther by combining the SS technique with other denoising techniques, by this way it is possible to reduce the transmitted power more and more and reduce the interference. Most of the denoising techniques are transform based, which means that the signal plus noise is transformed from the time domain to another domain that able to localize the signal within the noise so that it is possible to remove the noise and keep the signal by applying a certain threshold. The most important aspect in the transform based denoising techniques is to found a linear transform, which should have an inverse that can well localizing the signal. There are two will known transforms used in this field, the Fourier transform and the wavelet transform. In [81], the noise (in pulsed radar) was removed using a non-linear time-frequency filter, which is based on the discrete windowed Fourier transform. It's known [82], that the wavelet transform gives better localization in the time-frequency domain than the discrete windowed Fourier transform. In this thesis we proposed using the wavelet packet transform for denoising the radar signal. The noise is removed by thresholding the wavelet-packet-transform coefficients of the received radar signal. The threshold level selection is based on the higher-order-statistics (HOS) of the coefficients. Using a threshold that is based on HOS proved to be more efficient than the usual way of wavelet thresholding [83], which is based on the estimate of the amount of noise, especially at very low SNR conditions. By combining the wavelet packet transform and HOS correct detection with a SNR down to -24 dB can be achieved.

Another potential application of the SS technique in the field of navigation, especially indoor location system, was investigated in this thesis. The SS was used previously in GPS. The limitations of using the GPS for indoor location system are; very weak signal inside building due to signal attenuation and poor accuracy, 1 to 10 m, which is not suitable for indoor applications. Various methods exist for determining the location of a people or object. All of them involve gathering data by sensing a real-world physical quantity, and using it to calculate or infer a position estimate. The data can be gathered via a number of physical media. Previously developed location systems have used infrared light [43–45], visible light [84], [85], ultrasound [46, 47, 55], and wireless LAN-based radio [48], [49]. The desirable property of ultrasonic location system is that they have the capability to be fine-grained, meaning they can estimate location with a high degree of resolution. This is because the speed of ultrasound in air is sufficiently slow to allow the time-of-arrival (TOA) of a signal to be accurately measured between a fixed unit in the environment and a mobile unit functioning as a tag on a person or object. Fine-grained ultrasonic location data has been used for context-aware applications including mobile desktop control [86], 3D mice and virtual buttons [87], and augmented reality [46].

There are number of ultrasonic location systems presented in the literature. The constellation system [46] tracks a mobile unit consisting of a 3D inertial sensor and a number of ultrasonic sensors. Location is calculated using the TOA measurements between the mobile unit and fixed transmitters in the environment. An accuracy of

approximately 5 mm is reported, but the mobile tracking unit, worn on the head and belt of a user, is too obtrusive for the goals of ubiquitous computing. In the Bat system [55, 87, 88] users wear small badges, which emit an ultrasonic pulse when radio-triggered by a central system. The system determines the pulse TOA from the badges to a network of receivers on the ceiling, and calculates the 3D positions of the badges using a multilateration algorithm. The system yields location information with an accuracy of approximately 3 cm. The Cricket location system [48, 88] consists of independent, unconnected beacons distributed throughout a building. The beacons send an RF signal while simultaneously sending ultrasonic pulses. Small devices called listeners, carried by users, infer their locations using TOA methods, with accuracies on the order of 6 cm in the best cases. The beacons broadcast at random times in order to minimize signal collisions. The listeners can independently locate themselves, avoiding the compromises of user privacy involved with centralized systems. A similar approach [89] uses four ultrasonic transducers placed at the corners of a square on the ceiling, and wired to a controller. The controller sends an RF trigger, and then issues a pulse from each of the four transmitters in succession. A mobile receiver unit connected to a hand-held computer receives the pulses, and estimates its location with accuracies between 10 and 25 cm.

The above four systems share one common trait: they utilize narrowband ultrasonic transducers for ranging measurements. Generally speaking, narrowband systems have three inherent disadvantages.

- Single-user access, if multiple co-located transmitters send at the same time, their signals can interfere with one another, and make it difficult for the receiver to distinguish between them.
- Poor performance in the presence of in-band noise.
- Poor resolution in multi path reflections situations.

The systems described above avoid the first problem by attempting to ensure that co-located transmitters send their signals one-at-a-time (An exception to this is the Bat system, which uses a differential-phase modulation technique, allowing up to three tags to transmit simultaneously [87]). This solution comes at the expense of a slower update rate; allowing only one transmitter to send at a time constrains the number of location updates possible for a given time interval. The second problem, however, has not been addressed. People create ultrasonic noise through their every-day actions, although they are rarely aware of it because ultrasound is inaudible. Examples include the clink of a pencil dropping onto a desk, the clacking of someone typing on a computer keyboard, or the rustling of a bag of potato chips being opened. These kinds of sounds occur frequently in typical indoor environments. For the duration of such an occurrence, existing ultrasonic location systems are prohibited from generating accurate, up-to-date position estimates for mobile units co-located with the noise

source. In [56,57] a broadband spread spectrum technique has been used to overcome these two limitations, facilitating multiple-access location systems, which are robust in the presence of noise. As reported in [56] both the transmitter and the receiver are too large and bulky to be used as mobile tags. In the same time the power drawn by the unit is over than 1 w. For these reasons this system is unsuitable for mobile devices.

Indoor multipath interference is the main factor that limits deploying indoor positioning systems, the multipath is sever and complex which leads to inaccurate estimate of the TOA using conventional techniques, especially for the systems that utilize narrowband transducers. For such systems it is important to find alternative TOA estimation techniques. In this thesis we present a high resolution spread spectrum ultrasonic indoor positioning system based on a commercially available narrowband ultrasonic sensor. The use of such a sensor will reduce the cost of the system. In the same time it can be used as mobile tag regarding to the small size and low power that is required for the transmitter. In the same time the proposed system is able to determine the positions of objects with a high degree of accuracy and resolution. Most of the existing ultrasonic transducers have a limited bandwidth, which leads to a poor resolution in locating the position of a target duo to multipath reflections from the surroundings. The proposed system solves the problem of limitation in ultrasonic transducers bandwidth by applying a super resolution technique such as the root multiple signal classification (RMUSIC) [90] to estimate the TOA of ultrasonic signal. This technique has been previously used for estimating the TOA of the signal in limited bandwidth applications [91,92]. In this thesis the super resolution technique has been tested in the proposed SS ultrasonic indoor location system to overcome for the problem of narrowband ultrasonic sensor. The ultrasonic sensor used in this work has a bandwidth of 2 kHz the corresponding resolution is 35 cm. Tests indicate that using the super resolution technique can improve the resolution of such sensor to be around 5 mm instead of the nominal value of 35 cm.

A third potential application of the SS technique is in the field of NDT or NDE, especially in ultrasound imaging, will be discussed in this thesis. The field of NDT is a very broad, interdisciplinary field that plays a critical role in assuring that structural components and systems perform their function in a reliable and cost effective fashion. NDT technicians and engineers define and implement tests that locate and characterize material conditions and flaws that might otherwise cause planes to crash, reactors to fail, trains to derail, pipelines to burst, and a variety of less visible, but equally troubling events. These tests are performed in a manner that does not affect the future usefulness of the object or material. In other words, NDT allows parts and material to be inspected and measured without damaging them. Because it allows inspection without interfering with a product's final use, NDT provides an excellent balance between quality control and cost-effectiveness. Generally speaking, NDT applies to industrial inspections. Technology that is used in NDT is similar to those

used in the medical industry; yet, typically nonliving objects are the subjects of the inspections.

The tradeoff between resolution and noise effect is well known issue in ultrasound imaging. Given a short pulse the noise effect can be decreased by either increasing the pulse amplitude or the pulse duration (decreasing the bandwidth). However, The pulse amplitudes of commercial scanners are limited by the mechanical index (MI). The only feasible alternative is to extend the pulse duration, which has the undesirable consequence of reducing the axial resolution. O'Donnell [93] predicted that the transmitted energy can be increased up to 15-20 dB by coded excitation before reaching particular intensity limits. This additional SNR can be used to increase resolution and/or penetration. With proper decoding, the SNR of the imaging pulse is improved by the increased average power in the coded excitation compared to an equivalent impulse excitation of the same peak power. Any decoding system with a finite time-bandwidth product, however, cannot produce an ideal impulse without range side lobes. For high-quality imaging, range side lobes must be managed. Practical coded excitation systems have a tradeoff between range side lobes and SNR improvements. Traditional coded excitation system uses chirp codes, M-sequence, or Barker codes. To decode the coded excitation signal we should look for a transform, which is able to localize the signal and reduce the noise effect. In general any transform is a correlation between the coded signal and the kernel of that transform. To satisfy high correlation between the coded signal and the kernel of the transform we should use the code itself as the kernel of that transform. For the above explained reason the coded signal is decoded with correlation-based procedures such as matched filtering or mismatched filtering. Duo to the limitation in time bandwidth product the decoding process will leads to a range side lobes effect. There are two common approaches to solve for the problem of range side lobes in coded excitation. In the first approach [94, 95] the researchers trying to find an optimal code that has minimum range side lobes. In the second approach [96–100] the researchers trying to find an optimal decoding filter to minimize the range side lobes. In both of the above-mentioned techniques the researcher are able to reduce the range side lobes effect. In this thesis we propose the using of a super resolution technique to overcome the problem of range side lobes. The super resolution technique previously used for estimating the TOA in limited bandwidth applications. In this thesis we extend the application of RMUSIC algorithm to reconstructs the decoded pulse from the frequency domain. As the results will indicate the proposed technique is able to reconstruct the decoded pulse without any range side lobes.

In recent years the use of microwaves for the imaging of materials and biological bodies, and for the remote sensing of underground metallic/non-metallic objects has gained much attention. Over the last few decades, much research has been done in the field of inverse scattering in general, and in the field of microwave inverse scattering in particular. Reconstruction of permittivity profiles constitutes a major part of the

electromagnetic inverse scattering problem and has been of great interest since many years because of many practical applications. One of the potential examples is the biomedical microwave imaging, which deals with the reconstruction of muscles, tissues and different organs of a human being [101–105]. The overall reconstruction process, in general, involves the measurement of scattering data such as the reflection coefficient due to an illuminating wave with known characteristics. Information about the unknown permittivity profile of the illuminated object in terms of these measured values is obtained by using some inverse techniques. Several approaches have been proposed to solve the inverse scattering problem in microwave imaging [106–126]. Most of them depend mainly on a source reconstruction philosophy in either the spectral domain or the spatial domain, leading to a strong nonlinearity inherently connected with non-uniqueness and uncertainty of the achieved solution [103], [127–129]. Only if the "Born approximation" is used, a linear problem with a unique solution can be obtained [130–132]. This approximation limits the validity of such reconstructions to objects with low permittivity contrast. In order to increase the validity of the linearization to cover moderate contrast, some of the previously mentioned techniques suggested inverting an auxiliary reflection coefficient, which is nonlinearly related to the measured one [106], should be used. The inversion is usually done using the conventional Fourier transform. The problem arises here is the effect of limiting the measurements bandwidth on the inversion of the reflection coefficients using Fourier transform. Limiting the bandwidth leads to a side lobe effect on the inverted measurements. These side lobes can degrade the resolution of the reconstructed profile and in some cases, especially with band pass measurements, can lead to un-stability in the reconstruction process.

In this thesis, we propose to use the super resolution technique RMUSIC to overcome the problem of side lobes effect on the reconstruction of permittivity profiles. This technique has been previously used in other disciplines for estimating the TOA of the signal in limited bandwidth applications. In this thesis we extend the application of this technique to estimate the local reflection coefficients in the time domain using the measured total reflection coefficient in the frequency domain. The reconstruction of the permittivity profile will be done using a numerical iterative algorithm based on the estimated local reflection coefficients in time domain. The proposed technique is shown to be able to reconstruct permittivity profiles with high resolution.

After exploring the difficulties with SS techniques in the different applications we found that with some how it is common problems for all the applications. The noise and the available bandwidth are playing very important role in the performance of any system. If the system is noise free we can still get complete information about the system whatever the available bandwidth. On the other hand, if the available bandwidth is infinite we can still get full information whatever the value of the noise exist in the system. In practical situations, most of the systems have limited bandwidth and also associated with noise measurements. If its possible, with the help of



---

signal processing, to improve the noise performance of the system this will lead to improving the capability of the limited bandwidth systems.

# Chapter 2

## Fundamentals of Spread Spectrum

### 2.1 Introduction

Spread spectrum techniques originated in answer to the needs of military communications. They are based on signaling schemes, which greatly expand the transmitted spectrum relative to the data rate. In recent years, multiple civilian uses of SS were found. There is a growing interest in these techniques for use in mobile radio networks and for both communication and positioning applications in satellites. Designers of communication systems are often concerned with the efficiency with which the systems utilize the signal energy and bandwidth. In most communication systems these are the most important issues. In some cases, however, there exist situations in which it is necessary for the system to resist external interference, to operate at low spectral energy, to provide multiple access capability without external control, and to provide secure channel inaccessible to the outside listeners. Thus, it is sometimes necessary to sacrifice some of the efficiency of the system in order to enhance these features. Spread spectrum techniques allow accomplishing such objectives [133].

The theoretical aspects of using SS in a strong interference environment have been known for over sixty years. It is only recently that practical implementations became feasible. Initially, SS techniques were developed for military purposes and their implementations were exceedingly expensive. New technological advancements such as VLSI, and advanced signal processing techniques made it possible to develop less expensive SS equipment for civilian use. Applications of this technology include cellular telephones, wireless data transmission, satellite communications, automotive radar, indoor positioning systems, and NDE.

Bandwidth expansion in SS systems is achieved by using a function that is independent of the message, thus it is more susceptible to white noise as opposed to other communication techniques, such as FM and PCM. SS techniques have other applications that make it unique and useful. These applications include [133]:

- Anti-jam capability-particularly for narrow-band jamming.

- Interference rejection.
- Multiple-access capability.
- Multi-path protection.
- Covert operation or low probability of intercept (LPI).
- Secure communications.
- Improved spectral efficiency in special circumstances.
- Ranging.
- Navigations.
- NDT and NDE systems.

The objective of this chapter is to introduce the reader to the concept of SS in general terms and then proceed with a detailed, technical discussion of various signaling techniques, including mathematical derivations. It is hoped that this chapter will introduce the reader to SS techniques through theoretical discussion and multiple examples. It will also provide information beyond the introductory materials through a description of specific application of SS technique.

## 2.2 History of the Development of SS techniques

The development of SS started in the 1940's. Perhaps the best way to describe the history of SS is to first briefly describe the techniques in communication theory and technology that were available during this period. Some of the developments are listed below [1]:

### 2.2.1 Radar Techniques

- mid-1920: birth of RADAR.
- 1940: chirp pulse radar, patented by Prof. E. Huttman (Germany).
- 1945: chirp pulse radar, R. H. Dickie (USA).
- mid-1940: formulation of the matched filter concept.
- early 1950's: P.M. Woodward, resolution, accuracy, and ambiguity properties of pulse waveforms finally were placed on a sound theoretical basis.
- 1938: among Gunella's approximately 100 patents is one containing all the technical characteristics of Satellite Remote Sensing Services.

### 2.2.2 Communication Theory

- 1930: Norbert Wiener of MIT publishes "Generalized Harmonic Analysis". Wiener is the inventor of probabilistic modeling of information flow in communication and control systems.
- beginning in 1947: Shannon develops his communication theories. Shannon's and Wiener's theories stimulate the Institute of Radio Engineers (IRE) to form the Professional Group on Information Theory, which began publishing in 1953. Nathan Marchand and Louis deRosa, chairmen of IRE, were at the time playing key roles in the development of SS systems.

### 2.2.3 Other Developments

- 1942: A 26-year-old engineer, Nathan Marchand, working for ITT's Federal Telephone and Radio Corporation in New York, patented first bandpass correlator.
- 1947: Lee, Wiesner and Cheatham of MIT developed first high performance electronic correlators. They also reported applications of correlation techniques to detection problems.
- 1924: Alfred Goldsmith, one of the founders of IRE, filed a patent being SS in nature. His patent described a system using a form of FM-SS transmission.
- 1935: German engineers working for Telefunken, Paul Kotowski and Kurt Dannehl applied for a patent on a device used for masking voice signals by combining them with an equally broadband noise signal produced by a rotating generator. Receiver had another rotating generator, which was synchronized and used in order to recover the noisy voice signal. This invention was a starting point in the development of DSSS communication systems.
- sometime during World War II: Henri Businger, inventor of moving-target indicator for radars, together with Louis deRosa applied for an on facsimile communication system with anti-jamming capabilities. It was a time wobbling system, which was an early relative of modern time hopping SS systems.
- World War II: Many missile guidance systems were developed, i.e. radar controlled glides bombs. Many of these systems were protected from jamming by SS like systems.

### 2.2.4 Early SS Systems

The SS concept was developed gradually during the same time that Shannon's work on information theory became appreciated. J.R. Pierce commentary describes the

significance of Shannon's work [134]:

"It is hard to picture the world before Shannon as it seemed to those who lived in it. In the face of publications now known and what we now read into them, it is difficult to recover innocence, ignorance, and lack of understanding. It is easy to read into earlier work a generality that came only later."

The developments such as Shannon's theories and other research mentioned earlier contributed to the emergence of SS, as it is known today. Although SS systems were being developed for military, and under secrecy, there was still some exchange of information between different researchers. Many SS systems emerged during that time. Some of them are WHYN, noise wheels, and NOMAC. WHYN (Wobulated Hyperbolic Navigation) was developed by Sylvania during mid 1940's. This navigation system was used to guide missiles and was one of the first TR-FM-SS systems.

Another example of SS systems is a full-fledged SRSS single-sideband communication system based on Rogoff's noise wheels. Patent for this invention was filed in March 1953. One of the ITT engineers: Mortimer Rogoff, an avid photographic hobbyist, conceived of using photographic techniques to store a noise-like signal and for building an ideal cross correlator. Rogoff prepared sheets of film whose transmissivity varied linearly in both directions, thus creating a mask. At every point (X, Y) on the mask, transmission characteristics were proportional to the product XY. The two signals would then be correlated by using them as the X and Y inputs to the oscilloscope, reading the light emitted from the masked oscilloscope face with a photo-multiplier, and low-pass filtering the resultant output.

Extensive studies of SS techniques were done at MIT and MIT's Lincoln Laboratories. Much of the research was performed by graduate students, guided by Group Leaders Fano and Davenport. The techniques under study were named NOise Modulation And Correlation or NOMAC. The first of NOMAC's systems was used for comparison of the performances of transmitted and stored reference systems operating in the presence of broadband Gaussian noise. Research done at MIT led to development of several TRSS systems [133].

Many SS technologies have been declassified since World War II and are now available for commercial use. Commercial applications of SS have attracted considerable attention because of its possible use for CDMA. SS also reduces detrimental effects of multipath. Today, both voice and data oriented systems employ SS systems. Modern applications of SS range from low-speed fire safety devices to high-speed wireless local area networks [135].

## 2.3 General Concepts Related to SS

Scholtz describes the basic characteristics of SS system in communication as follows [1]:

- The carrier is an unpredictable, or pseudo-random, wide-band signal.
- The bandwidth of the carrier is much wider than the bandwidth of the data modulation.
- Reception is accomplished by cross correlation of the received wide-band signal with a synchronously generated replica of the wide-band carrier.

In case of SS systems, if a signal is called PN, it means that it appears to be random but in fact the information is contained within it. One of the most important features of the SS signal is that it contains large number of very different signaling formats used for communicating data symbols. It means that the receiver, which detects one of these formats, cannot detect any other format within a single message. The number of formats used in SS system is called the multiplicity factor of the communication link. Most of the well-known communication systems have a multiplicity factor near unity while SS systems have multiplicity factors in the thousands. Thus, it can be seen that a jammer attempting to interfere with SS communication has to know exactly which signaling factors are being used, which is not very likely considering the size of SS multiplicity factor, or the jammer has to reduce significantly his power per each signaling format by jamming all of the formats.

Scholtz [1] recognizes at least five important performance attributes of SS systems, which are due to the nature of their signal characteristics:

- Low probability of intercept (LPI) can be achieved with high processing gain and unpredictable carrier signals when power is spread thinly and uniformly in the frequency domain, making detection against noise by the surveillance receiver difficult. A low probability of position fix (LPPF) attribute goes one step further in including both intercept and direction finding in its evaluation. Low probability of signal exploitation (LPSE) may include additional effects, e.g., source identification, in addition to intercept and direction finding.
- Anti-jam (AJ) capability can be secured with an unpredictable carrier signal. The jammer cannot use signal observations to improve its performance in this case, and must rely on jamming techniques, which are independent of the signal to be jammed.
- High time resolution is attained by the correlation detection of wide-band signals. Differences in the TOA of the wide-band signal, on the order of the reciprocal of the signal bandwidth, are detectable. This property can be used to suppress multipath and, by the same token, to render repeater jammers ineffective.
- Transmitter-receiver pairs using independent random carriers can operate in the same bandwidth with minimal co-channel interference. These systems are called CDMA systems.

- Cryptographic capabilities result when the data modulation cannot be distinguished from the carrier modulation, and the carrier modulation is effectively random to an unwanted observer. In this case the SS carrier modulation takes on the role of a key in a cipher system. A system using indistinguishable data and SS carrier modulation is a form of privacy system.

There are three basic configurations used for recovery of the SS carrier [1]:

- Transmitted reference (TR) system achieves detection by transmitting two versions of the carrier, one modulated by data and other unmodulated. These two signals enter a correlation detector, which extracts the message.
- In a stored reference (SR) system, both receiver and transmitter keep a 'copy' of the same pseudo-random signal. Carrier generator at the receiver is adjusted automatically in order to synchronize its output with the arriving carrier. Detection is then similar to TR system.
- Matched filtering can also be used for reception of SS signals. Filter systems produce a wide-band, PN impulse response. Matched filter with such response is used at the receiver in order to recover transmitted signal. PN characteristic of the impulse response ensures security of the transmitted signal.

## 2.4 Direct Sequence Spread Spectrum (DSSS)

Direct sequence (or, to be more exact, directly carrier-modulated, code sequence modulation) systems are the best-known and most widely used SS systems. This is because of their relative simplicity from the standpoint that they don't require a high-speed, fast settling frequency synthesizer. Today, direct sequence modulation is being used for communication systems and test systems, and even laboratory test equipment capable of producing a choice of a number of code sequences or operating modes is available. The terms direct sequence and pseudo-noise are used interchangeably throughout the literature and both of them pertain to the same spread spectrum techniques. It can be assumed that the information signal in DSSS transmission is spread at base band, and the spread signal is then modulated in a second stage. By using this approach the modulation is separate from the spreading and the base band spreading can be discussed separately. At the receiver, the signal is first demodulated and then despread to recover original information. A typical DSSS transmitter is represented in Fig. 2.1. Such transmitter is composed of a PN code generator, digital multiplier (which can be implemented using XNOR logic gate) and balanced modulator. The output of the multiplier is used to modulate a carrier. The modulation can be biphasic or phase reversal modulation so that the output becomes a phase shift keyed signal. The DSSS transmitted signal in Fig. 2.1 can be written as:

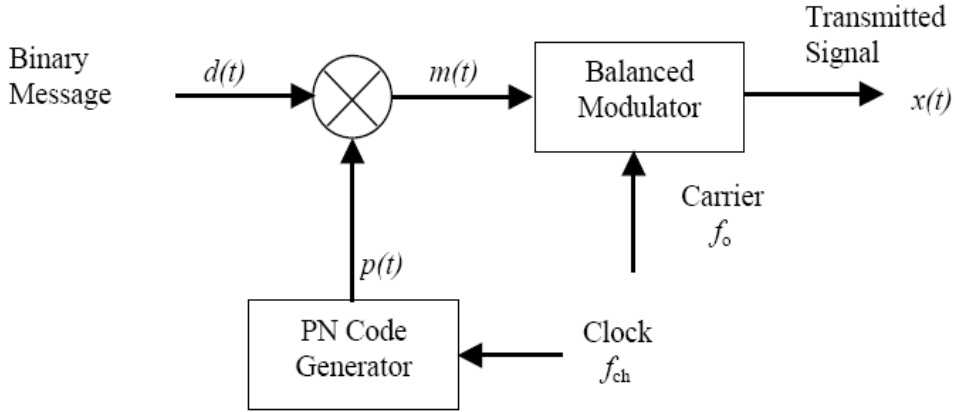
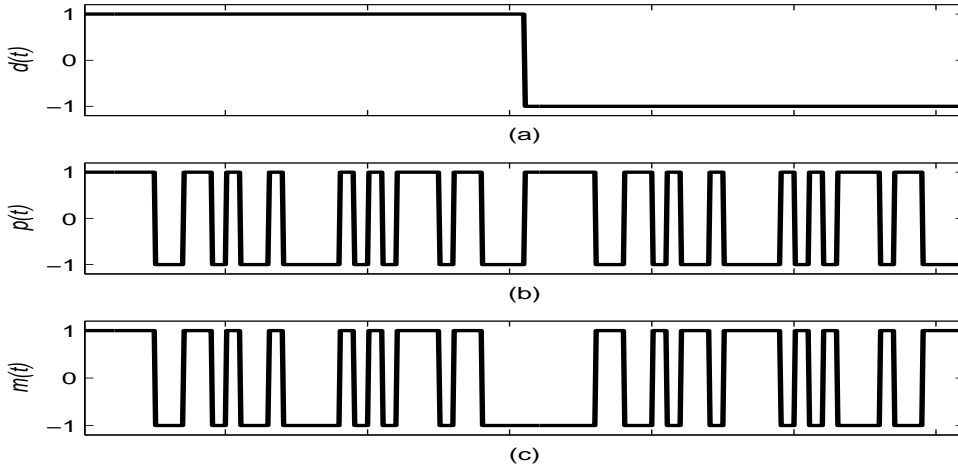


Figure 2.1: Direct sequence spread spectrum transmitter.

Figure 2.2: (a) The waveform of the data bit stream  $d(t)$ . (b) The PN code  $p(t)$ . (c) The waveform of the product  $m(t)$ .

$$x(t) = m(t) \cdot \cos(\omega_o t) = d(t) \cdot p(t) \cdot \cos(\omega_o t) \quad (2.1)$$

where  $d(t)$  is a binary data stream representing the information,  $p(t)$  is a PN random binary sequence having the values  $\pm 1$  and  $\omega_o$  is the carrier frequency. For the purpose of analysis (2.1) will be rewritten as:

$$x(t) = s(t) \cdot p(t) \quad (2.2)$$

where  $s(t)$  is the binary phase shift keying (BPSK) sequence  $d(t) \cdot \cos(\omega_o t)$ .

The characteristics of  $p(t)$  are extremely interesting and are discussed in some detail in section 2.6. Here we merely assume that  $p(t)$  is a binary sequence as is the data  $d(t)$ . The sequence  $p(t)$  is generated in deterministic manner and is repetitive.



However, the sequence length before repetition is usually extremely long and to all intents and purposes, and without serious error, we can assume that the sequence is truly random, i.e., there is no correlation at all between the value of a particular bit and the value of another bits. Furthermore, the bit rate  $f_{ch}$  of  $p(t)$  is usually so much greater than the bit rate  $f_d$  of  $d(t)$ . As a matter of fact the rate of  $p(t)$  is usually so much greater than  $f_d$ , we say that  $p(t)$  "chops the bits of data into chips", and we call the rate of  $p(t)$  the chip rate.

To see that multiplying the BPSK sequence  $s(t)$  by  $p(t)$  spreads the spectrum we refer to Fig. 2.2 which shows a data sequence  $d(t)$ , a PN sequence  $p(t)$  and the product sequence  $m(t)$ . The product sequence is seen to be similar to  $p(t)$ , indeed if  $p(t)$  were truly random, the product sequence would be another random sequence having the same chip rate. Since the bandwidth of the BPSK signal  $s(t)$  is nominal  $2f_d$  the bandwidth of the BPSK SS signal  $x(t)$  is  $2f_{ch}$  and the spectrum has been spread by the ratio  $f_{ch}/f_d$ . Since the power transmitted by  $s(t)$  and  $x(t)$  is the same, the power spectral density  $G_s(f)$  is reduced by the factor  $f_{ch}/f_d$ .

To recover the DSSS signal, the receiver shown in Fig. 2.3 first multiplies the received signal by the carrier  $\cos(\omega_o t)$  and then by the PN code  $p(t)$ . The resulting waveform is then integrated for the bit duration and the output of the integrator is sampled, yielding the data  $d(kT_b)$ . We note that at the receiver it is necessary to regenerate both the sinusoidal carrier of frequency  $\omega_o$  and also to generate the PN waveform  $p(t)$ .

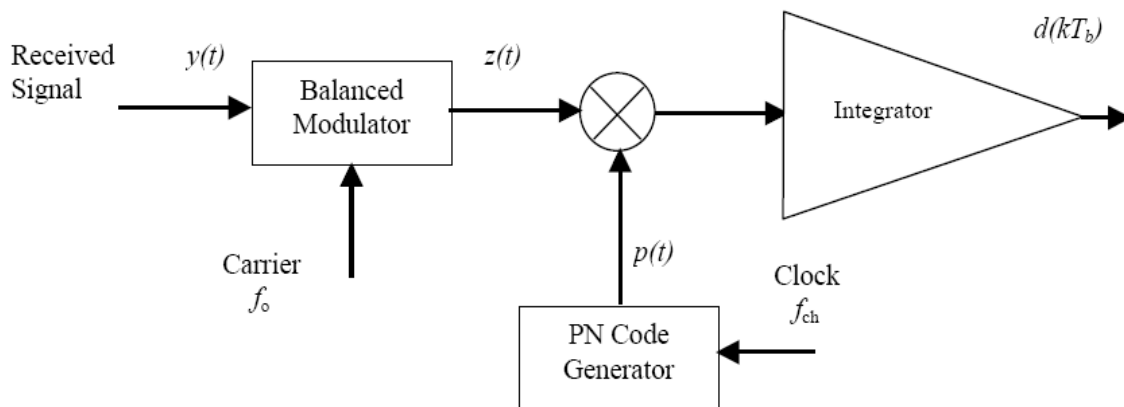


Figure 2.3: Direct sequence spread spectrum receiver.

## 2.5 Ranging Using (DSSS)

Another application of DSSS is for ranging. In this application, which is illustrated in Fig. 2.4, a DSSS signal

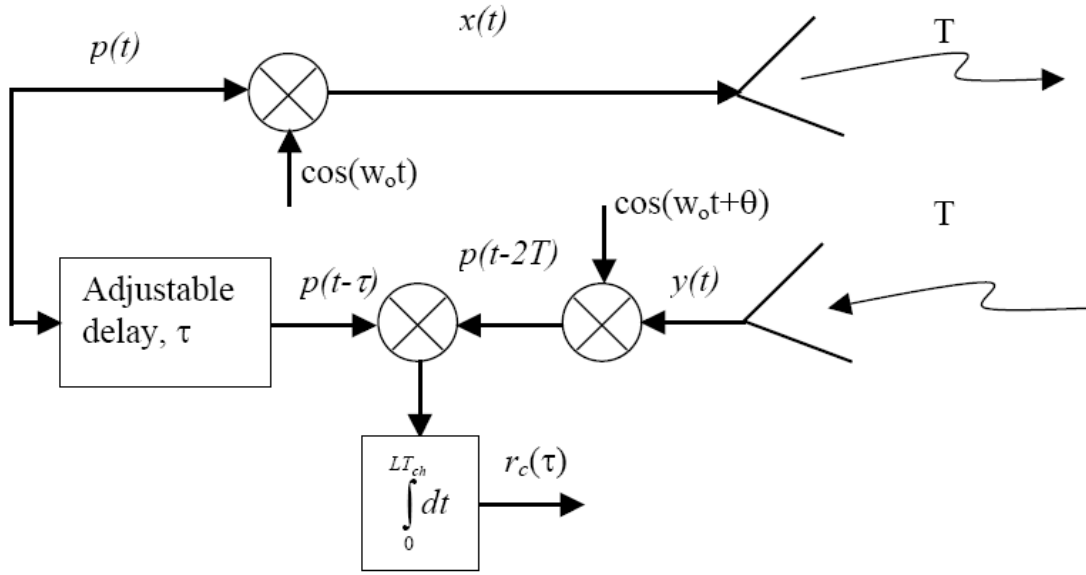


Figure 2.4: Ranging using DSSS.

$$x(t) = p(t) \cdot \cos(\omega_0 t) \quad (2.3)$$

is transmitted. The signal is reflected from the intended target and received  $2T$  seconds later as  $y(t)$ ,

$$y(t) = a \cdot x(t - 2T) = a \cdot p(t - 2T) \cdot \cos(\omega_0 t + \theta) \quad (2.4)$$

where  $a$  represents the signal attenuation and  $\theta$  is a random phase caused by the time delay, i.e.,  $\theta = -\omega_0 \cdot (2T)$ . The received carrier  $\cos(\omega_0 t - \theta)$  can be extracted using squaring circuit (not shown in Fig. 2.4) or equivalent and the received PN sequence  $p(t - 2T)$  is extracted.

The PN waveform  $p(t - 2T)$  having been recovered, is correlated with the waveform  $p(t - \tau)$  which is the PN waveform delayed by a known time interval  $\tau$ . The correlation function  $r_p(\tau)$ , which is the output of the integrator in Fig. 2.4 is

$$r_p(\tau) = \frac{1}{LT_{ch}} \int_0^{LT_{ch}} p(t - 2T)p(t - \tau)dt \quad (2.5)$$

The integration interval in (2.5) extends over the length of the PN sequence. This length is given by the product of the number of bits in the sequence (i.e., the sequence length  $L$ ) and the period  $T_{ch}$  of the chipping.

The special and important characteristic of the PN waveform in the present application is that the correlation  $r_p(\tau)$  is negligibly small if the difference in delays, i.e.  $\tau - 2T$  exceeds the chip duration and  $r_p(\tau)$  is a maximum when  $\tau = t_d = 2T$ .

Accordingly, in Fig. 2.4, the range is determined by adjusting  $\tau$  to maximize  $r_p(\tau)$ . If the velocity of light is  $c = 3 \times 10^8 \text{ m/s}$ , the range of the target is

$$d = c \cdot \tau_d / 2 \quad (2.6)$$

Furthermore, the precision of the measurements is the chip duration  $T_{ch}$  which corresponds to a distance  $c \cdot T_{ch} / 2$  so that

$$d = c(t_d \pm T_{ch}) / 2 \quad (2.7)$$

and the measurement accuracy can be improved by decreasing  $T_{ch}$  relative to  $t_d$ .

## 2.6 Generation and Characteristics of PN Sequences

It is intended in this section to discuss the codes used in communications and ranging systems, those that act as noise like (but deterministic) carriers for the information being transmitted. The code sequences of interest are of much greater length than those considered in the usual areas of coding for information transfer, since they are intended for bandwidth spreading and not for the direct transfer of information.

The importance of the code sequence to a SS communications or ranging system is difficult to overemphasize, for the type of code used, its length, and its chip rate set bounds on the capability of the system that can be changed only by changing the code. A greatest emphasis will be placed on linear codes, or to be more specific, on maximal length codes. The maximum length codes sequences (often called m-sequences or PN codes) are unexcelled for general use in communications and ranging. (Other codes can do no better than equal their performance). Therefore, it is proper that they and some of their applications and variations be given adequate exposure. It is also proper that we point out here that the most advanced systems ever constructed employ linear codes internal to themselves.

### 2.6.1 Maximal Length Sequences

Maximal codes are, by definition, the longest codes that can be generated by a given shift register or a delay element of a given length. In binary shift register sequence generators, which are the only type considered here, the maximum length sequence is  $2^{N-1}$  chips, where  $N$  is the number of stages in the shift register. A shift register sequence generator consists of a shift register working in conjunction with appropriate logic, which feeds back a logical combination of the state of two or more of its stages to its input. The output of a sequence generator, and the contents of its  $N$  stages at any sample (clock) time, is a function of the outputs of the stages feed back at the preceding sample time. Feedback connections have been tabulated for maximal code generator from 3 to 100 stages, so that some sequences of any length from 7 through  $2^{36} - 1$  chips readily available. A number of feedback connections are given in [2].

A piece of hardware, which is widely used to generate PN sequences, is shown in Fig. 2.5. It consists initially of a shift register. We have selected D-type flip-flops and arranged that each data input except  $D_0$  is the Q output of the preceding flip-flop. The input  $D_0$  is the output of a parity generator. A parity generator (generally constructed of an array of XOR logic gates) generates an output which is at logic 0 when an even number of inputs are at logic 1 and generates an output which is at logic 1 when odd number of inputs are at logic 1. The parity generator inputs are the outputs of the flip-flops. We have shown a portion of each connection to the parity generator input as dashed in order to indicate that not all outputs Q need to be connected to the parity generator. As a matter of fact, the character of the PN sequence generated depends on the number  $N$  of flip-flops employed and on the selection of which flip-flop outputs are connected to the parity generator.

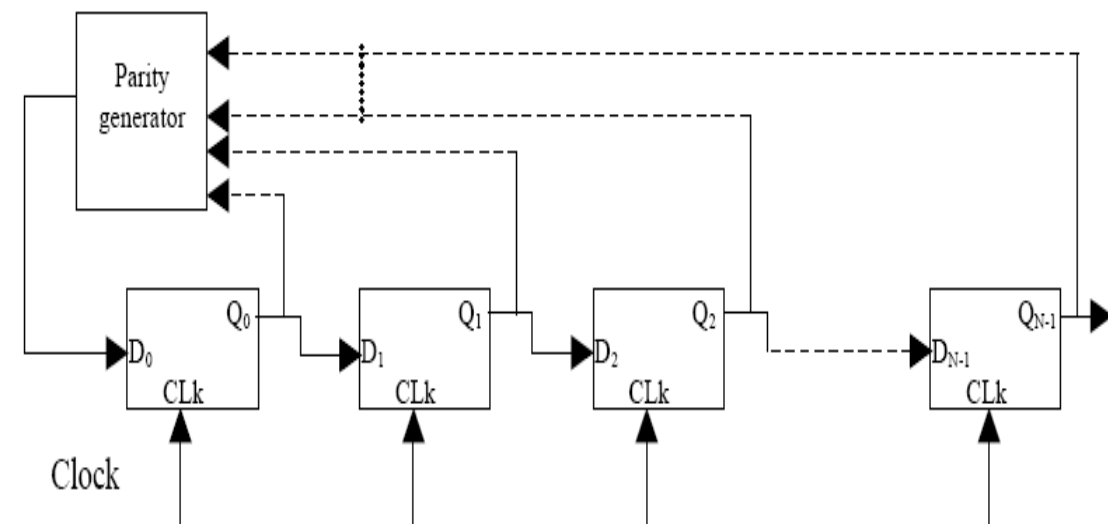


Figure 2.5: A pseudo-random sequence generator.

The state of a sequential system such as in Fig. 2.5 is specified by stating the logic values of all the Q's of the flip-flops. During the course of a clock cycle the state of the shift register remains fixed, but in general, the state changes each advance from one clock cycle to the next. A register of  $N$  flip flops has states from  $Q_0Q_1Q_2\dots Q_{N-1} = 000\dots 0$  to  $Q_0Q_1Q_2\dots Q_{N-1} = 111\dots 1$ . It is clear that the hardware of Fig. 2.5 cannot generate a truly random sequence since it is a deterministic structure. It is also clear that whatever the sequence states through which the sequence generator progresses, the sequence will repeated. That is, it will be periodic. Such is the case because each state is uniquely determined by the immediately preceding state. Thus, each time the generator arrive at some particular state, the subsequent sequences of states will always be the same. While, as we have noted, a truly random sequence is not possible, we may intuitively anticipate that a sequence with a long enough period will have some of the characteristic of a random sequence. The first step in

that direction is taken by using a large number of flip-flops. For, if we can make the sequence generator go through all its states the sequence length will be  $2^N$ . Actually the maximum sequence length is  $2^N - 1$  since the state 000...0 must be excluded. Such is the case because, as is easily verified, if the register should ever arrive at this all zero state, it will remain in that state permanently. We shall now set down some of the characteristics of the PN sequences produced by the generator of Fig. 2.5.

### 2.6.2 Autocorrelation of a PN Sequence

Autocorrelation in this context refers to the degree of correspondence between a code and a phase-shifted replica of itself. The autocorrelation function  $R_{PN}(\tau)$  of a PN sequence is

$$R_{PN}(\tau) = E \{p(t)p(t - \tau)\} = \frac{1}{LT_{ch}} \int_0^{LT_{ch}} p(t)p(t - \tau)dt \quad (2.8)$$

From the characteristics of the PN code the autocorrelation function will give maximum value 1 at  $\tau = 0$  and it will give very small value ( $-1/L$ ) for  $|\tau| = nT_{ch}$ , where  $n$  is an integer number and  $T_{ch}$  is the chip duration of the PN code as indicated in Fig. 2.6. Finally, as shown in Fig. 2.6 the autocorrelation sequence has a period  $LT_{ch}$  so too has the PN code.

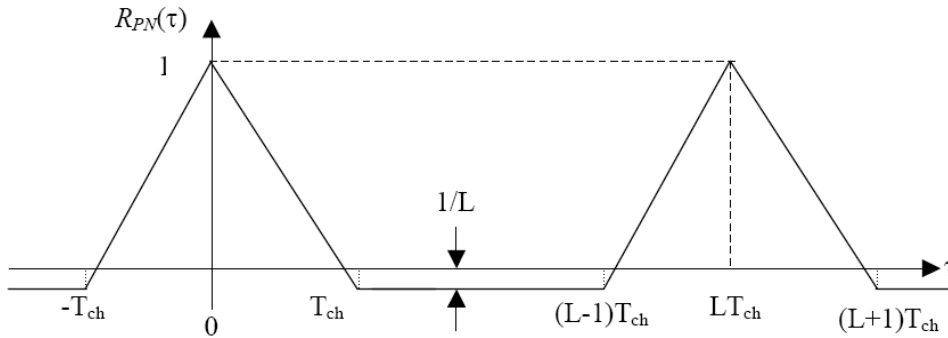


Figure 2.6: The autocorrelation function of the PN code.

### 2.6.3 Power Spectral Density of a PN Sequence

We now determine the power spectral density  $G_{PN}(f)$  of the PN code sequence. The power spectral density  $G_{PN}(f)$  is the Fourier transform of  $R_{PN}(\tau)$ . Since  $R_{PN}(\tau)$  is periodic with period  $LT_{ch}$ ,  $G_{PN}(f)$  must consist of impulses at multiples of the frequency  $f_{ch}/L$ .  $G_{PN}(f)$  will also display at  $f = 0$  since the impulse  $G_{PN}(0)$  is the dc power of the PN sequence. The PN sequence  $p(t)$  consists of excursions between  $+V$  (logic 1) and  $-V$  (logic 0). In a sequence of  $L$  chips there is one more logic

1 than logic 0, hence the dc voltage of  $p(t)$  is  $V/L$  and the normalized dc power is  $(V/L)^2$ . Hence  $G_{PN}(0) = (V/L)^2\delta(f)$ . Finally, we recall that if  $p(t)$  were truly random its power spectral density would have the form  $\left[\frac{\sin(\pi f/f_{ch})}{(\pi f/f_{ch})}\right]^2$ . Altogether, then, the spectral density  $G_{PN}(f)$  is as shown in Fig. 2.7 and can be shown to be

$$G_{PN}(f) = \frac{V^2}{L^2}\delta(f) + \frac{V^2}{L} \sum_{i=-\infty}^{\infty} \delta\left(f + i\frac{f_{ch}}{L}\right) \left[\frac{\sin \pi(f + i f_{ch}/L)}{\pi(f + i f_{ch}/L)}\right]^2 \quad (2.9)$$

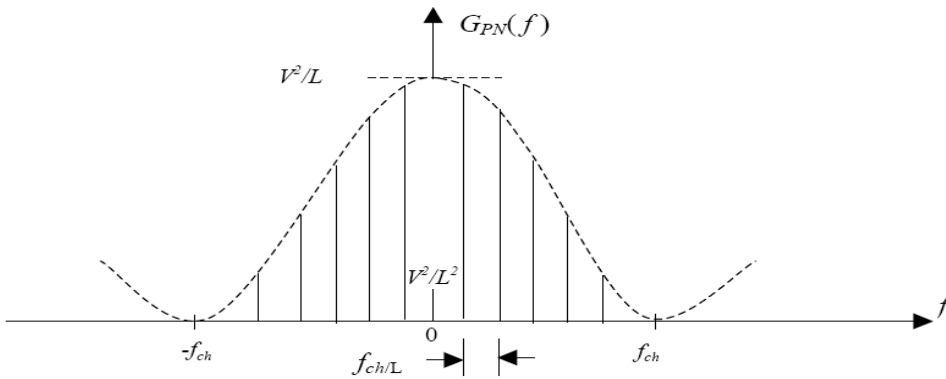


Figure 2.7: Power spectral density of a PN sequence.

### 2.6.4 Chip Rate and Code Length

Code chip rates in SS systems affect their systems in many ways. The most obvious in a BPSK direct sequence system, in which the transmission bandwidth is a direct function of the code chip rate (i.e., main lobe null, null-null RF bandwidth is twice the code chip rate). Code repetition rate is also a function of the chip rate; that is, code repetition rate is simply

$$R_{rep} = \frac{\text{clock rate in chips per second}}{\text{code length in chips}}$$

This repetition rate determines the line spacing in the RF output spectrum and is an important consideration in a system design. One criterion for selecting code repetition rate is that the period of the code must exceed the length of any mission in which it is to be used. Other considerations that bear on the choice of the code rate and length are the relationship of the repetition rate to the information baseband and use of the system for ranging. It is advisable that a direct sequence system's code repetition rate be adjusted by choosing a satisfactory code length so that it will not lie in the information band. Otherwise, unnecessary noise will be passed into the information demodulators, especially under jammed conditions.

When ranging is important, a properly chosen code rate can ease the measurement problem and some times even improve the resolution. If the chip rate is chosen in

such a way that an integer number of code chips is accumulated for each mile of delay (propagation time), a simple count of code offset can be used to measure range without elaborate correction.

### 2.6.5 Choosing a Linear Code

Among the biggest problem in code generation are (1) finding feedback logic gives the desired code length and (2) checking the code once a sequence generator has been constructed to ensure that it is operating properly. It is of little use to know how to construct a shift register generator unless one also knows the feedback connections necessary to generate a useful code sequence. Of course, it is possible to find a set of feedback connections experimentally, but this requires not only constructing a shift register generator but also taking the time to check the length of codes generated until one changes on a maximal connection. Happily, tables of feedback connections and tables of irreducible polynomials have been generated [2] which make the job much easier.

## 2.7 Software-Implemented Codes

It is, of course quite practical to use a more general-purpose machine such as a computer to generate codes. In some cases, it may not be practical to do so because of other loading, but where machine time is available the flow diagram shown in Fig. 2.8 illustrates technique for generating maximal length code.

The diagram in Fig. 2.8 requires that a number of memory locations equal to the degree of the code be set aside (one location per register stage). Then, with all locations set to one, count the number of ones in the stages from which feedback is taken. If there is an odd number of ones, set the first stage to one and shift all to the right. If the number of ones is even, set the first stage to zero and again shift to the right. Repetition of this procedure will produce a code at a rate equal to the algorithm repletion rate.

## 2.8 Hardware-Implemented Codes

The hardware-implementation of the PN sequence can be done using different technologies. In this thesis the implementation of the PN code was done using the following technologies Linear Feedback Shift Register (LFSR), Peripheral Interface Controller (PIC), Field Programmable Gate arrays (FPGA) and Arbitrary Waveform Generator (AWG). Each of the above technologies has its own limitations as we will show in the next subsections.

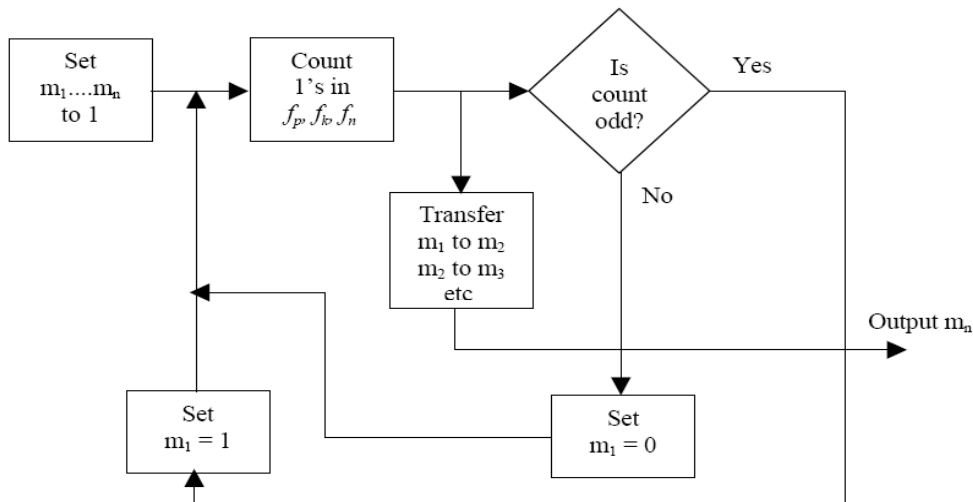


Figure 2.8: Flow diagram for m-sequence generator.

### 2.8.1 Linear Feedback Shift Register (LFSR)

Generating the PN code using LFSR is based on using discrete logic Integrated Circuit (IC). The components required here are shift registers, such as 74HC74, which contains 2-bit shift register and XOR logic gate, such as 74HC86, which has 4 two inputs XOR gates. The components are connected as indicated in Fig. 2.5 where the D-type flip flops are implemented here using the shift register 74HC74 IC and the Parity generator is implemented using the XOR 74HC86. One important thing one should take care with it, when implementing the PN code generator using LFSR, is to avoid the all zero state. To do this a push bottom switch is used to set all the values of the shift registers during the warm up of the circuit. Fig. 2.9 shows a simple 6 stages ( $L = 63$  bit) PN code generator. The limitations of using LFSR technology are (1) it requires large area; (2) maximum chip rate is 30 MHz, which is not suitable for applications that need high resolution; (3) nonflexible implementation for prototype systems (4) external clock is required.

### 2.8.2 Peripheral Interface Controller (PIC)

The microchip PIC processor family is really growing! Many applications use these powerful, RISC-like microprocessors because of their simplicity and low cost. We have used them in the SS system as a PN code generator. The PIC12F629 was chosen as the PN code generator due to the following characteristics:

- 35 Single Word Instructions.
- 1792 bit Program Memory Size.
- 64 bit RAM Size.



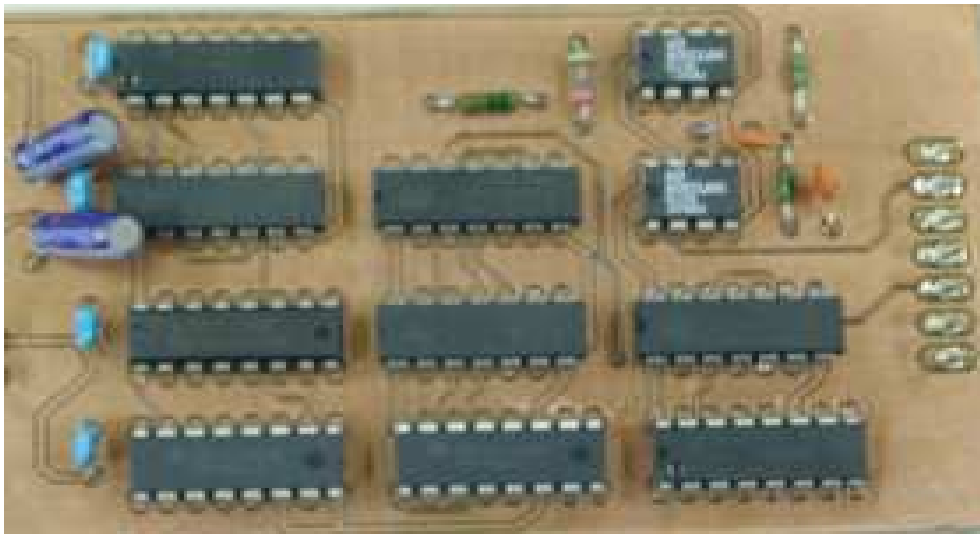


Figure 2.9: A simple 6 stages PN code generator using LFSR.

- Re-programmable Flash-based.
- 8 Bit Controller.
- 8 Pin Package (6 I/O).
- 4 MHz internal RC Oscillator with Programmable Calibration.
- In circuit serial programming.

There are several ways of programming the PIC - using BASIC, C, or assembly language. In this thesis we used the assembly language. There are only 35 instructions to learn, and it is the cheapest way to program the PICs, as you do not need any extra software other than the freebies. Fig. 2.10 is a pin diagram showing the pin-outs of the PIC12F629 which is used to generate the PN code.

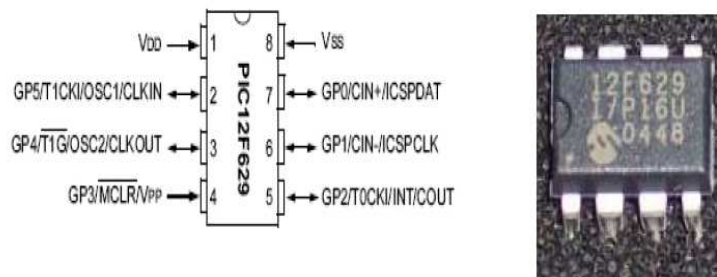


Figure 2.10: 8 Pin diagram of the PIC12F629.

The limitation of using LFSR technology is low chip rate especially for large length codes. The reason for this is that the max clock rate for the available PIC is around

40 MHz, this clock rate determines the rate of executing the program instructions, which can lead to maximum chip rate of 4 MHz. Increasing the length of the code will lead to increasing the required instructions to generate this code, which at the end will lead to decreasing the maximum chip rate of the generated code.

### **2.8.3 Field Programmable Gate Arrays (FPGA)**

Field programmable gate arrays are specialized integrated circuits, consists of an array of logic cells that can be interconnected by programming to realize different digital design. Interconnections are programmed using electrically programmable switches. Vendors produce a single standard device that users program to produce their required functions. Configuration is performed through programming by the end user. Largest devices are now 2Mega gates, large enough to implement many digital systems on a single chip. Typically they are used for rapid product development, prototyping and/or low volume gate count design. Programmable logic devices contain a number of logic cells, they can be as simple as a transistor or as complex as a microprocessor. Typically they are used to implement combinational logic and sequential logic functions.

When designing circuits for implementation in FPGA, it is essential to employ Computer-Aided Design (CAD) programs. A typical CAD system for FPGA would include software for the following tasks: initial design entry, logic optimization, device fitting, simulation, and configuration. This design flow is illustrated in Fig. 2.11. Design entry may be done either by creating a schematic diagram with a graphical CAD tool, by using a text based system to describe a design in a simple hardware description language, or with a mixture of design entry methods. Since initial logic entry is not usually in an optimized form, algorithms are employed to optimize the circuits, after which additional algorithms analyze the resulting logic equations and "fit" them into the FPGA. Simulation is used to verify correct operation, and the user would return to the design entry step to fix errors. When a design simulates correctly it can be loaded into a programming unit and used to configure an FPGA. One final detail to note about Fig. 2.11 is that while the original design entry step is performed manually by the designer, all other steps are carried out automatically by most CAD systems.

### **2.8.4 Arbitrary Waveform Generator (AWG)**

First, let's discuss what an AWG is. Fundamentally, the AWG is a sophisticated playback system that produces waveforms based on a stored digital data that describes the constantly changing voltage levels of an analog signal. The analog output signal is generated by converting these stored digital data into analog signal using Digital to Analog converter (DAC). Today's AWG are designed to provide improved phase, frequency, and amplitude control of the output signal. Moreover, many AWG offer

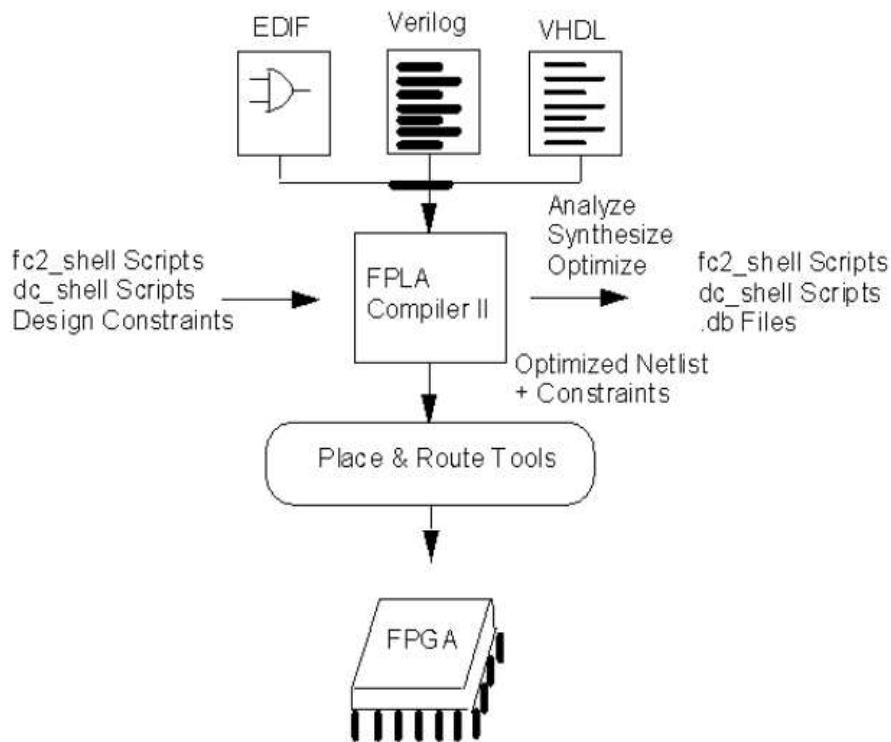


Figure 2.11: CAD design flow for FPGA.

a way to modulate the signal from internal or external sources, which is essential for some types of standards compliance testing.

After exploring the different technologies used to generate the PN code let us make a comparison between them. The comparison will include the cost, size, flexibility (in generating different sequences) and maximum chip rate. Table 2.1 shows the comparison between the above-mentioned technologies.

Technology	Cost	Size	Flexibility	$f_{ch}$ max. (MHz)
LFSR	Low	Medium	No	30
PIC	Very Low	Very Small	Yes	4
FPGA	Low	Small	Yes	100
AWG	Very High	Large	Yes	500

Table 2.1: Comparison between the different technologies used to generate the PN code

# Chapter 3

## Wavelet Transform and Higher Order Statistics

### 3.1 Introduction

As was mentioned in chapter 1, the objective of this thesis is to enhance the performance of the spread spectrum technique in different applications. These enhancements will include the noise performance and the resolution of the systems, which are based on spread spectrum technique. The purpose of this chapter is to give a general explanation for the different signal processing algorithms, which will be used in this thesis to enhance the performance of the SS technique. These signal processing tools will include the use of wavelet and wavelet packet transform [82] and higher order statistics [136] to improve the noise performance of SS system. Different examples will be given here to indicate the use of the above-mentioned signal processing algorithms.

### 3.2 Fourier, Wavelet and Wavelet Packet Transforms

First of all, why do we need a transform, or what is a transform anyway? Mathematical transformations are applied to signals to obtain further information from the signal that is not readily available in the raw signal (signal in time domain).

There are numbers of transformations that can be applied, among which the Fourier transform (FT) are probably by far the most popular. Most of the signals in practice are time-domain signals in their raw format. That is, whatever that signal is measuring, is a function of time. When we plot time-domain signals, we obtain a time-amplitude representation of the signal. This representation is not always the best representation of the signal for most signal processing related applications. In many cases, the most distinguished information is hidden in the frequency content of the signal. The frequency spectrum of a signal is basically the frequency components (spectral components) of that signal. The frequency spectrum of a signal shows what

frequencies exist in the signal. So how do we measure frequency, or how do we find the frequency content of a signal? The answer is FT. If the FT of a signal in time domain is taken, the frequency-amplitude representation of that signal is obtained. In other words, we now have a plot with one axis being the frequency and the other being the amplitude. This plot tells us how much of each frequency exists in our signal.

Although FT is probably the most popular transform being used, it is not the only one. There are many other transforms that are used quite often by engineers and mathematicians. Hilbert transform, Short-Time Fourier Transform (STFT), Wigner distributions, the Radon transform, and of course our featured transformation, the wavelet transform (WT), constitute only a small portion of a huge list of transforms that are available at engineer and mathematician's disposal. Every transformation technique has its own area of application, with advantages and disadvantages, and the WT is no exception.

For many signals, FT is extremely useful because the signal's frequency content is of great importance. So why do we need other techniques, like WT? FT has a serious drawback. In transforming to the frequency domain, time information is lost. When looking at a FT of a signal, it is impossible to tell when a particular event took place. If the signal properties do not change much over time that is, if it is what is called a stationary signal this drawback isn't very important. However, most interesting signals contain numerous nonstationary or transitory characteristics: drift, trends, abrupt changes, and beginnings and ends of events. These characteristics are often the most important part of the signal, and FT is not suited to detecting them.

In an effort to correct this deficiency, Dennis Gabor (1946) adapted the FT to analyze only a small section of the signal at a time a technique called windowing the signal. Gabor's adaptation, called the STFT, maps a signal into a two-dimensional function of time and frequency.

Time-frequency representations show the distribution of the energy of a signal in the time-frequency plane; in such a way that relevant information can be extracted to achieve good detection. The results generally depend on the method used as a time-frequency representation.

For example, STFT tile the time-frequency plane in regular cells all of which have the same uncertainties. The STFT represents a sort of compromise between the time- and frequency-based views of a signal. It provides some information about both when and at what frequencies a signal event occurs. However, you can only obtain this information with limited precision, and that precision is determined by the size of the window. While the STFT compromise between time and frequency information can be useful, the drawback is that once you choose a particular size for the time window, that window is the same for all frequencies. Many signals require a more flexible approach one where we can vary the window size to determine more

accurately either time or frequency. Discrete wavelet transform bases tile the time-frequency plane more naturally. A low frequency needs to be observed for a long time to be correctly estimated whereas a high frequency can rapidly change at any time. Hence, time-frequency localization naturally depends on the 'observation scale'. It is possible, using adapted wavelet transform, to obtain adapted tiling in the time-frequency plane, which is automatically generated based on the signal observation. On the other hand, the time-frequency plane tiling, using wavelet packet transform (WPT), corresponds to a complete set of admissible wavelets constituting a Hilbert space. The signal is projected on each element of this space producing decomposition coefficients. Fig. 3.1 shows the tiling of the time frequency plane for Short-Time Fourier transform (a), wavelet transform (b), and wavelet packet transform (c). The difference between Fourier transform, wavelet transform and wavelet packet transform will be indicated in the next sections.

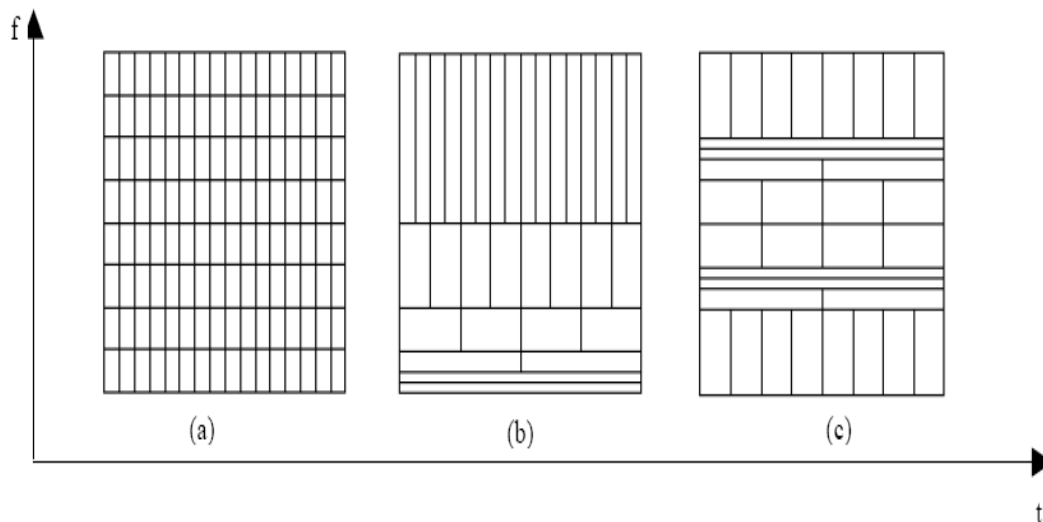


Figure 3.1: Tiling the time-frequency plane (a) Short-Time Fourier transform (b) Wavelet transform (c) Wavelet packet transform.

### 3.3 Fourier Transform

The Fourier transform lies in its ability to analyze a signal in the time domain for its frequency content. The transform works by first translating a function in the time domain into a function in the frequency domain. The signal can then be analyzed for its frequency content because the Fourier coefficients of the transformed function represent the contribution of each sine and cosine function at each frequency. An inverse Fourier transform does just what you expect, transform data from the frequency domain into the time domain.

### 3.3.1 The Continues Fourier Transform (CFT)

Let  $x(t)$  be a continues function in the time domain. The Fourier transform,  $X(\omega)$ , of  $x(t)$  is defined as follow:

$$X(\omega) = \int_{-\infty}^{\infty} x(t)e^{-j\omega t} dt \quad (3.1)$$

Given  $X(\omega)$ ,  $x(t)$  can be obtained by the inverse Fourier transform as follow:

$$x(t) = \frac{1}{2\pi} \int_{-\infty}^{\infty} X(\omega)e^{j\omega t} d\omega \quad (3.2)$$

### 3.3.2 The Discreet Fourier Transform (DFT)

The Discreet Fourier Transform (DFT) estimates the Fourier transform of a signal from a finite number of its sampled points. Suppose that a continues signal  $x(t)$  is discretized into a sequence  $x(n)$ , where  $n$  assumes the discreet values  $0, 1, \dots, N - 1$ . The DFT pair that applies to the sampled signal is given by:

$$X(k) = \frac{1}{N} \sum_{n=0}^{N-1} x(n)e^{-j2\pi \frac{nk}{N}}, n, k = 0, 1, \dots, N - 1 \quad (3.3)$$

$$x(n) = \sum_{k=0}^{N-1} X(k)e^{j2\pi \frac{nk}{N}}, n, k = 0, 1, \dots, N - 1 \quad (3.4)$$

### 3.3.3 Short Time Fourier Transform (STFT)

We saw earlier that FT is not well suited to describing local changes in "frequency content" because the frequency components defined by the Fourier transform have infinite (i.e., global) time support. The STFT could be defined as a method for Fourier analysis of non-stationary signals, based on a joint time-frequency signal representation. For a signal  $x(t)$ , the STFT pair can be written as:

$$X_{STFT}(\omega, \tau) = \int_{-\infty}^{\infty} x(t)w(t - \tau)e^{-j\omega t} dt \quad (3.5)$$

$$x(t) = \frac{1}{2\pi} \int_{-\infty}^{\infty} \int_{-\infty}^{\infty} X_{STFT}(\omega, \tau)w(t - \tau)e^{j\omega t} d\omega d\tau \quad (3.6)$$

assuming real-valued  $w(t)$  for which  $\int |w(t)|^2 dt = 1$ .

The STFT can be interpreted as a "sliding window CFT": to calculate  $X_{STFT}(\omega, \tau)$ , slide the center of the window  $w(t)$  to time  $\tau$ , window the input signal, and compute

the CFT of the result. The idea is to isolate the signal in the vicinity of time  $\tau$ , then perform a CFT analysis in order to estimate the "local" frequency content at time  $\tau$ . This can be understood as time and frequency shifts of the window function  $w(t)$ . The STFT basis is often illustrated by a tiling of the time-frequency plane, where each tile represents a particular basis element.

As an example to show how the STFT is working, assume that the signal under analysis  $y(n)$  is given as:

$$\begin{aligned} y(n) &= x(n) + z(n) \\ y(n) &= \cos(\omega_o n)p(n) + z(n) \\ y(n) &= \cos(\omega_o n) [u(n - n_1) - u(n - n_2)] + z(n) \end{aligned} \quad (3.7)$$

where  $x(n)$  is a received RF radar pulse exists from  $n = n_1$  to  $n = n_2$  with a carrier frequency  $\omega_o$ ,  $z(n)$  is a white Gaussian noise,  $n = 1, 2, \dots, N$ . Fig. 3.2(a) shows the received RF radar pulse signal  $x(n)$  in the time domain with number of data sample  $N = 4096$  sample,  $n_1 = 2049$  and  $n_2 = 2304$ . Fig. 3.2(b) shows the STFT transform coefficients of  $x(n)$  using a rectangular window  $w(n)$  of width 256, which is selected to be equal to the pulse width, this will leads to a number of decomposition frames equals to 16.

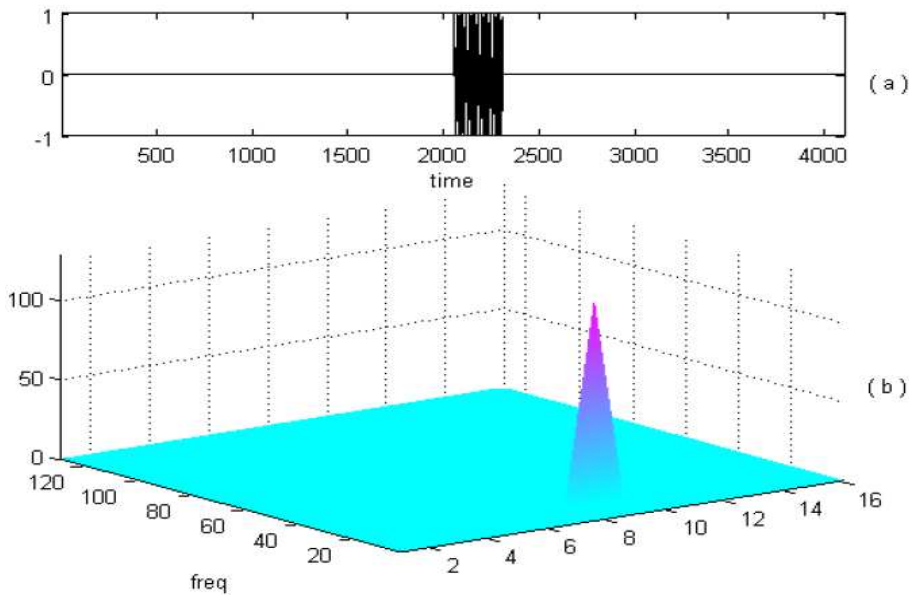


Figure 3.2: (a) The received radar pulse  $x(n)$ . (b) The STFT of  $x(n)$ .

To test the ability of the STFT in localizing a signal with the existence of noise, Fig. 3.3(a) shows a received RF radar pulse signal  $y(n)$  in the time domain with a SNR = -3 dB. Fig. 3.3(b) shows the STFT transform coefficients of  $y(n)$ . It is clear from Fig. 3.3(b) that the STFT is able to localize the signal with the existence of noise.



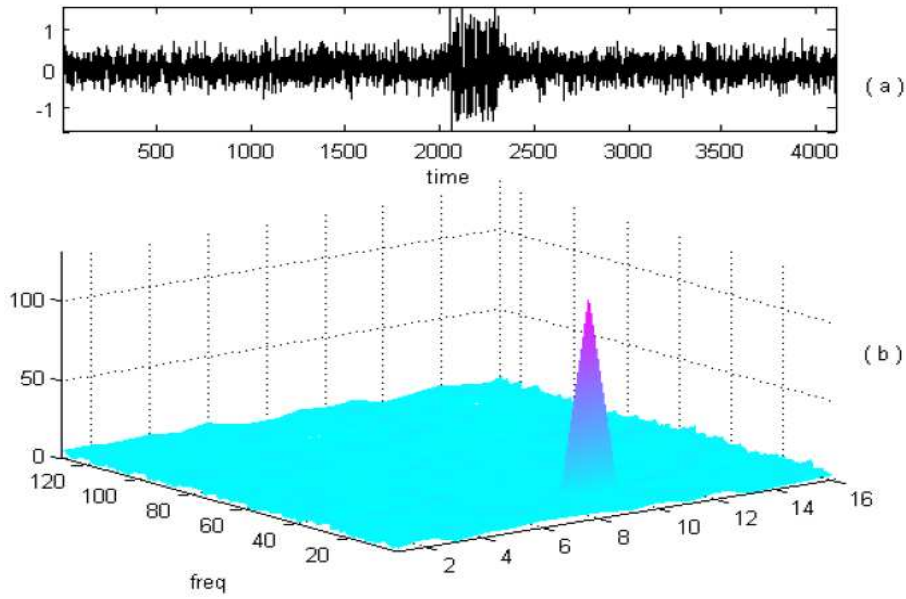


Figure 3.3: (a) The received noisy radar pulse  $y(n)$ , SNR = -3 dB. (b) The STFT of  $y(n)$ .

### 3.4 Wavelet Transform (WT)

Everywhere around us are signals that can be analyzed. For example, there are seismic tremors, human speech, engine vibrations, medical images, financial data, music, and many other types of signals. Wavelet analysis is a new and promising set of tools and techniques for analyzing these signals.

Wavelet analysis is perhaps best viewed in the context of multiresolution analysis as developed by Malat [137]. There are two functions to be consider in such an analysis: the scaling function,  $\phi_{j,k}(t) = 2^{j/2}\phi(2^j t - k)$ , and the mother wavelet,  $\psi_{j,k}(t) = 2^{j/2}\psi(2^j t - k)$ , where  $j$  and  $k$  are integers representing the scale factor and the translation factor respectively. In the time-scale (or time-frequency) joint representation the horizontal stripes of the wavelet transform coefficients are the correlations between the signal and the wavelets at given scale  $j$ . When the scale is small the wavelet is concentrated in time, and the wavelet analysis has a detailed view of the signal. When the scale increases the wavelet spreads out in time, and the wavelet analysis takes into account the long-time behavior of the signal. We define  $V_j$  to be the subspace spanned by  $\phi_{j,k}(t)$ , and require a nesting of the spanned spaces,  $\dots \subset V_{-1} \subset V_0 \subset V_1 \subset \dots \subset L_2$ . The space spanned by the mother wavelet at scale  $j$  is denoted  $W_j$  and constitutes the orthogonal complement of  $\phi_{j-1,k}$  in  $\phi_{j,k}$ . If we choose a coarsest scale  $j_0$  then we get that  $L_2 = V_{j_0} \cup W_{j_0} \cup W_{j_0+1} \cup \dots$ . A function  $f(t)$  then can be represented as:

$$f(t) = \sum_{k=-\infty}^{\infty} a_{j_0}(k)\phi_{j_0 k}(t) + \sum_{j=j_0}^{\infty} \sum_{k=-\infty}^{\infty} d(j, k)\psi_{j,k}(t) \quad (3.8)$$

The first summation in (3.8) provides us with a coarse approximation to  $f(t)$ , which is the projection of  $f(t)$  onto  $V_{j_0}$ . The second summation for each  $j$  provides finer details and is the projection of  $f(t)$  onto the  $W_j$  spaces.

In practice, the wavelet approximation coefficients  $a_{j_0}(k)$  and the detail coefficients  $d(j, k)$  are computed using Mallat's fast algorithm [137] which involves the following filtering operations:

$$a_j(k) = \sum_m h(m - 2k)a_{j+1}(m) \quad (3.9)$$

$$d_j(k) = \sum_m g(m - 2k)a_{j+1}(m) \quad (3.10)$$

where  $h(n)$  and  $g(n)$  are referred to as the scaling filter and wavelet filter, respectively. Equations (3.9) and (3.10) show how the discrete wavelet transform (DWT) is performed: By convolving the coefficients at scale  $j$  with the time reversed filter coefficients  $h(-n)$  and  $g(-n)$  and then down sampling to get the coefficients at scale  $j - 1$ . Figs 3.4(a) and 3.4(b) show a filter bank implementation for the decomposition and reconstruction of the wavelet transform. These filter structures are known in terms of subband coding as 2-band perfect reconstruction quadrature mirror filters (PRQMF). The PRQMF subband-coding scheme depicted in Figs. 3.4(a) and 3.4(b) adhere to a dyadic tree structure, which splits only the lower half of the signal spectrum at each successive level. When the subband-coding tree has been fully traversed, the approximation coefficients are produced at the final tree split, with the detail coefficients being produced at each tree split. A thorough treatment of wavelet decompositions as they relate to subband coding can be found in [138].

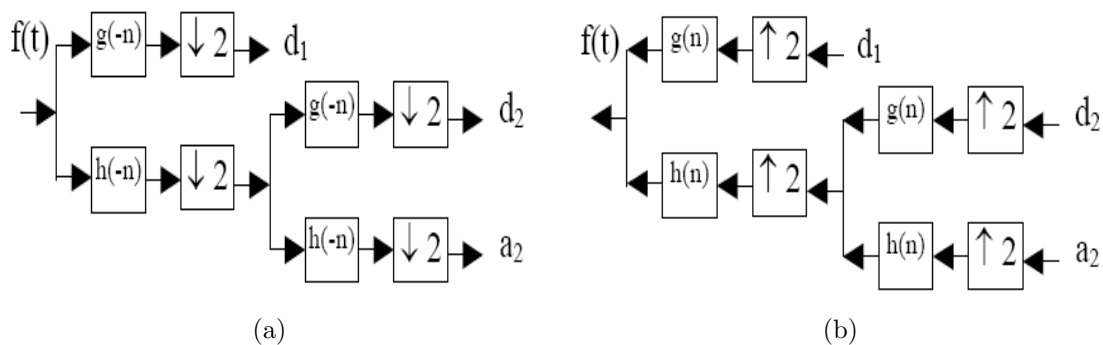


Figure 3.4: (a) Filter bank implementation of discrete wavelet decomposition. (b) Filter bank implementation of discrete wavelet reconstruction.

For many signals, the low-frequency content is the most important part. It is what gives the signal its identity. The high-frequency content, on the other hand, imparts flavor or nuance. Consider the human voice. If you remove the high-frequency

components, the voice sounds different, but you can still tell what's being said. However, if you remove enough of the low-frequency components, you hear gibberish. In wavelet analysis, we often speak of approximations and details. The approximations are the high-scale, low frequency components of the signal. The details are the low-scale, high frequency components. The filtering process, at its most basic level, is indicated in Fig. 3.5. The decomposition process can be iterated, with successive approximations being decomposed in turn, so that one signal is broken down into many lower resolution components this is called the wavelet decomposition tree, Fig. 3.5. Since the analysis process is iterative, in theory it can be continued indefinitely. In reality, the decomposition can proceed only until the individual details consist of a single sample or pixel. In practice, you'll select a suitable number of levels based on the nature of the signal, or on a suitable criterion such as entropy.

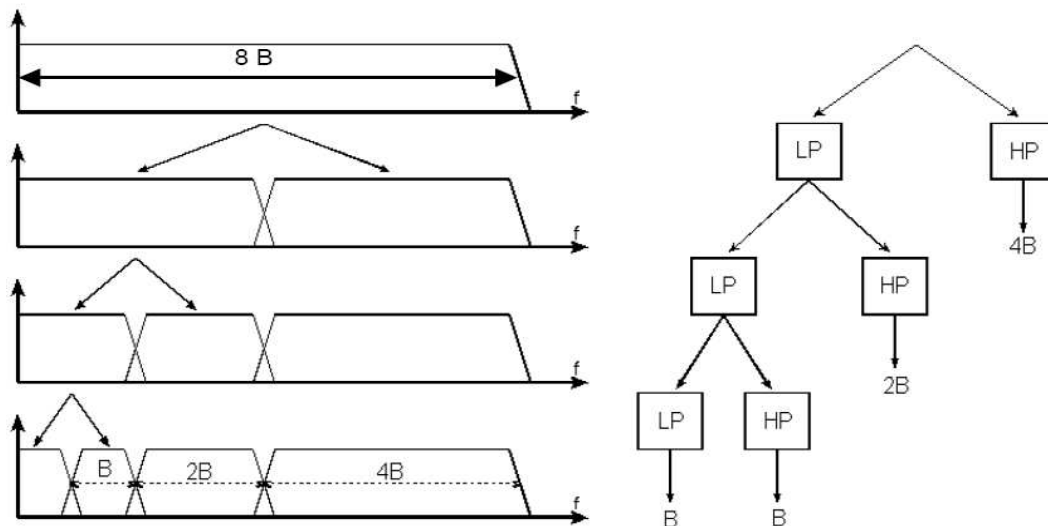


Figure 3.5: Spectral decomposition of the signal using wavelet transform.

As an example to show how the DWT is working, Fig. 3.6(a) shows a received RF radar pulse signal  $x(n)$ , which was given in Fig. 3.2(a), in the time domain. Fig. 3.6(b) shows the wavelet transform coefficients of  $x(n)$  using Daubechies wavelet of order 4 and number of decomposition levels  $J = 4$ . Fig. 3.7(a) shows a received noisy RF radar pulse signal  $y(n)$ , which was given in Fig. 3.3(a), in the time domain with a SNR = -3 dB. Fig. 3.7(b) shows the wavelet transform coefficients of  $y(n)$  using Daubechies wavelet of order 4 and number of decomposition levels  $J = 4$ .

The order of the Daubechies wavelet controls the number of vanishing moments, which is related to the regularity of the wavelet. Increasing the order of the Daubechies wavelet increases its regularity. On the other hand this will reduce the localization of the wavelet. Consequently, a tradeoff between the regularity and the localization of the wavelet should take place.

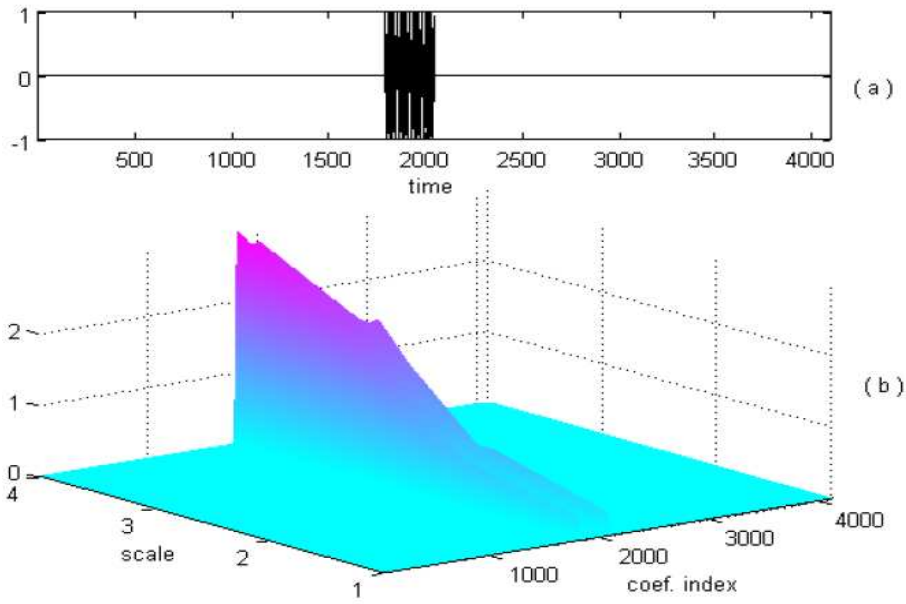


Figure 3.6: (a) The received radar pulse  $x(n)$ . (b) The wavelet transform coefficients of  $x(n)$ ,  $J = 4$ .

### 3.5 Wavelet Packet Transform (WPT)

The wavelet packet transform method is a generalization of wavelet decomposition that offers a richer range of possibilities for signal analysis. The wavelet packet transform has a number of applications. One of these involves the calculation of the best basis, which is a minimal representation of the data relative to a particular cost function. The best basis is used in applications that include noise reduction and in data compression. One step in the wavelet transform calculates a low pass (scaling function) result and a high pass (wavelet function) result. The low pass result is a smoother version of the original signal. The low pass result recursively becomes the input to the next wavelet step, which calculates another low and high pass result, until only a single low pass ( $2^0$ ) result is calculated. The wavelet transform applies the wavelet transform step to the low pass result. The wavelet packet transform applies the transform step to both the low pass and the high pass result.

For the received signal  $y(n)$ , which was given by (3.7), using the wavelet packet transform one can have a two dimension time-frequency wavelet packet coefficients as follow:

$$WP_{j,s}^y(i) = WP_{j,s}^x(i) + WP_{j,s}^z(i) \quad (3.11)$$

where  $WP_{j,s}^y(i)$ ,  $WP_{j,s}^x(i)$  and  $WP_{j,s}^z(i)$  are the wavelet packet coefficients of  $y$ ,  $x$  and  $z$  respectively,  $j = 1, 2, \dots, J$  while  $J$  is the number of decomposition levels and  $s = 1, 2, \dots, 2^j$ , is the number of scales and  $i = 1, 2, \dots, M$ , with  $M = N/2^j$  and  $N$  is the length of the signal. As an example, Fig. 3.8(a) shows the received signal  $x(n)$ ,

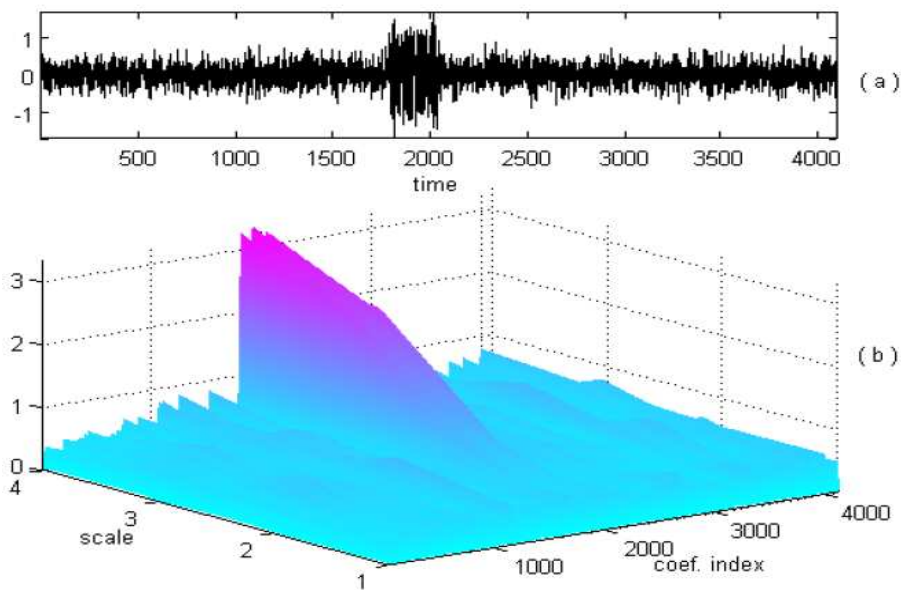


Figure 3.7: (a) The received noisy radar pulse  $y(n)$ , SNR = -3 dB. (b) The wavelet transform coefficients of  $y(n)$ ,  $J = 4$ .

which was given in Fig. 3.2(a), in the time domain. Fig. 3.8(b) shows the wavelet packet coefficients of  $x(n)$  using Daubechies wavelet of order 4 and number of levels  $J = 4$ . Fig. 3.9(a) shows the received noisy signal  $y(n)$ , which was given in Fig. 3.3(a), in the time domain with SNR = -3 dB. Fig. 3.9(b) shows the wavelet packet coefficients of  $y(n)$  using Daubechies wavelet of order 4 and number of levels  $J = 4$ .

## 3.6 Higher Order Statistics (HOS)

Higher order statistics is a rapidly evolving signal analysis area with growing applications in science and engineering. In recent years, much interest by academic, industrial, and government laboratories has focused around the research and development of HOS techniques. Applications of HOS-based methods span a remarkable broad range that includes telecommunications, sonar, radar, geophysics, image processing, speech processing, biomedicine, oceanography, plasma physics, economic series and fluid mechanics.

Although considerable work has been done in the area of power spectra estimation over the paste four decades, the information contained in the power spectrum is essentially that which is present in the second-order-statistics (e.g., autocorrelation) of a signal; this would suffice for a complete statistical description of a Gaussian processes only. Furthermore, second-order statistics are phase-blind and only describe linear mechanisms governing the process. However, there are signal processing situations in practice where signal analysts must look beyond the second-order statistics (or spectra), to extract phase information, as well as information due to deviations from

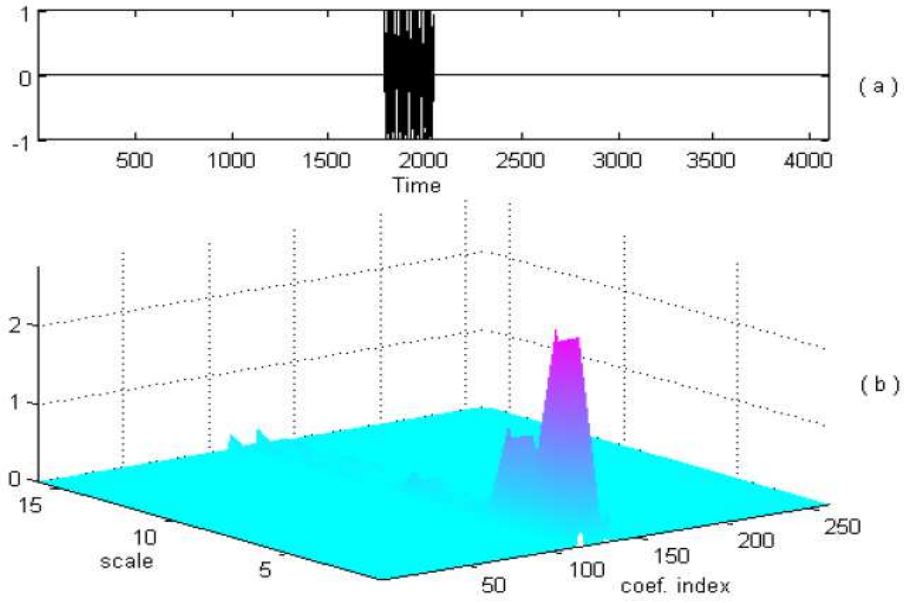


Figure 3.8: (a) The received radar pulse  $x(n)$ . (b) The wavelet packet coefficients of  $x(n)$ ,  $J = 4$ .

Gaussianity and the presence of nonlinearity. Under broad signal and signal conditions, HOS also become high SNR domains where detection, parameter estimation, and signal reconstruction can be performed.

### 3.6.1 Moments and Cumulants of Stationary Random Processes

In this subsection we are concerned primarily with the definitions and properties of moments, and cumulants of stationary random processes. Although the value of stochastic signal at each instant of time is not known exactly, their HOS (moments and cumulants), when they exist, are multidimensional deterministic functions that possess special symmetry properties.

If  $\{z(k)\}$ ,  $k = 0, \pm 1, \pm 2, \pm 3, \dots$  is a real stationary random process and its moments up to order  $n$  exist, then

$$Mom[z(k), z(k + \tau_1), \dots, z(k + \tau_{n-1})] = E\{z(k).z(k + \tau_1).....z(k + \tau_{n-1})\} \quad (3.12)$$

where  $Mom[z]$  is the moments of the random process  $z$ . The moment will depend only on the time difference  $\tau_1, \tau_2, \dots, \tau_{n-1}$ . We now write the moments of a stationary random process as:

$$m_n^z(\tau_1, \tau_2, \dots, \tau_{n-1}) = E\{z(k).z(k + \tau_1).....z(k + \tau_{n-1})\} \quad (3.13)$$

Similarly, the  $n^{th}$ -order cumulants of  $\{z(k)\}$  are  $(n - 1)$ -dimensional functions which can be written in the form:

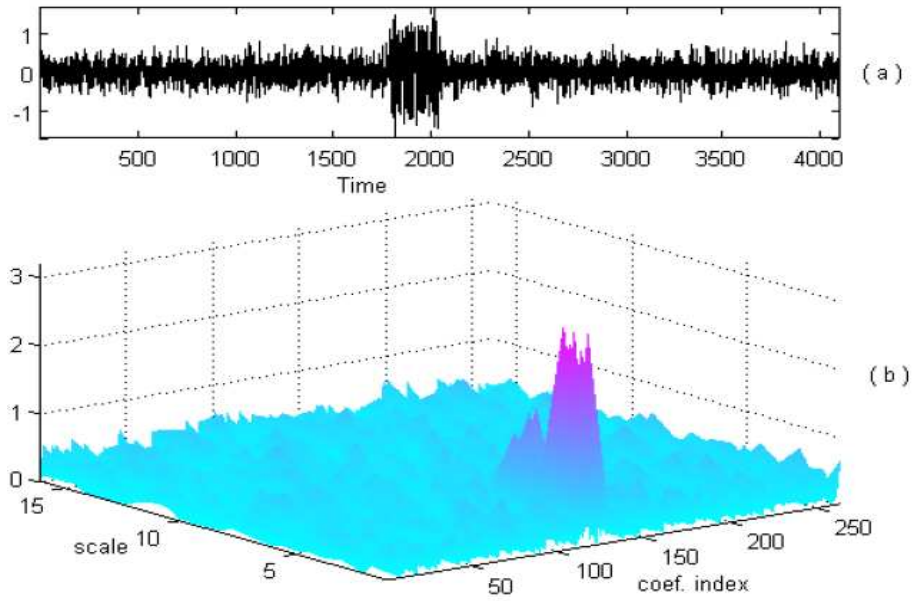


Figure 3.9: (a) The received noisy radar pulse  $y(n)$ , SNR = -3 dB. (b) The wavelet packet coefficients of  $y(n)$ ,  $J = 4$ .

$$c_n^z(\tau_1, \tau_2, \dots, \tau_{n-1}) = \text{Cum} \{z(k), z(k + \tau_1), \dots, z(k + \tau_{n-1})\} \quad (3.14)$$

The cumulants are related to the moments by the following relationships:

**1st-order cumulant:** (mean value)

$$c_1^z = m_1^z = E \{z(k)\} \quad (3.15)$$

**2nd-order cumulant:** (covariance sequence)

$$c_2^z(\tau_1) = m_2^z(\tau_1) - (m_1^z)^2 \quad (3.16)$$

**3rd-order cumulant:**

$$c_3^z(\tau_1, \tau_2) = m_3^z(\tau_1, \tau_2) - m_1^z [m_2^z(\tau_1) + m_2^z(\tau_2) + m_2^z(\tau_2 - \tau_1)] + 2(m_1^z)^3 \quad (3.17)$$

**4th-order cumulant:**

$$\begin{aligned} c_4^z(\tau_1, \tau_2, \tau_3) = & m_4^z(\tau_1, \tau_2, \tau_3) - m_2^z(\tau_1) \cdot m_2^z(\tau_3 - \tau_2) - m_2^z(\tau_2) \cdot m_2^z(\tau_3 - \tau_1) \\ & - m_2^z(\tau_3) \cdot m_2^z(\tau_2 - \tau_1) - m_1^z [m_3^z(\tau_2 - \tau_1, \tau_3 - \tau_1) \\ & - m_3^z(\tau_2, \tau_3) + m_3^z(\tau_2, \tau_4) + m_3^z(\tau_1, \tau_2)] \\ & + (m_1^z)^2 [m_2^z(\tau_1) + m_2^z(\tau_2) + m_2^z(\tau_3) + m_2^z(\tau_3 - \tau_1) + m_2^z(\tau_3 - \tau_2) \\ & + m_2^z(\tau_2 - \tau_1)] - 6(m_1^z)^4. \end{aligned} \quad (3.18)$$

If the process  $\{z(k)\}$  is zero-mean ( $m_1^z = 0$ ), it follows from (3.16) and (3.17) that the second- and third-order cumulants are identical to the second- and third-order moments, respectively. However, to generate the fourth-order, we need knowledge of the fourth-order and second-order moments in (3.18).

### 3.6.2 Variance, Skewness and Kurtosis Measures

By putting  $\tau_1 = \tau_2 = \tau_3 = 0$  in (3.16), (3.17), (3.18) and assuming ( $m_1^z = 0$ ) we get

$$\begin{aligned}\gamma_2^z &= E\{z^2(k)\} = c_2^z(0) && (\text{variance}) \\ \gamma_3^z &= E\{z^3(k)\} = c_3^z(0, 0) && (\text{skewness}) \\ \gamma_4^z &= E\{z^4(k)\} - 3[\gamma_2^z]^2 = c_4^z(0, 0, 0) && (\text{kurtosis})\end{aligned}\quad (3.19)$$

The third central cumulant (skewness) is a measure of symmetry of the random variable and some times a measure of skewness of the random variable. This coefficient is positive if the random variable has a probability density that is skewed to the right and negative if skewed to the left.

The fourth central cumulant is called the kurtosis and is a measure of peakedness of the random variable near the mean. The more values of the random variable concentrated near the mean of a probability density function, the larger the coefficient of kurtosis. This mean the density will have a large peak near the mean. Normalized kurtosis  $k_4^z$  is defined as

$$k_4^z = \gamma_4^z / [\gamma_2^z]^2 \quad (3.20)$$

### 3.6.3 Moments and Cumulants for Gaussian Distributed Random Processes

If  $\{z(k)\}$ ,  $k = 0, \pm 1, \pm 2, \pm 3, \dots$  is a real stationary random process and its probability distribution function (*pdf*),  $f(z)$ , is Gaussian with variance  $\sigma$ , which is given as:

$$f(z) = 0.5 \exp\left\{-\frac{z^2}{2\sigma^2}\right\} / \sqrt{2\pi\sigma^2} \quad (3.21)$$

The  $n^{\text{th}}$ -order moment  $m_n$  can be calculated from the following relation:

$$m_n^z = \int_{-\infty}^{\infty} z^n f(z) dz \quad (3.22)$$

The cumulants  $c_n^z$ ,  $n = 1, 2, 3, 4$  follow easily from the moments using the relationships between cumulants and moments. Fig.3.10 illustrates the moments and cumulants of  $z$  from the first to fourth order. Let us note that all cumulants of order greater than two ( $n > 2$ ) are zero.



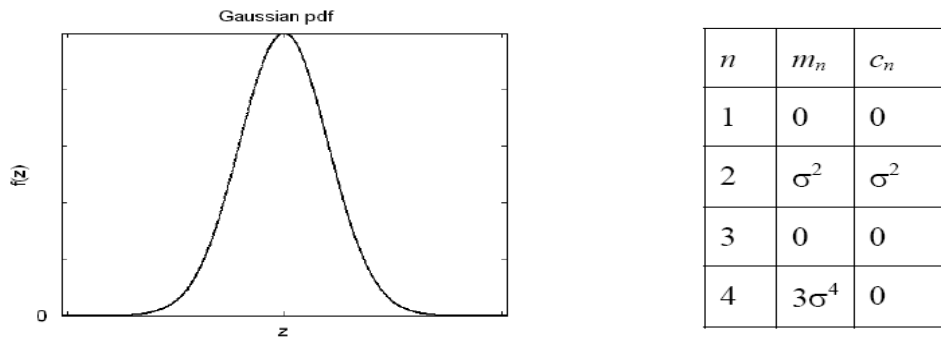


Figure 3.10: The  $n^{\text{th}}$ -order moments and cumulants,  $n = 1, \dots, 4$ , of the Gaussian *pdf*.

## 3.7 Denoising

When a signal is transformed or mapped to a different "space" and processed, the signal processing is said to have been performed in the transform domain, or, in other words, that one is using transform domain processing. Note that this mapping should be unique and unambiguous, and that an inverse mapping or transformation, which can return the signal to the time domain, should exist. The most widely used transform is the FT, but there are many others of importance such as the Hadamard, Fresnel, Hartley, Mellin and Hilbert transforms, to name but a few. In communications and radar applications, particularly ones using spread spectrum techniques, transform domain processing can be utilized to suppress undesired noise and interference and, consequently, improve performance. Here, the basic idea is to choose a transform such that the desired signal is nearly a delta function in the transform domain, while the undesired signal is transformed to a waveform that is very "flat". A simple threshold can then remove the noise without removing a significant amount of desired signal energy. An inverse transform then produces the nearly noise-free desired signal. This is the fundamental concept behind transform domain denoising.

### 3.7.1 Wavelet and Wavelet-Packet Denoising

Donoho and Johnstones's [139] wavelet shrinkage denoising technique (known as WaveShrink) consists three steps:

1. Transform data into wavelet domain.
2. Shrink the empirical wavelet coefficients towards zero.
3. Transform the shrunk coefficients back to the data domain.

The choice of shrinkage function and thresholds in step (2) plays an important role for WaveShrink both theoretically and in practice. The concept of denoising in wavelet and wavelet packet transform is the same. Donoho [139] used the same

approach to wavelet-based denoising. The idea is that only large wavelet coefficients contribute to the signal, and hence to obtain the estimated value of the noise-free signal  $x$  one needs to keep only those coefficients whose magnitudes are greater than a certain hard threshold with value  $\lambda$ . In recognizing that each wavelet coefficient contains a signal and noise portion, it is desirable to try removing the noisy portion. Soft thresholding like hard thresholding, aim to meet this objective by keeping only those coefficients whose magnitudes are greater than a certain level  $\lambda$ . However, the remaining coefficients are shrunk towards zero by an amount  $\lambda$  hence, soft thresholding is often referred to in wavelet literature as wavelet shrinkage.

Suppose we observe data  $y$  as given by (3.7), where  $x(n)$  are sampled values of a deterministic signal  $x$ . Our goal is to estimate the signal  $x$  form the noisy observation  $y$  with small mean-square-error (MSE), i.e. to find an estimate  $\hat{x}$  with small  $L_2$  risk:

$$MSE = R(\hat{x}, x) = \frac{1}{N} \sum_{n=1}^N E (\hat{x}(n) - x(n))^2 \quad (3.23)$$

From the linearity property of the wavelet or wavelet packet transform one can write the wavelet transform coefficients of (3.7) as follow:

$$W_j^y(i) = W_j^x(i) + W_j^z(i) \quad (3.24)$$

where  $W_j^y(i)$ ,  $W_j^x(i)$  and  $W_j^z(i)$  are the wavelet transform coefficients of  $y$ ,  $x$  and  $z$  respectively. Here we tray to find an estimate for  $x$  with desired properties, e.g. minimum mean square error (MSE), commonly used shrinkage functions include: the hard and the soft shrinkage functions. Hard thresholding and soft thresholding are given by the following

#### Hard threshold

$$W_j^{\hat{x}}(i) = \begin{cases} W_j^y(i), & |W_j^y(i)| \geq \lambda \\ 0, & |W_j^y(i)| < \lambda \end{cases} \quad (3.25)$$

#### Soft threshold

$$W_j^{\hat{x}}(i) = \begin{cases} \text{sgn} [W_j^y(i)] (|W_j^y(i)| - \lambda), & |W_j^y(i)| \geq \lambda \\ 0, & |W_j^y(i)| < \lambda \end{cases} \quad (3.26)$$

In applying wavelet thresholding the choice of  $\lambda$  is critical. Choosing too large threshold results in oversmoothing, whereas choosing too small threshold results in noisy estimates. In previous works of wavelet denoising the selection of the threshold  $\lambda$  is based on an estimate for the amount of noise in the wavelet coefficients. Applying such a technique in very low SNR situation can lead to completely losing the signal, which is hidden in noise. In this thesis a new technique for denoising based on wavelet packet transform is presented. To extract the RF radar pulse, a denoising procedure,

which is based on setting Gaussian coefficients (of the wavelet packet transform of the received signal) to zero, is performed [140], [141]. A denoised signal is then reconstructed from the retained coefficients. The problem becomes now how to get a Gaussianity measure. Higher-order-statistics are traditionally used to accomplish this task.

### 3.7.2 Threshold Selection Based on HOS

One of the key motivations behind the use of cumulants in signal processing problems is their ability to suppress additive Gaussian noise [136]. This ability of noise suppression is based on the fact that the  $n^{\text{th}}$  order cumulants of a Gaussian signal,  $c_n^z$ , are equal to zero for  $n > 2$ .

In the case under study the noise samples are Gaussian distributed when observed for a sufficiently long time. On the other hand the signal samples are not Gaussian. We will apply the Gaussianity measure for the wavelet packet coefficients of the received signal,  $WP_{J,s}^y(i)$ . The presence of the signal will give non-Gaussian coefficients at some frequency bands where the radar pulse exists. On the other hand, Gaussian coefficients will represent noise only. The wavelet coefficients of Gaussian noise clearly remain Gaussian when applying the linear wavelet transform [142]. A good candidate from the higher order cumulants is the kurtosis, which is the normalized version of the fourth-order cumulant as given by (3.20). The Gaussian process has a kurtosis value that theoretically equal to zero. The fourth-order cumulant is computed by a statistical expectation as (assuming zero mean of the wavelet packet coefficients):

$$c_4(WP_{J,s}) = E \{ WP_{J,s}^4 \} - 3 (E \{ WP_{J,s}^2 \})^2 \quad (3.27)$$

One should consider a normalized measure because the Gaussianity measure must not depend on the signal energy at each frequency band. In practice we have a limited number of data samples. So we are not able to have an exact value of the kurtosis. Instead we have an estimate value using time average. The estimation of the kurtosis can be calculated as:

$$\widehat{K}_4(WP_{J,s}) = M \frac{\sum_{i=1}^M WP_{J,s}^4(i)}{\left( \sum_{i=1}^M WP_{J,s}^2(i) \right)^2} - 3. \quad (3.28)$$

The estimated value is allowed to exist in a predetermined interval, which is conditioned by the probability properties of the estimator. Thus one needs to frame the estimator. By using the Bienayme-Tchebychev inequality, given a desired predetermined percentage, the estimator can be framed between two values depending on the first statistics of the estimator. In the case where the  $M$  coefficients  $WP_{J,s}$

are white and Gaussian, bias and variance of the kurtosis estimator when computed using (3.28) are given by [143]:

$$B(\widehat{K}_4) = -6/M, \quad , Var(\widehat{K}_4) = 24/M \quad (3.29)$$

The Bienyme-Tchebychev inequality allows a Gaussian estimator to move between

$$\pm \sqrt{24/M}/\sqrt{1-\alpha} + 6/M \quad (3.30)$$

with an  $\alpha$  authorized confidence percentage value. The simple test for Gaussianity measure is that:

$$\left| \widehat{K}_4 \right| < \sqrt{24/M}/\sqrt{1-\alpha} \quad (3.31)$$

Fig. 3.11 shows the Gaussianity measure for the example of Fig. 3.9. Fig. 3.11(a) is the wavelet packet coefficients and Fig. 3.11(b) shows the estimated kurtosis of the coefficients for each scale. The threshold is calculated using  $\alpha = 90\%$ . From Fig. 3.11 we notice that the coefficients at scale 2, 4 belong to the signal, whereas the coefficients of the other scales belong to the noise.

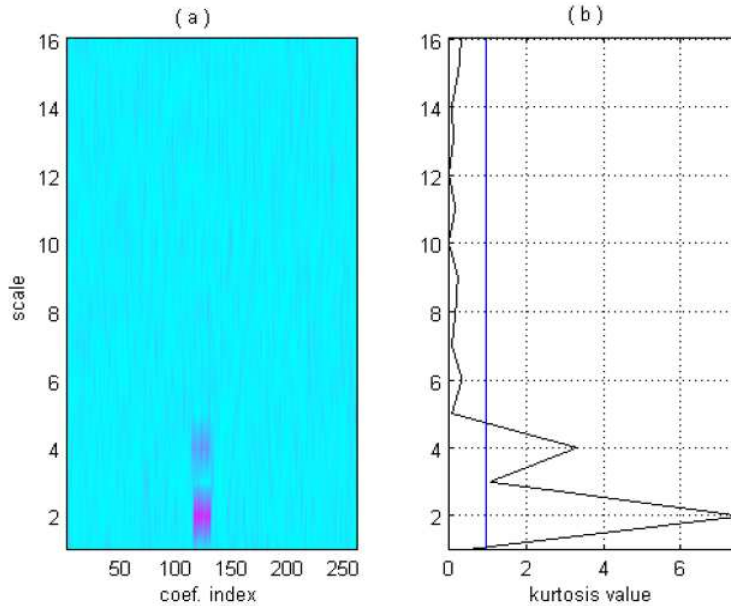


Figure 3.11: (a) The wavelet packet of  $y(n)$ . (b) The kurtosis of the wavelet packet.

### 3.7.3 Algorithms for Signal Denoising Using WPT and HOS

This algorithm is applied to denoising received RF radar pulses, which was given by (3.7). The algorithm is divided into two stages to decrease the computation complexity and hence increases the processing speed. The first stage is fundamental.

The second stage is used for further improvement in SNR if necessary. The steps of the first stage of the algorithm are as listed below:

1. Compute the wavelet packet coefficients of the received signal  $WP_{J,s}^y(i)$  at level  $J$ , scale  $s = 1, 2, 2^J$ .
2. Estimate the kurtosis for the wavelet packet coefficients of each scale using (3.28), (force the mean value of the coefficients at each scale to be zero).
3. Apply the Gaussianity test of (3.31).
4. Set the Gaussian coefficients to zero.
5. Count the number of the remaining non-Gaussian scales. If the number of the non-Gaussian scales is greeter than one go to the next stage. Otherwise go to the next step.
6. Reconstruct the signal from the retained coefficients.

The purpose of the next stage is to further improve the SNR. The steps of this stage of the algorithm are:

1. Apply a hard threshold to the remaining non-Gaussian coefficients scales. The threshold value is calculated using the following relation:

$$\lambda_s = \sigma_s \sqrt{2 \log(N)} \quad (3.32)$$

where  $\sigma_s = \text{Median}[|WP_{J,s}^y|]/0.6745$ , is the estimate of the noise at scale  $s$ , [82].

2. Reconstruct the signal from the retained coefficients.

Fig. 3.12 shows the result of the first and second stage of the algorithm for the example in Fig. 3.9.

### 3.7.4 Simulation and Results

The denoising of the received RF radar pulse is simulated in the presence of white Gaussian noise. The effect of signal parameter changes on the algorithm has been investigated. These parameters include the SNR and pulse repetition period (PRP) of the signal. The SNR is defined as the ratio of the signal power to the noise power in the entire period. Fig. 3.13 shows another example for denoising the RF radar pulse at SNR = -18 dB,  $N = 131072$ , which is equivalent to increasing the PRP. Using Daubechies wavelet of order 16 and number of levels  $J = 7$ . The threshold is calculated using  $\alpha = 90\%$ . From Fig. 3.13 it is clear that the proposed technique is still able to detect the radar pulse at SNR = - 18 dB.

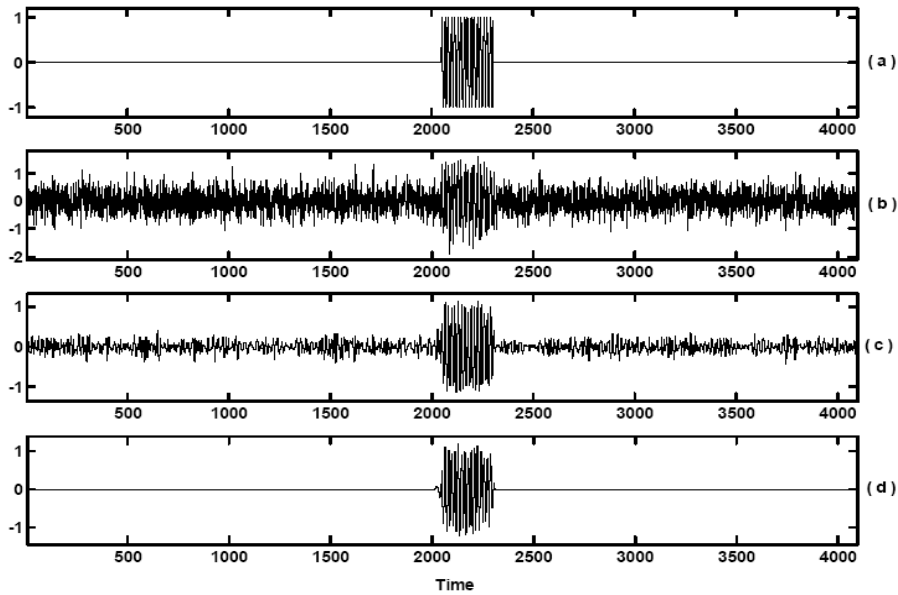


Figure 3.12: (a) The clean RF radar pulse  $x(n)$  (b) The received noisy RF radar pulse  $y(n)$ , SNR = -3 dB (c) The result of the first stage (d) The result of the second stage.

As a measure for the quality of the algorithm we calculated the RMSE (Root Mean Square Error) between the clean and the denoised signal. We made a comparison between the proposed algorithm and the wavelet de-noising technique available in MATLAB software using soft threshold with 'heursure' threshold selection. Fig. 3.14 shows a comparison for the RMSE between our proposed techniques (solid line) and that of the MATLAB (dashed line) with the same number of decomposition levels and the same mother wavelet (Daubechies order 16) for both techniques. It is clear from Fig. 3.14 that the proposed technique gives better results. The proposed technique gives very low RMSE value (maximum 0.02 at SNR = - 18 dB). Where the wavelet denoising technique using 'heursure' threshold selection gives RMSE = 1.6 at the same SNR.

### 3.7.5 Pulse Localization

In denoising the RF radar pulse, one of the important tasks is the localization of the received pulse in time domain. This means that our job is not only to see a clean signal in time domain but also undistorted information of the pulse (pulse width and position). Distorting the localization of the pulse in time domain will leads to an error in the radar ranging. As we mentioned in the previous sections that the wavelet transform gives better localization in the time-frequency domain than the STFT. To confirm the ability of the proposed technique in localizing the received RF pulse in time domain we will present a comparison between the proposed denoising technique and denoising using STFT.

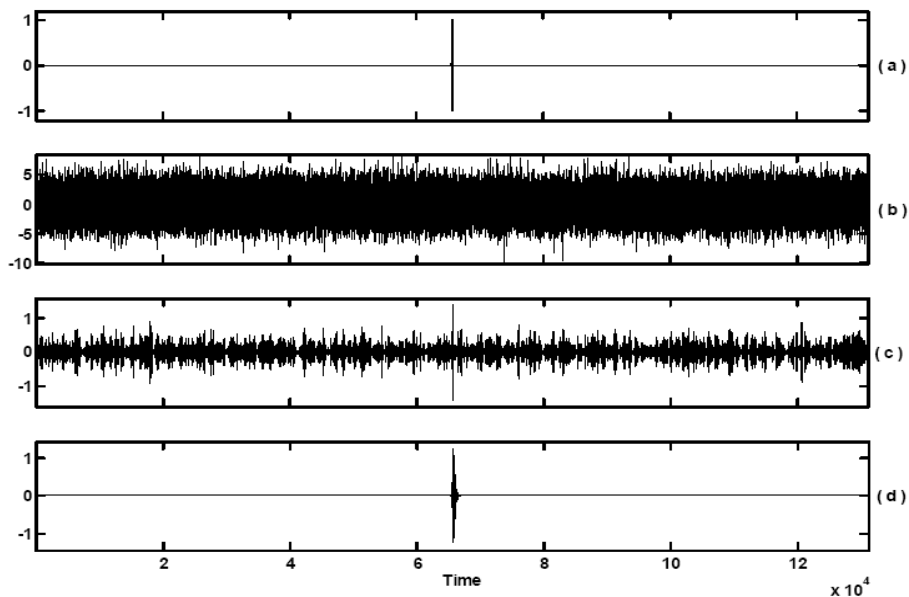


Figure 3.13: (a) Clean signal (b) Noisy signal SNR = - 18 dB (c) denoised signal after the first stage (d) denoised signal after the second stage.

Fig. 3.15 shows a comparison between the wavelet packet transform and STFT for the received RF pulse (in the upper panel of the figures) with a SNR -24 dB. Fig. 3.15(a) is the wavelet packet transform and Fig. 3.15(b) is the STFT for the noisy signal. Fig. 3.16 shows comparison between the wavelet packet transform and STFT for the same signal after denoising. Again Fig. 3.16(a) is wavelet packet transform of the signal after denoising and Fig. 3.16(b) is the STFT of the signal after denoising. From Figs. 3.15 and 3.16 it is clear that the STFT for the RF pulse is able to well localize the signal in the frequency domain in comparison with the wavelet packet transform. The reason for this is that the sinusoidal kernel of the Fourier transform is highly correlated with the carrier frequency of the received RF pulse. Figs. 3.17 shows a comparison between the denoised signals using the two techniques. Fig. 3.17(a) shows the result using the proposed technique and Fig. 3.17(b) shows the result using STFT. In each figure the clean signal (upper panel), noisy signal (middle panel), and the denoised signal (lower panel) was presented. It is clear from Fig. 3.17(b) that the STFT is not able to localize the signal in time domain. In the other hand as shown in Fig. 3.17(a) the wavelet packet transform is able to will localize the signal in time domain.

## 3.8 Wavelet Denoising of PN Codes

In this section we will discuss the application of the wavelet denoising technique to improve the SNR of the PN code. In the same time we will test the effect of the improvement in SNR of the PN code on a spread spectrum system, which utilize this

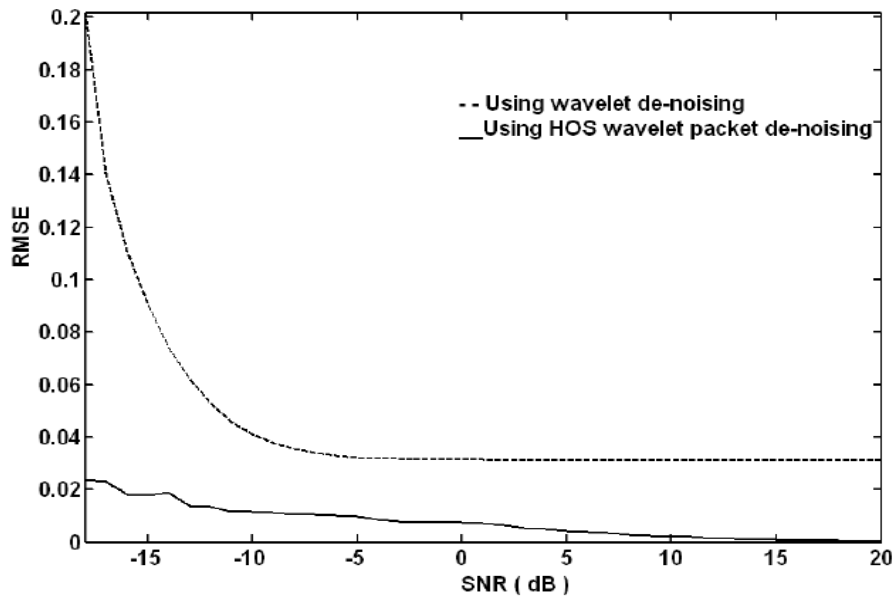


Figure 3.14: RMSE as a function in SNR for the proposed technique and the wavelet transform denoising in MATLAB.

PN code. There are a lot of parameters, which should be selected before applying the wavelet denoising technique. These parameters are:

1. Type of the mother wavelet.
2. Order of the selected mother wavelet.
3. Number of decomposition levels.
4. Threshold type.

The effect of the above mentioned parameters on the performance of the wavelet denoising technique would be considered and discussed. Different examples for applying the wavelet denoising will take place in this section.

In the field of the wavelet analysis there are different types of mother wavelets, which was developed and could be used. The effect of the used mother wavelet on the performance of the denoising technique is due to the fact that the obtained wavelet coefficients from the wavelet decomposition are the results of the correlation between the kernel of the wavelet transform (mother wavelet) and the signal under analysis. As was explained previously that the idea in the transform domain denoising is to localize the signal in that domain so that the signal could be represented with a small number of coefficients, which have large magnitudes compared to that for the noise. In order to satisfy this condition one should select a mother wavelet, which has a good similarity with the signal under investigation (if its a deterministic signal). Different examples using different mother wavelets will be given here to prove this fact.



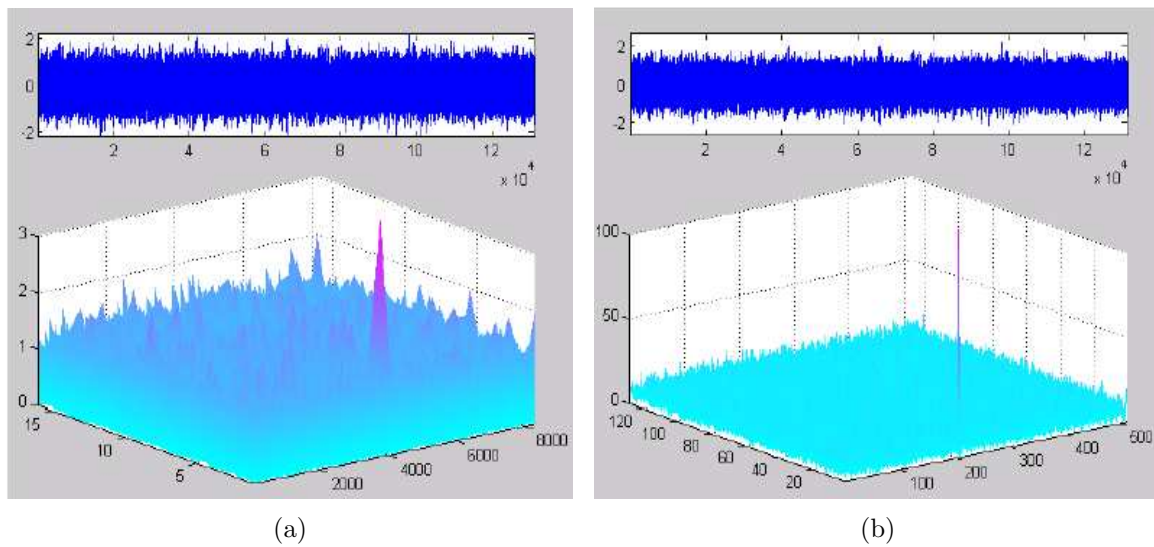


Figure 3.15: (a) WPT for noisy signal. (b) STFT for noisy signal.

### 3.8.1 Denoising PN Codes Using Harr Wavelet

Any discussion of wavelets begins with Haar wavelet, the first and simplest. Haar wavelet is discontinuous, and resembles a step function. Fig. 3.18 shows the Haar wavelet and Harr scaling function.

Fig. 3.19 shows the clean PN code signal upper panel, the noisy signal middle panel and the clean and the signal after denoising lower panel. Where the input signal to noise ratio before the denoising (SNRI) is 20 dB and the output signal to noise ratio after the denoising (SNRO) was found to be 34.86 dB, which means that there is a 14.86 dB improvement in the SNR of the PN code. Fig. 3.20 shows the wavelet transform of the above mentioned signals using Haar wavelet and the number of decomposition levels used was 6. The same example of Figs. 3.19 and 3.20 was repeated with a SNRI = 1 dB and the results are given in Figs. 3.21 and 3.22. It is found from this example that SNRO = 15.86 db, which means that the improvement in the SNR was 14.86 dB. In the above two examples the two types of thresholding (hard and soft threshold) was tested. It is found that the soft threshold gives good results than the hard threshold.

### 3.8.2 Denoising PN Codes Using Daubechies Wavelet

Ingrid Daubechies, one of the brightest stars in the world of wavelet research, invented what are called compactly supported orthonormal wavelets – thus making discrete wavelet analysis practicable. The names of the Daubechies family wavelets are written dbN, where N is the order, and db the "surname" of the wavelet. Fig. 3.23 shows the Daubechies wavelet and Daubechies scaling function of order 6 (db6).

Fig. 3.24 shows the clean PN code signal upper panel, the noisy signal middle

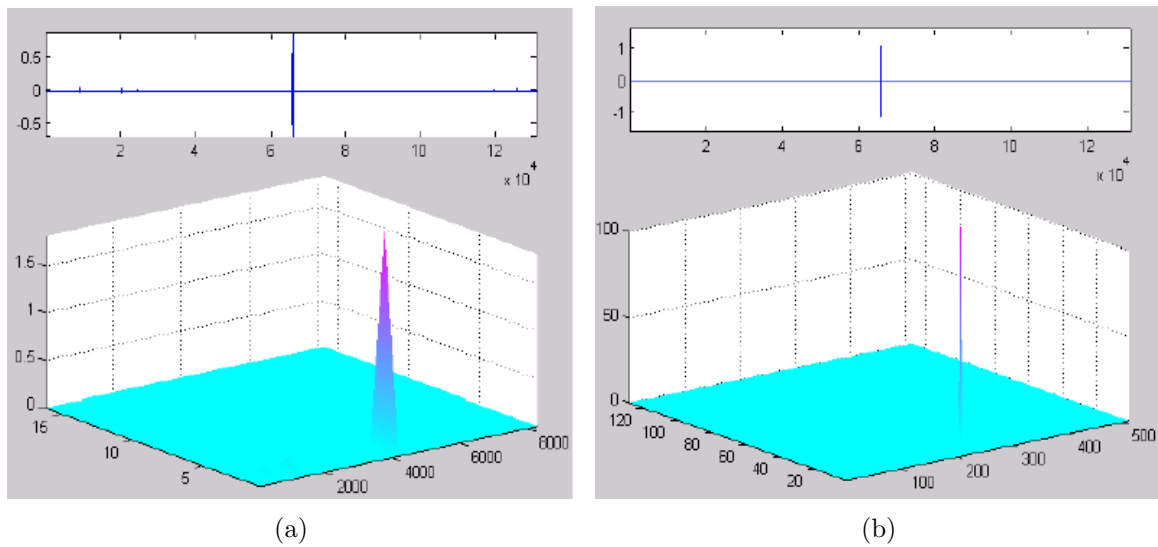


Figure 3.16: (a) WPT for signal after denoising. (b) STFT for signal after denoising.

panel and the clean and the signal after denoising lower panel. Where  $\text{SNRI} = 20$  dB and  $\text{SNRO} = 23.67$  dB, which means that there is a 3.67 dB improvement in the SNR of the PN code. Fig. 3.25 shows the wavelet transform of the above mentioned signals using db4 wavelet and the number of decomposition levels used was 5. The same example of Figs. 3.24 and 3.25 was repeated with a  $\text{SNRI} = 1$  dB and the results are given in Figs. 3.26 and 3.27. It is found from this example that  $\text{SNRO} = 9.27$  dB, which means that the improvement in the SNR was 9.27 dB.

### 3.8.3 Comparison of Different Mother Wavelets

Many other mother wavelets were tested here like symlets (sym4), coiflets (coif4), biorthogonal (Bior1.5), reverse biorthogonal (Rbio1.3) and Discrete approximation of Meyer (Dmey) wavelet. Fig. 3.28 gives a comparison between the above mentioned mother wavelet in terms of the output signal to noise ratio SNRO. It is clear that the Haar wavelet gives the best results in improving the SNR of the PN code. This is due to the great similarity between the PN code and the Haar wavelet, which confirm the fact indicated in section 3.8. The other mother wavelets give comparable results in improving the SNR of the PN code.

Table 3.1 gives a comparison, in terms of SNR improvements, for the different mother wavelets with the optimum parameters, which was selected to give larger improvements in the SNR, for each case. It is clear that the soft thresholding gives the best results for all types of mother wavelet. Farther discussion for the effect of the number of decomposition levels will take place in the next sections.

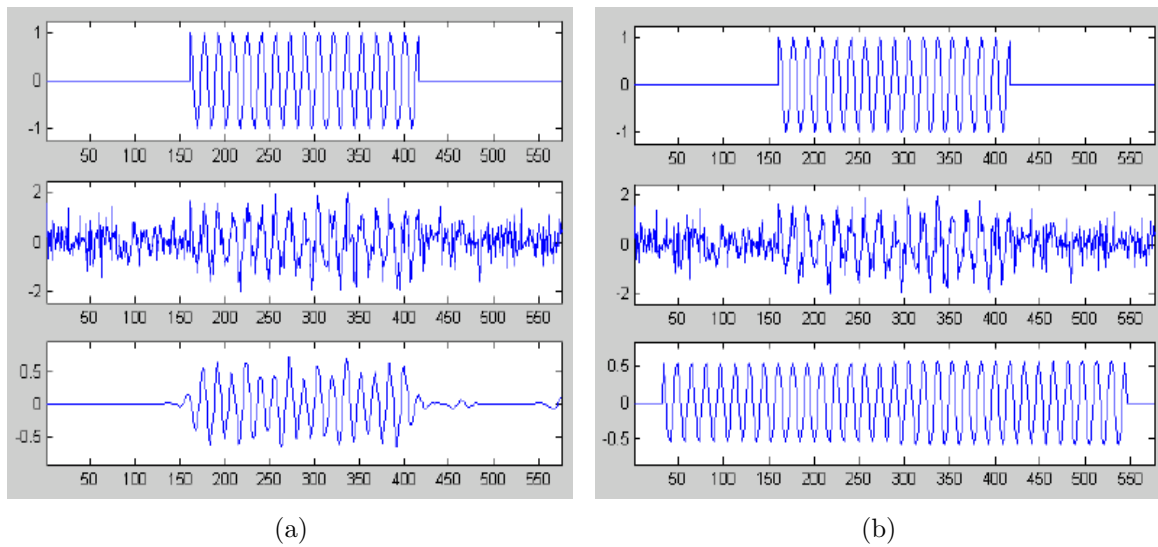


Figure 3.17: Result for signal denoising (a) (WPT). (b)(STFT).

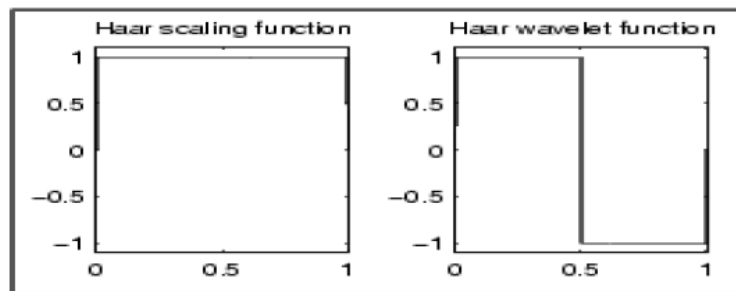


Figure 3.18: Harr scaling function and wavelet.

### 3.9 Applying the Wavelet Denoising to the SS Modulation

In this section we will discuss the effect of applying the wavelet denoising technique on the performance of a SS systems. The results of the previous section indicate that applying the wavelet denoising technique can improve the SNR of the PN code. It is known also that those systems, which utilize SS technique, could work at very low SNR (depend on the code length) due to spreading the spectrum of the signal these systems could work at negative SNR. In this section we tray to answer the following question. Is it possible to improve the performance of SS system (against noise) by combining the SNR improvements from the wavelet denoising with the system?

To answer the above question we selected a base band SS communication system. In this system we only modulate the PN code by the data bits and transmit it. At the receiving side we demodulate the received noisy signal using a synchronized version of the transmitted PN code. The performance of the system here is tested using the



Figure 3.19: Denoising of the PN code using Harr wavelet (SNRI = 20 dB and SNRO = 34.86 dB).

Wavelet	SNR Improve dB	Number of Levels	Threshold type
Haar	14.86	6	Soft
Sym4	6.11	5	Soft
Coif2	6.05	8	Soft
Bior1.5	5.65	6	Soft
Db4	5.49	5	Soft
Rbio1.3	5.42	6	Soft
Dmey	5.35	8	Soft

Table 3.1: Comparison between the different mother wavelets.

bit error rate (BER) at the receiver. The received signal can be written as:

$$y(t) = p(t).b(t) + n(t) \quad (3.33)$$

where  $p(t)$  is the PN code,  $b(t)$  random binary data bits which take the values 1 or -1 and  $n(t)$  is an additive white Gaussian noise.

Applying the wavelet denoising in such a system can take place either before the demodulator Fig. 3.29(a) or after the demodulator Fig. 3.29(b). Both situations will be investigated here.

Fig. 3.30 shows the relation between the BER and SNR after applying the wavelet denoising, before the demodulation for different mother wavelet, and on the same graph we plotted also the result without applying the wavelet denoising. Fig. 3.31 shows the same results but for applying the wavelet denoising after the demodulation. It is clear that applying the wavelet denoising technique did not lead to any improvement in the performance of the SS system. In the same time it's found that the BER is the same for all the cases for SNR greater than -10 dB, but the BER

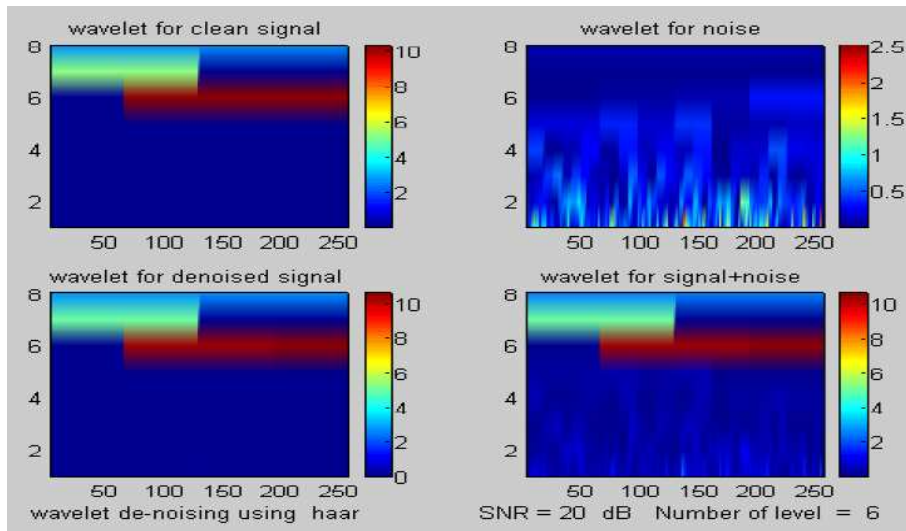


Figure 3.20: Wavelet decomposition using Harr wavelet (SNRI = 20 dB and SNRO = 34.86 dB).

with the denoising is high, in most of the cases, compared to the case without the denoising technique for SNR less than -10 dB.

### 3.10 Discussions and Conclusion

In sections 3.8 and 3.9 we presented the application of the wavelet denoising technique in two cases: first to denoise the PN code signal and second to a SS modulation system. In order to discuss the previously obtained results we need to answer the following questions.

1. Why the Haar mother wavelet gives the best result in denoising the PN code signal compared to other types of mother wavelets?
2. Why after combining the wavelet denoising technique with the correlator receiver in the SS system we did not have any improvements?
3. Why the BER, which obtained after combining the wavelet denoising with the correlator receiver, is high in the case of Haar, coif, bior, rbio and dmey wavelets compared to that of db and sym wavelets?
4. Is it possible to design another type of wavelet that can give us better results?
5. Is the wavelet suitable for denoising stationary and deterministic signal?

Regarding the first question an answer was already given in the beginning of section 8, which we will confirm it again here. The good results obtained in denoising

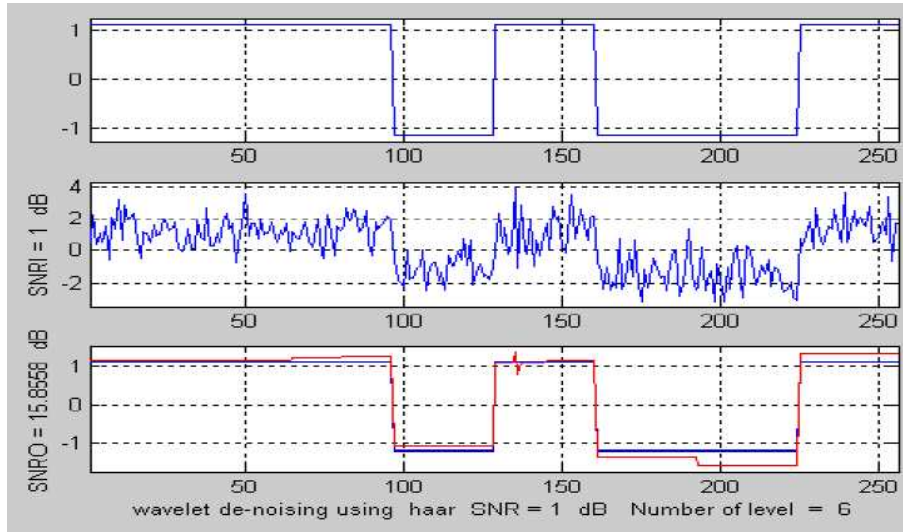


Figure 3.21: Denoising of the PN code using Harr wavelet (SNRI = 1 dB and SNRO = 15.86 dB).

the PN code signal is due to the large similarity between the PN code and the Haar mother wavelet.

To answer question number 2 first we need to present one fact. Assume that we have two systems, each has it's own impulse response  $h_n(t)$  and  $n = 1, 2$ , and the two systems are connected in cascade as indicated in Fig. 3.32. From the system analysis theory, if the two systems are linear time invariant (LTI), it is possible to combine the two systems in only one system, which has an impulse response  $h(t)$  given as:

$$h(t) = h_1(t) * h_2(t) \quad (3.34)$$

In the case presented here, one can consider  $h_1(t)$  as the wavelet denoising system (which is non LTI system) and  $h_2(t)$  as the correlator receiver (LTI system). Due to the nonlinearity in the wavelet denoising technique (in the wavelet thresholding process) we cannot combine the two systems in one, which has the combined effect of the two systems.

Before answering the third question let us present the sittings of the SS system presented in section 3.9. In a SS modulation system the relation between the chip rate,  $f_{ch}$ , of the PN code and the data bit rate,  $f_b$ , is the length of the PN code  $L$ , which can be written as:

$$f_{ch} = L.f_b \quad (3.35)$$

Here the length of the PN code is selected to be 7 bits. In the same time the sampling frequency used to digitize the system is selected as  $f_s = 32 f_{ch}$ . Also the bandwidth of the correlator integrator used in the receiver is equal to the data bit bandwidth  $f_b$ , which means that the correlator integrator (alone) can reject all



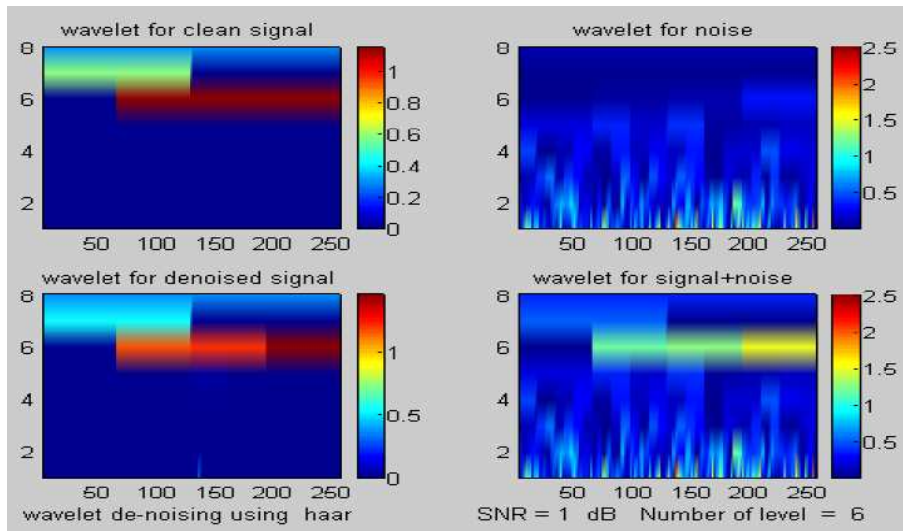


Figure 3.22: Wavelet decomposition using Harr wavelet (SNRI = 1 dB and SNRO = 15.86 dB).

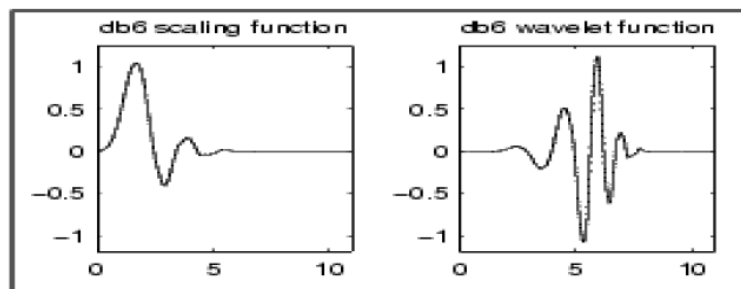


Figure 3.23: Harr scaling function and wavelet.

the existed noise outside that band. After exploring the sittings of the SS system and by using the help of the subband analysis of the wavelet, see Fig. 3.5, keeping in mind the distortions of the original signal due to the nonlinear process in the wavelet denoising (thresholding process) the answer for the third question becomes clear. From table 3.1 we found that the number of decomposition levels, which gives optimum results in denoising the PN code, is 6 (the remaining unprocessed signal approximation bandwidth is  $f_{ch}/4$ ) in the case of Haar, Biorth and Rbio wavelets and 8 in the case of Dmey and Coif wavelet. On the other hand the number decomposition levels is 5 in the case of db and sym wavelet. From the previous one can conclude that increasing the number of decomposition levels can improve the SNR of the signal but in the same time it leads to a great distortion to the signal which can distort the performance of the system.

To answer the fourth question, again we confirm the main idea in the transform domain denoising. The optimum transform that could be used is the one that satisfy a high correlation between the kernel of that transform and the signal under analysis.

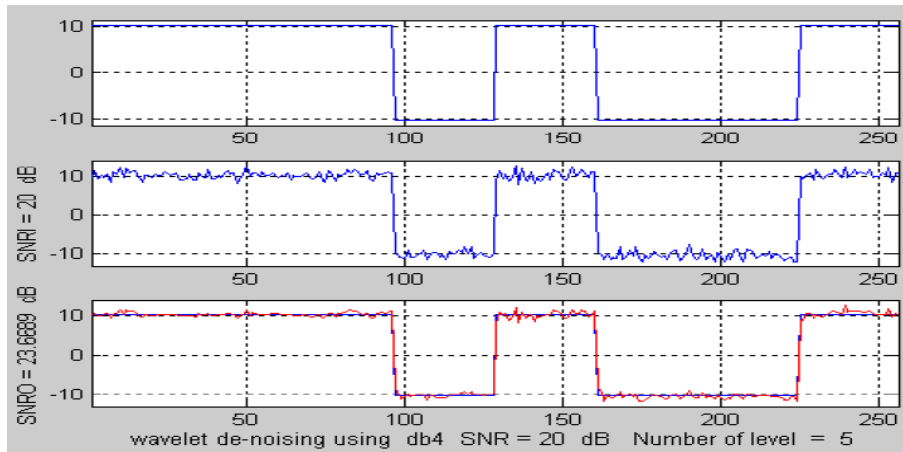


Figure 3.24: Denoising of the PN code using db4 wavelet (SNRI = 20 dB and SNRO = 23.67 dB).

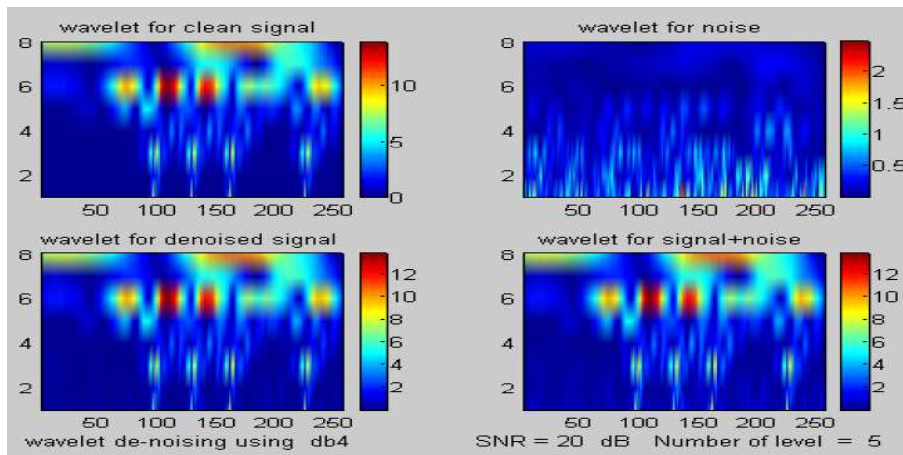


Figure 3.25: Wavelet decomposition using db4 wavelet (SNRI = 20 dB and SNRO = 23.67 dB).

In order to satisfy this condition one should use the signal itself as the kernel of the transform, which is the case in the correlator receiver of the SS system (without adding the wavelet denoising). The answers for question number 3 and 4 explain why the SS system gives good results without adding the wavelet denoising to the system.

Coming now to the last question (Is the wavelet suitable for denoising stationary and deterministic signal?). Let us first look at the various types of signals. From a theoretical and practical standpoint, it is possible to divide all time domain signals into several groups.

### Stationary Signals

The first natural division of all signals is into either stationary or non-stationary categories. Stationary signals are constant in their statistical parameters over time. If you look at a stationary signal for a few moments and then wait an hour and look



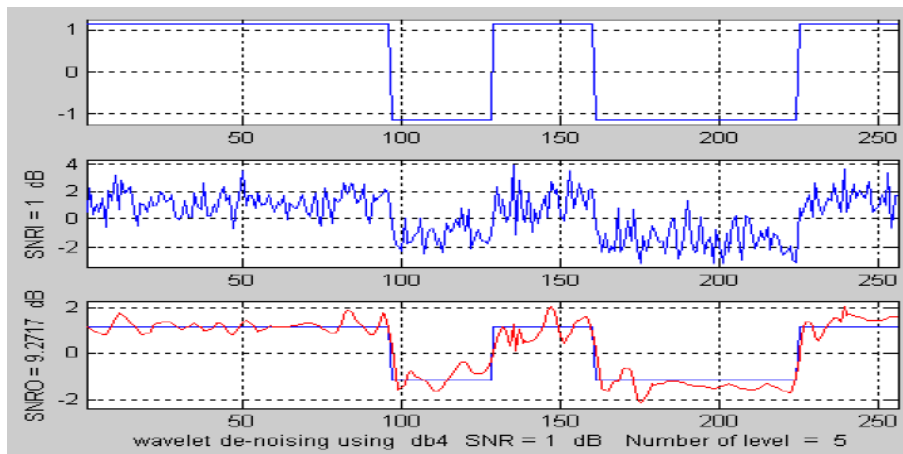


Figure 3.26: Denoising of the PN code using db4 wavelet (SNRI = 1 dB and SNRO = 9.27 dB).

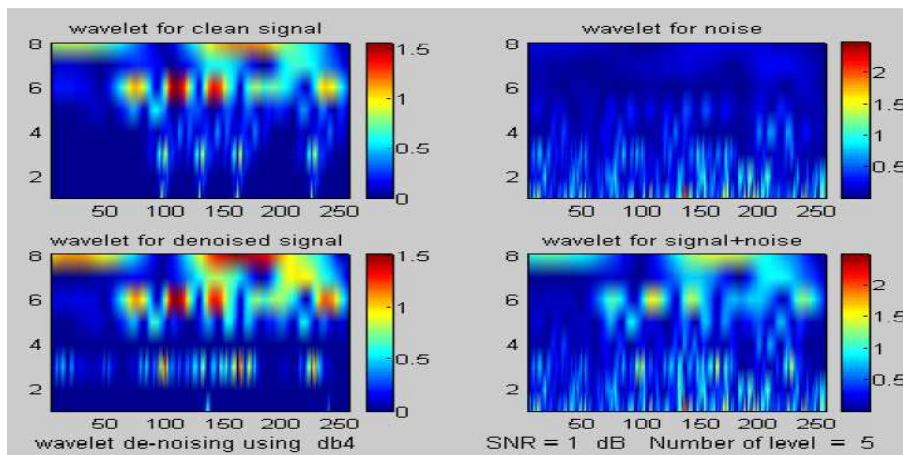


Figure 3.27: Wavelet decomposition using db4 wavelet (SNRI = 1 dB and SNRO = 9.27 dB).

at it again, it would look essentially the same, i.e. its overall level would be about the same and its amplitude distribution and standard deviation would be about the same. Rotating machinery generally produces stationary vibration signals. Stationary signals are further divided into deterministic and random signals. Random signals are unpredictable in their frequency content and their amplitude level, but they still have relatively uniform statistical characteristics over time.

### Deterministic Signals

Deterministic signals are a special class of stationary signals, and they have a relatively constant frequency and level content over a long time period. They are further divisible into periodic and quasi-periodic signals. Periodic signals have waveforms whose pattern repeats at equal increments of time, whereas quasi-periodic signals have waveforms whose repetition rate varies over time, but still appears to the eye

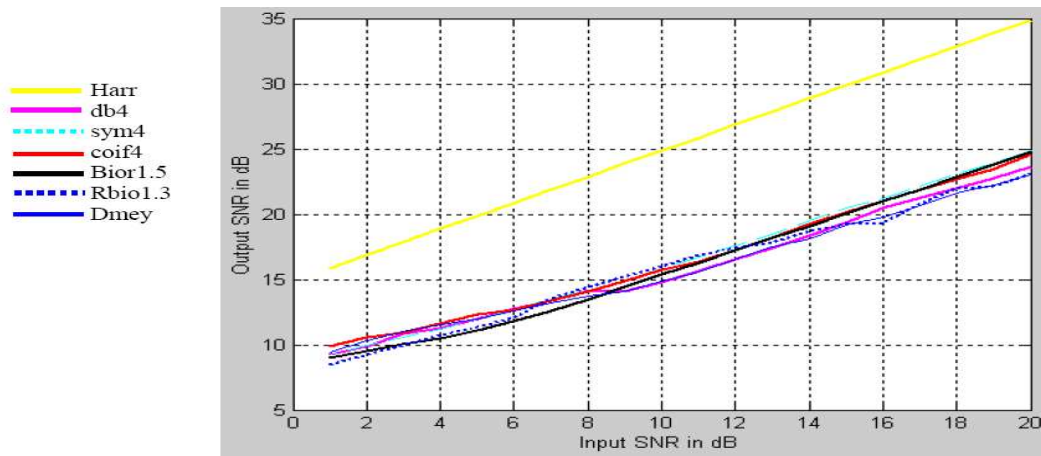


Figure 3.28: Relation between the input and output SNR for different types of wavelet.

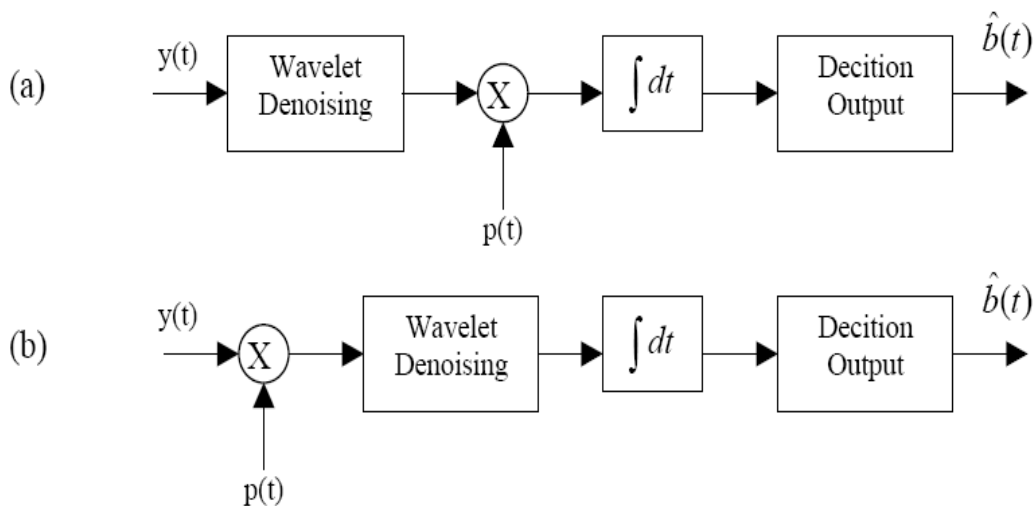


Figure 3.29: Applying the wavelet denoising in SS system (a) Before demodulation. (b) After demodulation.

to be periodic. Periodic signals always produce spectra with discrete frequency components that are a harmonic series. The term "harmonic" comes from music, where harmonics are multiples of the fundamental frequency.

### Non-Stationary Signals

Non-stationary signals are divided into continuous and transient types. Transient signals are defined as signals which start and end at zero level and last a finite amount of time. They may be very short, or quite long.

After exploring the different types of signal, one can conclude that the PN code signal used in the SS system can be considered as stationary and deterministic signal. Fig. 3.33 is a comparison between the Haar wavelet and digital low pass filter (LPF) in denoising the PN code. Filter specifications are as follow: Chebyshev Type II

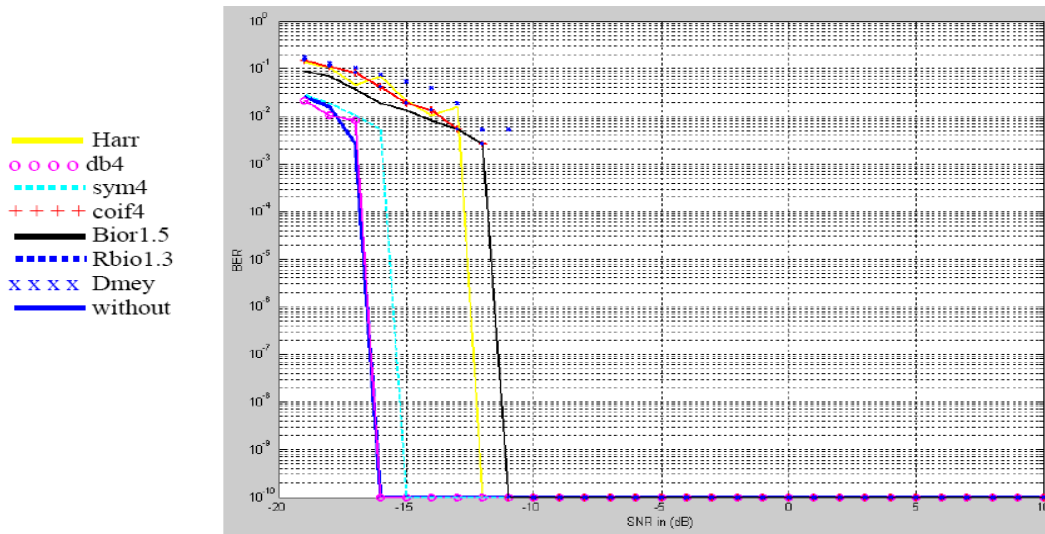


Figure 3.30: BER as a function in SNR after applying the wavelet denoising before demodulation.

IIR, order 14, sampling rate 1.6 GHz, pass band frequency  $f_p = 40$  MHz, stop band frequency  $f_{st} = 50$  MHz (which is equal to the chip frequency of the PN code), pass band attenuation  $R_p = 0.1$  dB, and stop band attenuation  $R_{st} = 60$  dB. From the figure it is found that the low pass filter gives 16.06 dB improvements in the SNR of the PN code, which is higher than that obtained from the Haar wavelet 14.86 dB.

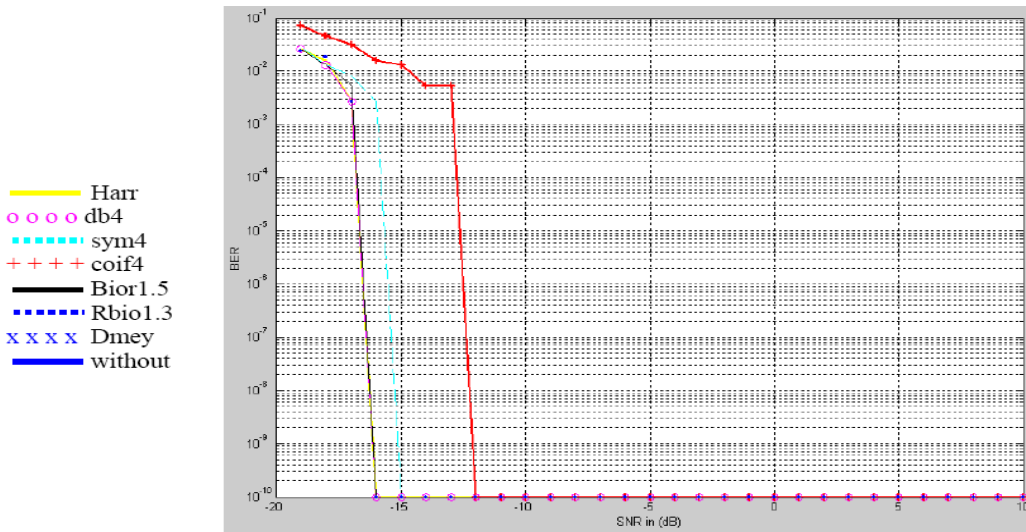


Figure 3.31: BER as a function in SNR after applying the wavelet denoising after demodulation.

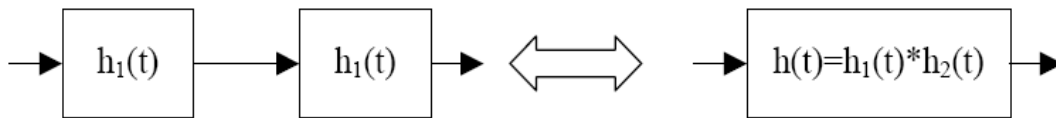


Figure 3.32: Cascaded LTI systems.

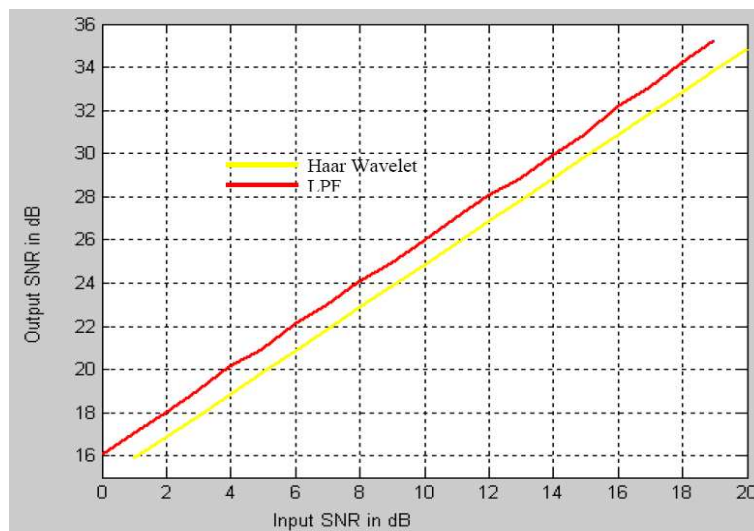


Figure 3.33: Comparison Between the Haar wavelet and LPF in denoising the PN code signal.

# Chapter 4

## Spread Spectrum Automotive Radar

### 4.1 Introduction

There is considerable public and private support for intelligent transport systems (ITS), which promise spectacular improvements in road traffic safety and transportation efficiency. ITS are under active development worldwide as means of reducing loss of life and limiting economic and environmental costs. Over the past few years, automotive sensors/radar have become an important and interesting area for microwave and millimeter wave (MMW) applications [11–40]. They not only have the huge market potential of the automotive industry but also will play an important safety role in the future intelligent vehicle highway systems (IVHS). The main idea is to avoid vehicle collisions in very much increasing traffic density. Unlike airbag systems, which react when an accident already happened, a radar system can even detect collisions before they happen and react very early to avoid an accident or minimize the consequences. Many automobile manufactures now believe that intelligent cruise control (ICC) systems go some way to alleviating these problems and that high definition radars operating in the millimetre wave bands are the ideal distance sensors for these systems. This chapter deals with research efforts relating to radar sensors using millimeterwave technology, which is fundamental to enabling all-weather operation of ITS. In this chapter an analyses to the different techniques used in this field and a focuses on the application of spread spectrum modulation in the MMW automotive radar will take place. Finally I will tray to add some improvements to the existing systems in order to make them more reliable for this very interesting field. It is hoped that the wider use of automotive millimeterwave radar will reduce serious traffic accidents that so frequently occur on limited-access highways in foggy or snowy conditions.

## 4.2 Different Types of Automotive Radars

Automotive radar systems for highway vehicles are designed to be a countermeasure to one or more classes of recognized crash types. Crash avoidance systems product development is currently focused on automotive systems, that is, systems that are totally self-contained within the host vehicle and require no external support from other vehicles or roadside infrastructure. Sensors for autonomous systems will be precursor to the sensor required for cooperative and fully automatic highway systems of the next decade. Autonomous crash avoidance systems generally fall into two main categories based on the application and the requirements of the radar.

- Intelligent Cruise Control (ICC):

An intelligent cruise control is a part of a closed-loop system serving around zero relative velocity. It requires high precision on the range and velocity measurements. It uses this information to control the car's throttle and brakes to keep a safe headway between the two vehicles.

- Collision Warning Radar (CWR):

Collision warning radar gives the driver warning of any possible hazards ahead of the car. Collision warning radar does not require high precision, but requires the capability to track closing velocities and acquire new target rapidly. Also it requires a detection probability as close to one as possible and a false alarm probability as close to zero as possible. The CWR reports the presence of hazards to the driver using a properly man machine interface (MMI) so that he can take appropriate action. In this case he have to ensure that his speed was sufficiently slow for him to be able to negotiate the hazards in safety, but he would not need to stop. The complexity of the decision, which needs to be made, indicates why a CWR must give warnings to the driver, rather than operate automatically as can the simple ICC.

## 4.3 Structure of the Automotive Radar

Whatever the application of the automotive radar, ICC or CWR, it has the same main structure as shown in the block diagram of Fig. 4.1. As indicated in Fig. 4.1 the radar system consists of four main parts.

- Antenna part.
- Radio Frequency (RF) Part.
- Intermediate Frequency (IF) Part.
- Radar Signal Processor (RSP) Part.

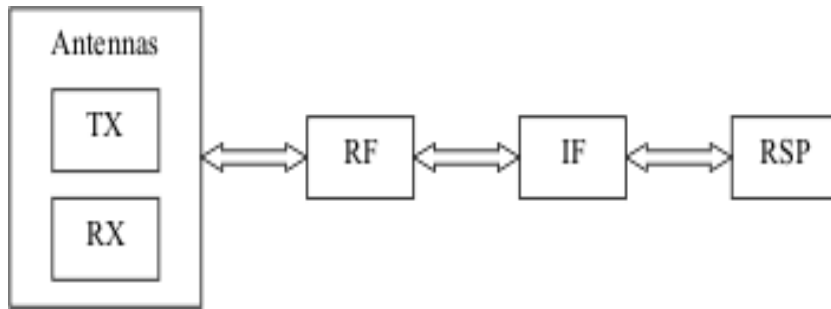


Figure 4.1: Block diagram indicates the main parts of the automotive radar.

### 4.3.1 Antenna

Normally as in any radar applications the radar system requires a transmitting antenna for transmitting the radar signal and receiving antenna for receiving the reflected signal from the target. Many radar based automotive products are possible. They range from using forward looking narrow beam radars for automotive cruise control and collision warning, to side looking broader beam radars for lane change and side impact-warning, to rear facing wide beam radar for backup warning. Numerous antenna configurations have been tried, including fixed field of few single beam configurations, mechanically scanned beam systems and electronically selected multi-beam systems. Obviously the latter is most preferable due to its ability to provide good angular resolution, thereby easing some of the digital signal processing (DSP) load. The continuing maturity of MMW and MMICS is making this approach economically viable.

The antenna must be capable of discriminating vehicle in lanes in front of the radar-equipped vehicle. It's not sufficient to illuminate the entire area ahead of the radar but also the antenna must actually switch the beams in order for the sensor to build up a picture of the highway "scene". For typical forward-looking radar (FLR) applications, a lot of discussion has dealt with the issue of beam-width. To perform the important functions of correctly identifying the lead-vehicle target, and accurately reporting it's distance and relative speed, high resolution spatial selectivity is required. To cover all vehicle types at different weather conditions on US interstate-type highways, general consensus is that  $3^\circ$  elevation and  $9^\circ$  azimuth field of view is desired for the forward looking radar. Fig. 4.2(a) indicates the necessary field of view chosen for the forward looking radar [19], which is characterized in a distance of 100 m by a width of five lanes divided into four and in a second step into eight angular resolution cells. In radial direction an operating range of about 100 m starting at a distance of 20 m is covered. The vertical angle of only  $3^\circ$  avoids reflections from bridges and tunnels. Fig. 4.2(b) indicates an experimental image for the side ways looking radar as given by [29] more details about the field of view of the side objects detection system and the rear objects detection systems are available in [31–33].

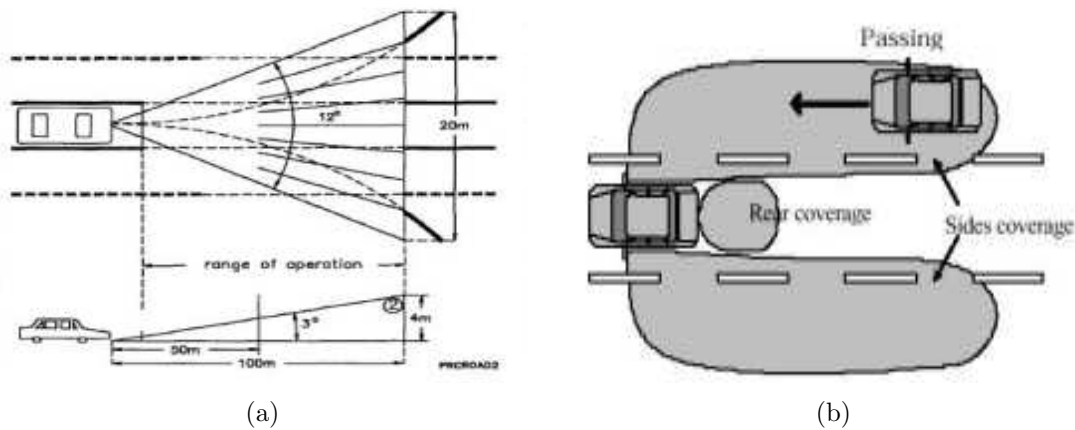


Figure 4.2: (a) Field of view for the forward-looking radar, [19].(b) Experimental image of side way looking radar, [29].

In [18], staring antenna was used for ICC system and for the CWR they use scanning antenna to view the area in front of the car. The radar head is about 100 mm long as indicated in Fig. 4.3(a). In [19], [20], [25] a single transmitting antenna illuminates the total field of view. While four real or later, [27], eight effective receiving antennas are used to sample the reflected fields. The beam width of the receiver antenna is  $3^\circ$ . The antennas consist of rectangular horns with cylindrical dielectric lenses. The aperture of one horn is  $21 \times 70$  mm, the depths of a horn is 60 mm as shown in the drawing of Fig. 4.3(b). The whole width of 4 horns is 88 mm as shown in Fig. 4.4. In [11] a beam-switching antenna has been produced which uses quasi-optical principles in its design. Plastic lenses are mounted above patches formed on microstrip as indicated in Fig.4.5(a). It use one  $10^\circ$  beam width patch antenna and 3 receiving antennas each with  $3^\circ$  beam width as shown in Fig. 4.5(b).

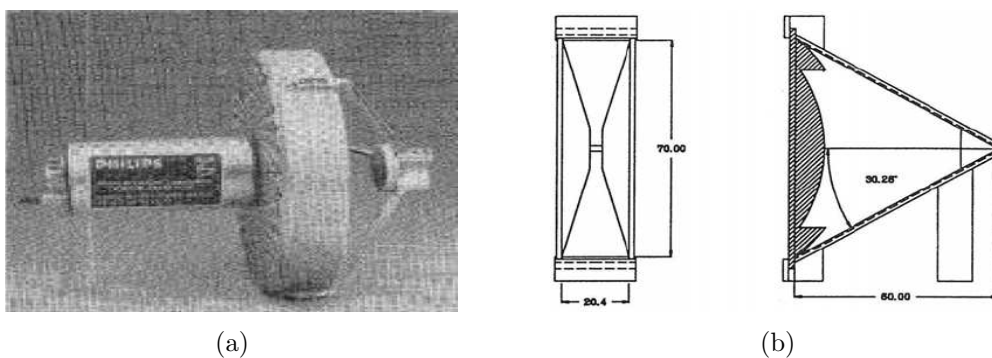


Figure 4.3: (a) Experimental radar head system, [18]. (b) Horn antenna with dielectric lens, [25].

In [30] the antenna features low side-lobes, high efficiency, minimum size and low cost. The desired beam angle of  $2^\circ$  results in a 140 mm aperture for the antenna.



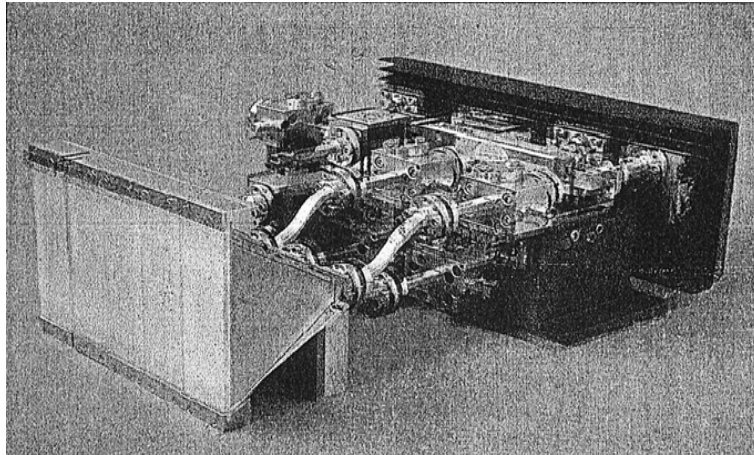


Figure 4.4: MMW radar frontend with 5 antennas, [25].

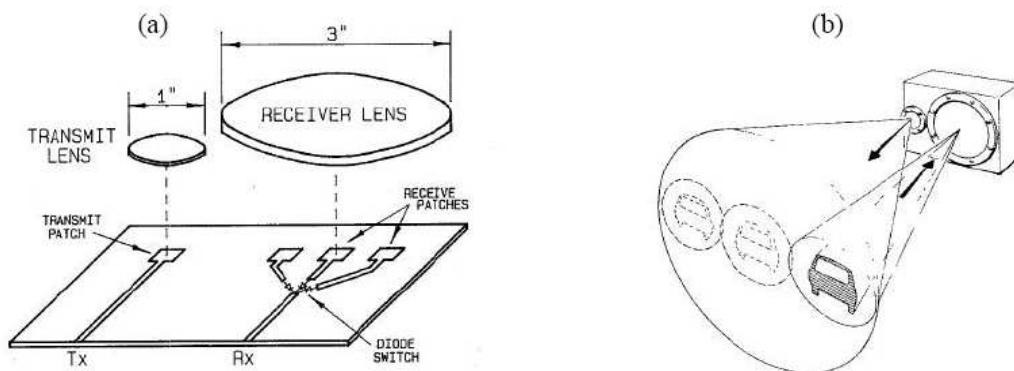


Figure 4.5: Antenna configuration of [11].

This beam width is able to resolve a 3.5 m lane of traffic at a distance of 100 m, the optimal maximum sensing range. Fig. 4.6(a) indicates the forward looking radar (FLR) sensor design of this system. In [12] two antennas were used, each with  $3^\circ$  by  $3^\circ$  beam width. Two different types of antennas have been utilized to evaluate the prototype. The first one is  $3^\circ$ -beam parabolic dish antenna. Another one is an off-the shelf optical lens antenna as shown in Fig. 4.6(b). It has 35.6 dB gain and greater than 25 dB sidlobe rejection.

In [13] the output power required at the antenna flange is dependent on the antenna design. Because more than one beam is required, the insertion loss from the source output to the antenna port, increases with the number of feeds. The switch matrix in front of the antenna increases the insertion loss by around 3 dB. An alternative antenna configuration that doesn't require the switch matrix is realized by a mechanically scanned single beam solution. In [14] electronically selected multi-beam system is most preferable due to its ability to provide good angular resolution. The block diagram of the multi-beam radar system used in [14] is shown in Fig. 4.7(a). In [15] a low cost automotive multi-beam Doppler radar based on Silicon Monolithic

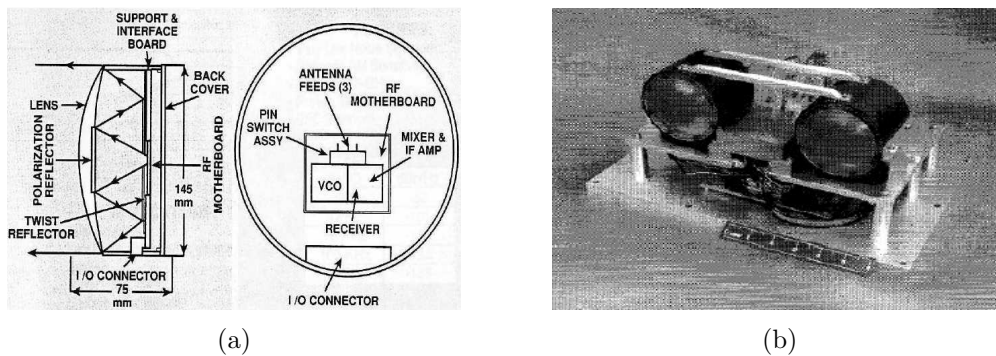


Figure 4.6: (a) The FLR sensor layout of, [30]. (b) Photography of the FLR unit, [12].

Millimeter Wave Integrated Circuit (SIMMWIC) components is presented in this paper. They use 4-beams antenna, a specially designed polystyrene dielectric lens as shown in Fig. 4.7(b) shapes the radiation pattern of the active antennas.

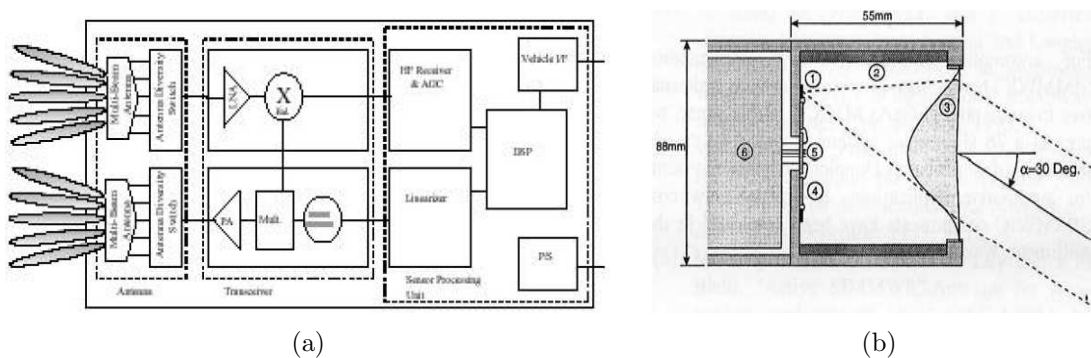


Figure 4.7: (a) Representative sensor block diagram, [14]. (b) RF front end and beam shaping principle using a bifocal dielectric lens.

In [38] the RF signal to the two transmit antennas is time-multiplexed on a per sweep basis. The three receiver channels work in parallel. Thus with 5 antennas 6 propagation paths of different length are obtained to enable the location of objects in 3D space. The antennas are located in the vertical plane on a support of 2.5 m width and 1 m height on the front of the automatically guided vehicle. The antennas are microstrip like waveguide antenna (MLA). In [16] the radar uses a patented bistatic antenna system obtained approximately 80 dB of transmit-receive isolation to prevent receiver desensitization. The two antennas are printed circuits mounted on the front face of the radar enclosure and covered by a flat Radome. The antenna produces several overlapping beams to cover the field of view and employs sequential loping techniques in order to locate targets in azimuth. The novel printed-circuit antenna consists of a Rotman-Turner lens beam former and an array of series-fed patch antennas built on a 5-mil-thick soft-substrate material. Beam position is controlled by electronically switching the Rotman-Turner lens feed point. The approach

provides both fine special resolution and a broad field of view, while minimizing volume and aperture size. With this approach they have built antennas that provide an azimuth coverage of  $8.8^\circ$  using four beams and  $15.4^\circ$  using seven beams, each with an individual beam width of  $2^\circ$  as indicated in Fig. 4.8. A mechanically scanned antenna design was considered in the early stages of development, but eliminated as a candidate due to concerns about reliability. A frequency-scanned antenna was eliminated due to the limitations it imposes on the waveform. Though probably the most appealing technical solution is a phase-scanned approach, the technology at millimeter-wave frequencies is in its infancy. In [27] a crucial system parameter, which essentially determines the necessary effort and the complexity of the system, is the number of the receivers. So methods of increasing the effective number of receivers while maintaining the actual number are of great interest [34], [35]. The extension to a configuration of eight effective receivers, which was realized in a second step, was obtained by alternatively using two transmit locations, as indicated in Fig. 4.9. The side ways looking radar system in [29] use one transmitting and one receiving antenna as prototype system. Fig. 4.10 indicates the radar system used in [24].

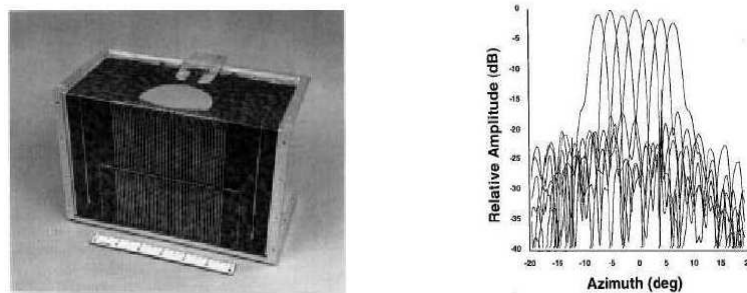


Figure 4.8: Seven beam antenna design and performance of [16].

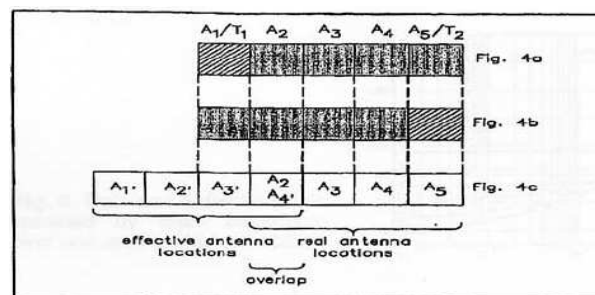


Figure 4.9: Realized five antenna configuration [27]. (a) antenna  $A_1$  transmits, (b) antenna  $A_5$  transmits, (c) effective aperture.

After this brief description of the different types of antennas used in previous research works it is still need more investigation to determine the optimum antenna system for the automotive applications, which is beyond the scope of this thesis. The

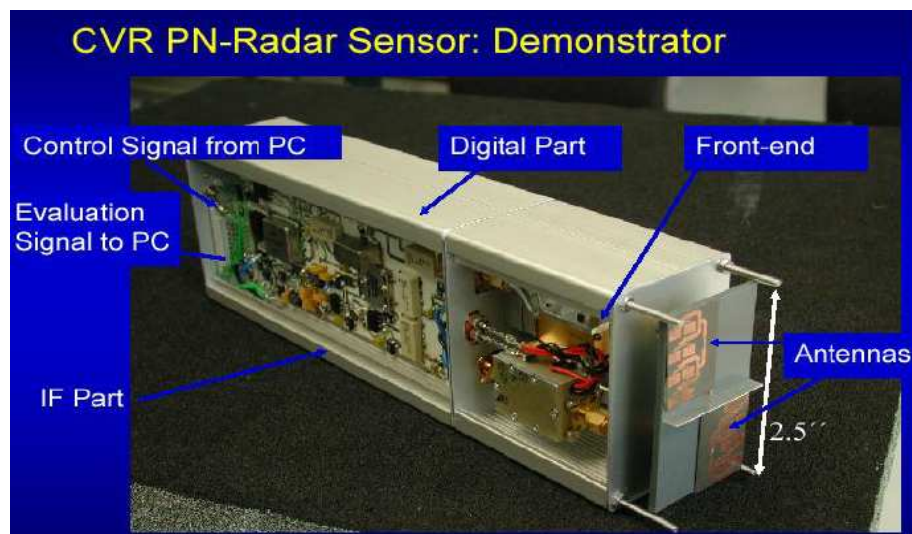


Figure 4.10: PN-radar sensor used in [24].

choice of the optimum antenna system must base in three mean targets, low cost, minimum size and high efficiency.

### 4.3.2 Radio Frequency (RF) Part of the Automotive Radar

The RF part of the automotive radar has two jobs. First its up converting the radar signal from the IF frequency to the RF frequency and deliver it to the antenna for transmission. The second job is to down convert the received radar signal from the RF frequency to the IF frequency.

A band of 76-77 GHz has been made available for automotive radar in Europe. For the introduction of novel low-cost radar system with improved performance further advancement in MMW technologies, like high yield semiconductor processes with high throughput, highly integrated MMW circuit with high efficiency and sensitivity, and innovative antennas are required. Advances in GaAs or Silicon MMIC technology enable operation at millimeter wavelengths, providing reduction in size, weight, and production costs. Higher resolution radar and fusion with other on board sensors will improve the performance and functionality of future car electronic systems which finally will lead to novel intelligent features such as automatic tracking or autonomous driving.

### 4.3.3 Intermediate Frequency (IF) Part of the Automotive Radar

The function of the IF part of the radar is to modulate and demodulate the radar signal. The spread spectrum modulation has a number of features that makes it easy to achieve the following characteristics:

- Accurate distance measurement.
- Separation and detection of multiple vehicles located in the range direction.
- Accurate measurement of the reception power.
- Interference eliminating capability.

For the reasons mentioned above, the spread spectrum modulation was considered more suitable for automotive radar, and it was used in the development of the millimeter-wave radar.

### 4.3.4 Radar Signal Processing (RSP)

The radar signal processing part in the automotive radar has three main jobs:

- Processing for distance measurements.
- Processing for velocity measurements.
- Processing for angle measurements.

To meet the signal processing requirements within the cost constraints of the commercial automotive market, we chose to perform the signal processing digitally with a commercial programmable digital signal processor. Utilizing DSP rather than analog signal processing allows some very sophisticated algorithms to be used in a low cost system. In addition, the algorithms can be easily reprogrammed and are immune to factors such as temperature and aging. The requirements of these three measurements are the accuracy and the processing time of the measurements. In the next section a focus on the DSP for spread spectrum automotive radar will take place.

## 4.4 Spread Spectrum Automotive Radar Signal Processing

Fig. 4.11 shows the block diagram of the spread spectrum automotive radar. In this section a focus on the DSP part will take place.

### 4.4.1 Processing of Distance Measurement

To measure the distance from the vehicle, which is occupied by the radar, one needs to measure the traveling time of the reflected wave. This distance  $d$  is calculated using the following relation [8]:

$$d = c.T_d/2. \tag{4.1}$$

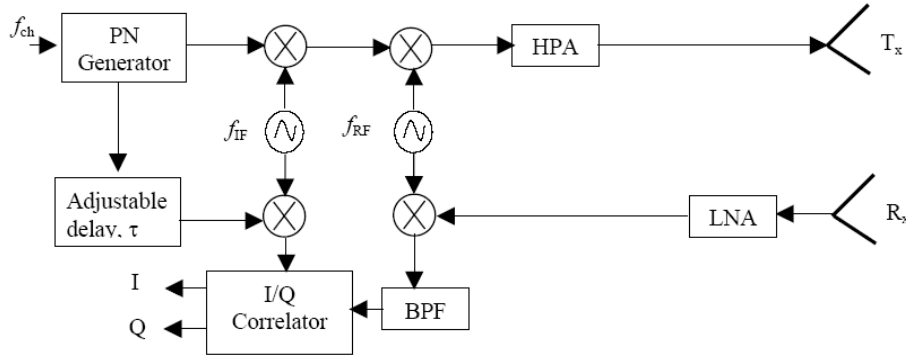


Figure 4.11: The block diagram for the spread spectrum automotive radar.

Where  $c$  is the speed of light and  $T_d$  is the traveling time to the target and back. To measure the distance, therefore, it is necessary to measure  $T_d$ . In this radar system, a spread spectrum technique is adopted for radar signal processing. Therefore the traveling time  $T_d$  is evaluated by the correlation between the received PN code and the reference PN code. The correlation function for the PN codes was given by (2.5) as:

$$r_p(\tau) = \int_0^{LT_{ch}} p(t - 2T_d)p(t - \tau)dt$$

In order to calculate the correlation function we need to shift the reference PN code with a known step  $\tau_s$ . The accuracy of the measured distance  $d_m$  as well as the measuring time  $T_m$  (processing time) will be affected by the selection of the shifting step of the reference PN code as follow.

$$d_m = c.(T_d \pm \tau_s)/2 \quad (4.2)$$

This means that the accuracy in measuring the distance  $\Delta d$  will be.

$$\Delta d = d - d_m = \pm c\tau_s/2 \quad (4.3)$$

In the same time the measuring time for this distance will be.

$$T_m = (T_d/\tau_s).(L/f_{ch}) \quad (4.4)$$

It is clear from (4.2) and (4.3) that the accuracy of measuring the distance is inversely proportional to the shifting step and the opposite for the measuring time. There are two commonly used methods for implementing the shifting of the reference PN code each method has its advantages and disadvantages, as is indicated in the next subsections.

### One Chip Shifting Method

In the one chip shifting method [19–28] the shifting step  $\tau_s$  is selected to be equal to the reciprocal of the chip rate  $f_{ch}$  as:

$$\tau_s = 1/f_{ch} = T_{ch} \quad (4.5)$$

There are a lot of techniques used to implement this type of shifting the reference PN code. In [19, 20, 25, 27] the PN code is not generated instantaneously by using shift registers but it is read out from a memory (EPROM) at the necessary rate. The code shift is obtained by the address offset between the transmitter and reference code generator. In [21] the shift of the code is achieved in a dual way. First, the shift register generating the PN code is extended from a length of 10 to 24 bits; at the additional outputs the code can be extracted with three to fourteen bit length delay. Secondly, for a fine adjustment, three delay chips based on cascaded gates provide additional delays in steps of 1 ns. Another technique used by [28], two identical feedback shift registers are used to generate the PN code and its delayed version. Having a second shift register allows for choosing the starting sequence of the delayed version thus generating unlimited in time-steps of about 2.2 ns (chip rate is 450 MHz). Additional fine delay in steps of about 17.5 ps generated by a programmable delay chip insures proper detection of correlation peaks. Whatever the technique used to implement this type of the delay between the two PN codes one can obtain a shifting step  $\tau_s = T_{ch}$ , which is equal to one chip period. This means that in order to improve the accuracy of measuring the distance and reduce the measuring time one needs to increase the chip rate. This will leads to some advantages and disadvantages. The advantages of this method are:

- Simplicity of implementation.
- No synchronization problem between the reference PN code and the transmitted PN code because both of them will be generated using the same clock source.
- The measuring time will be small ( $T_m = LT_d$ ) and will not depend on the chip rate.

In the other hand the disadvantages of this method are:

- The accuracy ( $\Delta d = 0.5.c.T_{ch}$ ) is limited by the bandwidth (the required bandwidth of the this radar system  $BW = 2f_{ch}$ ) that can be handled by the modulator/demodulator in the IF stage while still preserving phase and amplitude balance.
- Increasing the noise corrupting the radar signal due too increasing the bandwidth.
- Fixed accuracy (except if we have variable chip rate as in [24], which will be a complex implementation).

### Sliding Correlation Method

The automotive radar requires that the distance between the vehicle equipped with the radar and the target can be measured as accurate as possible. If the reference PN code is shifted by a time interval, which is equal to one chip period, as indicated by the previous method, and the correlation is calculated at the same time, the absolute accuracy of the distance measured is affected by the accuracy of a distance equal to one chip. In [29], another approach was used to measure the distance more precisely than the conventional method. The proposed technique in this contribution is based on the sliding correlation [4], in which the clock frequency of the reference PN code on the receiving side was set slightly lower than that of the modulation PN code on the transmitting side. The step of shifting using this method will be:

$$\tau_s = \frac{L}{F_2} - \frac{L}{F_1} = L \left( \frac{F_1 - F_2}{F_1 F_2} \right) \quad (4.6)$$

Where  $F_1$  is the clock frequency of the received PN code and  $F_2$  is the clock frequency of the reference PN code. Using this method to implement the shifting of the reference PN code the measuring time will be:

$$T_m = T_d \frac{F_1}{F_1 - F_2} \quad (4.7)$$

The sliding correlation will give better accuracy without increasing the required bandwidth of the system, because the accuracy obtained by this method is not depend directly on the chip rate of the PN code but depends on the difference in clock frequency between the two PN codes ( $F_1 - F_2$ ). The difficulty in the sliding correlation is that in order to have better accuracy one needs to implement two slightly different, synchronized and stable clock frequencies, which is a very difficult job in practical situation. In the same time it faces the same problem of the previous method, that the accuracy will be fixed we cannot change it after the implementation of the system, which is a very important requirement to switch the radar system from the detection to the tracking of the objects.

### Fraction of Chip Shifting Method

In this work we proposed a third method to implement the shifting of PN code. It is hoped that it will satisfy better accuracy for the radar system and in the same time will overcomes the disadvantages of the previous methods.

In this proposed method [144], the generation of the reference PN code will not depend on the linear feed back shift registers instead we will store a sampled version of the transmitted PN code in a memory, which has the facility to make a circular shift by one sample. The samples will be represented in the memory using one bit per sample. The number of stored samples per one chip will proportional to the required accuracy of the system in the same time the rate of reading out the stored PN code



will also be proportional to the required accuracy of the system. For example, if the required accuracy is  $T_{ch}/4$ , then we need to represent each chip of the transmitted PN code with 4 samples and the rate of reading out the reference PN code will be in this case  $4f_{ch}$ , where  $f_{ch}$  is the chip rate of the transmitted PN code. Table 4.1 indicates the transmitted and stored reference PN codes with code length  $L = 7$  and number of samples per chip  $m = 4$ .

Tx-code	1				1				0				1				0				0							
Re-code	1	1	1	1	1	1	1	1	0	0	0	0	1	1	1	1	0	0	0	0	0	0	0	0	0	0	0	0

Table 4.1: The transmitted PN code (Tx) and the stored reference PN code (Re).

The step of shifting using this method will be:

$$\tau_s = 1/(mf_{ch}) \tag{4.8}$$

The accuracy in measuring the distance using the proposed method will be

$$\Delta d = \pm 0.5c(1/mf_{ch}) \tag{4.9}$$

The measuring time will be

$$T_m = mLT_d \tag{4.10}$$

Using the proposed method leads to an improvement in the accuracy of measuring the distance without increasing the required bandwidth of the system. The proposed method can be implemented using different techniques, as indicated in the block diagrams in Figs. 4.12 and 4.13.

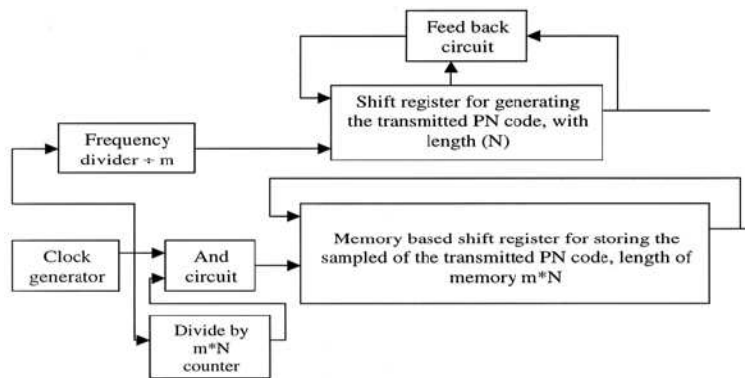


Figure 4.12: Block diagram of the first technique of implementing the delay of the reference PN code.

Fig. 4.12 indicates the block diagram of the first technique used for implementing the delay of the reference PN code. In this method the clock frequency of the reference PN code is blocked for one clock pulse each time the complete pattern is read out

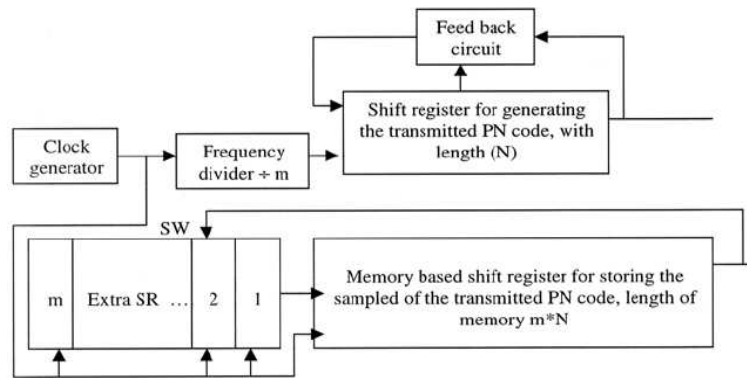


Figure 4.13: Block diagram of the second technique of implementing the delay of the reference PN code.

from the memory or every  $mL$  clock pulse. This is equivalent to a continuous delay of one sample between the two PN codes. The achieved accuracy is then equivalent to  $1/mf_{ch}$ . If we need to change the accuracy we can block the clock frequency for more than one clock pulse. By this way we are able to achieve variable accuracy. Fig. 4.13 indicates the block diagram of the second technique used for implementing the delay of the reference PN code. In this method the delay between the two PN codes is implemented by inserting extra samples (these extra samples will be 0 bits) through the feedback connection. The number of the inserted samples is based on the required accuracy. For example if we need an accuracy of  $1/mf_{ch}$  then we need to insert one sample and if the required resolution is equivalent to  $1/f_{ch}$  then we insert  $m$  samples. The third technique is based on [80], in which we can implement the delay between the two PN codes by changing the initial address of the read out reference PN code.

Fig. 4.14(a) shows the experimental prototype settings for implementing the proposed method of shifting the PN code. Fig. 4.14(b) shows the obtained delay step between the reference and transmitted PN codes. Fig. 4.15 indicates the correlation function implemented using the proposed method, with a chip rate of 50 MHz and  $m = 8$  which gives an accuracy equal to 2.5 ns in measuring the delay time  $T_d$ . Table 4.2 compares the processing time (normalized to  $T_d$ , where  $T_d$  being equal to  $1/450$  MHz,  $2/450$  MHz, ...,  $N/450$  MHz) and the required bandwidth for the above three methods. We assumed here an accuracy of 33 cm and the length of the PN code is 1023. From Table 4.2 we found that the proposed method can achieve the required accuracy without increasing the bandwidth. There is however a slightly increase in the processing time compared with that of the sliding correlation.

#### 4.4.2 Processing of Velocity Measurement

In Radar the frequency of the transmitted signal is affected by the Doppler shift phenomenon [4], when it is reflected from the surface of a moving target. A positive

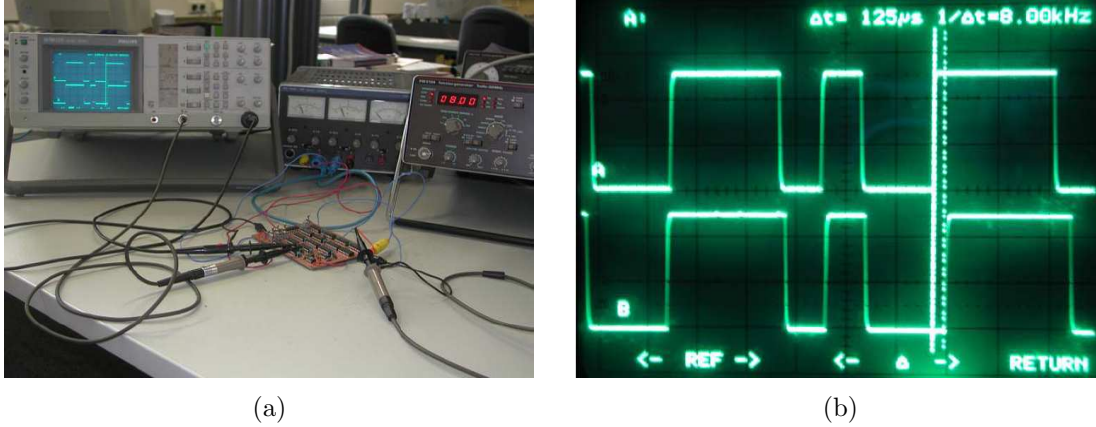


Figure 4.14: (a) experimental prototype settings. (b) Oscilloscope photography indicates the delay step.

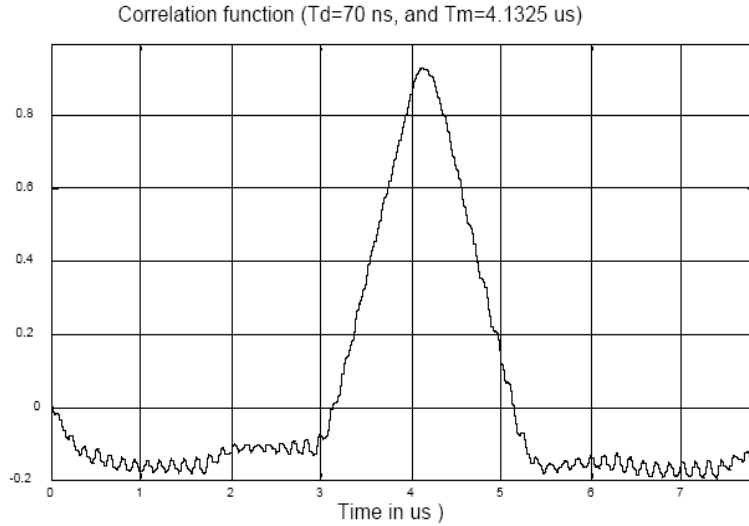


Figure 4.15: The obtained correlation function using the proposed method.

Doppler frequency is added to the frequency of the carrier wave when a target is closing, while a negative Doppler frequency is added when the target is moving away. When a target is either closing or departing, the received carrier will be:

$$x_{IF} = \cos [2\pi(f_o \pm f_d)t] \quad (4.11)$$

Where  $f_o$  is the IF carrier frequency and  $f_d$  is the Doppler frequency which can be calculated as follows:

$$f_d = 2f_{RF}(V/c) \quad (4.12)$$

Where  $V$  is the relative velocity,  $f_{RF}$  is the RF carrier frequency and  $c$  is the velocity of light.

Shifting method	Normalized Processing time	Bandwidth(MHz)	Chip rate(MHz)
One chip.	1023	900	450
Sliding correlation.	9208	100	50 and 49.995
Fraction of chip.	8184	112.5	56.25

Table 4.2: Comparison between the different methods of PN code shifting.

Using the conventional method, the Doppler frequency can be calculated by performing FFT calculations [19, 20, 22–25, 27, 28] using a DSP based on the values sampled by an A/D converter (the values are defined as the state of the beat signals obtained by subtracting the frequency components of a carrier wave from a received signal). There are two problems with this conventional method; first we cannot determine the sign of the Doppler frequency. This means that we cannot determine if the target is closing or moving away from our vehicle. The second problem is that the time taken to observe the beat signals is dependent on the velocity resolution, and therefore any attempt to increase the velocity resolution results in an increase in the observed time. Added to this is the complexity of the used system. In [29], another approach was used to measure the Doppler frequency by taking advantage of the gradient characteristics of the frequency and amplitude values processed through a digital filter. By this way of measuring the Doppler frequency [29] verifies that the time needed to calculate the Doppler frequency is about one tenth of the time needed to calculate them using the conventional FFT calculation method with a DSP. The accuracy of measuring the Doppler frequency by this method was 90.74 Hz as stated in [29]. The problem with this method is that the beat signal is firstly passed on a high pass filter to remove the low-frequency component, so an important event is lost, if the behind target moves with the same velocity as the vehicle that equipped by the radar. On the other hand the achieved resolution is still not so high. To solve these problems we propose a simple, accurate and less in the measuring time than the conventional method [78]. This method is based on counting the number of zero crossing in the beat signal obtained by subtracting the frequency of a carrier wave (added to it a frequency proportional to the velocity of the vehicle equipped by the radar  $f_V$ ) from the received signal as follows:

$$x_c = \cos [2\pi(f_o \pm f_V)t] \quad (4.13)$$

$$\begin{aligned} x_b(t) &= x_{IF}(t) \cdot x_c(t). \\ &= 0.5 \{ \cos [2\pi(\pm f_d - f_V)t] + \cos [2\pi(2f_o \pm f_d + f_V)t] \} \end{aligned} \quad (4.14)$$

After low-pass filtering, the beat signal will be:

$$x_b(t) = 0.5 \cos [2\pi(f_V \mp f_d)t] \quad (4.15)$$

So that the frequency of the beat signal will be less than  $f_V$  if the target is closing, and it will be larger than  $f_V$  if the target is moving away. By this procedure we haven't lost the sign of the Doppler frequency. And if the target moves with the same velocity as our vehicle we can still detect it. The accuracy of measuring the Doppler frequency by this method is 50 Hz and the measuring time is 10 msec.

Fig. 4.16 shows the block diagram of the proposed velocity measuring process based on counting the number of zero crossing in the beat signal. In this system counter 1 is used to count the positive zero crossing and counter 2 is used to count the negative zero crossing. The two counters are reset every 10 msec by using a clock with a frequency 100 Hz. The accuracy of measuring the Doppler frequency by this method is 50 Hz and the measuring time is 10 msec. Table 4.3 compares between the measuring time for the three methods, assuming that the maximum Doppler frequency is 6 kHz and the accuracy of measuring is 100 Hz.

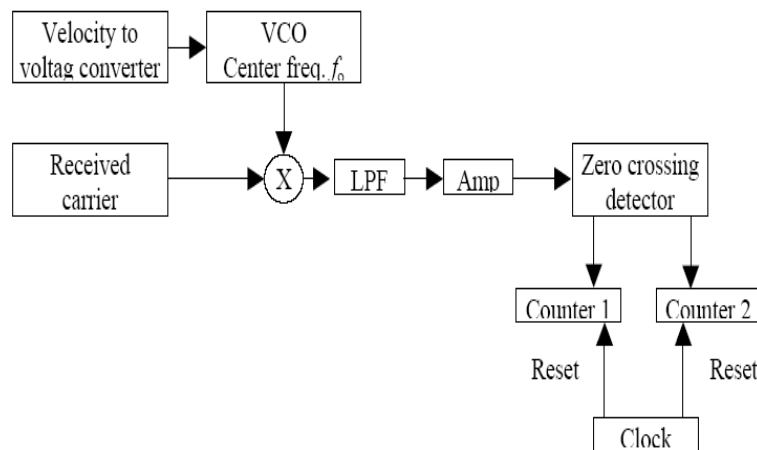


Figure 4.16: The velocity measuring system.

FFT Method	Gradient ch/s Method	Zero Crossing Method
20 ms	2 ms	10 ms

Table 4.3: Comparison between the measuring time for the three methods.

### 4.4.3 Processing of Angle Measurement

The mere detection of objects in front of a vehicle without relation to their environment is not sufficient to classify them as dangerous. To identify potential paths of collision, objects and their actual and expected future trajectories have to be estimated and additionally assigned to individual lanes. Automotive anticollision radar systems are under investigation since many years, but mainly the experiments have shown, that the false alarm rate in these systems was too high. One of the reasons was the lack of an angular resolution. In [19, 20, 25, 27], wave front reconstruction

was used for angular discrimination by generating calculated beams. Four suitably weighted samples of the complex field distribution received by the antennas are transformed using FFT into response of an equal number of antenna beams of about  $3^\circ$  width creating digitally four angular resolution cells. The evaluation of the angle of incident field of the wave front can be explained by the phase comparison of the voltages of the four channels according to the drawing of Fig. 4.17.

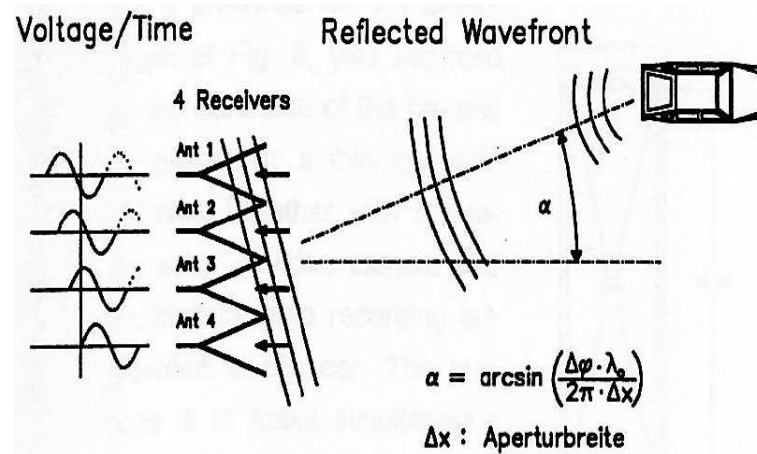


Figure 4.17: Wave front reconstruction.

# Chapter 5

## Spread Spectrum Indoor Ultrasonic Positioning System

### 5.1 Introduction

Many mobile applications can be greatly enhanced when provided with the locations of people and devices. Indoor ultrasonic positioning system provide fine-grained position data for such applications. For example, ubiquitous computing applications require context information in order to blend seamlessly into the environment and to unobtrusively aid people in their everyday lives. A particularly important component of context is the location of people and the objects they interact with. Numerous ubiquitous applications utilizing location information have been developed. Various methods exist for determining the location of people or objects. All of them involve gathering data by sensing a real-world physical quantity, and using it to calculate or infer a position estimate. The data can be gathered via a number of physical media.

A real-time positioning technology that can operate indoors and outside anywhere in the world, with sub-cm accuracy, and low cost is the ultimate goal for many researchers. GPS can achieve cm-level kinematical positioning accuracy, but with some major constraints. First and foremost the use of GPS signals for indoor positioning poses difficult challenges, due to the very weak signal levels. Indoor positioning using high sensitivity GPS receivers cannot be guaranteed in all situations, and accuracies are typically of the order of tens to hundreds of meters at best.

In this chapter we present a spread spectrum indoor ultrasonic positioning system based on a commercially available narrowband ultrasonic sensor. The use of such a sensor will reduce the cost of the system. In the same time it can be used as mobile tag regarding to the small size and the low power that is required for the transmitter. The desirable property of ultrasonic location system is that they have the capability to be fine-grained, meaning they can estimate location with a high degree of resolution. This is because the speed of ultrasound in air is sufficiently slow to allow the time-of-arrival of a signal to be accurately measured between a fixed unit

in the environment and a mobile unit functioning as a tag on a person or object. The use of spread spectrum in ultrasonic location system allows the system to work at a noisy environment. In the same time it solves the problem of signal collisions when more than one transmitter transmit at the same time. Test results demonstrate that the system is able to locate the position of a moving target with high accuracy. In the next sections details of the hardware structure of the system and the measurements result of its accuracy will be give.

## 5.2 Application Areas

Active Badge information has been used in a wide range of applications, including telephone call routing and security [43] and environmental control [145]. Harter and Hopper describe a nearest printer service offered to users of portable computers [146]. Equipment tags placed on the computer and printers report their positions, and the computer is automatically configured to use the nearest available printer as it is moved around a building.

Another application of Active Badge information is the Teleporting System [147], which allows a user to redirect their X Window System environment to different computer displays. The system can find personnel wearing Active Badges, and the set of computer displays located with them can be determined using information obtained from equipment tags. Personnel can redirect their windowing environment to one of these displays by using the buttons on their Active Badge, which acts as a ubiquitous authentication and control device. When a user leaves the location in which their windowing environment is displayed, the Teleporting System causes it to disappear to prevent unauthorized access.

Other researchers have proposed similar ideas. A framework for supporting location-aware multimedia applications is described by [148]. Mobile agents containing application code and execution state may be moved between hosts, following their users (who are tracked using Active Badges) around a building. Multimedia stream endpoint agents, such as video and audio sources, may also be transferred between devices in this way for example, a mobile music stream could follow its user by automatically selecting a new loudspeaker as an output device when they moved into a different room. The FLUMP (FLexible Ubiquitous Monitor Project) system uses a set of wall-mounted monitors to present information such as e-mail and diary entries to users [149]. Active Badge location data controls the migration of information from one display to another, based on the positions of users.

The work in [150] describes the use of the ParcTab system to implement applications involving context-triggered actions and automatic reconfiguration. An example is the Scoreboard application, which is displayed in a public area of a building and shows items of interest to those around it, the latest football scores, for example. The



authors also suggest user interface designs for situations in which manual configuration of applications based on context information is appropriate.

The ParcTab has been used to implement a memory prosthesis, which collects information about the user's context and organizes it to form a biography [151]. Later, the user, who may remember only some of the detail of an event in which they are interested, can query the biography to retrieve the details that had been forgotten. Brown et al. have used ParcTabs to prototype stick-e notes [152], which are context-aware electronic equivalents of post-it notes. Stick-e notes have two components their content, which may be text, an HTML page, multimedia content or even a program, and a context in which the content should be displayed or executed. A potential application of this technology is a tour guide for a museum, which shows stick-e notes associated with nearby exhibits. Similarly, the Audio Aura system described by [153] presents location-dependent auditory cues to users who wear wireless headphones and Active Badges.

## 5.3 System Hardware Structure

This section describes the design and properties of the transmitter and receiver prototype hardware used in the system. The units were designed to facilitate flexibility, in order to fully gauge the potential of this new technology. This meant tethering the units to a power supply and a workstation PC for signal synthesis and analysis. However, making the units into small, light, wireless, and battery-powered mobile tags is feasible, and the modifications needed in order to accomplish this are set out. The prototype system was not designed to operate outside of the frequency range of 20 to 100 kHz. Sounds below 20 kHz are perceivable by humans, and the use of frequencies above 100 kHz is limited by the attenuation of ultrasound in air. The system is designed to work at frequency 40 kHz with bandwidth of 2 kHz. These parameters are selected based on the commercially available ultrasonic sensors.

### 5.3.1 Ultrasonic Transducer

The ultrasonic transducer is used to convert the applied electrical signal to mechanical vibrations (transmitter) and the conversion of returned mechanical vibrations back into electrical energy (receiver). The active element is the heart of the transducer as it converts the electrical energy to acoustic energy, and vice versa. The active element is basically a piece polarized material (i.e. some parts of the molecule are positively charged, while other parts of the molecule are negatively charged) with electrodes attached to two of its opposite faces. When an electric field is applied across the material, the polarized molecules will align themselves with the electric field, resulting in induced dipoles within the molecular or crystal structure of the material. This alignment of molecules will cause the material to change dimensions.

This phenomenon is known as electrostriction. In addition, a permanently polarized material such as quartz ( $\text{SiO}_2$ ) or barium titanate ( $\text{BaTiO}_3$ ) will produce an electric field when the material changes dimensions as a result of an imposed mechanical force. This phenomenon is known as the piezoelectric effect.

The narrowband transducers used in the existing ultrasonic location systems rely on piezoelectric ceramics as their active elements. These kinds of transducers are inexpensive, small, rugged, and have a high sensitivity. However, they are highly resonant, and in most cases have a usable bandwidth of less than 5 kHz. Electrostatic transducers, on the other hand, possess high sensitivity and extremely wide bandwidth. However, they are not very rugged, and are expensive, making their deployment on a large scale prohibitive. The indoor positioning system presented in this thesis is designed to work at frequency 40 kHz with bandwidth of 2 kHz. These parameters are selected based on the commercially available ultrasonic sensors. The transducers rely on piezo-electric ceramics as its active elements.

To measure the resonance frequency and the bandwidth of the used ultrasonic sensor we need to measure its transfer function. Fig. 5.1 shows the sittings used to measure the transfer function of the sensor. The ultrasonic receiver used in Fig. 5.1 is a standard ultrasonic transducer, which has flat response in the frequency range from 20 KHz to 100 KHz. A frequency generator is used to excite the transducer under test, which is used as a transmitter, with a sinusoidal, which has constant amplitude and varying frequency. The output of the standard ultrasonic receiver is connected to a spectrum analyzer to measure the power of the received signal at different frequencies. The measurement was done in a chamber, which is isolated to prevent reflections from the walls of the chamber that can affect the measurements.

Fig. 5.2(a) indicates the measured transfer function of the used ultrasonic transducer. From the measurements of the transfer function of the sensor it is found that the sensor has a resonance frequency 40.2 KHz and a 3dB bandwidth 1.7 kHz. The bandwidth of the sensor plays an important role in the resolution of the range measurements for the system, as it will be indicted later.

The same sitting in Fig. 5.1 is used to measure the radiation pattern of the ultrasonic transducer. The measurement was done at the resonance frequency of the transducer. Fig. 5.2(b) indicates the obtained radiation pattern of the transducer, it is found that the 3 dB beam width of the transducer is around  $30^\circ$ .

### 5.3.2 Transmitter Unit

As shown in Fig. 5.3(a), the transmitter is designed to convert an electrical voltage signal into an ultrasonic one. For the prototype system, the signal was synthesized digitally on a PC, to allow the structure of the ranging message (PN code) to be changed easily in software. The signal was sent out through the sound card, which performs digital-to-analogue conversion, and carried to an external modulator via

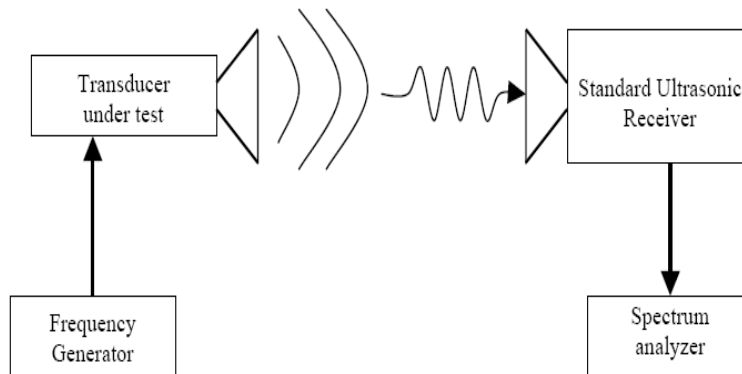


Figure 5.1: Settings for measuring the transfer function of the ultrasonic transducer.

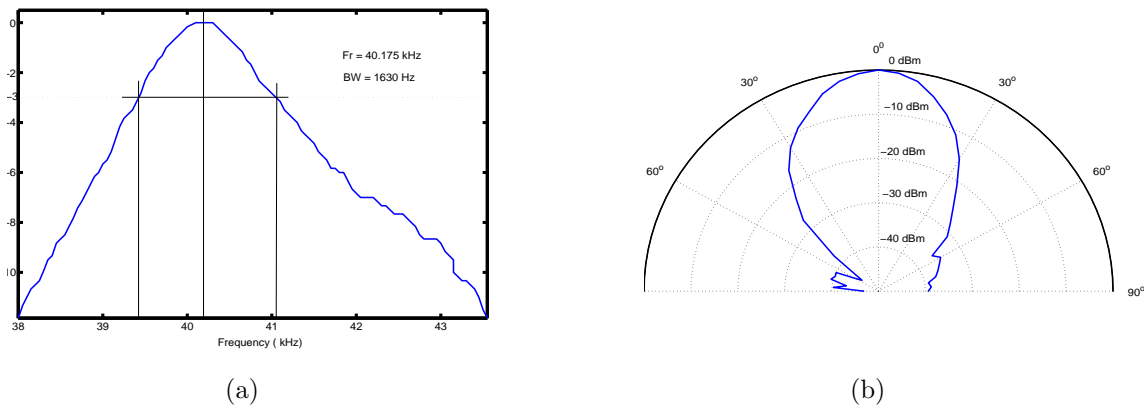


Figure 5.2: (a) Transfer function of the ultrasonic sensor. (b) Radiation pattern of the ultrasonic transducer.

coaxial cable to modulate the PN code with a carrier frequency, which is adjusted to be equal to the resonance frequency of the transducer. The prototype transmitter unit, which is indicated in Fig. 5.3(b), shows the transmitter unit, which contains only an amplifier and ultrasonic transducer. The transmitter unit was designed to drive its ultrasonic transducer with a maximum signal level 20 volts peak-to-peak. The signal from the modulator is connected to the transmitter unit via coaxial cable. This prototype transmitter unit is used only for testing the performance of the system.

For practical applications the transmitter unit should include the signal generator and the modulator in one mobile tag unit. Fig. 5.4 shows the modified transmitter unit. In this unit the PN code is generated using PIC technology, which can generate the PN code with a precise adjustable chip rate through the internal clock of the PIC. Beside generating the PN code the PIC generate also a synchronization pulse which is required to synchronize the transmitter and receivers units of the system. The unit also includes an oscillator for generating the carrier with a frequency equal to the resonance frequency of the transducer. A voltage multiplier IC is used in the unit as a modulator for modulating the carrier with the PN code. This unit needs a 9 V

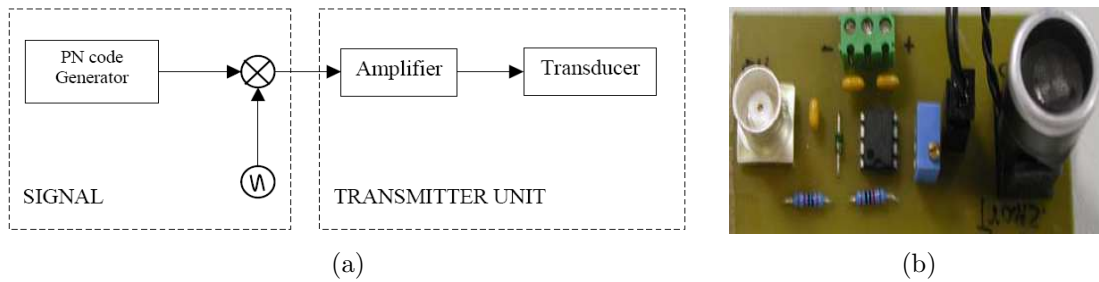


Figure 5.3: (a) Block diagram of the indoor ultrasonic transmitter. (b) Prototype ultrasonic transmitter unit.

battery to drive the required voltages for the electronic components.

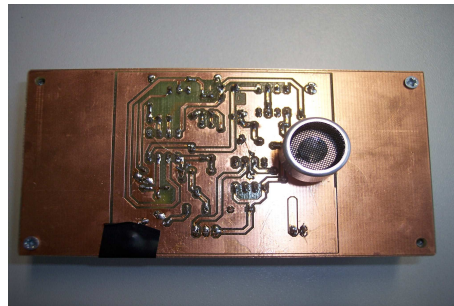


Figure 5.4: Mobile tag transmitter unit used in the ultrasonic indoor positioning system.

### 5.3.3 Receiver Unit

Traveling ultrasound waves through the air are converted by the receiver transducer into an electrical signal that is buffered by an amplifier. The circuit of Fig. 5.3(b) can be used also as the receiver unit by changing the input output terminals of the unit. Using coaxial cable, the signal outputs of the receiver units were connected to data acquisition cards at a PC. The PCI data acquisition card performs analog-to-digital conversion. A sampling rate of 100 KHz, which is larger than twice the highest frequency in the signal, was chosen for each receiver. The converted signals are then processed using c++ program running on a PC. This method allows flexibility when conducting experiments with our prototype system, as signals can be analyzed in real time using a variety of methods, implemented as c++ software.

### 5.3.4 Signal Generation

The ranging messages used in the measurements consisted of a 40.2 kHz carrier, modulated by M-sequence pseudo random code of length 63 bits. The chip rate of the code was selected to be 1 kHz, which leads to a bandwidth of 2 kHz. The selection

of the chip rate of the PN code is determined based on the available bandwidth of the ultrasonic transducer. The transmitted signal  $s(t)$  can be described as follow:

$$s(t) = p(t) \cdot \cos(\omega_o t) \quad (5.1)$$

Where  $p(t)$  is the M-sequence pseudo random code and  $\omega_o$  is the carrier frequency. Fig. 5.5(a) indicates the generated M-sequence pseudo random code and Fig. 5.5(b) indicates the power spectral density (PSD) of the transmitted signal.

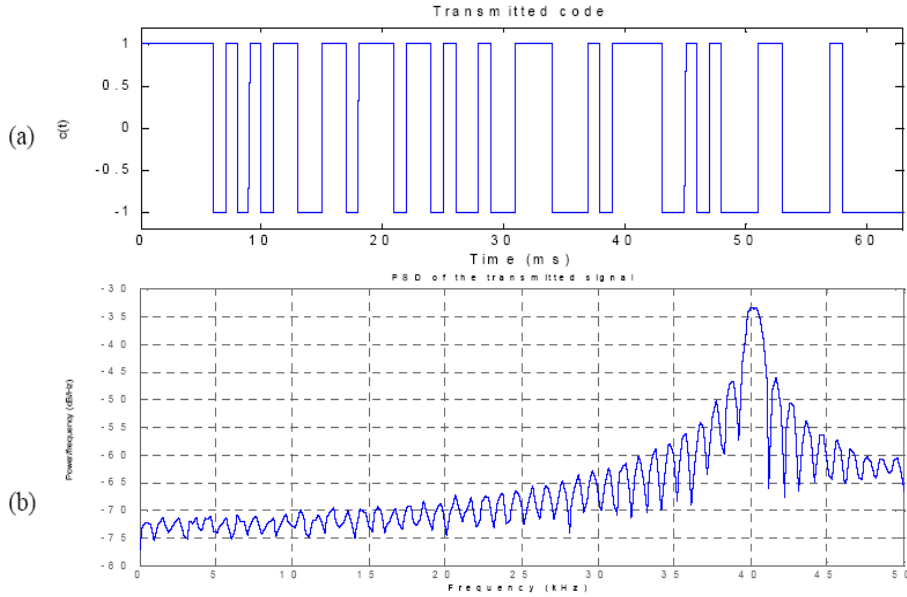


Figure 5.5: (a) The transmitted code. (b) The PSD of the transmitted signal.

### 5.3.5 Digital Signal Processing

The location of a transmitter unit (T) was estimated using the following steps.

1. The time-of-arrival for the transmitter unit ranging message were measured by correlating the receivers' signal against the expected signal. The time-of-arrival was defined as the time between the triggering time and the first peak in the correlated data.
2. The time-of-arrival is converted to distance using the speed of sound in air.
3. Using the accurately surveyed positions of the receivers and the transmitter-to-receivers distances, location was estimated by employing the multilateration algorithm described by [41]. Since the receivers are coplanar, a minimum of two distances is needed to estimate the 2D transmitter position.

## 5.4 Multilateration Algorithm

Position-based location systems track objects by reporting their coordinates in a frame of reference. The actual position measurements may be made in many ways. Object (or marker) locations can be sensed directly, using measurements of fields emanated or affected by them, or by contact methods. Alternatively, locations can be deduced from measurements of other physical properties of the object. Inertial schemes determine the acceleration or velocity of objects, and integrate those measurements to obtain their positions relative to initial points. Triangulation systems use measurements of the bearings of objects from known, fixed points to find their locations. Similarly, trilateration (or multilateration) schemes find object positions by determining their distances from fixed points. Fig. 5.6 shows how the position in 3D space of a transmitting device may be determined by measuring its distance from three receivers fixed at known locations. In general, to find the 3D position of an object by multilateration, distances must be measured to it from four known, non-coplanar points or three known, coplanar points.

Ultrasonic multilateration systems determine the positions of objects by measuring distances between ultrasound sources and detectors. In some systems, a transmitter is mounted on the object, and several fixed receivers detect its signal. In others, a number of fixed transmitters generate signals that are picked up by a single receiver on the object to be tracked.

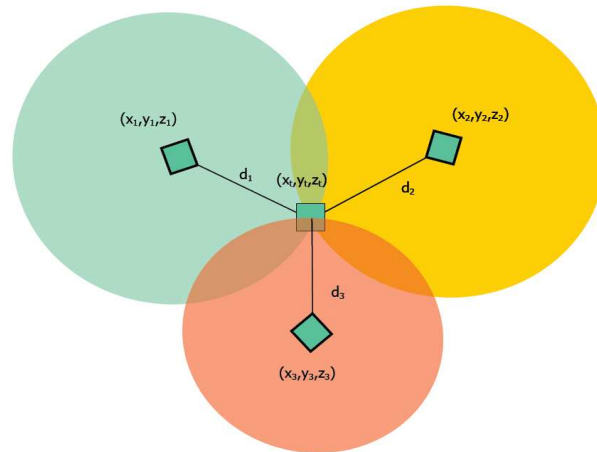


Figure 5.6: Multilateration in three dimensions.

### 5.4.1 Processing of Distance Measurements

The distance between the transmitter and the receiver is calculated by measuring the time-of-arrival for the transmitter ranging message. The time-of-arrival is measured by calculating the correlation between the received signal and the reference signal.

The received signal can be described as a summation of delayed copy of the transmitted signal, which was described by (5.1). Using (5.1) one can describe the received signal as:

$$z(t) = \sum_{k=1}^p A_k s(t - \tau_k) \quad (5.2)$$

where  $p$  represents the number of multi-path reflections, including the direct path between the transmitter and receiver,  $A_k$  is the amplitude of the  $k$  path and  $\tau_k$  is the time-of-arrival of the  $k$  path signal. Substituting for  $s(t)$  from (5.1), Then (5.2) can be written as:

$$\begin{aligned} z(t) &= \sum_{k=1}^p A_k p(t - \tau_k) \cos(\omega_o(t - \tau_k)) \\ &= \sum_{k=1}^p A_k p(t - \tau_k) \cos(\omega_o t - \theta_k) \end{aligned} \quad (5.3)$$

where  $\theta_k = \omega_o \tau_k$ . The time-of-arrival can be calculated by calculating first the correlation between the received signal  $z(t)$  (after demodulation by the carrier) and the transmitted code  $p(t)$ . Two-channel demodulator was used to overcome the problem of the phase shift between the received carrier and the reference carrier. Fig. 5.7 indicates the block diagram of the two-channel correlator receiver used in the system, which was software implemented.

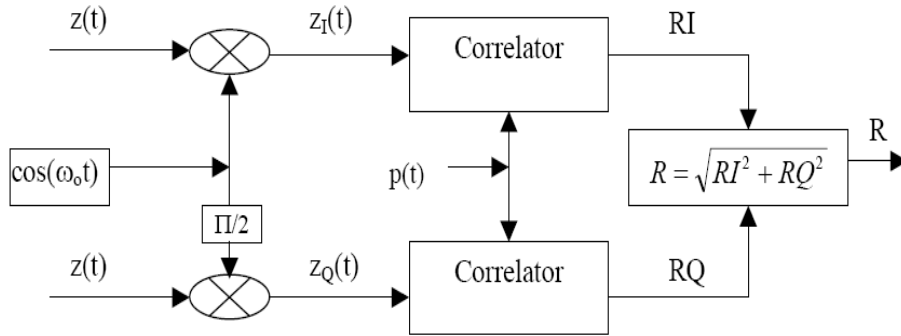


Figure 5.7: Two-channel correlator receiver.

After demodulation and low pass filtering the received signal can be written as:

$$z_I(t) = \sum_{k=1}^p A_k p(t - \tau_k) \cos(\theta_k) \quad (5.4)$$

$$z_Q(t) = \sum_{k=1}^p A_k p(t - \tau_k) \sin(\theta_k) \quad (5.5)$$

where  $z_I(t)$  is the In-phase signal and  $z_Q(t)$  is the Quadrature signal. By using the reference PN code  $p(t)$  the correlation can be calculated. The correlation was calculated using FFT as follows:

$$RI = IFFT \{Z_I(f).conj [P(f)]\} \quad (5.6)$$

$$RQ = IFFT \{Z_Q(f).conj [P(f)]\} \quad (5.7)$$

Where  $Z_I(f)$ ,  $Z_Q(f)$  and  $P(f)$  are the Fourier transforms of  $z_I(t)$ ,  $z_Q(t)$  and  $p(t)$  respectively and IFFT denotes the Inverse Fast Fourier Transform. The total correlation was calculated as shown by the block diagram of Fig. 5.7. Fig. 5.8 indicates the obtained correlations of the received signal.

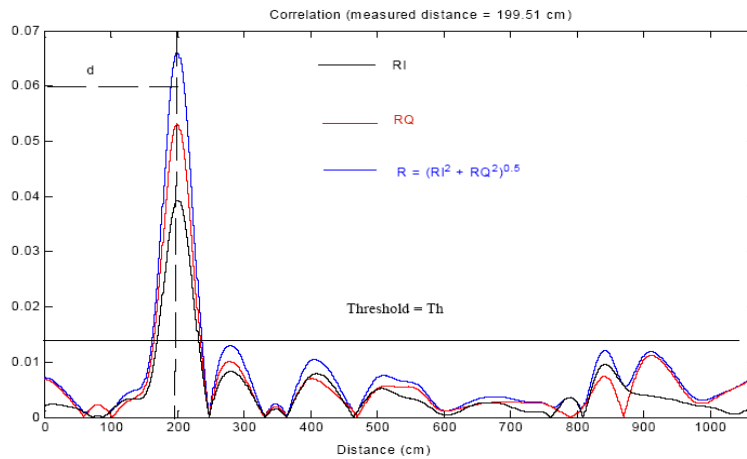


Figure 5.8: The correlation for the measured signal at distance (200 cm).

The correlation is passed through a threshold to remove the effect of noise and side loops. There are different methods for calculating the value of the threshold. In this work the value of the threshold was calculated based on the average value of the correlation as.

$$Th = a.mean(R) + b \quad (5.8)$$

Where  $a$  and  $b$  are constants calculated based on the observed values of the correlation.

The time-of-arrival between the transmitter and receiver  $\tau_1$  was taken as the time of the occurrence of the first peak in the correlation curve (the short path is the direct path between the transmitter and receiver). Using the speed of sound in air ( $c = 341$  m/s) one can calculate the distance between the transmitter and receiver using:

$$d = \tau_1.c \quad (5.9)$$

## 5.4.2 Position Finding

In this thesis a two-dimensional (2D) positioning system is presented. To find the unknown 2D position  $(x_t, y_t)$  of the target one needs two distances to be measured



between the transmitter and a well-defined receivers position  $(x_i, y_i)$  (we assume that the transmitter exist inside the test area). By the knowing of the height of the receivers ( $h$ ) and the measured two distances ( $d_1, d_2$ ) between the transmitter and receivers we can find the  $x - y$  position of the transmitter by solving the following equations.

$$(x_t - x_i)^2 + (y_t - y_i)^2 = r_i^2, \quad \text{and } i = 1, 2 \quad (5.10)$$

where  $r_i^2 = (h^2 + d_i^2)$  and  $h$  again is the height of the receiver as indicated in Fig. 5.9. Where  $Lx$  and  $Ly$  in the figure indicate the area under test.

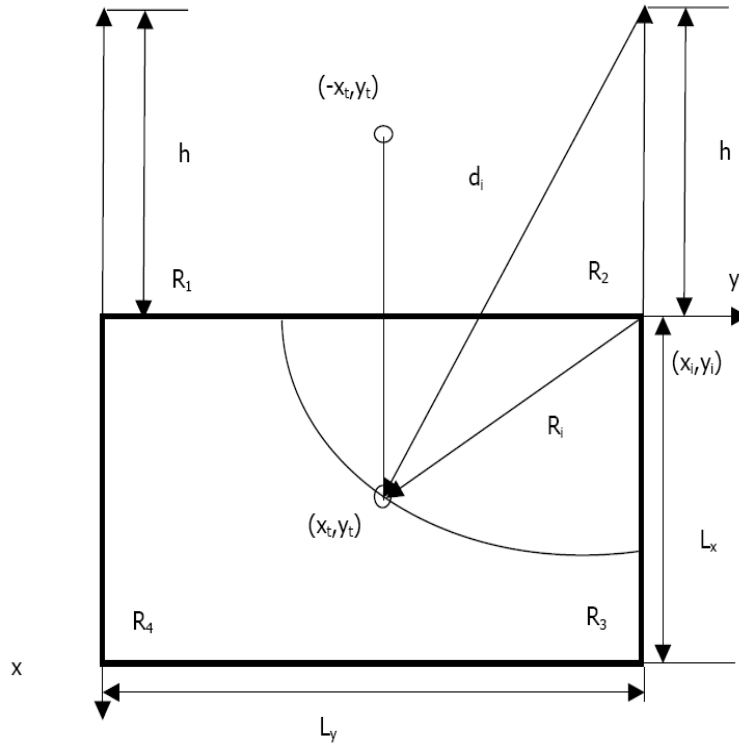


Figure 5.9: Setting for the 2D position finding system.

For example, if receivers  $R_1$  and  $R_2$  are used to determine the position of the transmitter then  $x_1, x_2, y_1 = 0$  and  $y_2 = L_y$ . Using (5.10) we found that:

$$y_t = \frac{r_1^2 - r_2^2 + L_y^2}{2L_y} \quad (5.11)$$

and

$$x_t = \pm \sqrt{r_1^2 - y_t^2} \quad (5.12)$$

The positive sign in (5.12) is selected if we assume that the transmitter exist only inside the area  $L_x.L_y$ . If it is allowed for the transmitter to exist at any place

(outside or inside the indicated area) then a third distance is required to determine the position of the transmitter. In the proposed system the transmitter is allowed to exist only inside the indicated area of Fig. 5.9.

## 5.5 Test Configurations

The system was installed in an area of 2.5 m x 2.5 m. Four receivers  $R_1$  to  $R_4$ , as indicated in Fig. 5.10, were installed on stands in the corners of this area. The height of the stands ( $h$ ) is 2.0 m. A mobile transmitter unit (T) was attached to a moving object within this area. As indicated in the previous section, we need only two receivers to find the x-y position of the target. In the proposed system we installed four receivers to overcome the problem of multi-path reflections, which can lead to large errors in measuring the distance when there are obstacles exist between the transmitter and receiver and also to increase the coverage area of the system.

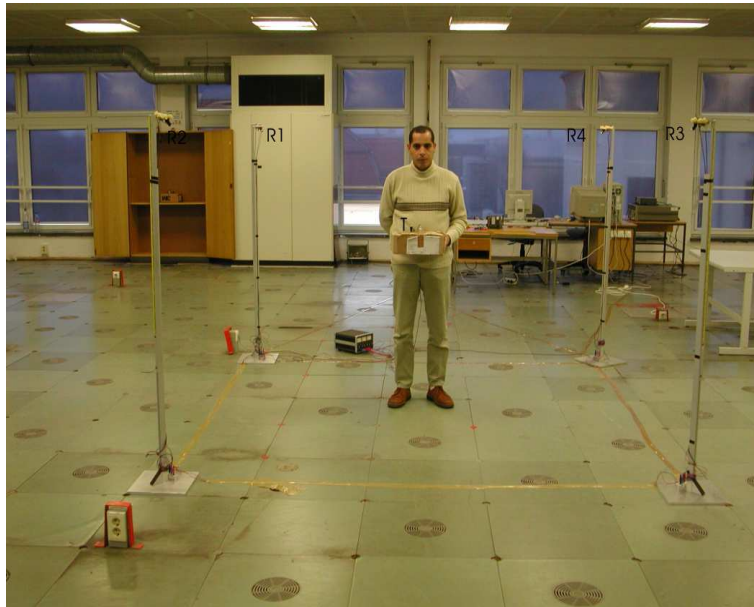


Figure 5.10: Ultrasonic location system lab.

The system measures four distances from these four-measured distances we need to use only two to calculate the position. The roles for selecting the required two distances are.

1. The difference between the two distances should be less than that between these two receivers.
2. The sum of the two distances should be larger than that between these two receivers. Assume that the two receivers that will be used are  $R_i$  and  $R_j$  then the above two conditions can be written as:

$$d_i - d_j < \sqrt{(x_i - x_j)^2 + (y_i - y_j)^2} \quad (5.13)$$

$$d_i + d_j > \sqrt{(x_i - x_j)^2 + (y_i - y_j)^2} \quad (5.14)$$

3. Each distance should be larger than  $h$  and smaller than the maximum distance within the test area, which can be written as:

$$h < d_i < \sqrt{h^2 + L_x^2 + L_y^2} \quad (5.15)$$

### 5.5.1 System Problems

In this section we will present the problems, which appear during the sitting and testing of the system. Also we will present solutions for the mentioned problems.

#### Large Error In Measuring the Distance

The expected theoretical error,  $Ed_e$ , in measuring the distance (which is also related to the accuracy) for the proposed system could be obtained using the following relation:

$$Ed_e = \pm c/f_s \quad (5.16)$$

where  $f_s$  is the sampling frequency of the A/D converter.

As was mentioned previously the sampling frequency was adjusted to be 100 KHz. Using (5.16) the error should be equal to 0.341 cm but by measuring the error in the distance,  $Ed_m$ , we found that its around 5.5 cm.

To analyze this problem we will start with the obtained correlation function. Fig. 5.11 shows a zoom to the first peak in the correlation function. The figure indicates the total, in phase and quadrature correlation function. Theoretically, the peaks of the above mentioned correlation functions should take place at the same time delay with different amplitudes, which is not the case in Fig. 5.11. The correlation function was obtained using the inverse Fourier transform of the cross power spectral density between the received signal and the reference signal. Fig. 5.12 shows the PSD of the received signal. Fig. 5.12(a) represents the total frequency band (0 to  $f_s/2$ ) and Fig. 5.12(b) represents a zoom for the spectral around the carrier frequency (40 KHz). The PSD of the received signal should be symmetric around the carrier frequency but as its clear from Fig. 5.12(b) it's not symmetric. This means that that the carrier frequency is not equal to the resonance frequency of the transmitter receiver pair. Fig. 5.13 shows the transfer function of the transmitter receiver pair, which was obtained using the sitting of Fig. 5.1 by replacing the stander receiver with the receiver used in the system. It is found that the center frequency of the system is 40.6 KHz. By readjusting the carrier frequency to the center frequency of the system, its found the problem is solved as indicated in Figs. 5.14 and 5.15.

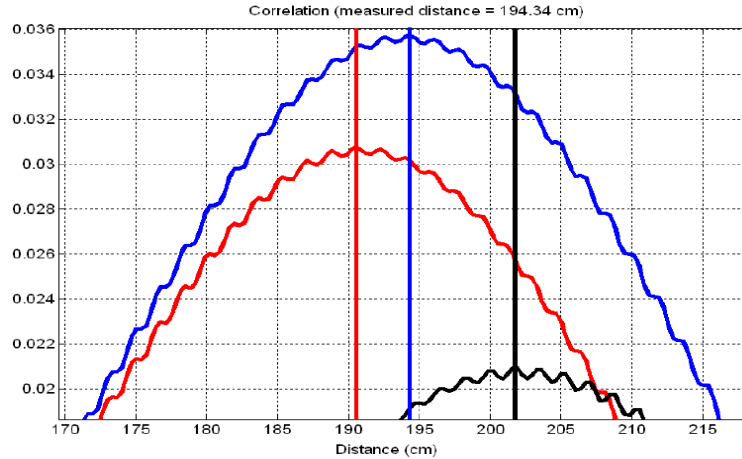


Figure 5.11: A zoom on the obtained correlation functions (actual distance 200 cm)  $f_o = 40$  KHz.

### Doppler Effect

As the name indicates, it is related to the speed of the object. It is noticed that during tracking the position of a moving target the system was failed in case of high speed and working probably when the speed of the object is low. The relation between the Doppler frequency,  $f_d$ , and the speed of the object,  $v$ , is given as:

$$f_d = (v/c) \cdot f_o \quad (5.17)$$

For the spread spectrum-positioning system there is a limitation for the maximum Doppler frequency  $f_{d_{\max}}$ , which is given by the following relation:

$$f_{d_{\max}} = f_{ch}/L \quad (5.18)$$

This maximum Doppler frequency is determined by the bandwidth of the correlation filter. Increasing the Doppler frequency above the maximum value will give zero output from the correlation filter, which makes the system failed in measuring the distance. To overcome this problem we should modify the carrier frequency of the reference signal by subtracting the Doppler frequency from it. The block diagram in Fig. 5.16 shows the required modification in the signal processing of the system. The Doppler frequency here is measured by calculating the FFT of the received signal.

### 5.5.2 Multipath Reflections

The most important parameter for accurate indoor positioning systems is the time of arrival TOA of the Direct Line of Sight DLOS path [91]. In this case accurate estimation of TOA from the received signal is required. Indoor multipath interference is the main factor that limits deploying indoor positioning systems, the multipath is severe and complex which leads to inaccurate estimate of the TOA using conventional

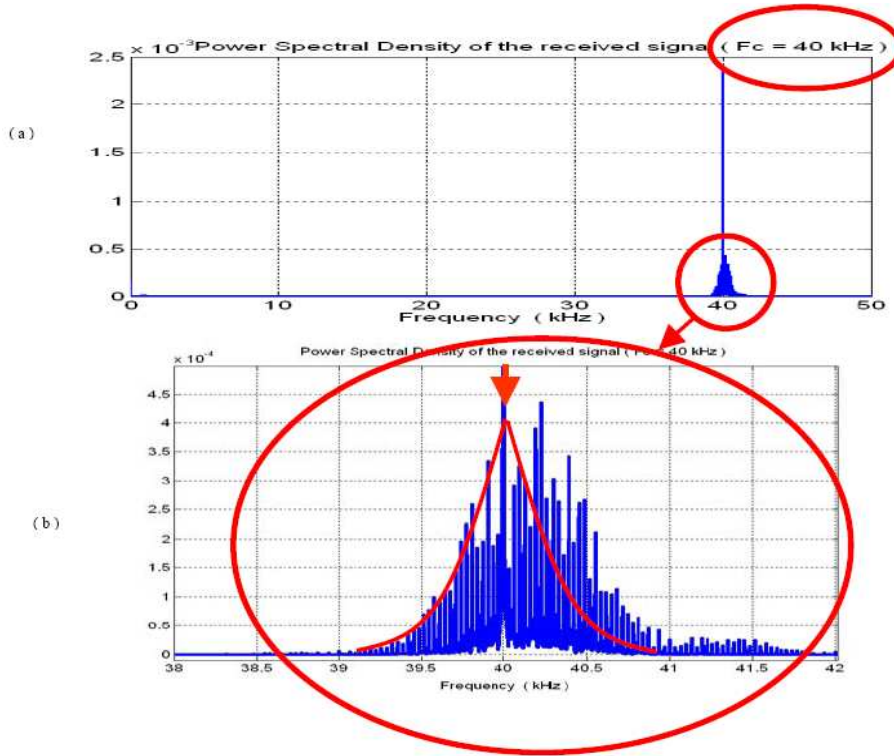


Figure 5.12: Power spectral density of the received signal, carrier frequency 40 KHz

techniques (correlation). Also in systems that have fixed bandwidth it is important to find alternative TOA estimation techniques.

Most of the existing ultrasonic transducers have a limited bandwidth, which leads to a poor resolution in locating the position of a target due to multi-path reflections from the surroundings. Different super resolution techniques such as Estimation of Signal Parameters via Rotational Invariance Techniques (ESPRIT) and Multiple Signal Classification (MUSIC) have been used for spectral estimation applications. Super resolution techniques are studied in the field of TOA estimation in indoor positioning systems such as multiple signal classification MUSIC [91] and RMUSIC [92]. Super resolution techniques can increase time domain resolution but in this case, the complexity of the system implementation also increases.

The proposed system in this thesis solves the problem of limitation in ultrasonic transducers bandwidth by applying the RMUSIC super resolution technique to estimate the time of arrival of ultrasonic signal.

The complicated indoor multipath propagation can be characterized using the baseband impulse response, which can be expressed as:

$$h(t) = \sum_{k=1}^L a_k \delta(t - \tau_k) \quad (5.19)$$

where  $L$  is the total number of the delayed paths,  $a_k$  is the amplitude,  $\tau_k$  is the

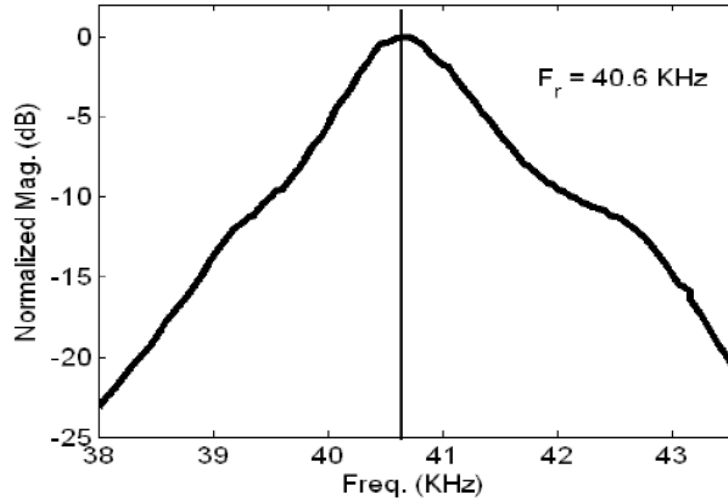


Figure 5.13: Transfer function of the ultrasonic Transmitter/Receiver sensors pair.

propagation delay, and  $\delta(t)$  is the Dirac delta function. The parametric model of the complex frequency domain indoor multipath propagation can be obtained from the Fourier transform of (5.19), which can be written as:

$$H(f) = \sum_{k=1}^L a_k e^{-j(2\pi f \tau_k)} \quad (5.20)$$

Fig. 5.17 shows a comparison between the conventional and RMUSIC algorithm in estimating the TOA. From the figure it is easily seen that the conventional technique is not able to resolve the DLOS from the multipath reflection on the other hand the RMUSIC technique resolves the multipath signal with a high resolution. More details about the super resolution techniques and how one can apply it in improving the resolution of the system will take place in the next chapter.

## 5.6 Experimental Results

Tests were conducted in order to assess the accuracy of the location system. Fig. 5.18 indicates the histogram of the measured distance error. This figure was obtained by varying the distance between the transmitter and receiver from 1m to 6 m with a step of 1 m and measures the distance at each point 1000 time. From the figure we found that 85 % from the measurements have a distance error less than 5 mm. The theoretical accuracy of the system is  $\pm 3.4$  mm, which is determined by the sampling frequency of the A/D converter. From Fig. 5.18 one can conclude that the accuracy of measuring the distance is within  $\pm 5$  mm. Fig. 5.19 indicates the online measured 2D position of a moving target.

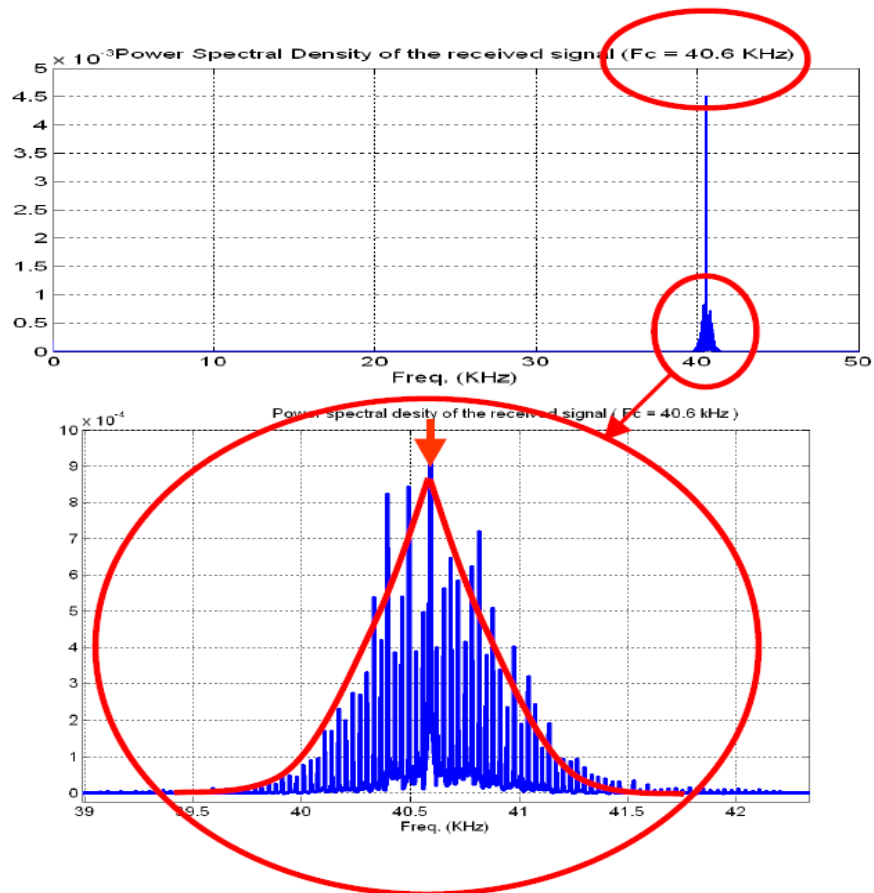


Figure 5.14: Power spectral density of the received signal, carrier frequency 40.6 KHz.

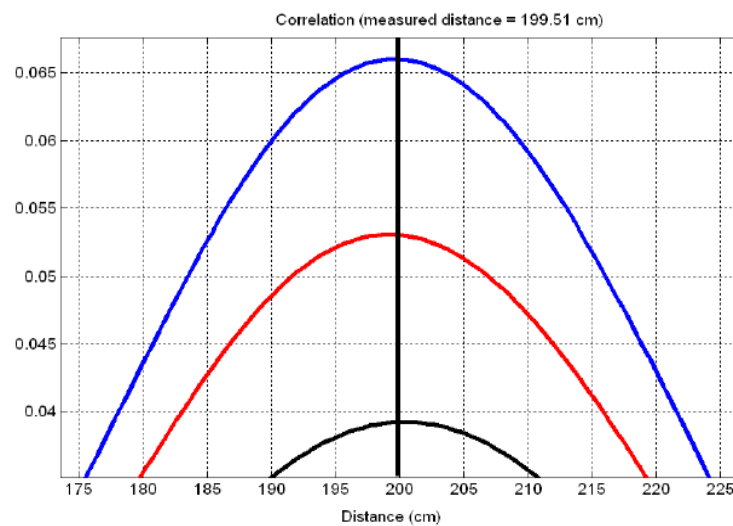


Figure 5.15: The obtained correlation functions (actual distance 200 cm) with  $f_o = 40.6$  KHz.

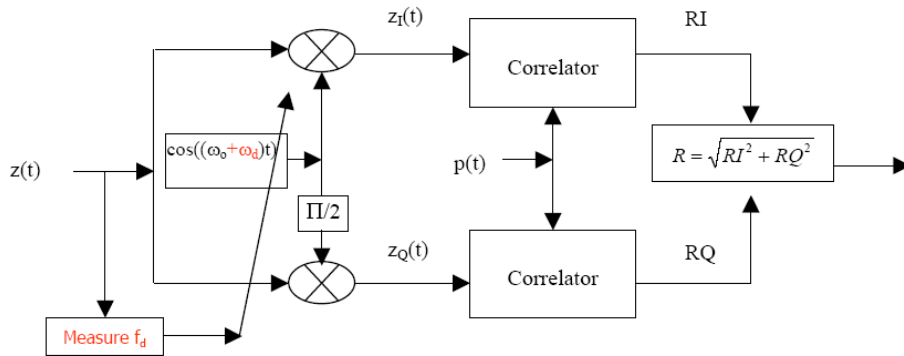


Figure 5.16: Modified two-channel correlator receiver.

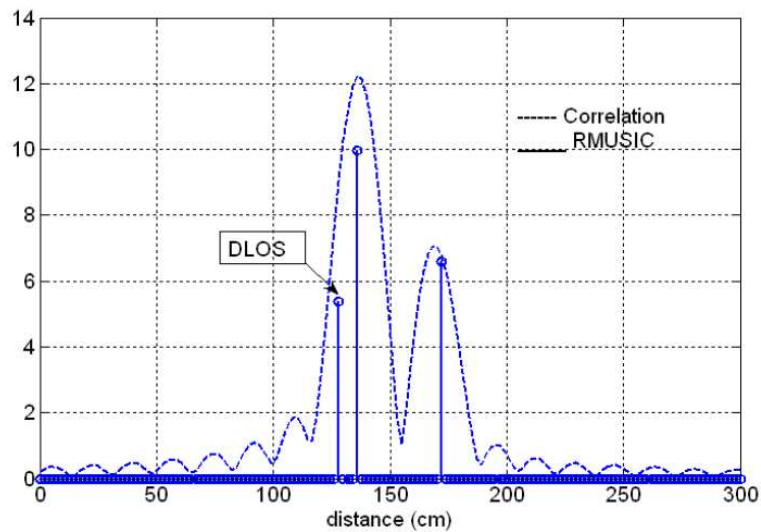


Figure 5.17: Performance of the RMUSIC compared with the conventional technique.



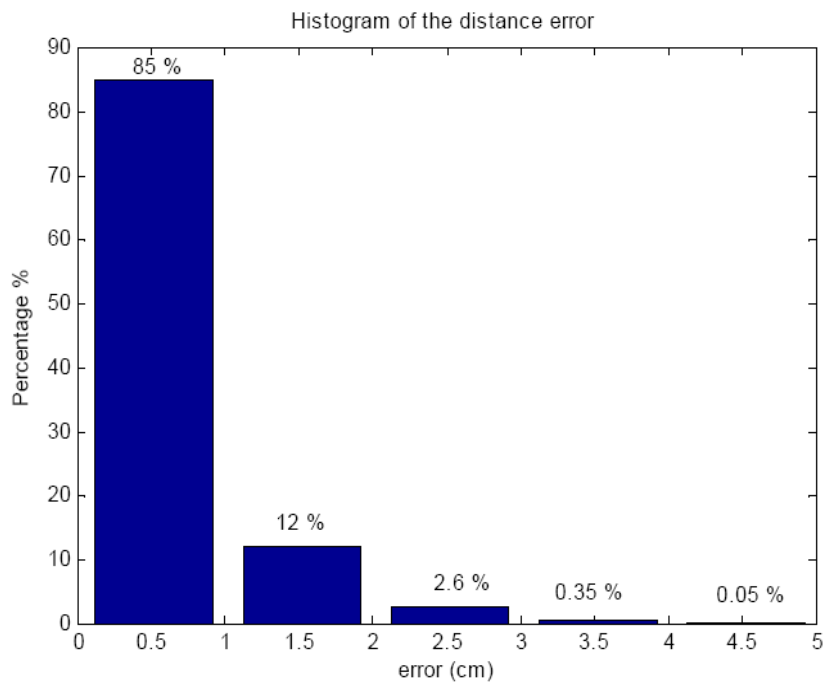


Figure 5.18: Histogram of the distance error.

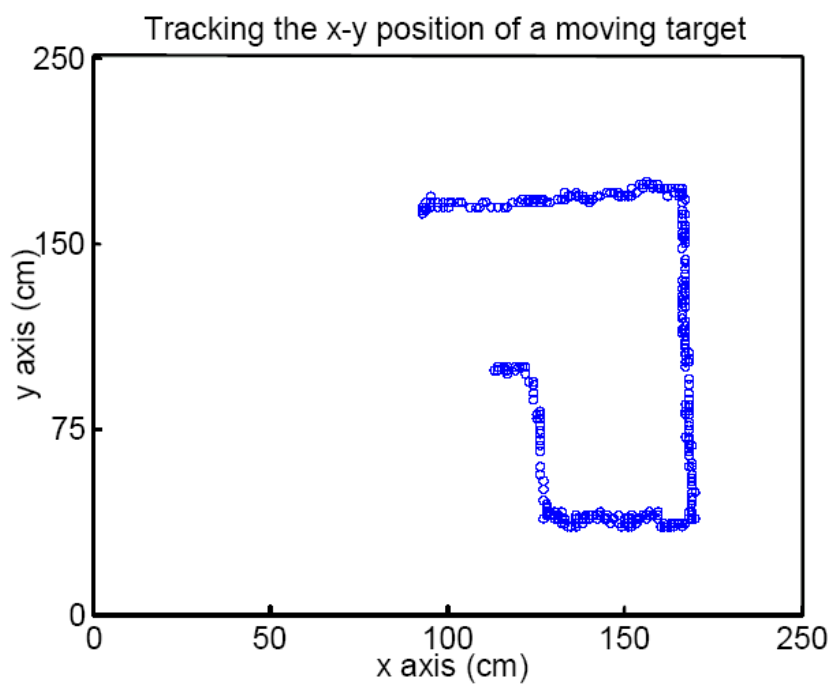


Figure 5.19: Measured location (x,y) of a moving target.

# Chapter 6

## Spread Spectrum Nondestructive Testing (NDT) & Nondestructive Evaluation (NDE)

### 6.1 Introduction

The field of Nondestructive Testing (NDT) is a very broad, interdisciplinary field that plays a critical role in assuring that structural components and systems perform their function in a reliable and cost effective fashion. NDT technicians and engineers define and implement tests that locate and characterize material conditions and flaws that might otherwise cause planes to crash, reactors to fail, trains to derail, pipelines to burst, and a variety of less visible, but equally troubling events. These tests are performed in a manner that does not affect the future usefulness of the object or material. In other words, NDT allows parts and material to be inspected and measured without damaging them. Because it allows inspection without interfering with a product's final use, NDT provides an excellent balance between quality control and cost-effectiveness. Generally speaking, NDT applies to industrial inspections. Technology that is used in NDT is similar to those used in the medical industry; yet, typically nonliving objects are the subjects of the inspections.

Nondestructive evaluation (NDE) is a term that is often used interchangeably with NDT. However, technically, NDE is used to describe measurements that are more quantitative in nature. For example, an NDE method would not only locate a defect, but it would also be used to measure something about that defect such as its size, shape, and orientation. NDE may be used to determine material properties, such as fracture toughness, formability, and other physical characteristics.

## 6.2 Some NDT/NDE Technologies

Many people are already familiar with some of the technologies that are used in NDT and NDE from their uses in the medical industry. Most people have also had an X-ray taken and many mothers have had ultrasound used by doctors to give their baby a checkup while still in the womb. X-rays and ultrasound are only a few of the technologies used in the field of NDT/NDE. The number of inspection methods seems to grow daily, but a quick summary of the most commonly used methods is provided below.

### 6.2.1 Visual and Optical Testing (VT)

The most basic NDT method is visual examination. Visual examiners follow procedures that range from simply looking at a part to see if surface imperfections are visible, to using computer controlled camera systems to automatically recognize and measure features of a component.

### 6.2.2 Radiography (RT)

RT involves the use of penetrating gamma- or X-radiation to examine material's and product's defects and internal features. An X-ray machine or radioactive isotope is used as a source of radiation. Radiation is directed through a part and onto film or other media. The resulting shadowgraph shows the internal features and soundness of the part. Material thickness and density changes are indicated as lighter or darker areas on the film.

### 6.2.3 Magnetic Particle Testing (MT)

This NDT method is accomplished by inducing a magnetic field in a ferromagnetic material and then dusting the surface with iron particles (either dry or suspended in liquid). Surface and near-surface flaws produce magnetic poles or distort the magnetic field in such a way that the iron particles are attracted and concentrated. This produces a visible indication of defect on the surface of the material.

### 6.2.4 Ultrasonic Testing (UT)

In ultrasonic testing, high-frequency sound waves are transmitted into a material to detect imperfections or to locate changes in material properties. The most commonly used ultrasonic testing technique is pulse echo, whereby sound is introduced into a test object and reflections (echoes) from internal imperfections or the part's geometrical surfaces are returned to a receiver.

### **6.2.5 Penetrant Testing (PT)**

The test object is coated with a solution that contains a visible or fluorescent dye. Excess solution is then removed from the surface of the object but leaving it in surface breaking defects. A developer is then applied to draw the penetrant out of the defects. With fluorescent dyes, ultraviolet light is used to make the bleedout fluoresce brightly, thus allowing imperfections to be readily seen. With visible dyes, vivid color contrasts between the penetrant and developer make "bleedout" easy to see.

### **6.2.6 Electromagnetic Testing (ET)**

Electrical currents (eddy currents) are generated in a conductive material by a changing magnetic field. The strength of these eddy currents can be measured. Material defects cause interruptions in the flow of the eddy currents, which alert the inspector to the presence of a defect. Eddy currents are also affected by the electrical conductivity and magnetic permeability of a material, which makes it possible to sort some materials based on these properties.

### **6.2.7 Leak Testing (LT)**

Several techniques are used to detect and locate leaks in pressure containment parts, pressure vessels, and structures. Leaks can be detected by using electronic listening devices, pressure gauge measurements, liquid and gas penetrant techniques, and/or a simple soap-bubble test.

### **6.2.8 Acoustic Emission Testing (AE)**

When a solid material is stressed, imperfections within the material emit short bursts of acoustic energy called "emissions." As in ultrasonic testing, acoustic emissions can be detected by special receivers. Emission sources can be evaluated through the study of their intensity and arrival time to collect information about the sources of the energy, such as their location.

## **6.3 History of Ultrasonic Imaging**

Prior to World War II, sonar, the technique of sending sound waves through water and observing the returning echoes to characterize submerged objects, inspired early ultrasound investigators to explore ways to apply the concept to medical diagnosis. In 1929 and 1935, Sokolov studied the use of ultrasonic waves in detecting metal objects. Mulhauser, in 1931, obtained a patent for using ultrasonic waves, using two transducers to detect flaws in solids. Firestone (1940) and Simons (1945) developed pulsed ultrasonic testing using a pulse-echo technique.

Shortly after the close of World War II, researchers in Japan began to explore medical diagnostic capabilities of ultrasound. The first ultrasonic instruments used an A-mode presentation with blips on an oscilloscope screen. That was followed by a B-mode presentation with a two-dimensional gray scale imaging.

Japan's work in ultrasound was relatively unknown in the United States and Europe until the 1950s. Then researchers presented their findings on the use of ultrasound to detect gallstones, breast masses, and tumors to the international medical community. Japan was also the first country to apply Doppler ultrasound, an application of ultrasound that detects internal moving objects such as blood coursing through the heart for cardiovascular investigation.

Ultrasound pioneers working in the United States contributed many innovations and important discoveries to the field during the following decades. Researchers learned to use ultrasound to detect potential cancer and to visualize tumors in living subjects and in excised tissue. Real-time imaging, another significant diagnostic tool for physicians, presented ultrasound images directly on the system's CRT screen at the time of scanning. The introduction of spectral Doppler and later color Doppler depicted blood flow in various colors to indicate speed of flow and direction.

The United States also produced the earliest hand held "contact" scanner for clinical use, the second generation of B-mode equipment, and the prototype for the first articulated-arm hand held scanner, with 2-D images.

### 6.3.1 History of Nondestructive Evaluation

Nondestructive testing has been practiced for many decades, with initial rapid developments in instrumentation spurred by the technological advances that occurred during World War II and the subsequent defense effort. During the earlier days, the primary purpose was the detection of defects. As a part of "safe life" design, it was intended that a structure should not develop macroscopic defects during its life, with the detection of such defects being a cause for removal of the component from service. In response to this need, increasingly sophisticated techniques using ultrasonic, eddy currents, x-rays, dye penetrants, magnetic particles, and other forms of interrogating energy emerged.

In the early 1970's, two events occurred which caused a major change. The continued improvement of the technology, in particular its ability to detect small flaws, led to the unsatisfactory situation that more and more parts had to be rejected, even though the probability of failure had not changed. However, the discipline of fracture mechanics emerged, which enabled one to predict whether a crack of a given size would fail under a particular load if a material property, fracture toughness, were known. Other laws were developed to predict the rate of growth of cracks under cyclic loading (fatigue). With the advent of these tools, it became possible to accept structures containing defects if the sizes of those defects were known. This formed

the basis for new philosophy of "fail safe" or "damage tolerant" design. Components having known defects could continue in service as long as it could be established that those defects would not grow to a critical, failure producing size.

A new challenge was thus presented to the nondestructive testing community. Detection was not enough. One needed to also obtain quantitative information about flaw size to serve as an input to fracture mechanics based predictions of remaining life. These concerns, which were felt particularly strongly in the defense and nuclear power industries, led to the creation of a number of research programs around the world and the emergence of quantitative nondestructive evaluation (QNDE) as a new discipline. The Center for Nondestructive Evaluation at Iowa State University (growing out of a major research effort at the Rockwell International Science Center); the Electric Power Research Institute in Charlotte, North Carolina; the Fraunhofer Institute for Nondestructive Testing in Saarbrücken, Germany; and the Nondestructive Testing Centre in Harwell, England can all trace their roots to those.

## 6.4 The Concept of Imaging

The overall process of imaging can be well understood with the help of Fig. 6.1, where  $h(t)$  represents the impulse response of the object under test. It is possible to get some useful information (like mechanical or electrical properties) about this object if we are able to measure its impulse response  $h(t)$ . To measure the impulse response of the object it is required to illuminate it with a signal  $x(t)$ , which can be electromagnetic wave or ultrasonic wave, and measure the scattered signal  $y(t)$  interacting with the object to obtain the image of the distribution of the properties of the object from these measurements. The relation between the transmitted signal  $x(t)$ , the received signal  $y(t)$  and  $h(t)$  is given as:

$$\begin{aligned} y(t) &= x(t) * h(t) \\ &= \int_{-\infty}^{\infty} h(\tau)x(\tau - t)d\tau. \end{aligned} \quad (6.1)$$

The process of obtaining the impulse response of the object is called the direct problem, which is associated with an inverse problem to get some information about the properties of the object using the result of the direct problem.

### 6.4.1 Format of the Transmitted Signal

To obtain the exact impulse response,  $h(t)$ , from the received signal, (6.1) suggested that  $x(t)$  should be an impulse signal  $\delta(t)$ , which has zero duration or infinite bandwidth ( $BW = \infty$ ) and infinite amplitude. Substituting for  $x(t)$  with  $\delta(t)$  in (6.1) gives:

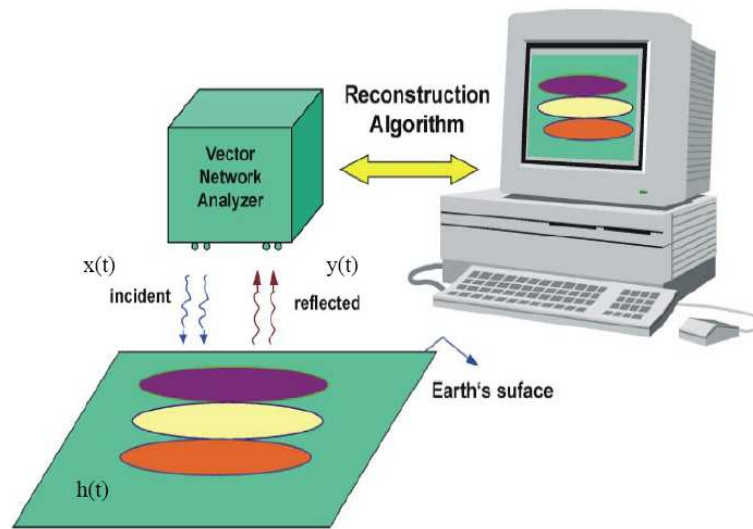


Figure 6.1: A typical example of imaging

$$y(t) = \int_{-\infty}^{\infty} h(\tau)\delta(\tau - t)d\tau = h(t) \quad (6.2)$$

In practice it is not possible to generate a signal with zero duration and infinite amplitude, instead a modulated (the carrier frequency is selected to be equal to the center frequency of the sensor) pulse  $p(t)$  of finite duration  $\tau$  or finite bandwidth ( $BW = 1/\tau$ ) and finite amplitude, as indicated in Fig. 6.2, is used. The used pulse can be either rectangular or Gaussian pulse (to minimize the side lobe effect due to bandwidth limitation).

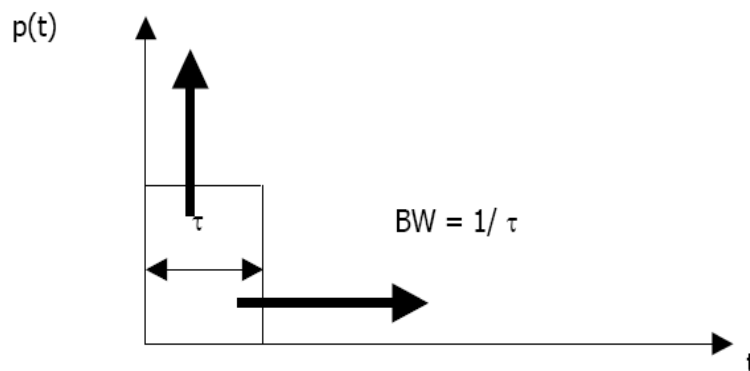


Figure 6.2: Time domain rectangular pulse.

Using pulsed signal in the excitation leads to a trade-off between resolution and noise effect, which is well known in ultrasonic imaging. Given a short pulse the noise effect can be decreased by either increasing the pulse amplitude or the pulse duration (decreasing the bandwidth). However, The pulse amplitudes of commercial

scanners are limited by the mechanical index (MI). The only feasible alternative is to extend the pulse duration, which has the undesirable consequence of reducing the axial resolution. O'Donnell [93] predicted that the transmitted energy can be increased up to 15-20 dB by coded excitation before reaching particular intensity limits. This additional SNR can be used to increase resolution and/or penetration. With proper decoding, the SNR of the imaging pulse is improved by the increased average power in the coded excitation compared to an equivalent pulse excitation of the same peak power. Any decoding system with a finite time-bandwidth product, however, cannot produce an ideal impulse without range side lobes. For high-quality imaging, range side lobes must be managed. Practical coded excitation systems have a trade-off between range side lobes and SNR improvements.

### 6.4.2 Pulse Compression Techniques

The method of pulse-compression found its first widespread applications during the years 1940-1950, when it was implemented into radar-systems independently by several developers. Proceeding from the original linear frequency modulated pulses, several related signal-types were examined with the aim to improve the range and/or resolution. The linear frequency modulated pulses technique based on changing the frequency of the carrier linearly. Another technique, which is spread spectrum (coded excitation) technique, based on changing the phase of the carrier using a certain will known code.

### 6.4.3 Principle of Pulse Compression

Pulse compression is a signal processing procedure that converts long bursts of small amplitude into short pulses of high amplitude. Figs. 6.3 and 6.4 show the principle of pulse compression techniques using linear frequency modulated signal and spread spectrum signal respectively.

In the conventional pulse echo ultrasonic imaging, the transmitted signal can be written in the following form:

$$x(t) = p(t) \cos(\omega_c t) \quad (6.3)$$

where  $p(t)$  could be a rectangular pulse (with extended duration and reduced amplitude) as indicated in Fig. 6.2.

The frequency modulated puls  $x(t)$  is a signal, whose instantaneous frequency  $f(t)$  changes according to a well defined time-function. The transmitted signal  $x(t)$  can be written as follow:

$$x(t) = p(t) \cos(\omega_c t + \phi(t)) \quad (6.4)$$



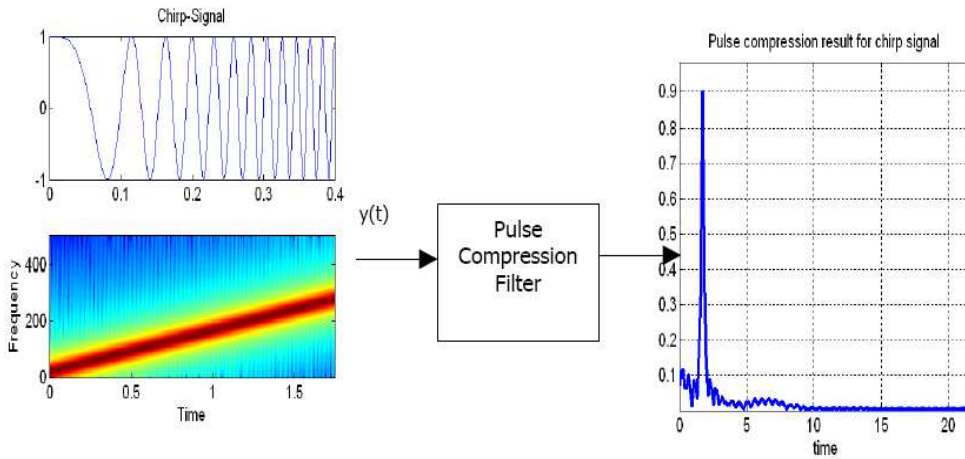


Figure 6.3: The principle of pulse compression using linear frequency modulated signal.

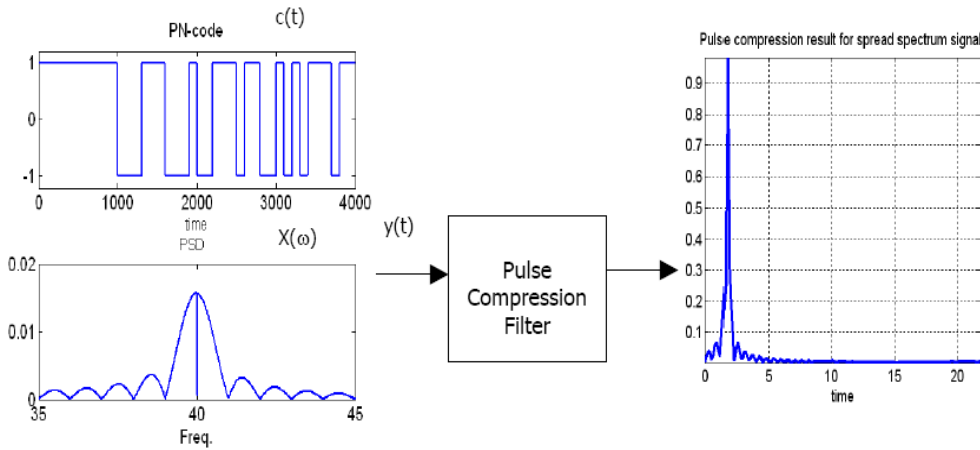


Figure 6.4: The principle of pulse compression using spread spectrum signal.

$$f(t) = \frac{1}{2\pi} \frac{d\phi(t)}{dt} \tag{6.5}$$

For linear frequency modulated signal, the instantaneous frequency  $f(t)$  changes linearly with time, which can take the following form.

$$f(t) = k.t \tag{6.6}$$

In the case of spread spectrum pulse compression technique the transmitted signal can be written as follow:

$$x(t) = p(t).c(t). \cos(\omega_c t) \tag{6.7}$$

where  $c(t)$  is a PN code sequence, which take the values 1 and -1, this will lead to a phase modulation of the carrier.

Pulse compression techniques can be implemented into ultrasonic pulse-echo-systems to increase the SNR of the echo signals. The gain in SNR is achieved mainly by an increase of the energy of the transmitted signal. An additional reduction of interfering signals is caused by the fact that short pulses within the echo signal are transformed to long bursts of low amplitude by the pulse compression procedure.

## 6.5 Spread Spectrum Ultrasonic Imaging

Coded excitation (spread spectrum) is well established in radar, producing dramatically improved SNR at modest peak power levels compared to conventional pulsed techniques. Pseudo-random noise and coherent broadband excitations have been explored as codes for ultrasound imaging. Unfortunately, none of these early attempts were successful. Most relied on large time-bandwidth codes those are not practical for ultrasound array systems using dynamic focusing on receive.

Traditional coded excitation system uses chirp codes, M-sequence, or Barker codes. To decode the received coded excitation signal one should search for a transform, which is able to localize the signal and reduce the noise effect. In general any transform is a correlation between the coded signal and the kernel of the transform. To satisfy high correlation between the coded signal and the kernel of the transform one should use the code itself as the kernel of that transform. For the above explained reason the coded signal is decoded with correlation-based procedures such as matched filtering or mismatched filtering.

Fig. 6.5 shows the block diagram of the spread spectrum ultrasonic imaging system used in the echo mode to measure the reflection coefficient. The same system could be used in the through mode by changing the position of the ultrasonic receiver to be on the other side of the material under test and measuring the transmission coefficient.

### 6.5.1 Signal Coding and Modulation

Traditional coded excitation systems use chirp codes, M-sequence, Goaly, or Barker codes. A comparison in performance between the chirp and Goaly code was given in [154]. In this thesis the M-sequence code will be used. The advantages in using the M-sequence code are: it is simple in implementation and available with large length for applications that have large time-bandwidth product. In the other hand it has great range side lobes particularly in applications that have small time-bandwidth product.

In most of the coded excitation applications the coded signal is transmitted in the base band (without modulation). Although this approach works, it suffers from poor efficiency because the spectrum of the transmitted code peaks at zero frequency and spreads over all frequencies. In the same time the ultrasonic transducers act

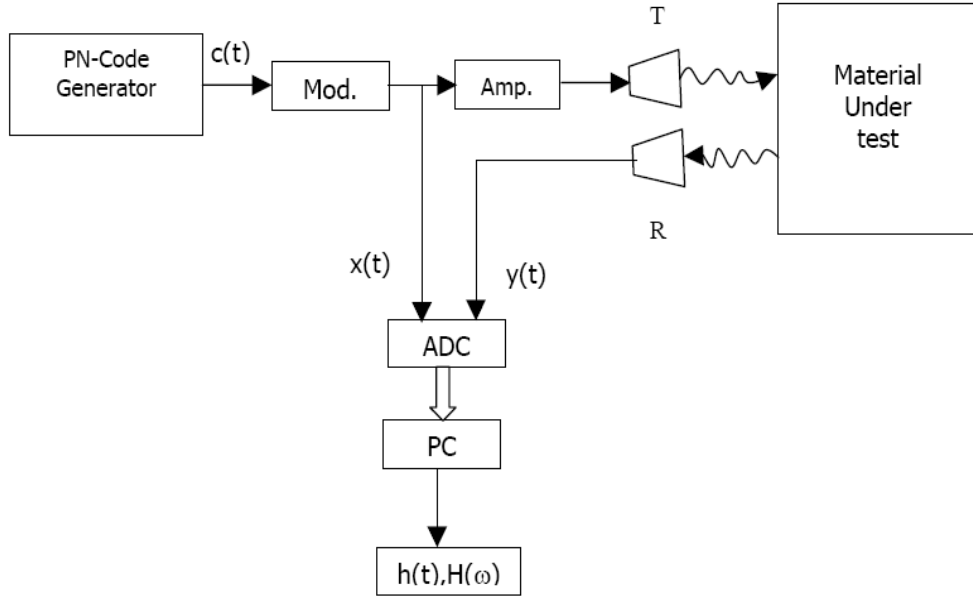


Figure 6.5: Block diagram of spread spectrum ultrasonic imaging system.

as a band-pass filter with a center frequency  $f_c$  and limited bandwidth  $BW_s$ , which means that the majority of the energy in the transmitted code cannot pass through the system. Different approaches [95] were studied to improve the coupling efficiency.

In this thesis the transmitted signal is a modulated M-sequence code with length 15 bits. The carrier frequency is selected to be equal to the center frequency  $f_c$  of the ultrasonic transducer. This will improve the coupling efficiency as indicated in Fig. 6.6. The transmitted signal can be written as:

$$x(t) = c(t) \cdot \cos(\omega_c t) \quad (6.8)$$

Where  $\omega_c = 2\pi f_c$  and  $c(t)$  is the M-sequence code with a chip rate  $f_{ch} = BW_s/2$ . The received signal can be written as:

$$y(t) = x(t) * h(t) + w(t) \quad (6.9)$$

where  $h(t)$  represents the impulse response of the system and  $w(t)$  is an additive white Gaussian noise (AWGN). The impulse response of the system can be estimated in the frequency domain using the Welch [90] Method as follow:

$$\hat{H}(f) = \frac{S_{xy}(f)}{S_{xx}(f)} = H(f) + \frac{W(f)}{X^*(f)} = H(f) + Z(f) \quad (6.10)$$

Where  $S_{xy}(f)$  is the cross power spectral density of  $x$  and  $y$ ,  $S_{xx}(f)$  is the power spectral density of  $x$ ,  $W(f)$  is the Fourier transform of  $w(t)$ ,  $\hat{H}(f)$  is the estimated system transfer function in frequency domain and  $X^*(f)$  is the complex conjugate of the Fourier transform of  $x(t)$ , which represents the inverse of the decoding matched filter. Both  $S_{xy}(f)$  and  $S_{xx}(f)$  can be calculated as follow.

$$\begin{aligned} S_{xy}(f) &= X(f)Y^*(f) = X(f)[X^*(f)H(f) + W(f)] \\ S_{xx}(f) &= X(f)X^*(f) \end{aligned} \quad (6.11)$$

As indicated in (6.10),  $H(f)$  should be recovered perfectly. However the second term in the right hand side of (6.10) means that  $X(f)$  must be prudently chosen so that the processed noise is kept as low as possible in the same time the spectrum of  $X(f)$  should not contain nulls. Unfortunately the spectrum of the M-sequence code contains nulls, which take places at multiple of the chip frequency  $f_{ch}$  of the code as indicated by Fig. 6.6. By probably choosing the chip frequency of the code these nulls will exist outside the frequency band of interest, which will not affect the reconstruction of  $H(f)$  in the frequency band of interest.

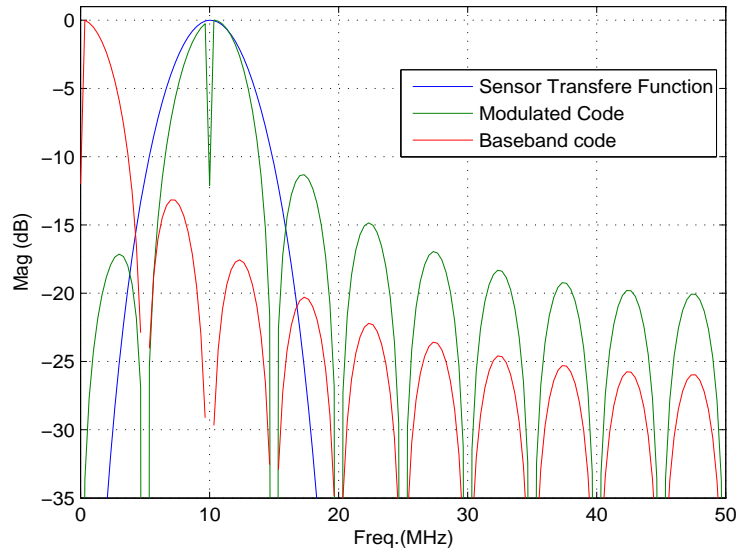


Figure 6.6: The spectrum of the baseband code and modulated code in comparison with the Transfer function of the ultrasonic sensor.

### 6.5.2 Measurement of Reflection and Transmission Coefficients

In this section we present an example for the measured reflection and transmission coefficient for the material to indicate how the spread spectrum can be used for material testing. The measurements here were done using an ultrasonic sensor, which has center frequency 40.6 KHz and bandwidth 1.6 KHz. Fig. 6.7 shows the measured reflection coefficient, upper panel represents the magnitude in dB and lower panel represents the phase in radian. Fig. 6.8 represents the obtained impulse response. This impulse response was obtained by calculating the inverse Fourier transform of

the reflection coefficients obtained in Fig. 6.7, which also can be done using chirp z-transform (CZT) to improve the accuracy of the obtained impulse response. The first peak in Fig. 6.8 represents the coupling between the transmitter and receiver sensors and the second beak due to the reflections from the material under test. Both of Fig. 6.7 and 6.8 represents A-scan mode where the x-axis in Fig. 6.8 represents the depth or the thickness of the material under test. A B-scan can be obtained by moving the sensor through one of the dimensions of the material under test.

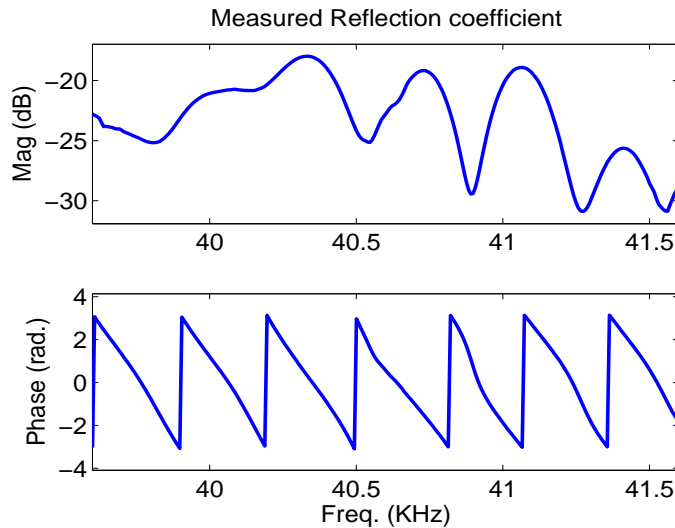


Figure 6.7: Measured reflection coefficient.

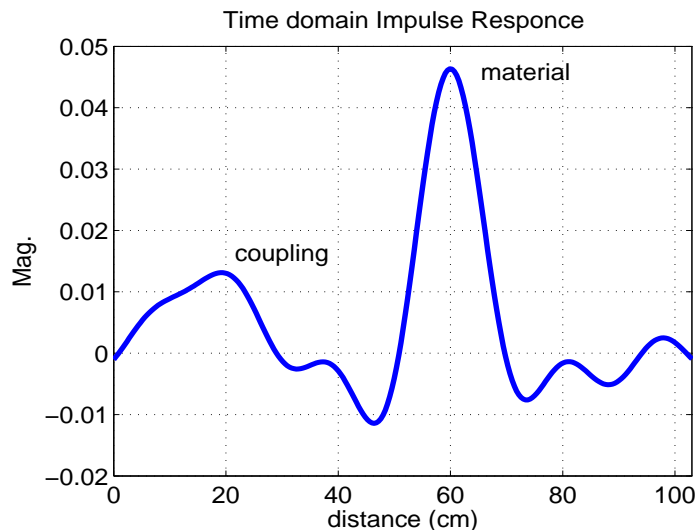


Figure 6.8: Time domain impulse response.

Fig. 6.9 represents the measured transmission coefficients in frequency domain in B-scan mode where the x-axis represents the x-dimension of the material. Fig. 6.10 indicates the measured transmission coefficients in the time domain in B-scan mode

for a material (foam), which has an internal defect. The x-axis here also represents the x-dimension of the material where the y-axis represents the thickness of the material. From Fig. 6.10 one can localize the position of the defect and also get some information about the size of this defect.

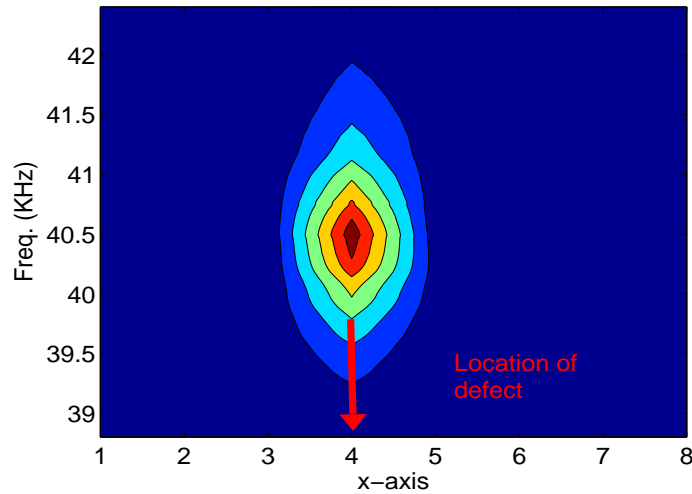


Figure 6.9: Measured transmission coefficients in frequency domain (B-Scan).

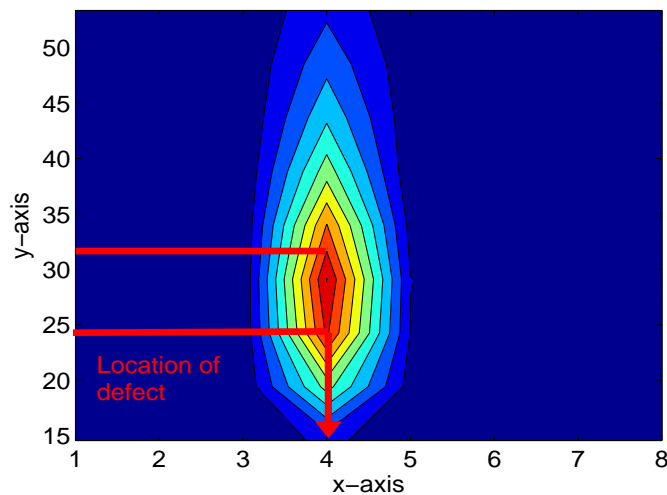


Figure 6.10: Measured transmission coefficients in time domain (B-Scan).

### 6.5.3 Time Domain Impulse Response

To obtain the compressed output pulse (the system impulse response) in the time domain conventionally the inverse Fourier transform IFT of (6.10) is calculated, using the following relation:

$$\tilde{h}(t) = \int_{f_1}^{f_2} \hat{H}(f) e^{j2\pi ft} df = \int_{-\infty}^{\infty} \hat{H}(f) P(f) e^{j2\pi ft} df \quad (6.12)$$

Where  $P(f)$  is a rectangular window in frequency domain representing the limitation in the bandwidth,  $f_1 = f_c - BW_s/2$  and  $f_2 = f_c + BW_s/2$ .  $P(f)$  can be described as follow:

$$P(f) = \begin{cases} 1 & f_1 \leq f \leq f_2 \\ 0 & otherwise \end{cases} \quad (6.13)$$

and  $p(t)$  it's inverse Fourier transform can be written as:

$$p(t) = -BW_s \cdot e^{j2\pi f_c t} \text{Sinc}(BW_s t) \quad (6.14)$$

From (6.12) we found that:

$$\tilde{h}(t) = \hat{h}(t) * p(t) = h(t) * p(t) + z(t) * p(t) \quad (6.15)$$

It is clear from (6.15) that reconstructing the system impulse response in the time domain using the conventional Fourier transform leads to great range side lobes due to the effect of the limited bandwidth of the sensor. If we neglect the effect of the ultrasonic sensor and assuming non-dispersive media then  $h(t)$  can be modeled as follow:

$$h(t) = \sum_{i=1}^L a_i \delta(t - \tau_i) \quad (6.16)$$

where  $L$  is the model order (related to the number of scatterer),  $a_i$  is the scattering coefficients and  $\tau_i$  is the propagation time. The Fourier transform of (6.16) can be written as:

$$H(f) = \sum_{i=1}^L a_i e^{j2\pi f \tau_i} \quad (6.17)$$

Substitute  $H(f)$  from (6.17) into (6.10) then (6.10) can be written as:

$$\hat{H}(f) = \sum_{i=1}^L a_i e^{j2\pi f \tau_i} + Z(f) \quad (6.18)$$

To reconstruct the system impulse response  $h(t)$  from (6.18) one needs to find the model parameters  $(L, a_i, \tau_i)$  from the available measurements  $\hat{H}(f)$  in the frequency domain. In the next section the RMUSIC algorithm will be used to determine the model parameters in (6.18).

### Model Sampling

In practical medical ultrasonic imaging we are not dealing with analog signal  $x(t)$  and  $y(t)$  instead we are dealing with a sampled version  $x(n)$  and  $y(n)$ , where  $n = 0, 1, \dots, N - 1$  and  $N = Kf_s/f_{ch}$ , is equal to the length of the measured data in time domain. The Parameter  $K$  is equal to the length of the code and  $f_s$  is the sampling frequency of the system. Equation (6.18) can be rewritten in discrete format as:

$$\hat{H}(f_m) = \sum_{i=1}^L a_i e^{j2\pi f_m \tau_i} + Z(f_m) \quad m = 0, 1, \dots, M - 1 \quad (6.19)$$

Where  $M$  is the number of points of interest in the frequency domain which can be calculated as  $M = NBW_s/f_s$  and  $f_m$  is the discrete frequency values, which can be calculated from the following relation  $f_m = f_1 + m\Delta f$  and  $\Delta f = f_s/N$ . In the same time the system impulse response in (6.16) can be rewritten in discrete format as:

$$h(t_n) = \sum_{i=1}^L a_i \delta(t_n - \tau_i) \quad n = 0, 1, \dots, M - 1 \quad (6.20)$$

Where  $t_n = n\Delta t$ , and  $\Delta t = TIS/M$ , where  $TIS$  is the time of interest where we need to observe the system impulse response in the time domain. Here we should notice that the maximum value for  $TIS$  is not equal to  $N/f_s$  as in the conventional techniques instead it is value is  $M/(2BW_s)$ . Shortly we will write  $f_m$  as  $m$ . and  $t_n$  as  $n$  in the next section.

#### 6.5.4 The Root Multiple Signal Classification (RMUSIC) Algorithm

The RMUSIC algorithm is an eigen-based subspace decomposition method for estimation of the frequencies of complex sinusoids in additive white noise. In this paper we propose using the RMUSIC algorithm to obtain the system impulse response  $h(n)$  to overcome for the problem of range side lobes results from the limited time-bandwidth product if we use the conventional Fourier transform. As we will see from the results that the RMUSIC is able to reconstruct  $h(n)$  without any range side lobes effect. The block diagram for the ultrasound system based on RMUSIC algorithm is shown in Fig. 6.11. Fig. 6.12 indicates the received coded signal (upper panel) and the decoded pulse using the RMUSIC (lower panel).

The autocorrelation matrix of the noisy spectrum of (6.18) can be written as the sum of the autocorrelation matrices of  $H(m)$  and the noise  $Z(m)$  as:

$$R_{\hat{H}\hat{H}} = R_{HH} + R_{ZZ} \quad (6.21)$$

Where  $R_{HH}$  and  $R_{ZZ} = \sigma_{ZZ}.I$  are the autocorrelation matrices of  $H$  and the noise  $Z$  respectively and  $I$  is the identity matrix.



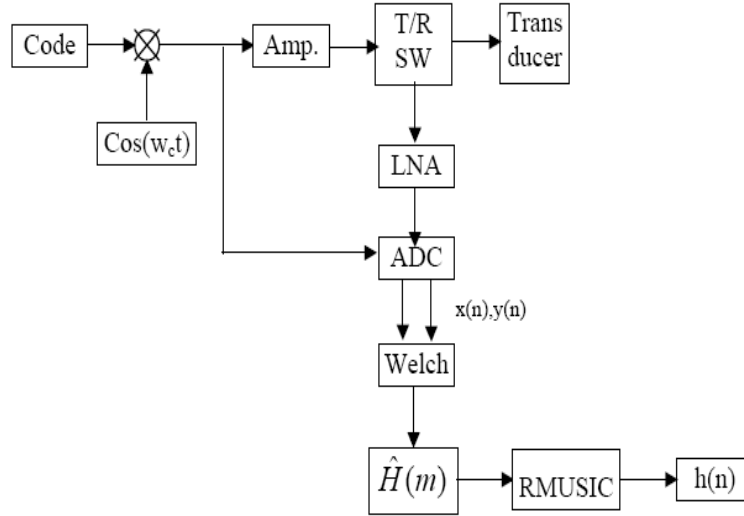


Figure 6.11: Ultrasound system block diagram with coded excitation

Now consider an eigen-decomposition of the  $M \times M$  correlation matrix in (6.21). Using singular value decomposition SVD the eigen-values and eigen-vectors can be calculated. From the eigen-values of (6.21) the order  $L$  of the model can be estimated. There are number of methods based on statistical classification criteria, which can be used to estimate  $L$  like the Minimum Descriptive Length (MDL) and Akiake Information Criteria (AIC) [155]. After separating the eigen-vectors into two subspaces signal and noise subspace. Since the signal and noise eigenvectors are orthogonal, it follows that the signal subspace and the noise subspace are orthogonal. Hence the sinusoidal signal vectors  $s_i$  which are in the signal subspace, are orthogonal to the noise subspace  $n_k$ , and we have.

$$s_i^H v_k = \sum_{m=0}^{M-1} v_k(m) e^{-j2\pi\tau_i m} = 0 \quad i = 1, \dots, L \quad k = L+1, \dots, M \quad (6.22)$$

where the vector  $s_i^H = \{1, e^{-j2\pi\tau_i}, \dots, e^{-j2\pi\tau_i(M-1)}\}$ , is the Hermitian transpose of the sinusoidal signal vectors  $s_i$ . Equation (6.22) implies that  $\tau_i$  and  $i = 1, 2, \dots, L$  can be obtained by solving for the zeros of the polynomial in (6.22). The scattering coefficients  $a_i$  can be obtained from the following relation

$$\hat{H}(m) = \sum_{i=1}^L a_i e^{j2\pi f_m \tau_i} \quad m = 0, 1, \dots, M-1 \quad (6.23)$$

The scattering coefficients  $a_i$  of the impulse response can be obtained by solving the linear system of (6.23) which can be formulated as a matrix equation.

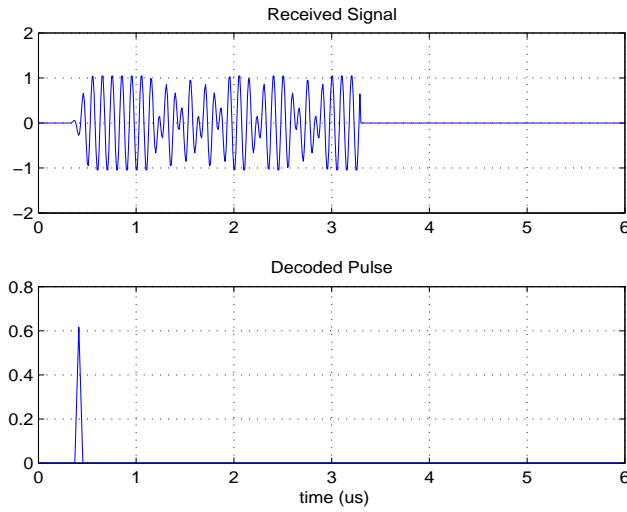


Figure 6.12: The received uncompressed pulse and the result compressed pulse (left)

### 6.5.5 Simulation Results

In this section computer simulations are given to demonstrate the validity of the proposed technique. The demonstration is performed by comparing the performance of the proposed system (realized by RMUSIC algorithm) with that of a similar system realized by matched filters on scatterer reconstruction.

In the simulation we consider a single element transducer. The work can be extended for 2-D imaging system in order to study the effect of code degradation, on the performance of the RMUSIC algorithm, result from dynamic receive focusing, time-varying delays to each channel before beam-sum.

The transducer, as a band-limited resonator, has a system transfer function that can be modeled as an  $N$ th-order Butterworth band-pass filter centered at  $f_c$  with some fractional bandwidth. Here we model it as 32-order Butterworth filter centered at 10 MHz with -3 dB bandwidth 6 MHz and -10 dB bandwidth  $BW_s=10$  MHz. Fig. 6.6 shows the transducer model frequency response. A sampling frequency,  $f_s$ , of 100 MHz has been assumed. The carrier frequency  $f_c$  was selected to be equal to 10MHz, which is equal to the center frequency of the transducer. The chip frequency of the code  $f_{ch}$  is selected to be 5 MHz, half the bandwidth. The code is selected to be M-sequence code of length 15 bits. From the above sitting we found that the length of the data in time domain is equal to  $N = 300$  samples. In the same time the number of samples in frequency domain in the frequency range of interest (from 5 MHz to 15 MHz)  $M = 30$  sample. Fig. 6.13(a)-(d) shows the excitation burst spectrum, the same spectrum passed through the system transfer function, the spectrum of the decoded result using matched filter, and the spectrum of the decoded result using RMUSIC in comparison with the spectrum of the system. Figs. 6.13(e) and (f) show the excitation burst passed through the system transfer function and the decoded

result in time domain, respectively.

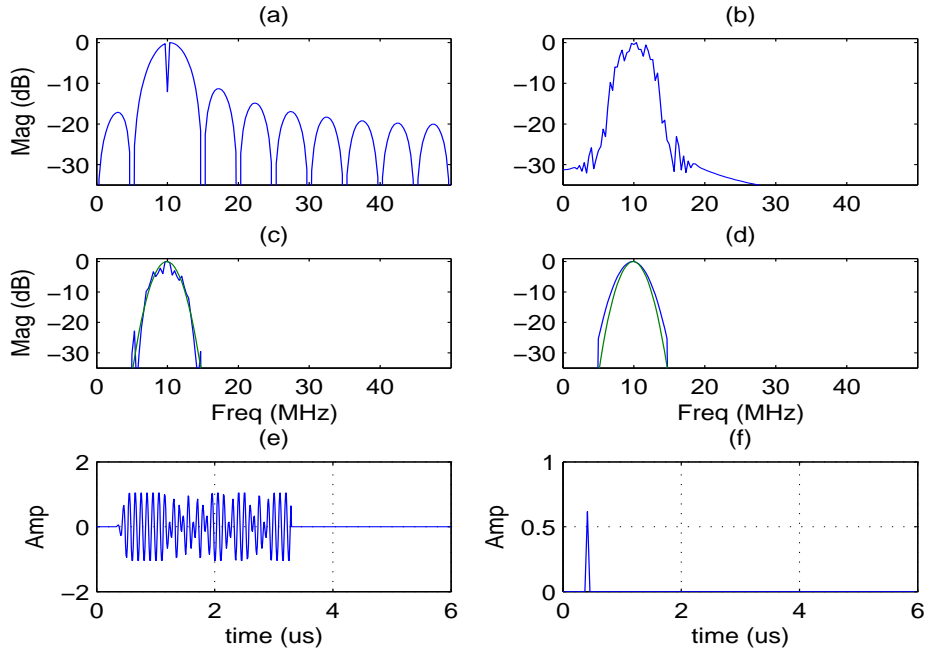


Figure 6.13: Demonstration of decoding 15-bit modulated code. (a) The spectrum of the excitation code. (b) The same spectrum passed through the system transfer function. (c) The spectrum of the decoded results using inverse filter. (d) The spectrum of the decoded results using RMUSIC. (e) Waveform of the code passed through the system transfer function. (f) The decoded waveform.

Assuming a single scatterer ( $L = 1$ ) with unit strength ( $a_1 = 1$ ) and propagation time 0.45 ms ( $\tau_1 = 0.45$  ms) is exists and no measurement noise exists. The scatterer reconstruction obtained by the RMUSIC and that obtained with matched filter implementation are compared in Fig. 6.14(a). Although the coded excitation is not ideal, the RMUSIC implementation approach can still obtain an exact reconstruction without range side lobes. To examine the effect of measurements noise on reconstruction quality a white Gaussian noise is added to the received signal. Fig. 6.14(b) shows the scatterer reconstruction by repeating the above test with SNR = 20 dB.

From Fig. 6.14(b) it's found that the RMUSIC is still able to obtain an exact reconstruction without range side lobes. We should indicate here that the actual value of the range side lobes by using RMUSIC is  $-\infty$  dB. But for the purpose of comparison in Fig. 6.14 we put it equal to -75 dB, which is equivalent to  $-\infty$  dB.

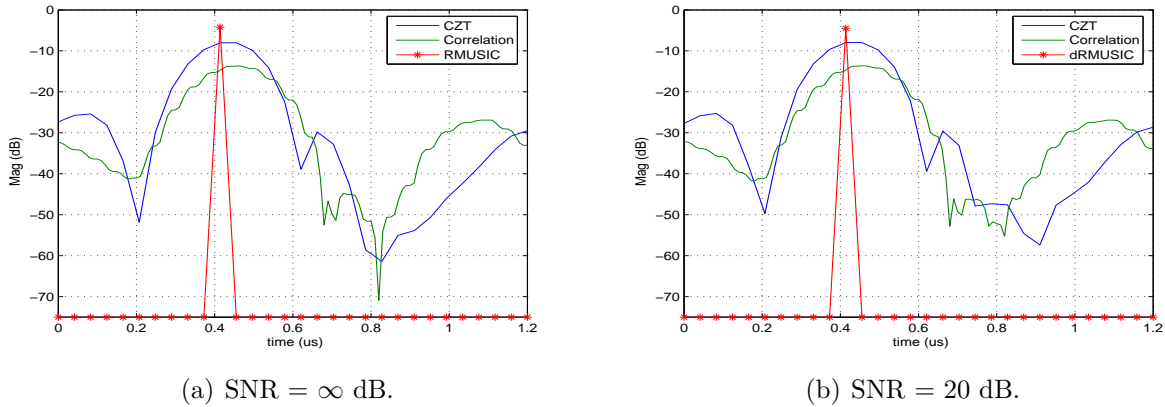


Figure 6.14: Reconstructed scatterer values using matched filter and RMUSIC.

## 6.6 Microwave Imaging

Reconstruction of permittivity profiles constitutes a major part of the electromagnetic inverse scattering problem and has been of great interest since many years because of many practical applications. The overall reconstruction process, in general, involves the measurement of scattering data such as the reflection coefficient due to an illuminating wave with known characteristics. Information about the unknown permittivity profile of the illuminated object in terms of these measured values is obtained by using some inverse techniques.

The problem arises here is the effect of limiting the measurements bandwidth on the inversion of the reflection coefficients using Fourier transform. Limiting the bandwidth leads to a side lobe effect on the inverted measurements. These side lobes can degrade the resolution of the reconstructed profile and in some cases, especially with band pass measurements, can lead to instability in the reconstruction process.

### 6.6.1 Problem Formulation

In this thesis we will discuss the reconstruction of a stratified 1-D permittivity profile. Fig. 6.15 illustrates such stratification. The profile consists of  $L + 1$  layers; each layer has a characteristic impedance  $Z_i$  and a physical length  $l_i$ , where  $i = 0, 1, 2, \dots, L$ . Assuming a TEM illumination, the characteristic impedance  $Z_i$  of  $i^{th}$  layer of the profile is given by:

$$Z_i = \frac{Z_o}{\sqrt{\epsilon_{r_i}}} \quad (6.24)$$

where  $Z_o$  is the free space characteristic impedance and  $\epsilon_{r_i}$  is the relative permittivity of the  $i^{th}$  layer. Following the small reflection theory described in [156], which implicitly means adopting the Born approximation, the total reflection coefficient  $\Gamma(\omega)$  observed outside the profile is given in the frequency domain as:

$$\Gamma(\omega) = \sum_{i=1}^L \Gamma_i e^{-j\omega\tau_i} \quad (6.25)$$

where  $\Gamma_i$  is the local reflection coefficient between the  $(i-1)^{st}$  and the  $(i)^{th}$  layer and  $\tau_i$  is twice the time delay due to the first  $(i-1)$  layers. Both of  $\Gamma_i$  and  $\tau_i$  are given by:

$$\Gamma_i = \frac{Z_i - Z_{i-1}}{Z_i + Z_{i-1}} = \frac{\sqrt{\varepsilon_{r_{i-1}}} - \sqrt{\varepsilon_{r_i}}}{\sqrt{\varepsilon_{r_{i-1}}} + \sqrt{\varepsilon_{r_i}}} \quad (6.26)$$

$$\tau_i = \frac{2}{c_0} \sum_{m=0}^{i-1} l_m \sqrt{\varepsilon_{r_m}} \quad i = 1, 2, \dots, L \quad (6.27)$$

where  $c_0$  is the speed of light in free space.

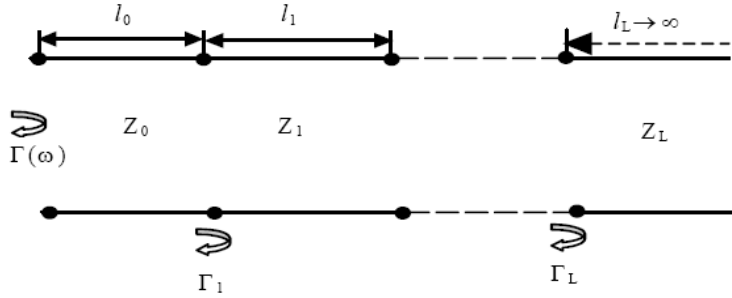


Figure 6.15: 1-D permittivity profile.

Assuming frequency independent local reflection coefficients within the frequency range of measurements, the total reflection coefficient can be written in a virtual time domain as:

$$h(t) = \sum_{i=1}^L \Gamma_i \delta(t - \tau_i) \quad (6.28)$$

where  $h(t)$  is the inverse Fourier transform of  $\Gamma(\omega)$ , which can be treated as the impulse response of the profile. The impulse response in (6.28) is based on infinite observation bandwidth of the total reflection coefficient in the frequency domain. In practical situations the measured reflection coefficient is available only within a limited bandwidth. The effect of such a spectral limitation is investigated in the following section.

### 6.6.2 Impact of Limited Bandwidth

In practical situations the measured reflection coefficient  $R(\omega)$  is available within a certain limited bandwidth. Let us assume that the measurements start at a frequency

$\omega_{st}$  and stop at a frequency  $\omega_{sp}$  with a measurement bandwidth  $B$ , where  $B = \omega_{sp} - \omega_{st}$ . The inversion of the measured reflection coefficient using the conventional Fourier transform can be written as:

$$\begin{aligned} r(t) &= \frac{1}{2\pi} \int_{\omega_{st}}^{\omega_{sp}} R(\omega) e^{j\omega t} d\omega \\ &= \frac{1}{2\pi} \int_{-\infty}^{\infty} \Gamma(\omega) W(\omega) e^{j\omega t} d\omega \end{aligned} \quad (6.29)$$

where  $r(t)$  is the inverse Fourier transform of  $R(\omega)$  and  $W(\omega)$  is a rectangular window that represents the limitation in the bandwidth, and is given by:

$$W(\omega) = \begin{cases} 1 & \omega_{st} \leq \omega \leq \omega_{sp} \\ 0 & otherwise \end{cases} \quad (6.30)$$

From the properties of the Fourier transform, (6.29) can be written as:

$$r(t) = h(t) * w(t) \quad (6.31)$$

where the  $*$  denotes convolution and  $w(t)$  is the inverse Fourier transform of the rectangular window function in (6.30), which can be written as:

$$w(t) = B e^{j\omega_o t} \text{sinc}(Bt) \quad (6.32)$$

where  $\omega_o$  is the center frequency of the measurements:

$$\omega_o = \omega_{st} + \frac{B}{2} \quad (6.33)$$

The convolution in (6.31) leads to a side lobe effect which can degrade the resolution of the reconstruction especially when we have a strong local reflection coefficient followed by a weak one (for low contrast profiles this will take place at the initial interface). In the next section, the super resolution technique is applied to determine the exact impulse response  $h(t)$  of the profile using the measured reflection coefficient  $R(\omega)$ .

### 6.6.3 Super Resolution Techniques

As has been mentioned before the super resolution root multiple signal classification algorithm has been used in communication engineering to estimate the time of arrival of the signal. Both (6.25) and (6.28) resemble the same pair of Fourier transforms as used in time of arrival detection. In both cases the exact impulse response in (6.28) is determined by estimating the parameters of the model in (6.25), namely  $L$ ,  $\Gamma_i$  and  $\tau_i$ , using the measured reflection coefficient  $R(\omega)$ . The accuracy of the estimation depends basically on that of the measurements. The latter is determined by the available signal-to-noise ratio and dynamic range of the measuring equipment.

A super resolution technique is therefore an application of the well-known tradeoff between the bandwidth and the signal-to-noise ratio.

### Discretization of The Problem

In practical situations we are not able to measure continues frequency responses, instead we can measure the reflection coefficient at discrete frequency steps. Discretizing (6.25) results in:

$$\Gamma(\omega_k) = \sum_{i=1}^L \Gamma_i e^{-j\omega_k \tau_i}, \quad 0 \leq k \leq M-1 \quad (6.34)$$

where  $\omega_k$  are the discrete frequency values ( $\omega_{st} \leq \omega_k \leq \omega_{sp}$ ) and  $M$  is the number of measured frequency points. For equidistant measurements,  $\omega_k$  is given by

$$\omega_k = \omega_{st} + k \frac{B}{M-1} \quad (6.35)$$

For a simpler appearance of the equations, we replace  $\Gamma(\omega_k)$  by  $\Gamma(k)$ .

### The Root Multiple Signal Classification Algorithm

In this subsection we will explain how the root multiple signal classification algorithm is used to estimate the model parameters ( $L, \Gamma_i, \tau_i$ ) using the measured reflection coefficient  $R(\omega)$ , which is identical to  $\Gamma(\omega)$  within the frequency range of interest. In order to take measurement noise into account, we allow for additive white Gaussian noise with frequency-domain sampling values  $Z(k)$  and variance  $\sigma^2$ . The measured noisy reflection coefficient in the frequency domain  $\hat{R}(k)$  is then given by

$$\begin{aligned} \hat{R}(k) &= R(k) + Z(k) = \Gamma(k) + Z(k) \\ &= \sum_{i=1}^L \Gamma_i e^{-j\omega_k \tau_i} + Z(k) \end{aligned} \quad (6.36)$$

The correlation matrix of the noisy reflection coefficient can be calculated from the following relation:

$$C_{\hat{R}}(i, j) = \frac{1}{M} \sum_{k=1}^M \hat{R}(k-i) \hat{R}(k-j) \quad (6.37)$$

where  $i, j = 1, 2, \dots, P$  and  $P$  is the maximum lag for the correlation matrix ( $2L < P < M$ ) (see, e.g. [91]). As the reflection coefficient is available only for  $0 \leq k \leq M$ , we need to modify (6.37) to take into account the effect of the limited number of available samples. Then (6.37) should be modified as:

$$C_{\hat{R}}(i, j) = \frac{1}{N} \sum_{k=\min(i,j)}^{M-\max(i,j)} \hat{R}(k-i) \hat{R}(k-j) \quad (6.38)$$

where  $\min(i, j)$  and  $\max(i, j)$  mean minimum and maximum value of  $i$  and  $j$ , respectively, and  $N = M - [\max(i, j) + \min(i, j)]$ . Assuming uncorrelated noise, the correlation matrix of the noisy reflection coefficient can be written as:

$$[C_{\hat{R}}] = [C_R] + [C_Z] \quad (6.39)$$

where  $C_R$  is the correlation matrix of the noise-free reflection coefficient and  $C_Z$  is the correlation matrix of the noise. Making use of (6.36) and the fact that independent noise samples are uncorrelated, the correlation matrix of the noise-free reflection coefficient can be written as:

$$[C_R] = \sum_{i=1}^L S_i S_i^H \Gamma_i^2 \quad (6.40)$$

where  $S_i^H = [e^{-j\omega_0\tau_i}, e^{-j\omega_1\tau_i}, \dots, e^{-j\omega_{P-1}\tau_i}]$  is the Hermitian transpose of the column vector  $S_i$ .

An eigenvalue decomposition of the correlation matrix of the noisy reflection coefficient can be expressed as:

$$[C_{\hat{R}}] = \sum_{i=1}^P V_i V_i^H \lambda_i \quad (6.41)$$

where  $V_i$  and  $\lambda_i$  are the eigenvectors and eigenvalues of the correlation matrix, which can be obtained using a singular value decomposition (SVD). The eigenvectors and eigenvalues of the correlation matrix of the noisy reflection coefficient can be partitioned into two disjoint subsets. The set of eigenvectors  $V_1, V_2, \dots, V_L$  associated with the  $L$  largest eigenvalues span the signal subspace and are called the principle eigenvectors. The second subset of eigenvectors  $V_{L+1}, \dots, V_P$  span the noise subspace and have  $\sigma^2$  as their eigenvalues.

$$[C_{\hat{R}}] = \sum_{i=1}^L V_i V_i^H \lambda_i + \sigma^2 \sum_{i=L+1}^P V_i V_i^H \quad (6.42)$$

Since the signal and noise eigenvectors are orthogonal [91], it follows that the signal subspace and the noise subspace are orthogonal. Hence the signal vectors  $S_i$  which belong to the signal subspace, are orthogonal to the noise subspace. This results in

$$S_i^H V_m = \sum_{k=0}^{P-1} V_{mk} e^{-j\omega_k \tau_i} = 0 \quad (6.43)$$

where  $i = 1, 2, \dots, L, m = L+1, \dots, P$ , and  $V_{mk}$  is the  $k^{\text{th}}$  element of  $V_m$ . The time delays  $\tau_i$  can be estimated by calculating the roots of the polynomial in (6.43). Estimation



values for the local reflection coefficients can be obtained by solving the following equation:

$$\hat{\mathbf{R}} = [S] \cdot \hat{\mathbf{A}} \quad (6.44)$$

where  $\hat{\mathbf{R}}$  is an  $M$ -element column vector containing the measured frequency domain samples of the reflection coefficient,  $[S]$  is an  $(M \times L)$  matrix, and  $\hat{\mathbf{A}}$  is an  $L$ -element column vector containing the  $L$  estimates for the local reflection coefficients. Both  $\hat{\mathbf{R}}$ ,  $[S]$  and  $\hat{\mathbf{A}}$  have the following forms:

$$\hat{\mathbf{R}} = [\hat{R}(0), \hat{R}(1), \dots, \hat{R}(M-1)]^T \quad (6.45)$$

$$\hat{\mathbf{A}} = [\hat{\Gamma}_1, \hat{\Gamma}_2, \dots, \hat{\Gamma}_L]^T \quad (6.46)$$

$$S = \begin{bmatrix} e^{-j\omega_0\tau_1} & e^{-j\omega_0\tau_2} & \dots & e^{-j\omega_0\tau_L} \\ e^{-j\omega_1\tau_1} & e^{-j\omega_1\tau_2} & \dots & e^{-j\omega_1\tau_L} \\ \vdots & \vdots & \vdots & \vdots \\ e^{-j\omega_{M-1}\tau_1} & e^{-j\omega_{M-1}\tau_2} & \dots & e^{-j\omega_{M-1}\tau_L} \end{bmatrix} \quad (6.47)$$

In the next section, an iterative algorithm to reconstruct the permittivity profile in the spatial domain using the inverted time-domain reflection coefficient is proposed.

#### 6.6.4 Reconstructing Permittivity Profiles

Equation (6.26) gives the relation between the local reflection coefficients and the relative permittivity of the different layers. It can be rewritten as:

$$\varepsilon_{r_i} = \varepsilon_{r_{i-1}} \left( \frac{1 - \Gamma_i}{1 + \Gamma_i} \right)^2, \quad i = 1, \dots, L, \quad \varepsilon_{r_0} = 1 \quad (6.48)$$

On the other hand, the physical length of the stratification layers is obtained using (6.27):

$$l_{i-1} = \frac{1}{2} c_0 \frac{\tau_i - \tau_{i-1}}{\sqrt{\varepsilon_{r_{i-1}}}}, \quad i = 1, \dots, L, \quad \tau_0 = 0 \quad (6.49)$$

The recursive relations in (6.48) and (6.49) can be used to reconstruct the relative permittivities (or simply permittivities from now on) and lengths of the stratification layers. The block diagram in Fig. 6.16 shows the steps of applying the root multiple signal classification algorithm to reconstruct the permittivity profile.

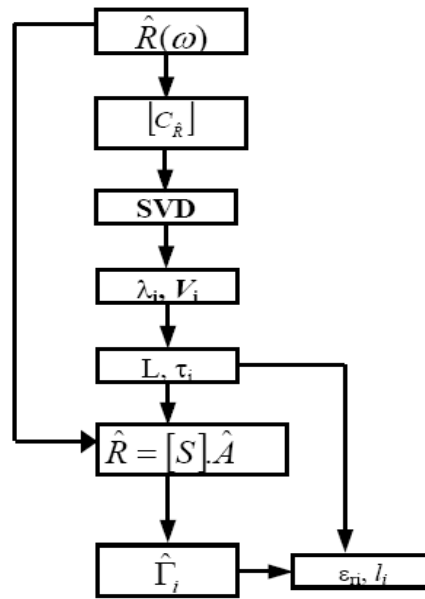


Figure 6.16: Block diagram for reconstructing permittivity profile using the root multiple signal classification algorithm.

### 6.6.5 Experimental Results

In this section the proposed technique is verified experimentally. At microwave frequencies, the reflection coefficient data are generally measured using a vector network analyzer (VNA). Fig. 6.17 shows the setting of the experimental measurements in our laboratory. A coaxial airline is used as a holder for the stratification. The small samples of the dielectric material under test are machined precisely to fill the cross-section of 20 cm coaxial airline. The two ports of the airline are connected to the VNA. A full two-ports calibration has been achieved using the Open-Short-Match-Thru method. The effect of any possible mismatches at either side of the airline has been therefore taken into account, so that the two air-filled end-layers can be considered matched (or equivalently, infinitely extended).

The reflection coefficient data in our case have been measured from  $\omega_{st}/2\pi = 1$  GHz to  $\omega_{sp}/2\pi = 10$  GHz with a number of frequency points  $M = 801$  using the Anritsu 37347A VNA. We have taken two different lossless dielectric samples, whose permittivities are known and are almost constant over the measured frequency range. Table 6.1 shows the nominal parameters of the materials under test. The lengths have been optically measured, while the permittivities were obtained from the data sheets of the manufacturer.

The Measurements were carried out for three different stratifications. In the first two tests each material was tested individually, using a three-layer stratification (air-dielectric-air). In the third test the two materials were cascaded giving rise to a 4-layer stratification (air-dielectric-dielectric-air). Fig. 6.18 shows a longitudinal section of

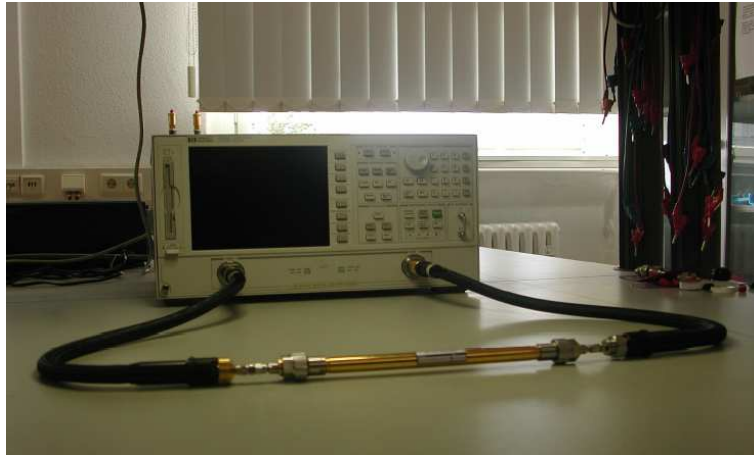


Figure 6.17: The measurements setup using the coaxial airline and the vector network analyzer.

Material	Length	$\epsilon_r$
Teflon	40 mm	2.04
PVC	30 mm	2.65

Table 6.1: Parameters of the materials under test.

the coaxial airline indicating the position of the material(s) under test inside the coaxial airline, where  $x_t$  in the figure is the length of the coaxial airline.

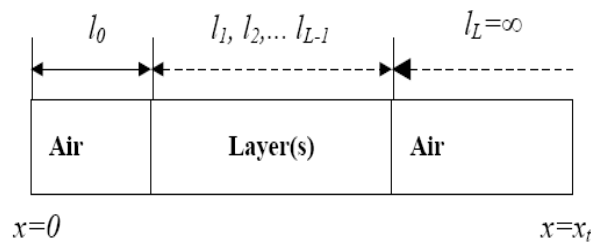


Figure 6.18: Cross-section of the coaxial airline.

Figs. 6.19-6.21 show a comparison between the measured complex reflection coefficient (solid line) and that obtained according to the super resolution model, (using Equation 6.34), (dashed line) for the Teflon (polytetrafluoroethylene), PVC, and Teflon-PVC samples, respectively. It is clear that there is an excellent match between the measured reflection coefficient and that obtained using the super resolution model.

Figs. 6.22-6.24 show a comparison between the inverted reflection coefficient using the chirp Z-transform (dashed line) and that obtained using the root multiple signal classification algorithm in conjunction with (6.28) (solid line) for the Teflon, PVC,

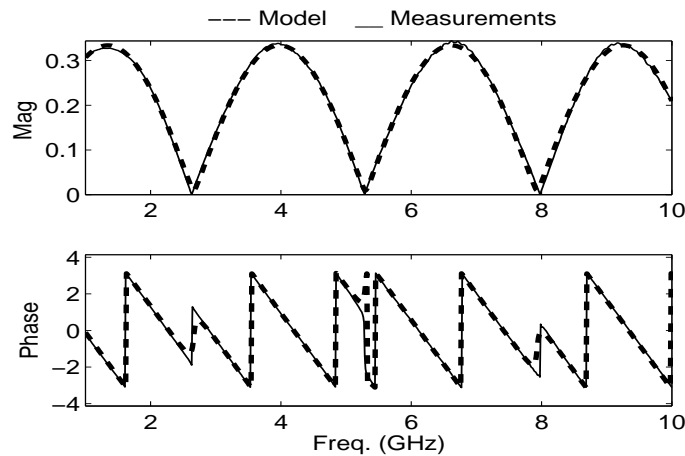


Figure 6.19: Reflection coefficient for the Teflon sample.

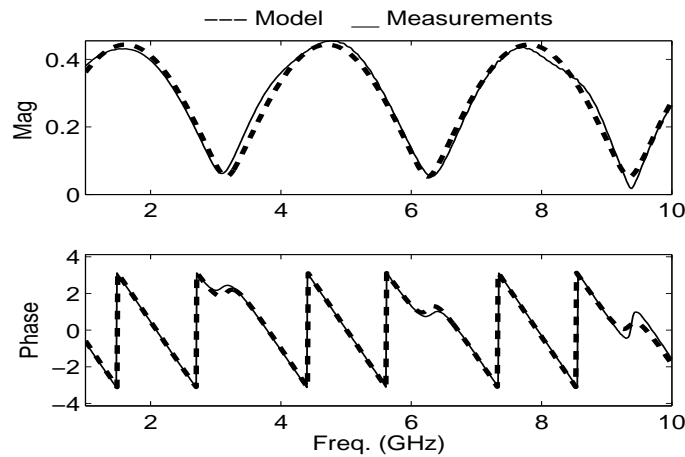


Figure 6.20: Reflection coefficient for the PVC sample.

and Teflon-PVC samples, respectively. For the inverted reflection coefficient using the chirp Z-transform the measured data were multiplied by a Gaussian window to reduce the effect of the side lobes (Gaussian window has much less side lobes than the default rectangular window). It is readily proved that the inverted reflection coefficient is proportional to the spatial derivative ( $-\frac{d}{dx}$ ) of the permittivity profile [106]. It is clear that the root multiple signal classification is able to invert the measured reflection coefficients with a much higher resolution. The resolution of the chirp Z-transform is limited by the width of the main lobe of the Gaussian window, which is dictated by the measurement bandwidth  $B$ .

Figs. 6.25-6.27 show the reconstructed permittivity profiles using the root multiple signal classification algorithm for the Teflon, PVC, and Teflon-PVC samples, respectively which resemble the actual profiles nearly perfectly.

Table 6.2 shows the reconstructed permittivities and lengths for the above three cases. Comparing the nominal values in Table 6.1 with the measured ones in Table

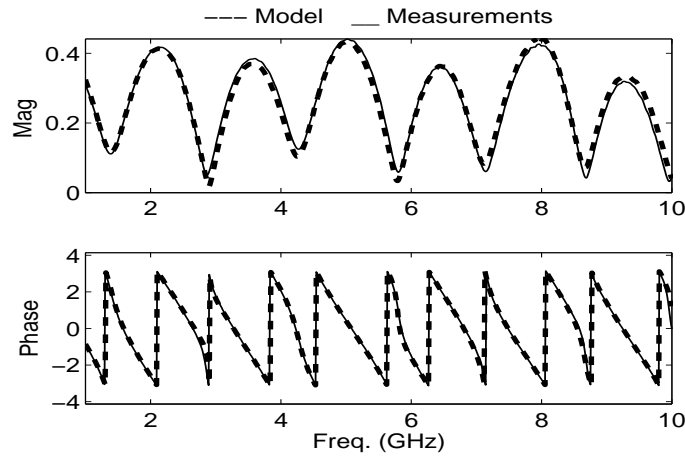


Figure 6.21: Reflection coefficient for the Teflon-PVC samples.

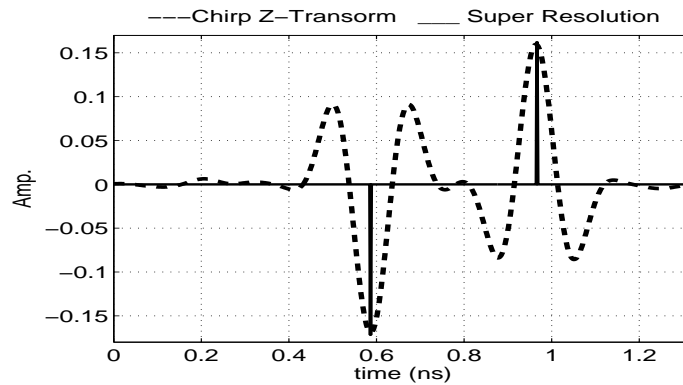


Figure 6.22: Inverted reflection coefficient for the Teflon sample.

6.2, it is clear that the proposed algorithm is able to reconstruct the permittivity for different materials with a maximum error of about 7.6 %. At the same time the maximum error in measuring the length of the samples is about 3 %. The error in reconstructing the permittivity of the Teflon is smaller than that of PVC. The reason for this difference is that we have assumed lossless dielectric materials, while both materials possess some dielectric losses. Such losses generally cause a proportional uncertainty (error margin) in the determination of the nominal permittivity value (which is usually done using resonant structures).

Profile	$\epsilon_r$			Length (mm)				
	1.0	2.01	1.04	88.2	40.2	$\infty$		
A-T-A	1.0	2.01	1.04	88.2	40.2	$\infty$		
A-P-A	1.0	2.76	1.25	103	29.1	$\infty$		
A-T-P-A	1.0	2.01	2.45	0.96	73.3	40.1	30.5	$\infty$

Table 6.2: Quantitative results of the reconstruction using root multiple signal classification algorithm A (Air), T (Teflon), and P (PVC).

The losses (and hence the permittivity error margin) of the Teflon sample are

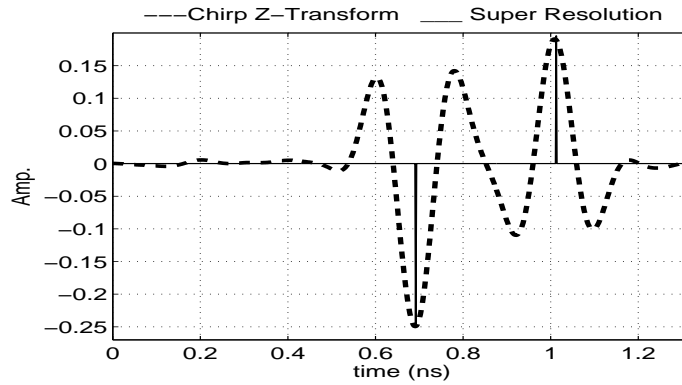


Figure 6.23: Inverted reflection coefficient for the PVC sample

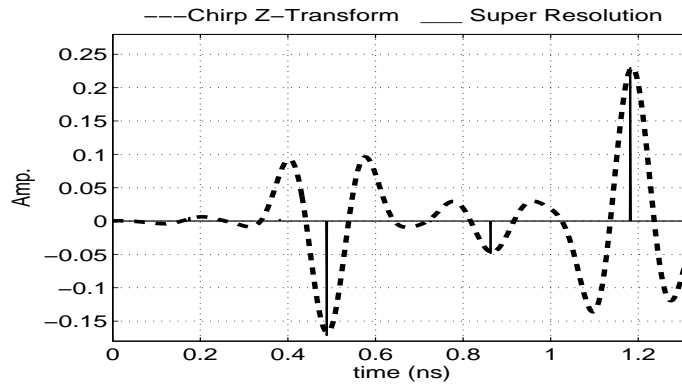


Figure 6.24: Inverted reflection coefficient for the Teflon-PVC samples.

smaller than that of the PVC. This explanation can be justified by comparing Figs. 6.22 and 6.23. In Fig. 6.22 (A-T-A) the two local reflections are nearly equal in magnitude but have different signs. On the other hand, the two local reflection coefficients in Fig. 6.23 (A-P-A) are not equal in magnitude due to the higher losses in the PVC sample. The difference between the magnitudes of such local reflection coefficients can therefore be used to estimate the material losses. This issue is being currently investigated. The large error (25 %) in the reconstructed permittivity of the last ( $L^{\text{th}}$ ) layer in Fig. 6.26 compared to both Fig. 6.25 and 6.27 can be attributed to the multiplicative accumulation of the errors in the reconstructed permittivity as being given by (6.48), which may be either constructive (strengthening) or destructive (weakening). In Fig. 6.26 the reconstructed permittivity of the  $(L - 1)^{\text{st}}$  layer (PVC) is larger than its nominal value. At the same time the losses in this layer leads to a smaller value for  $\Gamma_L$  (compared with the lossless case), combining these two effects leads to a constructive error accumulation in the reconstructed permittivity of the RHS air-filled layer in Fig. 6.26. On the other hand the reconstructed permittivity of the PVC layer in Fig. 6.27 is less than its nominal value. This leads to a destructive error accumulation in the reconstructed permittivity of the corresponding RHS air-filled layer.

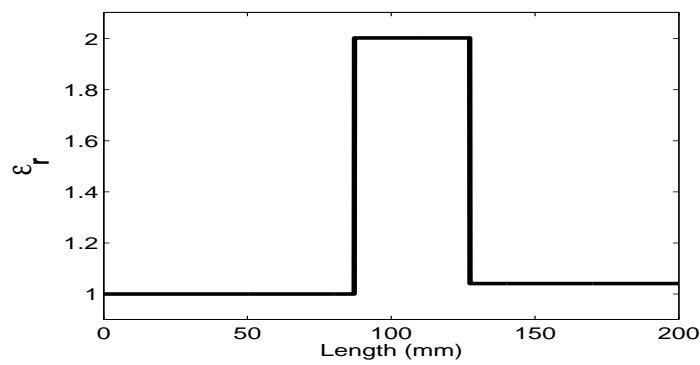


Figure 6.25: Reconstructed permittivity profile for Air-Teflon-Air.

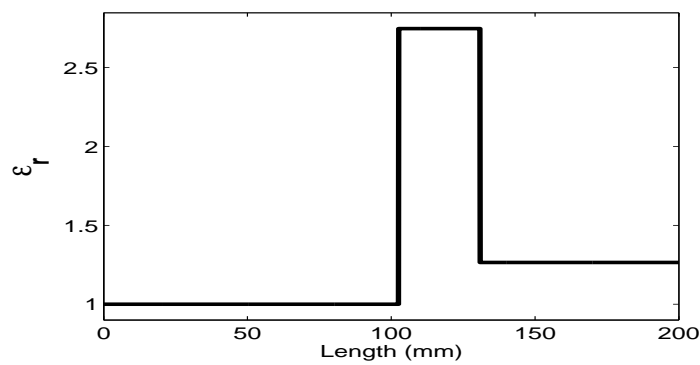


Figure 6.26: Reconstructed permittivity profile for Air-PVC-Air.

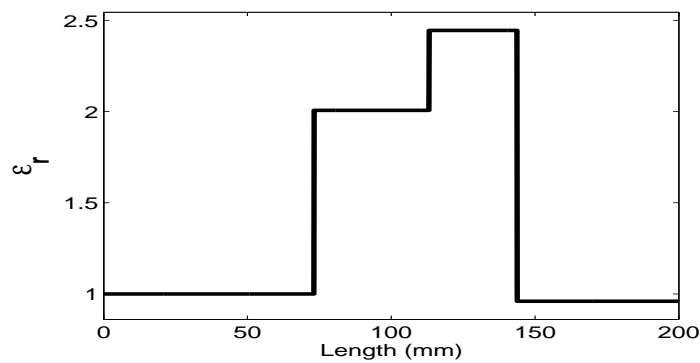


Figure 6.27: Reconstructed permittivity profile for Air-Teflon-PVC-Air.

# Chapter 7

## Conclusion and Future Work

Three different applications for the spread spectrum technique have been presented in this thesis. The associated problems with these applications have been investigated. To overcome these problems, different solutions have been presented. The validity of the proposed solutions have been verified by different simulations and measurements. Many improvements have been obtained after applying the the proposed solutions.

### 7.1 Spread Spectrum Automotive Radar

The automotive radar is considered as an important part for the intelligent transport systems (ITS), which promise spectacular improvements in road traffic safety and transportation efficiency. ITS are under active development worldwide as means of reducing loss of life and limiting economic and environmental costs. In the automotive radar application we are much interested in the digital signal processing part. Using the sliding correlation processing technique, we were able to measure the distance quite precisely. Additionally, by counting the number of zero crossing in the beat signal we were able to measure the velocity faster and more accurate than the conventional method . The proposed system is very simple to implement and the components used in it are commercially available. Also a method for implementing the shifting of the PN code, which we call it fraction of chip shifting method, has been proposed. The proposed technique leads to increasing the accuracy in measuring the target range without increasing the required bandwidth. Furthermore a variable accuracy can be achieved which is considered as an important requirement to switch the radar system from the detection phase to the tracking phase. To reduce the required transmitted power of the automotive radar an algorithm for denoising RF radar pulses has been described. The proposed algorithm combines two powerful tools; the wavelet packet transform and higher-order-statistics. The proposed algorithm is able to detect and well localize RF radar pulses without a prior knowledge of the pulse parameters (e.g., its frequency and duration). The proposed algorithm has been tested for SNR down to -24 dB and proved to work successfully. Using



such a technique in electromagnetic wave radar lead to a reduction on the required microwave power supplied to the radar or extending the detection range of the radar.

The work presented here in the automotive radar application consider only a single target situation. In the more practical situations this kind of radar is used in the existence of multi target. This means that the presented work need to be extended to consider the multi target situations, which will need the usage of antenna array systems for target identification in multi lane situations.

## 7.2 Spread Spectrum Ultrasonic Location System

Many mobile applications can be greatly enhanced when provided with the locations of people and devices. Indoor ultrasonic positioning system provide fine-grained position data for such applications. A real-time positioning technology that can operate indoors with sub-cm accuracy, and low cost is the ultimate goal for many researchers. In this thesis, we have proposed a spread spectrum ultrasonic location system using narrowband commercially available ultrasonic transducers. Using such sensors can reduce the cost of the system. At the same time it can be used as mobile tag due to the small size and the low power required for the transmitter. The desirable property of ultrasonic location system is that they have the capability to be fine-grained, meaning they can estimate location with a high degree of resolution. This is because the speed of ultrasound in air is sufficiently slow to allow the time-of-arrival of a signal to be accurately measured between a fixed unit in the environment and a mobile unit functioning as a tag on a person or object. The use of spread spectrum in ultrasonic location system allows the system to work in noisy environments. At the same time it solves the problem of signal collisions when more than one transmitter transmit at the same time. The experiments show that the proposed system is able to locate the 2D position (real-time) of a moving target within an accuracy of 0.5 cm with an update rate 300 ms (252 ms for signal capturing through the data acquisition card DAQ and 48 ms for signal processing and plotting). Most of the existing ultrasonic transducers have a limited bandwidth, which leads to a poor resolution in locating the position of a target due to multi-path reflections from the surroundings. The proposed system in this thesis solves the problem of limitation in ultrasonic transducers bandwidth by applying the RMUSIC super resolution technique to estimate the time of arrival of ultrasonic signals. Simulations and measurements have been done to indicate the great improvements in the system resolution due to applying super resolution technique.

As an extension to the current work still some points need to be discussed like.

1. The effect of increasing the number of users (transmitters), which will need to utilize PN codes with long lengths. The corresponding impact on the performance of the system (update rate of the system) should be investigated.

2. The effect of applying the RMUSIC in the complication and update rate (due to the required extra processing time) of the system specially with the existence of multi transmitter.

### **7.3 Ultrasonic and Microwave Imaging**

The fields of ultrasonic and microwave imaging are very broad, interdisciplinary ones, that play a critical role in assuring that structural components and systems perform their function in a reliable and cost effective fashion. NDT technicians and engineers define and implement tests that locate and characterize material conditions and flaws that might otherwise cause planes to crash, reactors to fail, trains to derail, pipelines to burst, and a variety of less visible, but equally troubling events. These tests are performed in a manner that does not affect the future usefulness of the object or material. Coded excitation is a powerful tool for the NDT system developer. In this thesis, we have presented a coded excitation approach based on spectrum inversion with using the RMUSIC algorithm that can provide good SNR gain while simultaneously producing no range side lobes for small time bandwidth product. We presented simulation results to demonstrate the validity of the proposed technique in removing the range side lobes for different ranges of SNR.

Further studies are needed to investigate the effect of code degradation result from frequency dependent attenuation, dynamic focusing, and nonlinear propagation on the quality of the algorithm.

Also, we have presented a new application for the super resolution technique RMUSIC in the field of microwave imaging. An iterative algorithm has been presented to reconstruct the relative permittivity of a profile using the relation between the local reflection between the layers and their relative permittivity. The quality of the algorithm has been verified by different measurements. A good agreement has been found between the original and reconstructed profiles.

The materials used here in testing the RMUSIC algorithm are lossless materials. As an extension to the work the algorithm need to be tested in more realistic situations using some lossy materials. The difference between the magnitudes of the successive local reflection coefficient can therefore be used to estimate the material losses. This issue need to be investigated.

# Bibliography

- [1] R. A. Scholz, "The origins of spread-spectrum communications," *IEEE Trans. On Comm.*, vol. COM-30, pp. 822–854, May 1982.
- [2] R. C. Dixon, "Spread spectrum techniques," IEEE Press, New York, Tech. Rep., 1976.
- [3] R. A. Dillard and G. M. Dillard, *Detectability of Spread-Spectrum Signals*. Boston. London: Artch House, 1989.
- [4] R. C. Dixon, *Spread Spectrum System*, 3rd ed. New York: Wiley, 1994.
- [5] H. Taub and D. L. Schilling, *Principles of communication systems*. New York: McGraw-Hill, 1986.
- [6] S. Haykin, *Communication systems*, 4th ed. New York: Wiley, 2001.
- [7] W. E. Kock, *Radar, Sonar, and Holography*. New York: Academic Press, 1973.
- [8] M. I. Skolnik, *Introduction to radar systems*, 3rd ed. New York: McGraw-Hill, 2001.
- [9] A. W. Rihaczek, *Principles of High-Resolution Radar*. Boston. London: Artch House, 1996.
- [10] R. Tanner and J. Woodard, *WCDMA - Requirements and Practical Design*. Chichester, West Sussex: Wiley, 2004.
- [11] D. Williams, "Millimeter wave radars for automotive applications," vol. 2. Albuquerque New Mexico: IEEE MTT-S International Microwave Symposium, June 1992, pp. 721–724.
- [12] K. W. Change and H. Wang, "Forward-looking automotive radar using a w-band single-chip transceiver," *IEEE Transactions on microwave theory and techniques*, vol. 43, no. 7, pp. 1659–1668, July 1995.
- [13] L. Raffaelli, "Millimeter-wave automotive radars and related technology." IEEE MTT-S International Microwave Symposium, 1996, pp. 35–38.

- 
- [14] R. Dixit, "Radar requirements and architecture trades for automotive applications," *IEEE MTT-S International Microwave Symposium*, 1997.
- [15] R. H. Rasshofer and E. M. Bieble, "A low cost w-band multi-beam doppler radar for automotive applications." *IEEE MTT-S International Microwave Symposium*, June 1997, pp. 971–974.
- [16] M. E. Russell, "Millimeter-wave radar sensor for automotive intelligent cruise control (icc)," *IEEE Transactions on microwave theory and techniques*, vol. 45, no. 12, pp. 2444–2453, December 1997.
- [17] R. Schneider and J. Wenger, "System aspects for future automotive radar." *IEEE MTT-S International Microwave Symposium*, 1999, pp. 1–4.
- [18] A. G. Stove, "Automotive radar at 80-90 ghz," vol. 2. Albuquerque, New Mexico: *IEEE MTT-S International Microwave Symposium*, June 1992, pp. 613–616.
- [19] J. Detlefsen, T. Troll, M. Rozman, and W. Zeilinger, "System aspects and design of an automotive collision warning pn code radar using wave front reconstruction," vol. 2. Albuquerque, New Mexico: *IEEE MTT-S International Microwave Symposium*, June 1992, pp. 625–628.
- [20] H. Groll, J. Detlefsen, M. Rozmann, and T. Troll, "Anticollision car radar in the mm-wave range with pseudo-noise-code modulation and digital angle evaluation." Poland: *International Conference MIKON*, May 1994, pp. 37–44.
- [21] W. Mezel, J. Buechler, and J. Taech, "An experimental 24 ghz radar using phase modulation spread spectrum techniques." Amsterdam: *28th European Microwave Conference*, 1998, pp. 56–60.
- [22] S. Nishikawa and H. Endo, "Applications of millimeter-wave sensors in its," *Furukawa Review*, no. 18, 1999.
- [23] M. Watanabe and K. Okazaki, "An obstacle sensing radar system for a railway crossing application: A 60 ghz millimetre wave spread spectrum radar." *IEEE MTT-S International Microwave Symposium*, June 2002.
- [24] S. Lindenmeier, S. Mayer, and D. Knopfle, "Communicating near range sensor system for automotive application." *IEEE MTT-S International Microwave Workshop*, June 2000.
- [25] H. Groll, J. Detlefsen, M. Rozmann, and T. Troll, "Car avoidance radar using mm-waves with pn-code modulation and digital collision wave front reconstruction." New Delhi, India: *Proc. 4th International Symposium on Recent Advances in Microwave Technology (ISRAMT 1993)*, Dec 1993, pp. 735–738.

- [26] A. Meinhaj and J. Assaad, "Study of radar waveforms coded by pseudorandom sequences automotive collision application." International Conference Signal Processing applications and Technology (ICSPAT), 1997.
- [27] J. Detlefsen, E. Schmidhammer, and T. Troll, "Collision warning radar using pn-code-modulation and wave front reconstruction." Munich, Germany: In IRS 98, September 1998, pp. 363 – 370.
- [28] V. Filimon and J. Buechler, "a pre-crash radar sensor system based on pseudo-noise coding." Boston: IEEE MTT-S International Microwave Symposium, June 2000.
- [29] M. Watanabe, K. Inomata, S. Noda, K. Okazaki, and H. Yamabuchi, "A sideways-looking radar and its measuring principles." London: 31st European Microwave conference, 2001, pp. 261–264.
- [30] M. Corporation, "Crash avoidance flr sensors," *Microwave Journal*, pp. 122–126, July 1994.
- [31] Reed, "Side zone automotive radar criteria for target classification," *Proc. Intelligent Vehicle Symp*, pp. 361–363, 1995.
- [32] G. et la, "Hardware evaluation of heavy truck side and rear object detection system," *SAE Technical Paper Series*, no. 951010, 1995.
- [33] Mazzae and Garrott, "Human performance evaluation of heavy truck side object detection system," *SAE Technical Paper Series*, no. 951011, 1995.
- [34] H. Groll, J. Detlefsen, N. Kees, and E. Schmidhammer, "Transmitter location multiplexing for an automotive collision warning system in the mm-wave range." In Proceeding ISRAMT, September 1995, pp. 31–34.
- [35] N. Kees, E. Schmidhammer, and J. Detlefsen, "Realization of transmitter location multiplexing for angular resolution enhancement of a collision warning radar." Sindelfingen: In Mikrowellen und Optronik, May 1995, pp. 618–622.
- [36] R. Dixit, "Automotive radar-development status." IEEE MTT-S International Microwave Symposium, 1996, pp. 317–320.
- [37] Zimmermann, B. Wiesbeck, and W. Kehrbeck, "24 ghz microwave close-range sensors for industrial measurement applications," *Microwave Journal*, pp. 228–238, May 1996.
- [38] P. F. Swart and L. R. Nieuwkerk, "Collision avoidance radar able to differentiate objects." Jerusalem: 27th EuMC'97, September 1997.

- [39] U. Siart and J. Detlefsen, "Modulation technique and data acquisition in a multifunctional polarimetric near range radar sensor." Nantes, France: In PIERS 98, July 1998.
- [40] H. O. Groll, J. Detlefsen, , and U. Siart, "Multi-sensor-systems at mm-wave range for automotive applications." Peking, China: CIE International Conference on Radar, October 2001, pp. 150–153.
- [41] J. B. Tsui, *Fundamentals of Global Positioning System Receivers: a Software Approach*. New York: Wiley, 2000.
- [42] G. D. Abowd and E. Mynatt, "Charting past, present, and future research in ubiquitous computing," *ACM Transactions on Computer-Human Interaction*, vol. 7, no. 1, pp. 29–58, 2000.
- [43] R. Want, A. Hopper, V. Falcao, and J. Gibbons, "The active badge location system," *ACM Transactions on Information Systems*, vol. 10, no. 1, pp. 91–102, 1992.
- [44] B. N. Schilit and N. Adams, "The parctab mobile computing system." Napa, California, USA: In Proceedings of the Fourth Workshop on Workstation Operating Systems, October 1993, pp. 34–39.
- [45] D. Kirsch and T. Starner, "The locust swarm: An environmentally-powered, networkless location and messaging system." Boston, Massachusetts, USA: In Proceedings of the First International Symposium on Wearable Computers, October 1997.
- [46] E. Foxlin, M. Harrington, and G. Pfeifer, "Constellation: A wide-range wireless motion-tracking system for augmented reality and virtual set applications." Orlando, Florida, USA: In Proceedings of the 25th Annual Conference on Computer Graphics, July 1998, pp. 371–378.
- [47] N. B. Priyantha, A. Chakraborty, and H. Balakrishnan, "The cricket location support system." Boston, Massachusetts, USA: In Proceedings of the Sixth International Conference on Mobile Computing and Networking (ACM MobiCom), August 2000.
- [48] P. Bahl and V. N. Padmanabhan, "Radar: An in-building rf-based user location and tracking system," vol. 2. Tel-Aviv, Israel: In Proceedings of IEEE Conference on Computer Communications (INFOCOM), March 2000, pp. 775–784.
- [49] P. Castro, P. Chiu, T. Kremenek, and R. Muntz, "A probabilistic room location service for wireless networked environments." Atlanta, Georgia, USA: In Proceedings of Ubicomp 2001, Ubiquitous Computing, September 2001, pp. 18–34.

- [50] Y. Wang, X. Jia, H. K. Lee, and G. Y. Li, "An indoor wireless positioning system based on wlan infrastructure." Melbourne, Australia: 6th Int Symp on Satellite Navigation Technology Including Mobile Positioning and Location Services, July 2003.
- [51] E. Elnahrawy, X. Li, and R. P. Martin, "The limits of localization using signal strength: A comparative study." Santa Clara, CA: Proceedings of the First IEEE International Conference on Sensor and Ad hoc Communications and Networks, October 2004.
- [52] K. Pahlavan, X. Li, and J. Makela, "Indoor geolocation science and technology," *IEEE Commun. Mag.*, vol. 40, pp. 112–118, Feb. 2002.
- [53] Z. Xiang, S. Song, J. Chen, H. Wang, J. Huang, and X. Gao, "A wireless lan based indoor positioning technology," *IBM J. Res. and Dev.*, vol. 48, no. 5/6, pp. 617–626, 2004.
- [54] G. Messier, M. Fattouche, and B. R. Petersen, "Locating an is-95 mobile using its signal," vol. II. Calgary, AB, Canada: The Tenth International Conference on Wireless Communications Wireless 98, July 1998, pp. 562–574.
- [55] A. Ward, A. Jones, and A. Hopper, "A new location technique for the active office," *IEEE Personal Communications*, vol. 4, no. 5, pp. 42–47, October 1997.
- [56] M. Hazas and A. Ward, "A novel broadband ultrasonic location system," vol. 2498. Sweden: In Proceedings of UbiComp 2002, Fourth International Conference on Ubiquitous Computing, September 2002, pp. 264–280.
- [57] —, "A high performance privacy-oriented location system." Dallas-Fort Worth, USA: In Proceedings of PerCom 2003, First IEEE International Conference on Pervasive Computing and Communications, March 2003, pp. 216–223.
- [58] E. Brookner, "Phase array radars," *Sci. Amer.*, vol. 252, no. 2, p. 94, 1985.
- [59] C. E. Cook and W. M. Siebert, "The early history of pulse compression radar," *IEEE Trans. Aerosp. Electron. Syst.*, vol. AES-24, no. 6, pp. 825–833, 1988.
- [60] V. L. Newhouse, D. Cathignol, and J. Y. Chapelon, "Introduction to ultrasonic pseudo-random code systems," in *Progressing Medical Imaging*. V. L. Newhouse. Ed. New Yourk: Springer-Verlag, 1988, pp. 215–226.
- [61] J. Y. Chapelon, "Pseudo-random correlation imaging and system characterization," in *Progressing Medical Imaging*. V. L. Newhouse. Ed. New Yourk: Springer-Verlag, 1988, pp. 227–246.

- [62] D. Cathignol, "Pseudo-random correlation flow measurements," in *Progressing Medical Imaging*. V. L. Newhouse. Ed. New Yourk: Springer-Verlag, 1988, pp. 247–279.
- [63] V. L. Newhouse, "Pseudo-random characterization of time varying media," in *Progressing Medical Imaging*. V. L. Newhouse. Ed. New Yourk: Springer-Verlag, 1988, pp. 281–290.
- [64] Y. Takeyuchi, "An investigation of a spread energy method for medical ultrasound system," *Ultrasonics*, vol. 17, pp. 219–224, 1979.
- [65] C. R. Meyer, "Preliminary results on a system for wideband reflection-mode ultrasonic attenuation imaging," *IEEE Trans. Sonics Ultrason.*, vol. SU-29, p. 12, 1982.
- [66] S. Kiryu, T. Moriya, M. Yosizawa, and T. Fuse, "Fm chirp pulse compression system for ultrasonic-tomography," in *Proc. Int. symp. Noise and clutter Rejection in Radars and Imaging Sensors*, p. 176, 1984.
- [67] J. K. Kayani, S. F. Russell, and S. J. Wormley, "Self-noise suppression in ultrasonic correlation systems." Plenum, New York: 23rd Annual Review of Progress in Quantitative Nondestructive Evaluation, August 1996.
- [68] S. F. Russell, J. K. Kayani, M. A. K. Afzal, and S. J. Wormley, "Integrity monitoring of pressurized gas cylinders using the spread-spectrum ultrasonic evaluation technique." University of Washington, Seattle Washington: 22nd annual Review of Progress in Quantitative NDE, August 1995.
- [69] J. K. Kayani and S. F. Russell, "Choice of spreading waveform and correlation filter for self-noise suppression in ultrasonic correlation systems." University of Washington, Seattle Washington: 22nd annual Review of Progress in Quantitative NDE, August 1995.
- [70] M. A. K. Afzal, S. F. Russell, J. K. Kayani, and S. J. Wormley, "Application of spread-spectrum ultrasonic evaluationsystem to flaw detection in concrete." University of Washington, Seattle Washington: 22nd annual Review of Progress in Quantitative NDE, August 1995.
- [71] S. J. Wormley and S. F. Russell, "An application of direct-sequence spread-spectrum ultrasonics to global inspection of bridge components." Snowmass Village, Colorado: 21st Review of Progress in Quantitative NDE Snowmass Conference Center, August 1994.



- [72] J. K. Kayani, S. F. Russell, M. A. K. Afzal, and K. F. Hoech, "Analysis and design of two lab-grade prototype instruments for direct-sequence spread-spectrum ultrasonic evaluation." Snowmass Village, Colorado: 21st Review of Progress in Quantitative NDE Snowmass Conference Center, August 1994.
- [73] S. F. Russell, J. K. Kayani, M. A. K. Afzal, , and S. Bae, "Direct-sequence spread-spectrum ultrasonic evaluation system design." Snowmass Village, Colorado: 21st Review of Progress in Quantitative NDE Snowmass Conference Center, August 1994.
- [74] S. F. Russell, "Theory of spread-spectrum ultrasonic evaluation," vol. 13A. Bowdoin College, Brunswick, Maine: 20th Review of Progress in Quantitative NDE, August 1993, pp. 841–846.
- [75] M. A. K. Afzal, S. F. Russell, and S. J. Wormley, "Signal processing simulations for a direct-sequence spread-spectrum ultrasonic evaluation system," vol. 13A. Bowdoin College, Brunswick, Maine: 20th Review of Progress in Quantitative NDE, August 1993, pp. 847–854.
- [76] S. Bae and S. F. Russell, "Partial-length correlation theory for spread-spectrum ultrasonic evaluation application," vol. 13A. Bowdoin College, Brunswick, Maine: 20th Review of Progress in Quantitative NDE, August 1993, pp. 825–832.
- [77] O. A. Aly and A. S. Omar, "New implementation of the correlation function of the pn code for application in automotive radars," vol. 3. Columbus Ohio USA: IEEE APS Int. Symp., June 2003, pp. 272–275.
- [78] —, "A sideways-looking radar signal processing," vol. 3. San Antonio Texas USA: IEEE APS Int. Symp., June 2002, pp. 376–379.
- [79] A. Meinhaj, J. Assaad, M. Zaizouni, N. Goudard, and J. M. Rouvaen, "Study of radar waveforms coded by pseudorandom sequences: automotive collision avoidance application." Int. Conf. Signal Processing Applications and Technology (ICSPAT), 1997.
- [80] J. Detlefsen, E. Schmidhammer, and T. Troll, "Collision warning radar using pn-code-modulation and wavefrontreconstruction." Munich, Germany: Int IRS, September 1998, pp. 360–370.
- [81] M. I. Sobhy, K. H. Moustafa, and M. Y. Makkey, "Real-time processing of noisy rf pulses." London, UK: in Proceeding of the 32st European Microwave Conference, September 2001.
- [82] A. Abbate, C. M. Decusatis, and P. K. Das, *Wavelets and Subbands Fundamentals and Applications*. Bosten: Birkhaeuser, 2002.

- [83] D. L. Donoho, "De-noising by soft-thresholding," *IEEE Transactions on Information Theory*, vol. 41/3, pp. 613–627, May 1995.
- [84] C. Wren, A. Azarbayejani, T. Darrell, and A. Pentland, "Pfinder: Realtime tracking of the human body," *IEEE Transactions on Pattern Analysis and Machine Intelligence*, vol. 19, no. 7, pp. 780–785, July 1997.
- [85] D. L. de Ipina, "Video-based sensing for wide deployment of sentient spaces." Barcelona, Spain: In Proceedings of the Second PACT 2001 Workshop on Ubiquitous Computing and Communications, September 2001.
- [86] A. Harter, A. Hopper, P. Steggles, A. Ward, and P. Webster, "The anatomy of a context-aware application." Seattle, Washington, USA: In Proceedings of the Fifth International Conference on Mobile Computing and Networking (MobiCom), August 1999.
- [87] M. Addlesee, R. Curwen, S. Hodges, J. Newman, P. Steggles, A. Ward, and A. Hopper, "Implementing a sentient computing system," *IEEE Computer*, vol. 34, no. 8, pp. 50–56, August 2001.
- [88] N. Priyantha, A. Miu, H. Balakrishnan, and S. Teller, "The cricket compass for context-aware mobile applications." Rome, Italy: In Proceedings of the Seventh International Conference on Mobile Computing and Networking (ACM MobiCom), July 2001.
- [89] C. Randell and H. Muller, "Low cost indoor positioning system." Atlanta, Georgia, USA: In Proceedings of Ubicomp 2001 Ubiquitous Computing, September 2001, pp. 42–48.
- [90] S. V. Vaseghi, *Advanced digital signal processing and noise reduction*, 2nd ed. New York, USA: LTD, John Wiley & Sons, 2000.
- [91] X. Li and K. Pahlavan, "Super-resolution toa estimation with diversity for indoor geolocation," *IEEE Transactions on Wireless Communications*, vol. 3, no. 1, pp. 224–234, Jan. 2004.
- [92] L. Dumont, M. Fattouche, and G. Morrison, "Super-resolution of multipath channels in a spread spectrum location system," *Electron. Lett.*, vol. 30, pp. 1583–1584, Sept 1994.
- [93] M. O'Donnell, "Coded excitation systems for improving the penetration of real-time phased-array imaging systems," *IEEE Trans. Ultrason., Ferroelect., Freq. Cont.*, vol. 39, pp. 341–351, May 1992.
- [94] J. Ruprecht and M. Rupf, "On the search for good aperiodic binary invertible sequences," *IEEE Trans. Inform. Theory*, vol. 42, pp. 1604–1612, Sep. 1996.

- [95] Y. Wang, K. Metzger, D. N. Stephens, G. William, and M. O'Donnell, "Coded excitation with spectrum inversion (cexsi) for ultrasound array imaging," *IEEE Trans. Ultrason., Ferroelect., Freq. Cont.*, vol. 50, no. 7, pp. 805–823, July 2003.
- [96] B. Haider, P. Lewin, and K. Thomenius, "Pulse elongation and deconvolution filtering for medical ultrasonic imaging," in *Proc. IEEE Ultrason. Symp.*, pp. 1303–1308, Oct. 1995.
- [97] A. R. Brenner, L. Eck, W. Wilhelm, and T. G. Noll, "Improved resolution and dynamic range in medical ultrasonic imaging using depth-dependent mismatched filter," in *Proc. IEEE Ultrason. Symp.*, pp. 1475–1480, Oct. 1997.
- [98] G. S. Jeng, S. Huang, P. C. Li, and J. Tsao, "A novel pulse compression technique using inverse filtering in frequency domain," in *Proc. IEEE Ultrason. Symp.*, pp. 1535–1538, Oct. 2001.
- [99] M. Ackroyd and F. Ghani, "Optimum mismatched filters for sidelobe suppression," *IEEE Trans. Aerosp. Electron. Syst.*, vol. 9, no. 2, pp. 214–218, 1972.
- [100] S. Zoraster, "Minimum peak range sidelobes filter for binary phased-coded waveforms," *IEEE Trans. Aerosp. Electron. Syst.*, vol. 16, no. 1, pp. 112–115, 1979.
- [101] D. K. Ghodgaonkar, O. P. Gandhi, and M. J. Haggmann, "Estimation of complex permittivities of a three-dimensional inhomogeneous biological bodies," *IEEE Trans. Microwave Theory Tech.*, vol. MTT-31, pp. 442–446, Jun. 1983.
- [102] A. Broquetas, J. Romeu, J. M. Rius, A. R. Elias-Fuste, A. Cardama, and L. Jofre, "Cylindrical geometry: A further step in active microwave tomography," *IEEE Trans. Microwave Theory Tech.*, vol. 39, pp. 836–844, May. 1991.
- [103] N. Joachimowicz, J. J. Mallorqui, J. C. Bolomey, and A. Broquetas, "Convergence and stability assessment of newton-kantorovich reconstruction algorithm for microwave tomography," *IEEE Trans. Med. Imag.*, vol. 17, pp. 562–570, Aug. 1998.
- [104] N. Joachimowicz, C. Pichot, and J. P. Hugonin, "Inverse scattering: An iterative numerical method for electromagnetic imaging," *IEEE Trans. Antennas Propagat.*, vol. 39, pp. 1743–1752, Dec. 1991.
- [105] S. Caorsi, G. L. Gagnani, and M. Pastorino, "Reconstruction of dielectric permittivity distributions in arbitrary 2-d inhomogeneous biological bodies by a multiviewmicrowave numerical method," *IEEE Trans. Med. Imag.*, vol. 12, pp. 232–239, Jun. 1993.

- [106] M. J. Akhtar and A. S. Omar, "Reconstructing permittivity profiles using integral transforms and improved renormalization techniques," *IEEE Trans. Microwave Theory Tech.*, vol. 48, pp. 1385–1393, Aug. 2000.
- [107] G. C. Giakos, M. Pastorino, F. Russo, S. Chowdhury, N. Shah, and W. Davros, "Noninvasive imaging for the new century," *IEEE Instrumentation Meas. Mag.*, vol. 2, pp. 32–35, Jun. 1999.
- [108] M. Pastorino, "Recent inversion procedures for microwave imaging in biomedical, subsurface detection and nondestructive evaluation," *special issue on Imaging Measurement Systems*, vol. 36, pp. 257–269, 2004.
- [109] K. Belkebir, R. E. Kleinman, and C. Pichot, "Microwave imaging location and shape reconstruction from multifrequency scattering data," *IEEE Trans. Microwave Theory Tech.*, vol. 45, pp. 469–476, Apr. 1997.
- [110] I. T. Rekanos and T. D. Tsiboukis, "A finite element-based technique for microwave imaging of two-dimensional objects," *IEEE Trans. Instrum. Meas.*, vol. 49, pp. 234–239, Apr. 2000.
- [111] S. J. Lockwood and H. Lee, "Pulse-echo microwave imaging for nde of civil structures: Image reconstruction, enhancement, and object recognition," *Int. Journal Imaging Systems and Technol.*, vol. 8, pp. 407–412, Apr. 1997.
- [112] R. E. Kleinman and P. M. van den Berg, "Two-dimensional location and shape reconstruction," *Radio Sci.*, vol. 29, pp. 1157–1169, Jul.-Aug. 1994.
- [113] A. G. Tjihuis, K. Belkebir, A. C. S. Litman, and B. P. de Hon, "Theoretical and computational aspects of 2-d inverse profiling," *IEEE Trans. Geosci. Remote Sensing*, vol. 39, pp. 1316–1330, Jun. 2001.
- [114] M. K. J. Langenberg and R. Schneider, "Microwave imaging of defects in solids." Snowmass Village, Colorado, USA: Proc. 21st Annual Review of Progress in Quantitative NDE, Jul.-Aug. 1994.
- [115] Z. Q. Zhang and Q. H. Liu, "Two nonlinear inverse methods for electromagnetic induction measurements," *IEEE Trans. Geosci. Remote Sensing*, vol. 39, pp. 1331–1339, Jun. 2001.
- [116] S. Caorsi, A. Massa, M. Pastorino, M. Raffetto, and A. Randazzo, "Microwave imaging of cylindrical inhomogeneities based on an analytical forward solver and multiple illuminations." Stresa, Italy: Proc. IEEE Int. Workshop on Imaging Systems and Techniques (IEEE IST 2004), May. 2004, pp. 100–105.

- [117] S. Caorsi, M. Donelli, A. Massa, and M. Pastorino, "Improved microwave imaging procedure for non-destructive evaluations of two dimensional structures," *IEEE Trans. Antennas Propagat.*, vol. 52, no. 6, pp. 1386–1397, Jun. 2004.
- [118] M. Pastorino, S. Caorsi, A. Massa, and A. Randazzo, "Reconstruction algorithms for electromagnetic imaging," *IEEE Trans. Instrum. Meas.*, vol. 53, no. 3, pp. 692–699, Jun. 2004.
- [119] M. Pastorino, "Short-range microwave inverse scattering techniques for image reconstruction and applications," *IEEE Trans. Instrum. Meas.*, vol. 47, no. 6, pp. 1419–1427, Dec. 1998.
- [120] S. Caorsi, A. Costa, and M. Pastorino, "Microwave imaging within the second-order born approximation: Stochastic optimization by a genetic algorithm," *IEEE Trans. Antennas Propagat.*, vol. 49, no. 1, pp. 22–31, Jan. 2001.
- [121] M. Pastorino, "A microwave tomographic approach based on a global optimization procedure." Pisa, Italy: Proc. Progress in Electromagnetics Research Symposium (PIERS 2004), Mar. 2004, pp. 28–31.
- [122] —, "Stochastic microwave inversion algorithms for image reconstruction and applications." Nice, France: International Symposium on Antennas (JINA '02), Mini-Symposium on Inverse Scattering, Nov. 2002, pp. 19–24.
- [123] C. Pichot, J. Y. Dauvignac, I. Aliferis, E. L. Brusq, R. Ferraye, and V. Chatele, "Recent nonlinear inversion methods and measurement systems for microwave imaging." Stresa, Italy: Proc. IEEE Int. Workshop on Imaging Systems and Techniques (IEEE IST2004), May 2004, pp. 95–99.
- [124] M. Lambert and D. Lesselier, "Binary-constrained inversion of a buried cylindrical obstacle from complete and phaseless magnetic fields," *Inverse Problems*, vol. 16, pp. 563–576, Jun. 2000.
- [125] X. Li, S. K. Davis, S. C. Hagness, D. W. van der Weide, and B. D. V. Veen, "Microwave imaging via space-time beamforming: experimental investigation of tumor detection in multilayer breast phantoms," *IEEE Trans. Microwave Theory Tech.*, vol. 52, pp. 1856–1865, Aug. 2004.
- [126] G. P. Otto and W. C. Chew, "Microwave inverse scattering - local shape function imaging for improved resolution of strong scatterers," *IEEE Trans. Microwave Theory Tech.*, vol. 42, pp. 137–141, Jan. 1994.
- [127] T. M. Habashy and R. Mittra, "Review of some inverse methods in electromagnetics," *J. Opt. Soc. Amer. A, Opt. Image Sci.*, vol. 4, pp. 281–291, Jan. 1987.

- [128] J. Xia, T. M. Habashy, and J. A. Kong, "Profile inversion in a cylindrically stratified lossy medium," *Radio Sci.*, vol. 29, pp. 1131–1141, July-Aug. 1994.
- [129] T. M. Habashy, W. C. Chew, and E. Y. Chow, "Simultaneous reconstruction of permittivity and conductivity profiles in a radially inhomogeneous slab," *Radio Sci.*, vol. 21, pp. 635–645, July-Aug. 1986.
- [130] P. V. Frangos and D. I. Jaggard, "A numerical solution to the zakharov-shabat inverse scattering problem," *IEEE Trans. Antennas Propagat.*, vol. 39, pp. 74–79, Jan. 1991.
- [131] W. Tabarra, "Reconstruction of permittivity profiles from a spectral analysis of the reflection coefficient," *IEEE Trans. Antennas Propagat.*, vol. AP-27, pp. 241–248, Mar. 1979.
- [132] A. K. Jordan and H. D. Ladouceur, "Renormalization of an inverse-scattering theory for discontinuous profiles," *Phys. Rev. A, Gen. Phys.*, vol. 36, p. 4245, Nov. 1987.
- [133] G. R. Cooper, *Modern Communications and Spread Spectrum*. McGraw-Hill Book Company, 1986.
- [134] C. E. Cook, "Spread-spectrum communications," *IEEE Press*, 1983.
- [135] K. Pahlavan and A. H. Levesque, *Wireless Information Networks*. Wiley and Sons, March 1995.
- [136] L. Nikias and A. P. Petropulu, *Higher-Order Spectra analysis: a nonlinear signal processing framework*. New Jersey: PTR Prentice Hall, 1993.
- [137] S. G. Malat, "A theory for multiresolution signal decomposition," *IEEE Transaction on Pattern Analysis and Machine Intelligence*, vol. 11, no. 7, pp. 674–693, 1989.
- [138] A. N. akansu and R. A. Haddad, *Multiresolution signal decomposition: transforms, subbands, and wavelet*. New York: Academic Press, 1992.
- [139] D. L. Donoho and I. Johnstone, "Ideal spatial adaptation by wavelet shrinkage," *Biometika*, vol. 81, pp. 425–455, 1994.
- [140] O. Aly, G. Nadim, and A. Omar, "Wavelet packets de-noising of rf pulses based on higher-order-statistic thresholding." Poland: 11th International Workshop on Systems, Signals and Image Processing, IWSSIP'04, September 2004.

- [141] O. A. Aly, A. S. Omar, and A. Z. Elsherbeni, "Detection and localization of rf radar pulses in noise environments using wavelet packet transform and higher order statistics," *Progress In Electromagnetics Research, PIER*, vol. 58, pp. 301–317, 2006.
- [142] G. Childers, *Probability and random processes*. McGraw-Hill, 1997.
- [143] P. Ravier and P. O. Amblard, "Wavelet packets and de-noising based on higher-order-statistics for transient detection," *Signal Processing*, vol. 81, no. 9, pp. 1909–1926, August 2001.
- [144] O. A. Aly and A. Omar, "New implementation of the correlation function of the pn code for application in automotive radars," vol. 3. Columbus Ohio USA: IEEE APS Int. Symp, June 2003, pp. 272–275.
- [145] S. Elrod, G. Hall, R. Costanza, M. Dixon, and J. Rivieres, "Responsive office environments," *Communications of the ACM*, vol. 36, no. 7, pp. 84–85, July 1993.
- [146] A. Harter and A. Hopper, "A distributed location system for the active office," *IEEE Network, Special Issue on Distributed Systems for Telecommunications*, vol. 8, no. 1, pp. 62–70, January 1994.
- [147] T. Richardson, G. Mapp, F. Bennett, and A. Hopper, "Teleporting in an x window system environment," *IEEE Personal Communications Magazine*, vol. 1, no. 3, pp. 6–12, 1994.
- [148] J. Bacon, J. Bates, and D. Halls, "Location-oriented multimedia," *IEEE Personal Communications Magazine*, vol. 4, no. 5, pp. 48–57, 1997.
- [149] J. Finney and N. Davies, "Flump: The flexible ubiquitous monitor project," Internal report MPG-96-18, Lancaster University, Tech. Rep., 1996.
- [150] B. Schilit, N. Adams, and R. Want, "Context-aware computing applications." Santa Cruz, CA: Proceedings of the Workshop on Mobile Computing Systems and Applications, December 1994, pp. 85–90.
- [151] M. Lamming and M. Flynn, "Forget-me-not -intimate computing in support of human memory." Meguro Gajoen, Japan: Proceedings of 166 FRIEND21, International Symposium on Next Generation Human Interface, 1994.
- [152] P. Brown, J. Bovey, and X. Chen, "Context-aware applications: From the laboratory to the marketplace," *IEEE Personal Communications Magazine*, vol. 4, no. 5, pp. 58–64, 1997.

- 
- [153] E. Mynatt, M. Back, R. Want, and R. Frederick, "Audio aura: Light-weight audio augmented reality." Banff: Proceedings of the 4th Annual Symposium on User Interface Software and Technology (UIST '97), October 1997, pp. 211–212.
- [154] R. Y. Chiao and X. Hao, "Coded excitation for diagnostic ultrasound: a system developer's perspective," *IEEE Trans. Ultrason., Ferroelect., Freq. Cont.*, vol. 52, no. 2, pp. 160–170, Feb. 2005.
- [155] M. Wax and T. Kailath, "Detection of signals by information theoretic criteria," *IEEE Trans. Acoust. Speech Signal Processing*, vol. ASSP-33, no. 2, pp. 387–392, Apr. 1985.
- [156] R. E. Collin, *Foundation for microwave engineering*. New York, USA: McGraw-Hill, 1992.



# Curriculum Vitae

Name Omar Abdel-Gaber Mohamed Aly  
Date of Birth September 24, 1970 in Assiut  
Nationality Egyptian

## Education

Jun. 1988 Secondary School Certificate, Assiut, Egypt  
May 1993 Bachelor of Science in Electronics and Communication Engineering,  
Assiut University, Assiut, Egypt.  
Feb. 1998 Master of Science in Electronics and Communication Engineering,  
Assiut University, Assiut, Egypt.

## Work Experience

May 95 – Feb. 98: Demonstrator in electrical engineering Department, Assiut  
University, Egypt.  
Mar. 98 – Sept. 01: Assistance lecturer in Electrical Engineering Department, Assiut  
University, Egypt.  
Oct. 01 – Oct. 06 : Research Assistant in Department of Microwave and Communication  
Engineering FEIT-IESK, OVG university Magdeburg , Germany.

## Publications

- [1] Omar A.M. Aly and A.S. Omar, "Reconstructing Stratified Permittivity Profiles Using Super Resolution Techniques," IEEE Transactions on Microwave Theory and Techniques, vol. 54, no. 1, January 2006.
- [2] Ali Aassie Ali, Omar A.M. Aly and A.S. Omar, "Application of ESPRIT in Super-Resolution Microwave Imaging," proceedings of the VI Mediterranean microwave symposium (MMS'2006).
- [3] Omar A.M. Aly, A.S. Omar, and A.Z. Elsherbeni, "Detection and Localization of RF Radar Pulses in Noise environments using Wavelet Packet Transform and Higher Order Statistics," Journal of Electromagnetic Waves and Applications. Progress In Electromagnetics Research, PIER, vol. 58, pp. 301-317, January 2006.
- [4] Ali Aassie Ali, Omar A.M. Aly and A.S. Omar, "High Resolution WLAN Indoor Channel Parameter Estimation and Measurements for Communication and Positioning Applications at 2.4, 5.2 and 5.8 GHz," Accepted in IEEE Radio and Wireless Symposium (RWS 2006) San Diego, CA, 17-19 January 2006.
- [5] Omar A.M. Aly, A.S. Omar, "Spread Spectrum Ultrasonic Positioning System," Workshop on positioning and communication WPNC05. pp. 109-114, 17 March 2005.
- [6] Omar A.M. Aly, G. Nadim and A.S. Omar, "Wavelet Packets De-noising of RF Pulses Based on Higher-Order-Statistic Thresholding," 11th International Workshop on Systems, Signals and Image Processing, IWSSIP'04, Poland, 13-15 September 2004.
- [7] Omar A.M. Aly, A.S. Omar, "New Implementation of the Correlation Function of the PN Code for Application in Automotive Radars," IEEE APS Int. Symp., Columbus Ohio USA, vol. 3, pp. 272-275, 22-27 June 2003.
- [8] Omar A.M. Aly, A.S. Omar, "A Sideways-Looking Radar Signal Processing," IEEE APS Int. Symp., San Antonio Texas USA, vol. 3, pp. 376-379, 16-21 June, 2002.

Magdeburg, 25.09.2006

(Omar Aly)